The Role of G protein alpha 11 in Calcium and Glucose Homeostasis

A thesis submitted to the

University of Oxford



in candidature for the degree of

Doctor of Philosophy

by

Anna Katharina Glück

Academic Endocrine Unit

Radcliffe Department of Medicine

University of Oxford

Somerville College,

University of Oxford

Trinity Term 2020

Acknowledgements

I would like to express my deepest gratitude to my supervisor Professor Rajesh Thakker who has given me the opportunity to undertake a DPhil in his group. His guidance has contributed significantly to my personal growth over the last four years, and he was always fully supportive of my scientific ideas and professional development. I am indebted to Dr. Kate Lines, my second supervisor, whose support has been instrumental for the success of my studies. Her constant motivation and positivity are inspiring, and have nurtured my passion for science. I would also like to thank Dr. Caroline Gorvin for her supervision during my first year and for introducing me to many useful techniques. Moreover, I am grateful to the funding bodies that have supported my work: the European Commission, the Wellcome Trust, Boehringer Ingelheim Fonds and the NIHR Oxford Biomedical Research Centre Programme.

A very special thanks to all members of the Thakker group for their collaborative spirit, and for making the lab such a cheerful and productive workplace. I am fortunate to have been part of the European Training Network CaSR Biomedicine, and I am grateful for all the valuable training and advice given by members of the consortium, especially Professor Isabella Ellinger, Dr. Rupert Ecker, Professor Enikö Kállay and Mie Kronborg Olesen.

One of the highlights of my DPhil was my research stay in the group of Professor Michel Bouvier at the University of Montreal. The warm welcome received by all members of the lab, particularly Dr. Shane Wright, Dr. Monique Lagacé, Dr. Christian Le Gouill, Mireille Hogue and Professor Bouvier himself, made my time there truly memorable.

I am immensely grateful for all the time and effort spent by Dr. Nicholas Jennings to help me with proofreading of this thesis.

Finally, I would like to express my appreciation to my friends and family for their never-ending support and understanding of my limited free time.

Statement of Originality

All results presented in this thesis were generated by myself except where explicitly stated. *In vivo* mouse studies were conducted in collaboration with the Mary Lyon Centre (MRC Harwell). Research staff at the Mary Lyon Centre undertook animal husbandry, genotyping, plasma biochemistry and IPGTTs. Dsk7 tissue preparation, embedding and sectioning were performed by Dr. Sian Piret, and H&E staining of sections was performed and quantified by Dr. Valerie Babinsky (University of Oxford). Sanger sequencing was undertaken by sequencing technicians at the University of Oxford Department of Zoology. HEK293-Flp-In-Flag-CaSR cells were generated by Mie Kronborg Olesen. Analysis of patient DNA for mutations in *GNAQ* was performed by Manesh Modi (University of Oxford). Fluo-4 calcium mobilisation assays and cloning of the pBI-CMV2-*GNAQ* vector were conducted by Dr. Mark Stevenson (University of Oxford). Site-directed mutagenesis to introduce *GNAQ* mutations, Western blots shown in Figure 6.4 and Figure 6.8 panel B, and HEK293-Flp-In-TREX-CaSR cells were generated by Dr. Sara Falcone (University of Oxford).

Abstract

Guanine nucleotide-binding (G) proteins act as molecular switches to transduce stimuli received by G protein-coupled receptors (GPCRs) into intracellular responses. For example, $G\alpha_{11}$ mediates signalling by the calcium-sensing receptor (CaSR), a class C GPCR, to regulate calcium homeostasis. Germline CaSR and $G\alpha_{11}$ inactivating and activating mutations cause calcitropic disorders such as familial hypocalciuric hypercalcaemia (FHH) and autosomal dominant hypocalcaemia (ADH) types-1 and -2, respectively. In addition, non-calcitropic disorders may also occur, e.g. Nuf mice (model for ADH1) have impaired glucose metabolism. This thesis aims to: identify and characterise rare $G\alpha_{11}$ variants from online databases; investigate glucose metabolism of Dsk7 mice (model for ADH2); study CaSR signalling differences between $G\alpha_{11}$ and the closely related $G\alpha_q$; and explore CaSR functional selectivity and G protein biased signalling. My analysis revealed novel $G\alpha_{11}$ variants that cause CaSR signalling abnormalities *in vitro* and are associated with hypercalcaemia in patients. Moreover, some $G\alpha_{11}$ variants also disrupted signalling by prototypical class A GPCRs and promoted biased and promiscuous signalling. In contrast, $G\alpha_{11}$ gain-of-function did not impair glucose homeostasis or pancreatic islet architecture in Dsk7 mice, indicating that other G proteins may be involved in these non-calcitropic CaSR functions. $G\alpha_q$ mutations were not found in patients with FHH or ADH, and engineering FHH2- and ADH2-associated $G\alpha_{11}$ mutations in $G\alpha_q$ did not alter $G\alpha_q$ function, thereby highlighting functional differences between them. Analysis of CaSR functional selectivity showed that the CaSR is a promiscuous receptor which activates eight G proteins and that clinically approved CaSR allosteric modulators can promote biased signalling. In summary, my thesis illustrates the importance of $G\alpha_{11}$ for CaSR signalling, demonstrated by identification of additional FHH2 mutants, and that $G\alpha_{11}$ mutations disrupt signalling by other GPCRs, thereby possibly leading to wider effects. Additionally, CaSR biased-signalling highlights the importance of G proteins other than $G\alpha_{11}$ for this GPCR.

Contents

Abstract iv

List of figures xi

List of tables xxii

Abbreviations xxv

1 Introduction 1

1.1 Heterotrimeric guanine nucleotide-binding (G) proteins 2

1.1.1 Overview of G proteins 3

1.1.2 G alpha q/11 7

1.1.3 G alpha s 13

1.1.4 G alpha i/o 14

1.1.5 G alpha 12/13 14

1.1.6 G beta gamma 14

1.2 G protein-coupled receptors (GPCRs) 15

1.2.1 Signalling and trafficking 15

1.2.2 Structure 16

1.2.3 The Calcium-Sensing receptor (CaSR) 18

1.3 The CaSR as a regulator of extracellular calcium homeostasis 19

1.3.1 CaSR actions in the parathyroid glands 21

1.3.2 CaSR actions in the kidneys 21

1.4 Calcitropic disorders of the CaSR signalling pathway 22

1.4.1 Hypercalcaemic disorders 24

1.4.2 Hypocalcaemic disorders 25
1.4.3 Disorders arising from CaSR Autoantibodies 26
1.4.4 Mouse models for inherited disorders of the CaSR signalling pathway 27
1.5 Non-calcitropic effects of the CaSR 29
1.5.1 Systemic glucose homeostasis 29
1.5.2 The role of the CaSR in systemic glucose homeostasis 32
1.6 CaSR structure and signalling 35
1.6.1 Crystal structure of the extracellular domain 35
1.6.2 Cell signalling and trafficking 37
1.6.3 Calcimimetics and calcilytics 38
2 Thesis objectives 47
3 Materials and methods 49
3.1 Buffer and stock solutions 50
3.1.1 For DNA-based techniques 50
3.1.2 For analysis of protein expression 50
3.1.3 For functional assays 52
3.2 Compounds 55
3.3 Primers 56
3.3.1 Sequencing primers 56
3.3.2 Site-directed mutagenesis primers 57
3.4 Antibodies 58
3.5 Cell culture 59
3.5.1 Cell lines 59

3.5.2 Media & Culture Conditions 59

3.5.3 Generation of stable cell lines 60

3.6 DNA-based techniques 61

3.6.1 Site-directed mutagenesis 61

3.6.2 Transformation of ultracompetent bacteria 61

3.6.3 Plasmid DNA extraction 62

3.6.4 Sanger sequencing 63

3.7 Analysis of protein expression 64

3.7.1 Western blot analysis 64

3.7.2 Immunocytochemistry 69

3.7.3 Haematoxylin and Eosin (H&E) staining 70

3.7.4 Immunohistochemistry 70

3.8 Functional assays 72

3.8.1 Luciferase reporter assays 72

3.8.2 NanoBiT assays 75

3.8.3 GTPase activity assays 78

3.8.4 Fluo-4 calcium mobilisation assay 80

3.8.5 AlphaScreen assays 83

3.8.6 Bioluminescence Resonance Energy Transfer (BRET) 86

3.8.7 IP-One assays 90

3.9 *In vivo* studies 93

3.9.1 Plasma Biochemistry 93

3.9.2 Intraperitoneal Glucose tolerance tests (IPGTTs) 93

3.9.3 Tissue preparation and embedding 94

3.10 Bioinformatics analysis **95**

3.10.1 Evolutionary conservation 95

3.10.2 Prediction of pathogenicity 95

3.10.3 Three-dimensional homology modelling 95

3.11 Data analysis **96**

3.11.1 Western blot quantification 96

3.11.2 Tissue cytometry 96

3.11.3 Statistical analyses 98

3.12 Patients and ethics **98**

4 Identification and characterisation of rare *GNA11* variants **100**

4.1 Aims **101**

4.2 Results **101**

4.2.1 Identification of *GNA11* variants in large-scale sequence databases. 101

4.2.2 Structural characterisation using PyMOL 106

4.2.3 Expression of selected $G\alpha_{11}$ variants. 109

4.2.4 Effects of rare $G\alpha_{11}$ variants on CaSR signalling 111

4.2.5 Effects on GPCRs other than CaSR 120

4.3 Discussion **125**

4.3.1 Prevalence of FHH2- and ADH2-causing mutations 125

4.3.2 $G\alpha_{11}$ structure-function 126

4.3.3 Effects on GPCRs other than CaSR 128

4.3.4 Biased and promiscuous mutations 129

5 Investigation of glucose metabolism in DSK7 mice **132**

5.1 Aims **133**

5.2 Results **134**

5.2.1 Viability 134

5.2.2 Fasted plasma biochemistry 135

5.2.3 Glucose metabolism 142

5.3 Discussion **149**

5.3.1 Fasted plasma biochemistry 149

5.3.2 Glucose metabolism 150

6 Differences between *GNA11* and *GNAQ* **155**

6.1 Aims **156**

6.2 Results **158**

6.2.1 Investigation of *GNAQ* as a candidate gene for FHH/ADH 158

6.2.2 Differences between $G\alpha_q$ and $G\alpha_{11}$ 164

6.2.3 Compensation of FHH-causing $G\alpha_{11}$ mutations 172

6.3 Discussion **176**

6.3.1 Investigation of *GNAQ* as a candidate gene for FHH/ADH 176

6.3.2 Expression studies 177

6.3.3 Functional effects on CaSR signalling 178

6.3.4 Allosteric CaSR modulators 180

6.3.5 Implications for FDA approved drugs 180

7 CASR functional selectivity **183**

7.1 Aims **184**

7.2 Results **185**

7.2.1 CaSR functional selectivity 185
7.2.2 Effects of CaSR modulators on functional selectivity 193
7.2.3 Effects of disease-causing CaSR mutations 214
7.3 Discussion **217**
7.3.1 CaSR functional selectivity 218
7.3.2 Ligand biased signalling 221
7.3.3 Effects of disease-causing CaSR mutations 225
8 Conclusion **226**
9 Future plans **229**
Appendix **233**
A. Tables **234**
Bibliography **246**

List of figures

Figure 1.1 Overview of G protein-coupled receptor (GPCR) signalling.....2

Figure 1.2 Structure of heterotrimeric G proteins and small GTPases. 4

Figure 1.3 Heterotrimeric G protein cycle. 5

Figure 1.4 Crystal structure of regulator of G protein signalling 8 (RGS8) (blue) in complex with activated $G\alpha_q$ (green).....5

Figure 1.5 Phylogenetic relationship of human Gα subunits. 6

Figure 1.6 Schematic overview of signalling pathways activated by the $G\alpha_{q/11}$ family...8

Figure 1.7 Structure of full-length phospholipase C β_3 ($PLC\beta_3$) (beige) in complex with activated $G\alpha_q$ (green) 9

Figure 1.8 Structure of the p63RhoGEF (p63) (beige) in complex with activated $G\alpha_q$ (green) and RhoA (blue).....10

Figure 1.9 Structural basis for the inhibition of $G\alpha_q$ (green) by YM-254890 (red) 11

Figure 1.10 90% of amino acids of *GNAQ* and *GNA11* are identical.....12

Figure 1.11 Cryo-electron microscopy structure of membrane-bound Adenylyl cyclase 9 (AC9) (beige) in complex with activated $G\alpha_s$ (green).....13

Figure 1.12 Crystal structures of class A, B, C and F GPCRs in complex with ligands. 17

Figure 1.13 Classification of Class C GPCRs according to evolutionary conservation. 18

Figure 1.14 CaSR expression across a range of tissues. 19

Figure 1.15 Overview of extracellular calcium (Ca^{2+}_e) homeostasis. 20

Figure 1.16 Overview of CaSR signalling in the chief cells of the parathyroid gland, and associated disorders. 23

Figure 1.17 Appearance of CASR +/+ (top), +/- (middle) and -/- (bottom) mice at 23 days of age. 28

Figure 1.18 Overview of systemic glucose homeostasis. 30

Figure 1.19 Schematic representation of pancreas histology. 31

Figure 1.20 Proposed model for CaSR-mediated functional coupling of pancreatic ß cells. 34

Figure 1.21 Structure of the active CaSR extracellular domain (ECD) 36

Figure 1.22 Overview of CaSR signalling pathways and cross-talk 38

Figure 1.23 Chemical structure of the CaSR positive allosteric modulator cinacalcet. 40

Figure 1.24 Chemical structure of the CaSR positive allosteric modulator AC-265347 42

Figure 1.25 Chemical structure of the CaSR positive allosteric modulator Etelcalcetide 43

Figure 1.26 Chemical structure of the CaSR positive allosteric modulator NPS-2143 44

Figure 3.1 pGL4.33[luc2P/SRE/Hygro] vector map. 73

Figure 3.2 Illustration of NanoBiT assays. 76

Figure 3.3 Glo™ assay principles. 78

Figure 3.4 Structure of Fluo-4 acetoxymethyl ester (AM). 81

Figure 3.5 Schematic illustration of AlphaScreen technology 84

Figure 3.6 Overview of BRET. 86

Figure 3.7 Schematic representation of ebBRET. 88

Figure 3.8 Schematic representation of IP-One assays. 91

Figure 3.9 Protocol for Dsk7 intraperitoneal glucose tolerance tests (IPGTTs) and terminal bleeds. 94

Figure 3.10 Overview of semi-automated detection of α, ß, and proliferating cells within pancreatic islets using StrataQuest. 97

Figure 4.1 Comparison of expected (shown in black) versus observed (diagonal lines) synonymous and missense (A) *GNAQ* (B) *GNA11* (C) *GNA14 and (D) GNA15* variants in the gnomAD database[241] 103

Figure 4.2 Evolutionary conservation of 79 *GNA11* variants found in the dbSNP database in $G\alpha_{11}$ orthologs (mouse, frog, zebrafish, chicken) and Gα paralogs (*GNAQ*, *GNAI1*, *GNAS2*, *GNA12*) 106

Figure 4.3 Rare *GNA11* variants selected from dbSNP (shown in orange) and the DiscoveEHR cohort (shown in blue) mapped to the 7 exomes of *GNA11*. 106

Figure 4.4 (A) Gly51 (orange) is forming hydrogen bonds with GDP (black), Thr54 and Phe55 in the α1 helix. 107

Figure 4.5 (A) Crystal structure (PDB code 3sn6) of B2AR (purple) in complex with $G\alpha_s$ (light grey) Gß (dark grey) and Gγ (turquoise). 108

Figure 4.6 (A) Arg37 (orange) in the αN helix of $G\alpha_{11}$ (green) forms polar contacts (black, dashed lines) with Arg134 and Ala135 (light pink) of M_1R (purple) 109

Figure 4.7 (A) Protein expression of selected *GNA11* variants from dbSNP, assessed by Western blot analysis..... 111

Figure 4.8 Overview of CaSR-mediated signalling and downstream assays..... 112

Figure 4.9 Six *GNA11* variants did not affect CaSR signalling in SRE and NFAT-RE luciferase reporter assays..... 113

Figure 4.10 Dose-response curves of HEK293AG$\alpha_{q/11}$-KO-CaSR cells (A,B,D,E) and (C,F) HEK293-Flp-In-Flag-CaSR cells transiently transfected with either WT (black) or variant (red) Gα_{11}..... 114

Figure 4.11 Dose-response curves of HEK293AG$\alpha_{q/11}$-KO-CaSR cells (SRE, NFAT-RE) and HEK293-Flp-In-Flag-CaSR cells (p63) expressing either WT (black line) or variant (red line) Gα_{11}..... 115

Figure 4.12 GTPase activity of Gα_{11} Gly51Arg..... 116

Figure 4.13 Gln152His (red line) shows significantly increased calcium-induced responses compared to WT (black line) in (A) SRE and (B) NFAT-RE luciferase reporter assays..... 117

Figure 4.14 (A) CaSR-mediated signalling responses of Gα_{11} Gly66Asp. NFAT-RE responses were significantly increased..... 118

Figure 4.15 (A) CaSR-mediated signalling responses of Gα_{11} Gly66Asp. P63 and rap1gap ebBRET assays, and p-ERK AlphaScreen responses were significantly increased..... 119

Figure 4.16 CaSR-mediated P63 ebBRET responses of Gα_{q} Gly66Asp..... 120

Figure 4.17 (A) Analysis of G$\alpha_{q/11}$ coupled receptors in the IUPHAR/BPS Guide to PHARMACOLOGY/GPCRdb..... 121

Figure 4.18 M_3R mediated p63 recruitment in response to acetylcholine..... 122

Figure 4.19 M_3R-mediated p63 recruitment in response to acetylcholine of $G\alpha_{11}$ Gln152His. 123

Figure 4.20 M_3R mediated p63 recruitment in response to acetylcholine of (A) $G\alpha_{11}$ Gly66Asp (B) $G\alpha_{11}$ Arg147Cys (C) $G\alpha_{11}$ Ala231Thr and (D) $G\alpha_q$ Gly66Asp. 123

Figure 4.21 B2AR-mediated p63 recruitment in response to isoproterenol..... 124

Figure 4.22 Radar plots show variant (black line) AUC normalised to WT (red line) of 7 different signalling assays for (A) $G\alpha_{11}$ Gly66Asp (B) $G\alpha_{11}$ Arg147Cys (C) $G\alpha_{11}$ Ala231Thr to facilitate comparison of variant effects across the 7 different assays. . 129

Figure 5.1 Overview of CaSR signalling via $G\alpha_{11}$. 133

Figure 5.2 Body weight of male (solid symbols) and female (hollow symbols) of +/+ (n=21), Dsk7/+ (n=24) and Dsk7/Dsk7 (n=9) mice. 135

Figure 5.3 Plasma calcium values (mmol/l) of (A) female (B) male and (C) gender pooled +/+, Dsk7/+ and Dsk7/Dsk7 mice 137

Figure 5.4 Plasma albumin levels (A-C) and total protein (D-F) of female, male and gender pooled +/+, Dsk7/+ and Dsk7/Dsk7 mice 137

Figure 5.5 Albumin corrected plasma calcium values (mmol/l) of (A) female (B) male and (C) gender pooled +/+, Dsk7/+ and Dsk7/Dsk7 mice 138

Figure 5.6 Inorganic phosphate values (mmol/l) of (A) female (B) male and (C) gender pooled +/+, Dsk7/+ and Dsk7/Dsk7 mice 139

Figure 5.7 Plasma sodium values (mmol/l) of (A) female (B) male and (C) gender pooled +/+, Dsk7/+ and Dsk7/Dsk7 mice 139

Figure 5.8 Plasma levels of chloride (A-C) and magnesium (D-F) of female, male and gender pooled +/+, Dsk7/+ and Dsk7/Dsk7 mice 140

Figure 5.9 Plasma levels of creatinine (A-C), High-density lipoprotein (HDL) (D-F) and Aspartate transaminase (AST) (G-I) of female, male and gender pooled +/+, Dsk7/+ and Dsk7/Dsk7 mice 141

Figure 5.10 Comparison of baseline plasma glucose values between genotypes. 142

Figure 5.11 Comparison of baseline glucose values (mmol/l) between genders 143

Figure 5.12 Intraperitoneal glucose tolerance tests (IPGTTs) 143

Figure 5.13 Quantification of islet area and number of H&E stain of pancreatic islet sections from Dsk7 mice. 144

Figure 5.14 Immunofluorescence staining of pancreatic islet sections from +/+, Dsk7/+ and Dsk7/Dsk7 mice for DAPI (blue), insulin (white), and either glucagon (red) (A,C,E) or Ki-67 (red) (B,D,F). 147

Figure 5.15 Quantification of glucagon positive (α) cells (A-C) and insulin positive (ß) cells (D-F) in pancreatic islet sections of +/+ (black), Dsk7/+ (blue) and Dsk7/Dsk7 (red) mice. 147

Figure 5.16 Proportion of proliferating (Ki-67 positive) insulin negative (predominantly α) cells in pancreatic islet sections of +/+ (black), Dsk7/+ (blue) and Dsk7/Dsk7 (red) mice. 148

Figure 5.17 Proportion of proliferating (Ki-67 positive) insulin positive (ß) cells in pancreatic islet sections of +/+ (black), Dsk7/+ (blue) and Dsk7/Dsk7 (red) mice..... 149

Figure 6.1 Overview of CaSR-mediated signalling and downstream assays used in this chapter 157

Figure 6.2 Evolutionary conservation of *GNAQ* variants found in the DiscovEHR cohort in $G\alpha_q$ orthologs and Gα paralogs. 159

Figure 6.3 Immunofluorescence microscopy of cells transfected with pBI-CMV2 constructs. 161

Figure 6.4 $G\alpha_q$ variants Arg19Trp, Ala110Val, Gln299His, Ala302Ser, Ala331Thr and Val344Ile are expressed at similar levels to WT $G\alpha_q$, as determined by western blot analysis of lysates from transfected HEK293A$G\alpha_{q/11}$-KO-CaSR cells. 162

Figure 6.5 (A) SRE luciferase reporter assays, (B) NFAT-RE assays and (C) Fluo-4 calcium mobilisation assays showed no significant differences in response to increasing concentrations of extracellular calcium between variant (red line) and WT (black line) $G\alpha_q$. 163

Figure 6.6 Normalised mRNA expression (NX) of *GNAQ* and *GNA11* across 21 tissues obtained from the FANTOM, GTEX and HPA RNA-Seq datasets. 165

Figure 6.7 Alignment of the $G\alpha_{11}$ GTPase domain (orange) (PDB code 6OIJ) and the GDP (black) bound structure of $G\alpha_q$ (grey) (PDB code 3AH8). 166

Figure 6.8 (A) FHH2-causing $G\alpha_{11}$ mutations Leu135Gln and Phe220Ser and (B) engineered $G\alpha_q$ variants Leu135Gln and Phe220Ser are expressed at similar levels to WT $G\alpha_{11}$ and $G\alpha_q$, respectively 166

Figure 6.9 (A) $G\alpha_{11}$ Leu135Gln shows significantly lower calcium-induced responses in SRE luciferase reporter assays, NFAT-RE reporter assays, and Fluo-4 calcium mobilisation assays when compared to WT $G\alpha_{11}$. 168

Figure 6.10 (A) Western blot showing $G\alpha_{11}$ protein expression in HEK293$G\alpha_{q/11}$-KO-CaSR cells transfected with NanoBit sensors 169

Figure 6.11 (A) Calcium-induced Nanoluc responses are significantly increased for cells transfected with $G\alpha_{11}$(97,98)-LgBiT and PLCβ_2(N)SmBiT, compared to control 170

Figure 6.12 (A) Western blot showing that transfection of HEK293-Flp-In-Flag-CaSR cells with increasing amounts (ng/ml) of *GNA11* cDNA results in increased $G\alpha_{11}$ protein expression in HEK293-Flp-In-Flag-CaSR cells..... 171

Figure 6.13 (A) Dose-response curves of BRET2 responses of increasing amounts of *GNA11* cDNA. Darker red shades indicate higher expression. (B) Dose-response curves of BRET2 responses of increasing amounts of *GNAQ* cDNA. Darker green shades indicate higher expression..... 172

Figure 6.14 Aberrant responses of the FHH2-causing $G\alpha_{11}$ mutations Leu135Gln and Phe220Ser..... 173

Figure 6.15 Aberrant CaSR-mediated, calcium-induced responses of the FHH2-causing $G\alpha_{11}$ mutations Leu135Gln and Phe220Ser..... 174

Figure 6.16 HEK293$G\alpha_{q/11}$-KO-CaSR cells transfected with SRE (top row) and NFAT-RE (bottom row) luciferase reporter constructs. 175

Figure 6.17 HEK293$G\alpha_{q/11}$-KO-CaSR cells transfected with SRE (top row) and NFAT-RE (bottom row) luciferase reporter constructs. 176

Figure 6.18 Number of FDA approved drugs (in brackets) that target receptors which primarily signal via $G\alpha_{q/11}$ mediated pathway. 181

Figure 6.19 Number of FDA approved drugs (shown in brackets) that target receptors which primarily signal via $G\alpha_{q/11}$ mediated pathway, grouped by anatomical main group (ATC index). 182

Figure 7.1 Acetylcholine-induced activation of (A) $G\alpha_q$, (B) $G\alpha_{11}$, (C) $G\alpha_{14}$ and (D) $G\alpha_{15}$ in HEK293 cells transiently transfected with the Muscarinic acetylcholine receptor M_3. 186

Figure 7.2 Activation of the $G\alpha_{q/11}$ family ($G\alpha_{q,11,14,15}$) by the CaSR in response to increasing concentrations of Ca^{2+}_e. 187

Figure 7.3 U46619-induced mediated activation of (A) p115 and (B) pdz by TPα in cells transfected with control (endogenous), $G\alpha_{12}$ and $G\alpha_{13}$. 188

Figure 7.4 CaSR mediated activation of (A) p115 and (B) pdz in response to increasing concentrations of Ca^{2+}_e in cells transfected with control (endogenous), $G\alpha_{12}$ and $G\alpha_{13}$. 189

Figure 7.5 Acetylcholine-induced activation of the $G\alpha_{i/o}$ family ($G\alpha_{i1,i2,i3,oA,oB,z}$) by the Muscarinic acetylcholine receptor M_2. 190

Figure 7.6 CaSR mediated activation of the $G\alpha_{i/o}$ family ($G\alpha_{i1,i2,i3,oA,oB,z}$). 191

Figure 7.7 Isoproterenol mediated recruitment of (A) ß-arrestin 1 and (B) ß-arrestin 2 in cells transfected with B2AR (black line) or control (red line). 192

Figure 7.8 Ca^{2+}_e mediated recruitment of (A) ß-arrestin 1 and (B) ß-arrestin 2 in cells stably expressing the CaSR (black line) or parental cells (red line)..... 193

Figure 7.9 CaSR mediated activation of pdz in response to increasing concentrations of Ca^{2+}_e and allosteric modulator or vehicle in cells transfected with control (endogenous), $G\alpha_{12}$ and $G\alpha_{13}$. 194

Figure 7.10 CaSR mediated recruitment of ß-arrestin 1 and 2 to the plasma membrane in response to increasing concentrations of Ca^{2+}_e and allosteric modulator or vehicle. 196

Figure 7.11 Activation of the $G\alpha_{q/11}$ family ($G\alpha_{q,11,14,15}$) by the CaSR in response to Ca^{2+}_e in cells treated with vehicle (black line) or 100nM cinacalcet (red line) 197

Figure 7.12 Activation of the $G\alpha_{i/o}$ family ($G\alpha_{i1,i2,i3,oA,oB,z}$) by the CaSR in response to increasing concentrations of Ca^{2+}_e in cells treated with vehicle (black line) or 100nM cinacalcet (red line). 198

Figure 7.13 Activation of the $G\alpha_{q/11}$ family ($G\alpha_{q,11,14,15}$) by the CaSR in response to increasing concentrations of Ca^{2+}_e in cells treated with vehicle (black line) or 100nM AC-265347 (red line) 200

Figure 7.14 Activation of the $G\alpha_{i/o}$ family ($G\alpha_{i1,i2,i3,oA,oB,z}$) by the CaSR in response to increasing concentrations of Ca^{2+}_e in cells treated with vehicle (black line) or 100nM AC-265247 (red line) 201

Figure 7.15 Activation of the $G\alpha_{q/11}$ family ($G\alpha_{q,11,14,15}$) by the CaSR in response to increasing concentrations of Ca^{2+}_e in cells treated with vehicle (black line) or 10mM L-Phenylalanine (L-Phe) (red line). 203

Figure 7.16 Activation of the $G\alpha_{i/o}$ family ($G\alpha_{i1,i2,i3,oA,oB,z}$) by the CaSR in response to increasing concentrations of Ca^{2+}_e in cells treated with vehicle (black line) or 10mM L-Phenylalanine (L-Phe) (red line). 204

Figure 7.17 Activation of the $G\alpha_{q/11}$ family ($G\alpha_{q,11,14,15}$) by the CaSR in response to increasing concentrations of Ca^{2+}_e in cells treated with vehicle (black line) or 1µM Etelcalcetide (red line). 206

Figure 7.18 Activation of the $G\alpha_{i/o}$ family ($G\alpha_{i1,i2,i3,oA,oB,z}$) by the CaSR in response to increasing concentrations of Ca^{2+}_e in cells treated with vehicle (black line) or 1µM Etelcalcetide (red line). 207

Figure 7.19 Activation of the $G\alpha_{q/11}$ family ($G\alpha_{q,11,14,15}$) by the CaSR in response to increasing concentrations of Ca^{2+}_e in cells treated with vehicle (black line) or 1µM KP-2067 (red line). 209

Figure 7.20 Activation of the $G\alpha_{i/o}$ family ($G\alpha_{i1,i2,i3,oA,oB,z}$) by the CaSR in response to increasing concentrations of Ca^{2+}_e in cells treated with vehicle (black line) or 1μM KP-2067 (red line). 210

Figure 7.21 Activation of the $G\alpha_{q/11}$ family ($G\alpha_{q,11,14,15}$) by the CaSR in response to increasing concentrations of Ca^{2+}_e in cells treated with vehicle (black line) or 100nM NPS-2143 (red line). 212

Figure 7.22 Activation of the $G\alpha_{i/o}$ family ($G\alpha_{i1,i2,i3,oA,oB,z}$) by the CaSR in response to increasing concentrations of Ca^{2+}_e in cells treated with vehicle (black line) or 100nM NPS-2143 (red line). 213

Figure 7.23 Activation of the $G\alpha_{q/11}$ family ($G\alpha_{q,11,14,15}$) by WT (black line) or Arg185Gln mutant (red line) CaSR in response to increasing concentrations of Ca^{2+}_e. 215

Figure 7.24 Activation of the $G\alpha_{q/11}$ family ($G\alpha_{q,11,14,15}$) by WT (black line) or Ser657Cys mutant (red line) CaSR in response to increasing concentrations of Ca^{2+}_e. 217

Figure 7.25 Radar plots of baseline-corrected area under the curve of Ca^{2+}_e induced activation of $G\alpha_q$, $G\alpha_{11}$, $G\alpha_{14}$, $G\alpha_{15}$, $G\alpha_{12}$, $G\alpha_{13}$, $G\alpha_{i1}$, $G\alpha_{i2}$, $G\alpha_{i3}$, $G\alpha_{oA}$, $G\alpha_{oB}$, $G\alpha_z$ and β-arrestin 1/2 in cells treated with vehicle (black line) or CaSR allosteric modulators (red line) 222

List of tables

Table 1.1 Mouse models for inherited disorders of the CaSR signalling pathway.....27

Table 1.2 Comparison of phenotypes between human ADH patients, Nuf mice (model for ADH1) and Dsk7 mice (model for ADH2). 35

Table 1.3 Orthosteric CaSR agonists (type 1 calcimimetics). 39

Table 1.4 Positive allosteric CaSR modulators (type 2 calcimimetics). 41

Table 1.5 Negative allosteric CaSR modulators (calcilytics). 44

Table 3.1 Reagents for 10x Phosphate-Buffered saline (PBS) 51

Table 3.2 Reagents for NP40 lysis buffer. 51

Table 3.3 Reagents for 5x complete imaging buffer 52

Table 3.4 Preparation of 1x complete imaging buffer 53

Table 3.5 Preparation of Fluo-4 AM working solution 54

Table 3.6 Reagents for 10x Tyrode's buffer. 54

Table 3.7 GPCR-targeting compounds used in this thesis. 56

Table 3.8 *GNA11* sequencing primers. 56

Table 3.9 Site-directed mutagenesis (SDM) primers to introduce *GNA11* variants found in dbSNP. 57

Table 3.10 Site-directed mutagenesis (SDM) primers to introduce *GNA11* variants found in the DiscovEHR cohort. 57

Table 3.11 Primary antibodies used for Western blot analysis. 58

Table 3.12 Primary antibodies used for Immunofluorescence Microscopy. 58

Table 3.13 Horseradish peroxidase (HRP) conjugated secondary antibodies used for Western blot analysis..... 58

Table 3.14 Secondary antibodies used for Immunofluorescence Microscopy..... 58

Table 3.15 QuikChange Lightning site-directed mutagenesis reaction 61

Table 3.16 BigDye master mix components (per well)..... 63

Table 3.17 Reagents for 10ml of 10% SDS-PAGE running gel. 66

Table 3.18 Reagents for 10ml of 6% SDS-PAGE running gel. 66

Table 3.19 Reagents for 10ml of 5% SDS-PAGE stacking gel..... 67

Table 3.20 Dewaxing and rehydration steps for paraffin-embedded pancreas sections. 70

Table 3.21 NanoBiT split luciferase constructs. 77

Table 3.22 Reagents for 1 ml GTPase-Glo™ reagent..... 80

Table 3.23 Treatment solutions used for Fluo-4 assays. 82

Table 3.24 Enhanced bystander (eb) BRET effectors and native G proteins used..... 89

Table 3.25 Crystal structures used in this thesis with corresponding PDB codes..... 96

Table 4.1 Genotypes and Phenotypes of selected *GNA11* variants from the DiscovEHR cohort (n=5)..... 104

Table 5.1 Proportion of +/+, Dsk7/+ and homozygous Dsk7/Dsk7 mice observed in a sample of 174 male and 167 female mice at >3 weeks bred between 2017 and 2019. 134

Table 5.2 Plasma biochemistry of electrolytes and metabolites that were similar in +/+, Dsk7/+ and Dsk7/Dsk7 mice..... 136

Table 5.3 Comparison of phenotypes between human ADH1/2 patients, Nuf mice (model for ADH1), and Dsk7 and R60C mice (models for ADH2)..... 153

Table 6.1 Genotypes and Phenotypes of patients with *GNAQ* variants from the DiscovEHR cohort..... 160

Table 9.1 Formalin-fixed, paraffin-embedded Dsk7 4.5µM pancreas slides used for histology. 234

Table 9.2 Synonymous *GNA11* variants found in dbSNP (n=170) 236

Table 9.3 *GNA11* missense variants in the dbSNP database (n=144)..... 240

Table 9.4 *GNA11* missense variants in gnomAD (n=90)..... 243

Abbreviations

1,25(OH)2D	1,25-dihydroxyvitamin D
25(OH)D	25-hydroxyvitamin D
7-TM	Seven-transmembrane
AC	Adenylyl cyclase
ADH	Autosomal dominant hypocalcaemia
AHH	Autoimmune hypocalciuric hypercalcaemia
AlF_4	Aluminium fluoride
ALP	Alkaline phosphatase
AlphaScreen	Amplified Luminescent Proximity Homogeneous Assay Screen
ALT	Alanine transaminase
AM	Acetoxymethyl ester
ANOVA	Analysis of variance
AP2S1	Adapter protein-2 sigma-1 subunit
ATC	Anatomical Therapeutic Chemical
ATP	Adenosine triphosphate
AUC	Area under curve
B2AR	β2 adrenergic receptor
BRET	Bioluminescence Resonance Energy Transfer
BS	Bartter syndrome Type 5
BSA	Bovine Serum albumin
Ca^{2+}_e	Extracellular calcium
Ca^{2+}_i	Intracellular calcium
CALM	Calmodulin
cAMP	cyclic adenosine monophosphate
CaN	Calcineurin
CAPS	N-cyclohexyl-3-aminopropanesulfonic acid
Cas9	CRISPR-associated protein 9
CaSR	Calcium-sensing receptor
CK	Creatine kinase
CLDN	Claudin
CNS	Central nervous system
CRD	Cysteine rich domain
CRISPR	Clustered regularly interspaced short palindromic repeats
dbSNP	Single Nucleotide Polymorphism database
DAG	Diacylglycerol
DAPI	4',6-diamidino-2-phenylindole
DMEM	Dulbecco's Modified Eagle Medium
DMSO	Dimethyl sulfoxide
ebBRET	Enhanced bystander BRET
ECD	Extracellular domain

EDTA	Ethylenediaminetetraacetic acid
EHR	Electronic Health Record
EMMA	European Mutant Mouse Archive
ENU	N-ethyl-N-nitrosourea
Erk	Extracellular signal-regulated kinase
FBS	Fetal bovine serum
FHH	Familial hypocalciuric hypercalcaemia
FRET	Förster resonance energy transfer
$G\alpha_{11}$	Guanine nucleotide-binding protein subunit alpha-11
GABAB1-2	Gamma-aminobutyric acid type B receptors
GAP	GTPase activating protein
GAPDH	Glyceraldehyde 3-phosphate dehydrogenase
GDP	Guanosine 5'diphosphate
GEF	Guanine nucleotide exchange factors
GFP	Green fluorescent protein
GHS	Geisinger Health System
GK	Glucokinase
GLP-1	Glucagon-like peptide-1
GPCR	G protein-coupled receptor
G protein	Guanine nucleotide-binding proteins
GRK	G protein-coupled receptor kinase
GTP	Guanosine 5'trisphosphate
GTPase	Guanosine triphosphatase
H&E	Haematoxylin and eosin
HPA	Human Protein Atlas
HRP	Horseradish peroxidase
HTRF	Homogeneous Time Resolved Fluorescence
ICD	Intracellular domain
ICD9	International Classification of Disease-9
ICL2	Intracellular loop 2
IP_1	Inositol 1 phosphate
IP_3	Inositol trisphosphate
IP_3R	Inositol trisphosphate receptor
IPGTT	Intraperitoneal glucose tolerance test
K_{ATP}	ATP-sensitive potassium channel
LA-PTH	Long-acting parathyroid hormone
LAR	Luciferase assay reagent
LB	Lysogeny broth
LDH	Lactate dehydrogenase
LDL	Low-density lipoprotein
L-Phe	L-Phenylalanine
L-Trp	L-Tryptophan
M_2R	Muscarinic acetylcholine receptor M_2
M_3R	Muscarinic acetylcholine receptor M_3

MAPK	Mitogen-activated protein kinase
MC1R	Melanocortin receptor 1
mGluR	metabotropic glutamate receptor
MM	Master mix
mRNA	Messenger ribonucleic acid
NAM	Negative allosteric modulator
NFAT	Nuclear factor of activated T-cells
NFAT-RE	Nuclear factor of activated T-cells Response Element
NSHPT	Neonatal Severe Hyperparathyroidism
p63	p63RhoGEF
PAM	Positive allosteric modulator
PBS	Phosphate-Buffered saline
PEI	Polyethylenamine
p-Erk	Phosphorylated ERK
PFA	Paraformaldehyde
Pi	Phosphate
PI3K	phosphoinositide 3-kinase
PIP2	Phosphatidylinositol 4,5-bisphosphate
PKA	Protein kinase A
PKC	Protein kinase C
PLB	Passive lysis buffer
PLC	Phospholipase C
PLCbeta1-4	Phospholipase C beta family
PLD	Phospholipase D
PM	Plasma membrane
PreProPTH	Preproparathyroid hormone
PTH	Parathyroid hormone
PTHR	Parathyroid hormone receptor
PTHrP	Parathyroid hormone-related protein
PTX	Pertussis toxin
PVDF	Polyvinylidene fluoride
rGFP	*Renilla reniformis* GFP
RGS	Regulator of G protein signalling
Rho	Ras homology
RhoA	Ras homology family member A
Rluc	*Renilla reniformis* luciferase
RT	Room temperature
S1-3	Flexible switch regions of the Gα subunit
SDM	Site-directed mutagenesis
SDS	Sodium dodecyl sulfate
SEM	Standard error of the mean
SIFT	Sorts intolerated from tolerated
SMO	Smoothened
SNV	Single nucleotide variant

SRE	Serum response element
SRF	Serum response factor
SSD	Salmon sperm DNA
TAL	thick ascending limb
TAS1R1-3	Taste type 1 receptors
TMD	Transmembrane domain
TPα	Thromboxane A2 receptor isoform alpha
VDCC	Voltage-dependent calcium channels
VFT	Venus flytrap domain
WT	Wild type

1 INTRODUCTION

1.1 Heterotrimeric guanine nucleotide-binding (G) proteins

Heterotrimeric guanine nucleotide-binding (G) proteins (Gα, Gß and Gγ) act as molecular switches which transduce stimuli received by G protein-coupled receptors (GPCRs) into intracellular responses which mediate diverse physiological functions (Figure 1.1)[1-4]. GPCRs are essential for communication between the external and internal environments of cells[2]. This introduction will review the molecular functions of G proteins (section 1.1) and GPCRs (section 1.2) as well as their roles in physiology and pathophysiology (sections 1.3-1.6).

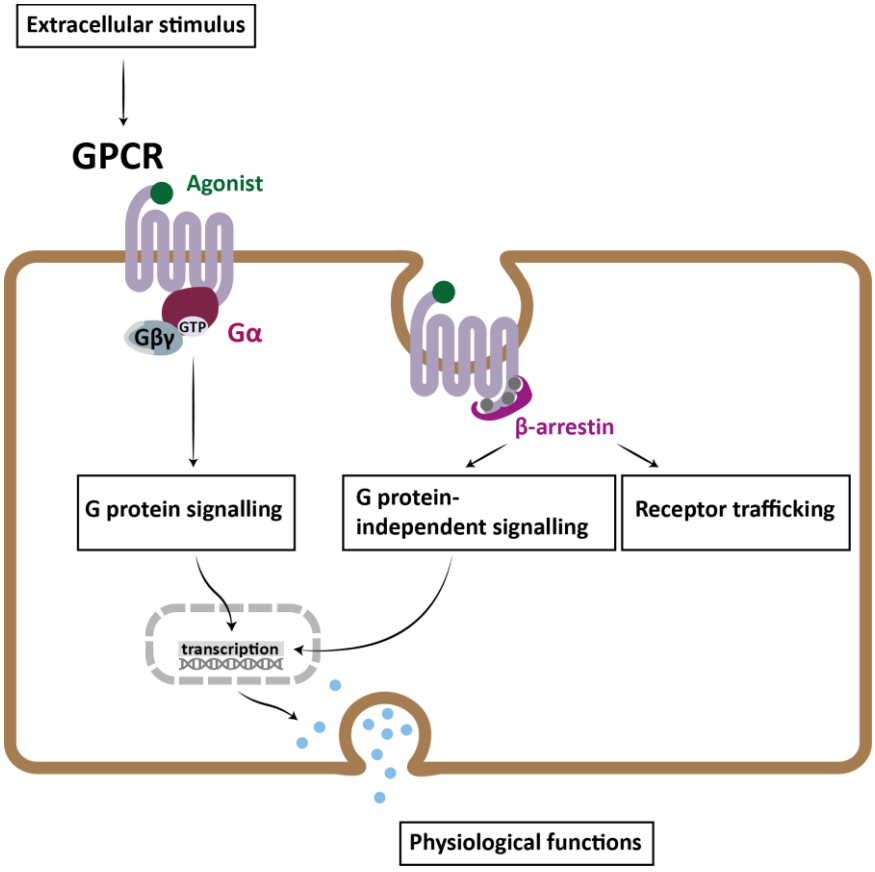


Figure 1.1 Overview of G protein-coupled receptor (GPCR) signalling. Extracellular stimuli received by GPCRs are transduced into intracellular signalling and physiological responses by heterotrimeric G proteins and receptor trafficking.

1.1.1 Overview of G proteins

G proteins are a superfamily of guanosine triphosphatases (GTPases) which are involved in nearly all aspects of cell biology[5-7]. In the active state, they catalyse hydrolysis of guanosine triphosphate (GTP) to guanosine diphosphate (GDP) and inorganic phosphate (Pi)[1,8]. G proteins are divided into two groups: small G proteins (or small GTPases) and heterotrimeric G proteins[1,7], which are composed of 3 subunits – Gα, Gß, and Gγ (Figure 1.2A). The Gß and Gγ subunits form an undissociable complex and are regarded as one functional unit, referred to hereafter as the Gßγ subunit[6,9].

All members of the G protein superfamily share a highly conserved GTPase (or Ras homology) domain which binds and hydrolyses guanine nucleotides[5,10]. Small G proteins, such as KRAS (Figure 1.2B), are monomeric and consist entirely of this GTPase domain[1,7]. In contrast, in heterotrimeric G proteins the GTPase domain forms part of the Gα subunit (Figure 1.2C) and provides binding surfaces for the Gßγ subunit and effectors. In addition to the enzymatically active GTPase domain, the Gα subunit also contains a helical domain consisting of 6 α-helices, which is thought to provide structural support[9,11].

Heterotrimeric G proteins cycle between a basal and an activated state (Figure 1.3). In the basal state, the Gα subunit is bound to GDP and forms a complex with the Gßγ subunit. This complex can be recognised by a GPCR, which upon agonist binding has the ability to act as a guanine nucleotide exchange factor (GEF). This leads to conformational changes within three flexible switch regions (S1-3) of the Gα subunit which facilitate the release of GDP and the binding of GTP (referred to as nucleotide exchange). The GTP-bound Gα subunit then dissociates from the receptor and the Gßγ subunit, allowing both the Gα subunit and the Gßγ subunit to activate downstream effector proteins[4-6,9,12].

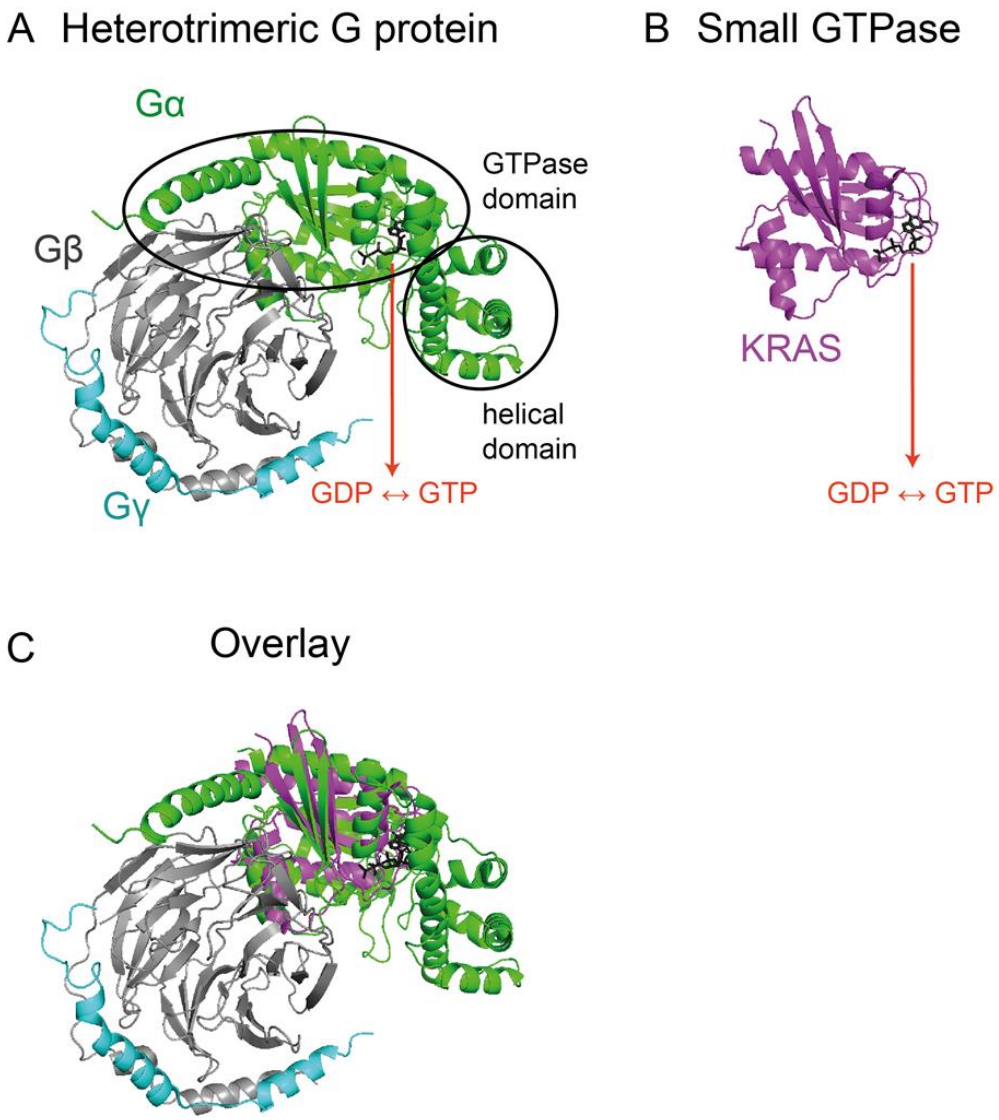


Figure 1.2 Structure of heterotrimeric G proteins and small GTPases. (A) Gα (green) in complex with Gβ (grey) and Gγ (turquoise). GDP/GTP exchange is indicated in red (PDB code 3AH8). (B) Crystal structure of the small GTPase KRAS (purple) (PDB code 6MBt). (C) Overlay of a heterotrimeric G protein and KRAS, demonstrating homology of the GTPase domain.

Signalling of the Gα subunit is terminated by the hydrolysis of GTP to GDP. This is accelerated by GTPase activating proteins (GAPs), such as the regulator of G protein signalling (RGS) family[8]. In turn, signalling of the Gβγ subunit is terminated by re-association with the Gα subunit[9]. Figure 1.4 shows the structure of an activated Gα subunit ($G\alpha_q$) in complex with RGS8[13].

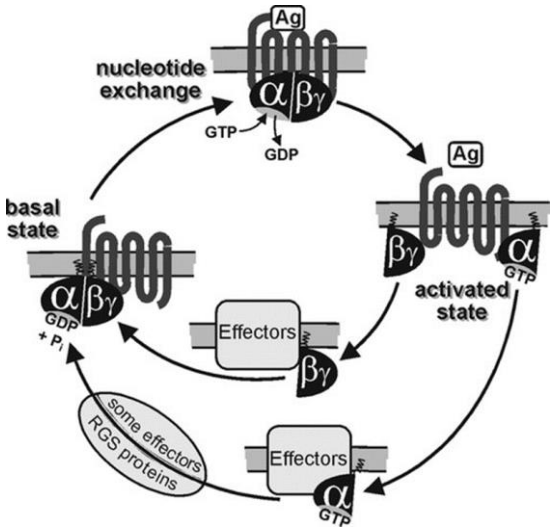


Figure 1.3 Heterotrimeric G protein cycle. In the basal state, the Gα subunit is bound to GDP and forms a complex with the Gβγ subunit. This complex can be recognised by GPCRs. Upon activation of the GPCR by an agonist, GDP is exchanged for GTP which leads to dissociation of the Gα subunit from the Gβγ subunit and the GPCR (activated state). Subsequently, both the Gα subunit and the Gβγ subunit activate downstream effectors. This is terminated by GTP hydrolysis to GDP and phosphate (Pi) which is facilitated by regulator of G protein signalling (RGS) proteins. Re-association of the Gα subunit with Gβγ returns the heterotrimeric G protein to the basal state. Adapted from Wettschureck and Offermanns[6].

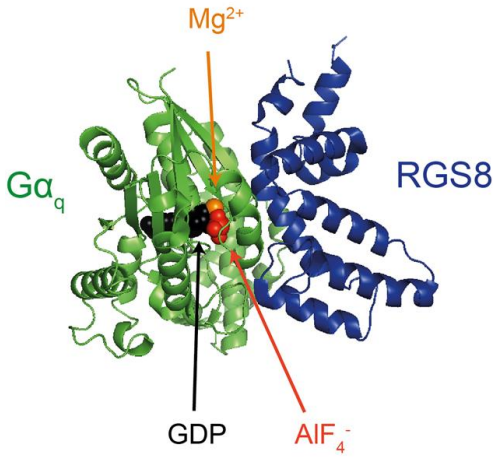


Figure 1.4 Crystal structure of regulator of G protein signalling 8 (RGS8) (blue) in complex with activated $G\alpha_q$ (green). GDP (black), AlF_4 (red) and Mg^{2+} (orange) were used experimentally to imitate GTP (PDB code 5DO9).

The human genome contains 16 genes encoding 19 Gα subunits, 5 genes encoding 6 Gß subunits, and 12 genes encoding 12 Gγ subunits[6,14-16]. This leads to a large number of Gαßγ combinations which give rise to a diverse range of intracellular signalling profiles. Heterotrimeric G proteins are typically classified by their Gα subunits, which are grouped into 4 families according to amino acid sequence similarity (Figure 1.5): $G\alpha_s$ ($G\alpha_{sS,sL,sXL,olf}$), $G\alpha_{i/o}$ ($G\alpha_{i1,i2,i3,oA,oB,z,t1,t2,gust}$), $G\alpha_{q/11}$ ($G\alpha_{q,11,14,15/16}$[a]), and $G\alpha_{12/13}$ ($G\alpha_{12,13}$)[6,9].

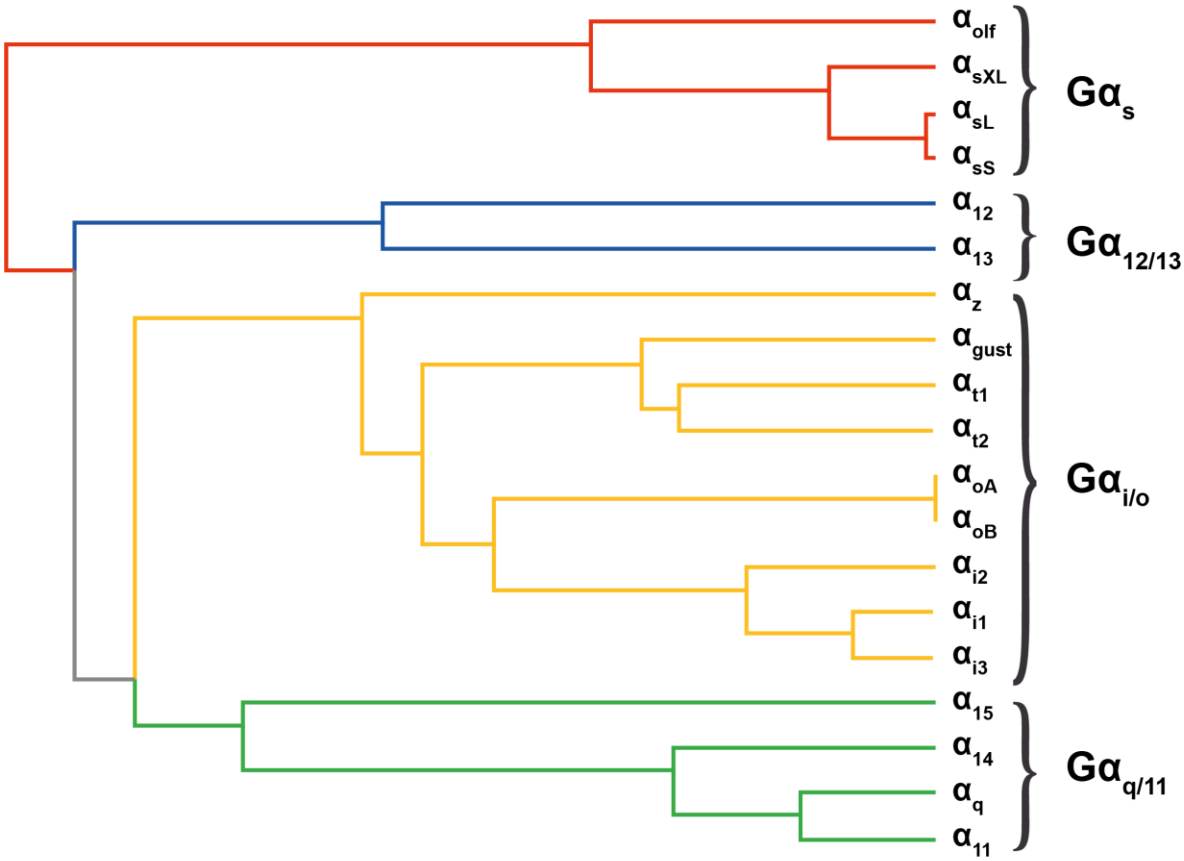


Figure 1.5 Phylogenetic relationship of human Gα subunits. Gα subunits are grouped into 4 families according to evolutionary conservation ($G\alpha_s$, $G\alpha_{12/13}$, $G\alpha_{i/o}$, $G\alpha_{q/11}$). Amino acids were aligned using Clustal Omega[17].

[a] The $G\alpha_{15}$ subunit is sometimes referred to as $G\alpha_{16}$, which is the mouse orthologue of human $G\alpha_{15}$[9].

While the overall structure of the various Gα subunits is highly conserved, each one couples differently to GPCRs and activates distinct downstream effectors[8,18]. Receptor coupling specificity is mediated by small differences in the receptor-G protein interface[5]. Mutational studies have shown that the C terminus of the Gα subunit is an important determinant for receptor specificity[19-21]. For example, when the C terminus of $G\alpha_q$ is replaced with that of $G\alpha_i$ this results in a G protein which is able to recognise $G\alpha_i$-coupled receptors, but still stimulates the $G\alpha_q$ effector phospholipase C (PLC)[22]. Moreover, it has been shown that sites which are allosterically coupled to the receptor-G protein interface can also be important for GPCR-G protein coupling. For example, mutation of Gly66 in the linker 1 region of $G\alpha_q$ to Asp66 caused it to become promiscuous, i.e. couple to both $G\alpha_i$- and $G\alpha_s$-coupled receptors[23,24].

1.1.2 G alpha q/11

The most prominent members of the $G\alpha_{q/11}$ family are the $G\alpha_q$ and $G\alpha_{11}$ subunits. They are both ubiquitously expressed, with the exception of platelets where only $G\alpha_q$ is present[6]. In contrast, $G\alpha_{14}$ is predominantly expressed in pancreatic islets, taste tissue, spleen, lung, kidney, testis, and haematopoietic cells, and $G\alpha_{15}$ is only present in haematopoietic cells[6,9,25,26]. Members of the $G\alpha_{q/11}$ family activate multiple signalling pathways, an overview of which is presented in Figure 1.6.

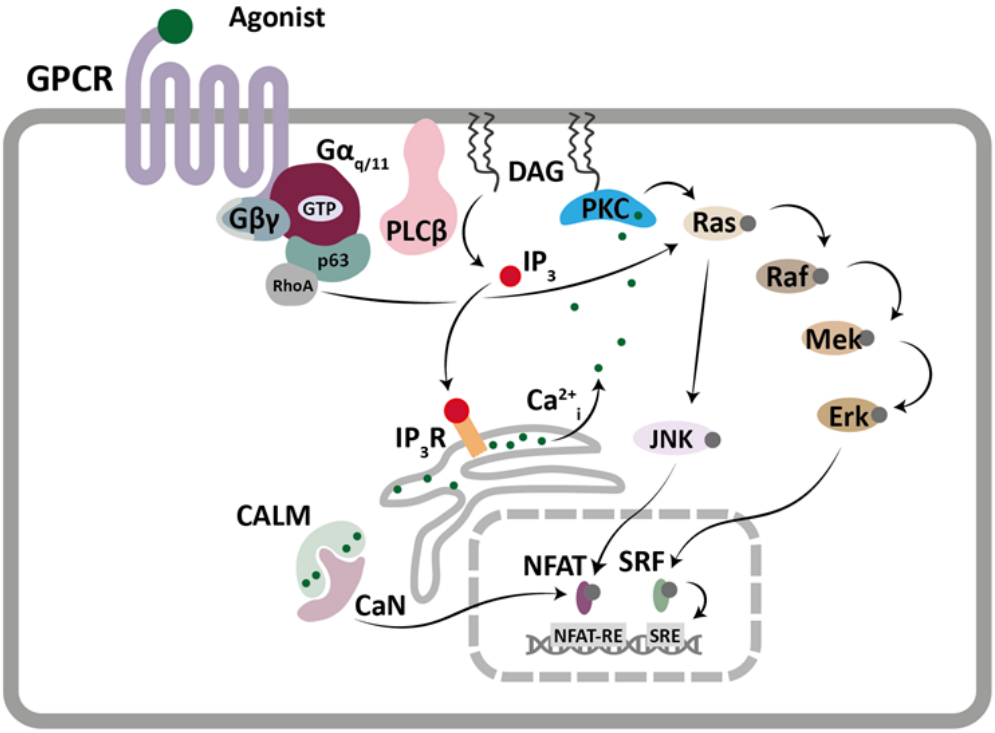


Figure 1.6 Schematic overview of signalling pathways activated by the $G\alpha_{q/11}$ family.

Upon activation by a GPCR, $G\alpha_{q/11}$ stimulates the Phospholipase C beta family (PLCß1-4) (Figure 1.7), which are enzymes that catalyse hydrolysis of Phosphatidylinositol 4,5-bisphosphate (PIP_2) to Inositol trisphosphate (IP_3) and diacylglycerol (DAG). IP_3 then binds to IP_3 receptors (IP_3R) to release calcium from intracellular stores[9,27]. Increased calcium concentrations stimulate the association of the calcium-binding protein calmodulin (CALM) and the serine/threonine phosphatase calcineurin (CaN). CaN then activates transcription factors, such as Nuclear Factor of Activated T-cells (NFAT) which binds to NFAT Response Element (NFAT-RE). Calcium and DAG also activate Protein kinase C (PKC), which phosphorylates members the map kinase (MAPK) pathway, including Ras, Raf, Mek, Erk and JNK. Subsequently, Erk and JNK induce transcriptional changes, such as Serum Response Factor (SRF), which binds to serum response element (SRE)[9,28].

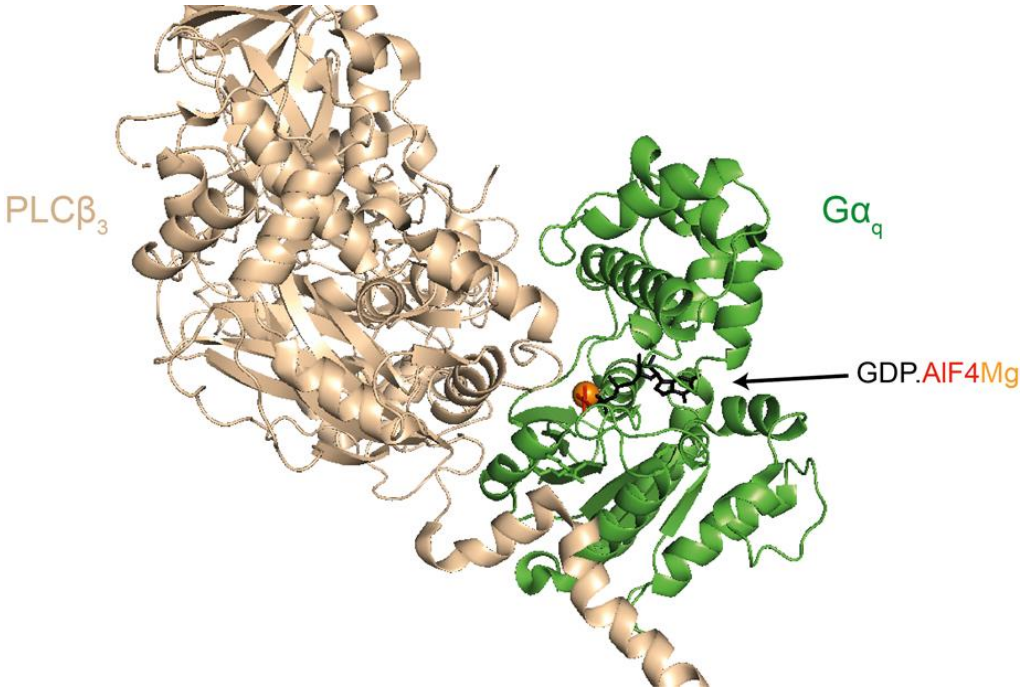


Figure 1.7 Structure of full-length phospholipase C ß3 (PLCß3) (beige) in complex with activated Gαq (green) (PDB code 4gnk). GDP (black), aluminium fluoride (AlF_4) (red) and Mg^{2+} (orange) were used experimentally to imitate GTP.

GTP bound $G\alpha_{q/11}$ also recruits the GEF p63RhoGEF (hereafter referred to as p63) which leads to activation of Ras homology family member A (RhoA) (Figure 1.8) and the Phospholipase D (PLD) signalling pathway. RhoA also activates the MAPK pathway, resulting in changes in SRF and NFAT transcription[29-31].

1.1.2.1 Diversity within the G alpha q/11 family

Among all G protein families, members of the $G\alpha_{q/11}$ family have the most diverse primary structures (Figure 1.5). Moreover, their unique distribution pattern across tissues suggests tissue-specific functions. However, the significance of diversity within the $G\alpha_{q/11}$ family is disputed[6,26,32].

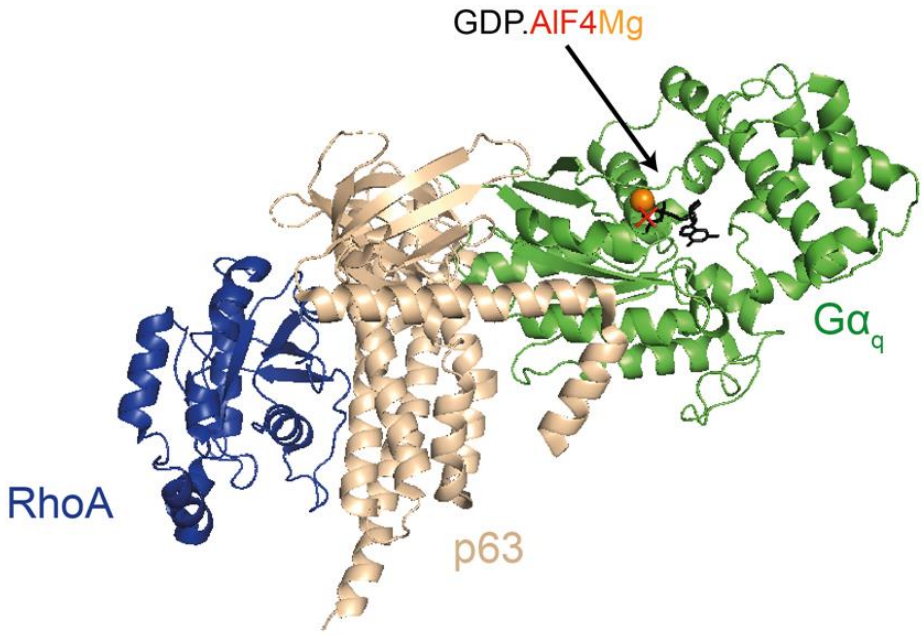


Figure 1.8 Structure of the p63RhoGEF (p63) (beige) in complex with activated $G\alpha_q$ (green) and RhoA (blue) (PDB code 2RNG). GDP (black), AlF_4 (red) and Mg^{2+} (orange) imitate GTP.

Somatic, constitutively activating mutations of $G\alpha_q$ and $G\alpha_{11}$, but not $G\alpha_{14}$ and $G\alpha_{15}$, cause both uveal melanoma[33] and congenital haemangioma[34] in humans. Similarly, gain-of-function mutations of $G\alpha_q$ and $G\alpha_{11}$, but not $G\alpha_{14}$ and $G\alpha_{15}$, cause increased skin pigmentation in mice. This suggests that the $G\alpha_q$ and $G\alpha_{11}$ subunits are particularly important for skin function[33-36].

Interestingly, activation of $G\alpha_q$, $G\alpha_{11}$ and $G\alpha_{14}$, but not $G\alpha_{15}$, is inhibited by the naturally occurring depsipeptide YM-254890[32,37,38]. The structure of YM-254890 in complex with $G\alpha_q$ and the Gβγ subunit has been solved, which reveals that YM-254890 blocks GDP release (Figure 1.9)[38]. This results in the inability of the Gα subunit to bind GTP, prohibiting its activation[26,32].

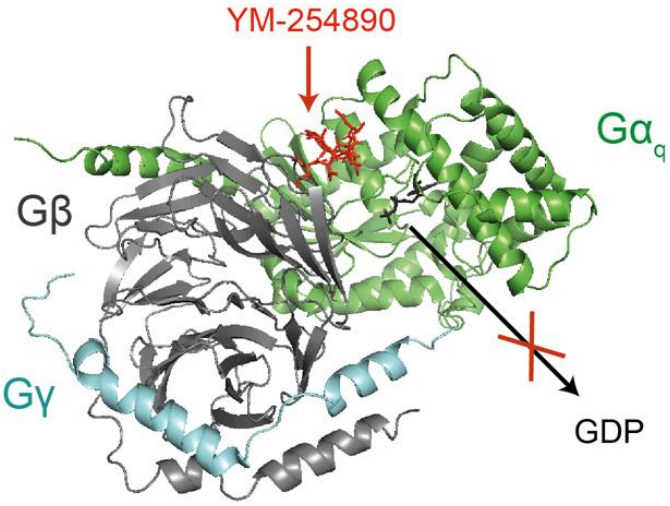


Figure 1.9 Structural basis for the inhibition of $G\alpha_q$ (green) by YM-254890 (red) (PDB code 3AH8). The Gß subunit is shown in grey, and the Gγ subunit is shown in turquoise. YM-254890 blocks GDP (black) release.

The greatest sequence diversity within the $G\alpha_{q/11}$ family is observed in the N-terminal region: while $G\alpha_q$ shares 83% of its first 40 amino acids with $G\alpha_{11}$, it only shares 65% with $G\alpha_{14}$ and 35% with $G\alpha_{15}$. This translates into differences in receptor coupling: studies have found that $G\alpha_{15}$, and to a lesser extent $G\alpha_{14}$, show promiscuity (i.e. couple to a large number of receptors) when co-expressed with GPCRs *in vitro*. However, the biological significance of this phenomenon is disputed due to the limited expression of $G\alpha_{14}$ and $G\alpha_{15}$ across tissues. In contrast, the widely expressed $G\alpha_q$ and $G\alpha_{11}$ subunits couple more selectively to GPCRs[26].

Very few differences have been observed between $G\alpha_q$ and $G\alpha_{11}$, and for historic reasons most studies have been conducted on $G\alpha_q$ with similar mechanisms inferred for $G\alpha_{11}$[6,26,32,39]. Sequence alignment using ClustalOmega[17] showed that approximately 324 (90%) of their amino acids are identical and a further 17 amino acids (5%) have similar chemical properties (Figure 1.10). Out of the 18 amino acids that are not similar, 13 (70%) are located in the helical domain, 3 (20%) are located in the N-terminal helix, and only 2 (10%) are located in the enzymatic GTPase domain[2,32,37,44].

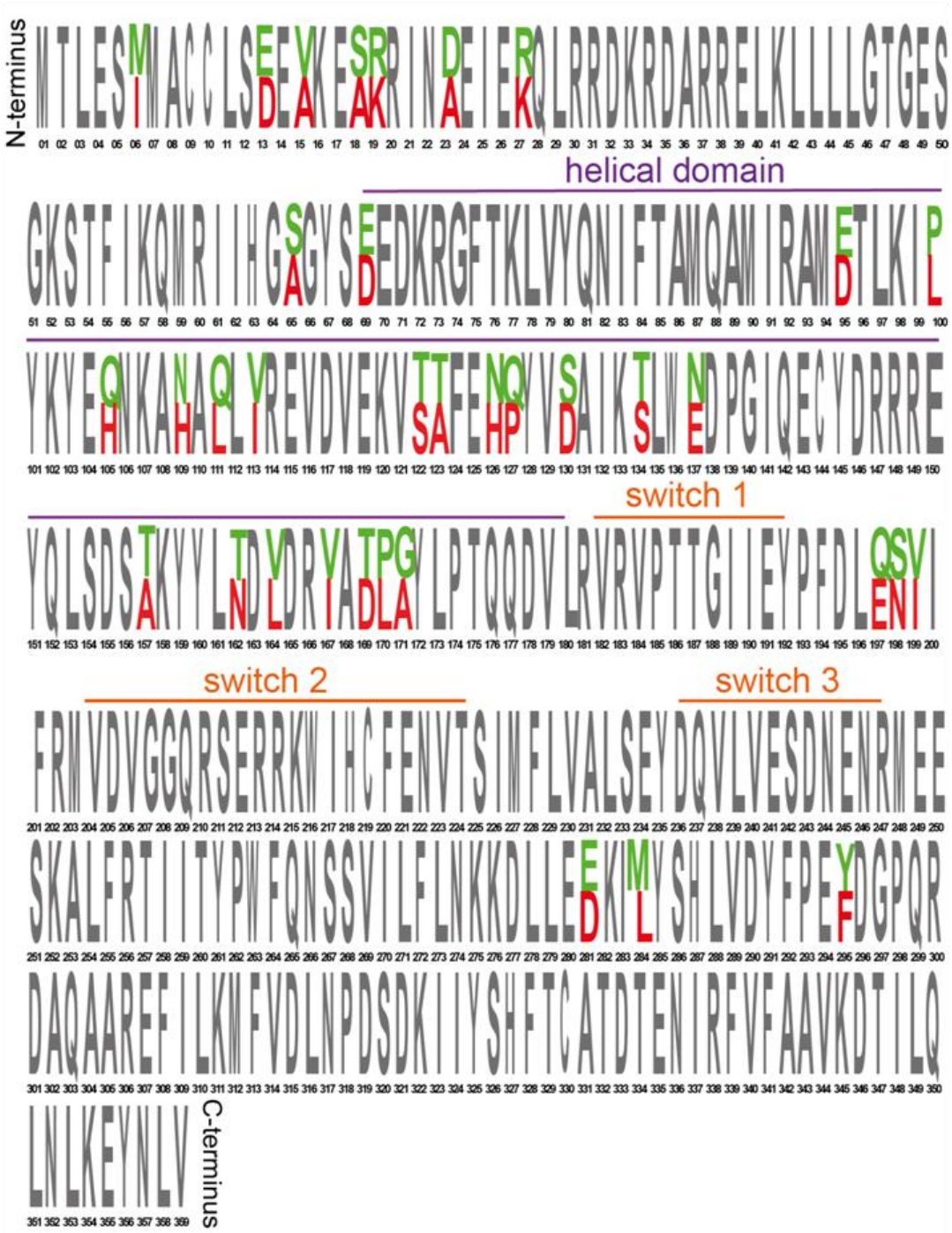


Figure 1.10 90% of amino acids of *GNAQ* and *GNA11* are identical (shown in grey). Amino acids that are only present in *GNAQ* are shown in green. Amino acids that are only present in *GNA11* are shown in red. The helical domain (indicated in purple) and the N terminus show the highest variation, whereas the three switch regions, which undergo conformational changes during G protein activation, (indicated in orange) are completely conserved.

1.1.3 G alpha s

The $G\alpha_s$ (stimulatory) family comprises $G\alpha_{olf}$ and three splice variants of the complex imprinted *GNAS* gene: a short variant ($G\alpha_{sS}$); a long variant ($G\alpha_{sL}$); and an extra-large variant ($G\alpha_{XL}$). $G\alpha_{sS}$ and $G\alpha_{sL}$ are ubiquitously expressed, whereas $G\alpha_{XL}$ is mainly present in the central nervous system (CNS), neuroendocrine tissues, and muscle[15,40,41]. $G\alpha_{olf}$ is predominantly expressed in olfactory neurons[6,9]. All $G\alpha_s$ family members stimulate adenylyl cyclases (ACs) in the activated state (Figure 1.11)[42,43]. ACs are membrane-bound enzymes which catalyse the conversion of adenosine triphosphate (ATP) to cyclic adenosine monophosphate (cAMP)[3,44-46], an important second messenger which activates downstream effectors such as protein kinase A (PKA). Overall, these signalling events result in cellular excitation, which promotes vital physiological functions such as heart muscle contraction, excitatory neurotransmission and hormone secretion[6,9].

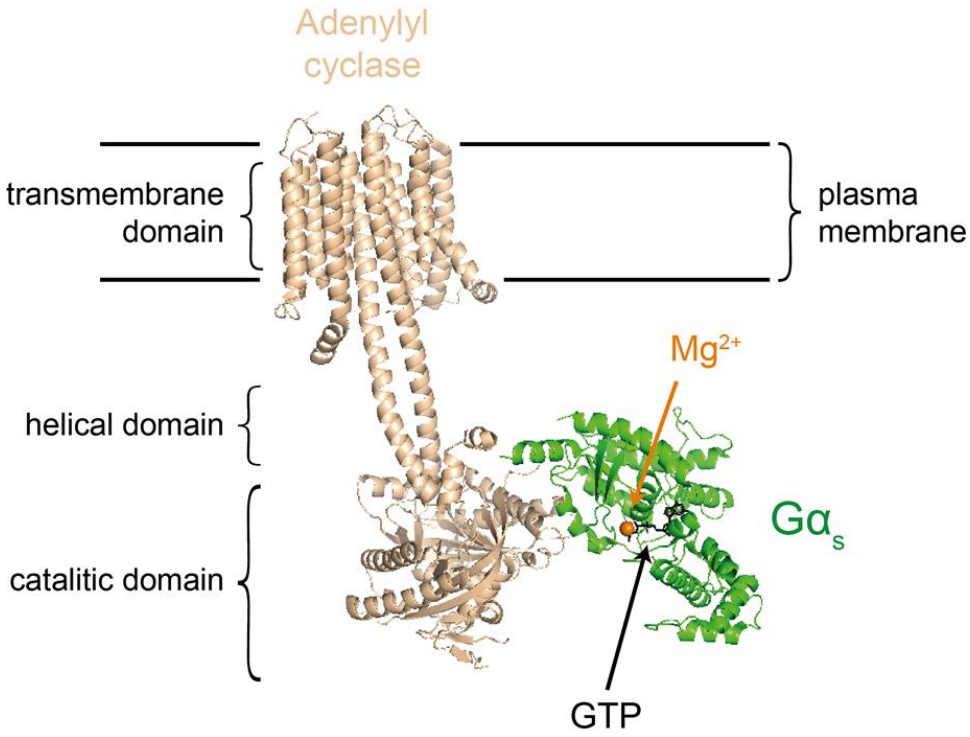


Figure 1.11 Cryo-electron microscopy structure of membrane-bound Adenylyl cyclase 9 (AC9) (beige) in complex with activated $G\alpha_s$ (green) (PDB code 6R3Q).

1.1.4 G alpha i/o

The $G\alpha_i$ family is the largest Gα family, consisting of 9 members[6]. The $G\alpha_{i1}$, $G\alpha_{i2}$ and $G\alpha_{i3}$ subunits are widely expressed, while $G\alpha_{oA}$, $G\alpha_{oB}$ and $G\alpha_z$ are predominantly expressed in neurons. $G\alpha_{T1}$ and $G\alpha_{T2}$ (transducin) are expressed in the retina, and $G\alpha_{gust}$ (gustatory) is expressed in taste cells.

In contrast to the $G\alpha_s$ family, members of the $G\alpha_i$ family cause inhibition of ACs rather than stimulation. They can stimulate other downstream effectors, such as the GAP rap1gap. Notably, pertussis toxin (PTX) selectively inhibits $G\alpha_{i/o}$ subunits, excluding $G\alpha_z$, and prevents their interaction with GPCRs. Hence, PTX is widely used as a tool to study $G\alpha_{i/o}$ signalling[6].

1.1.5 G alpha 12/13

Both $G\alpha_{12}$ and $G\alpha_{13}$ are ubiquitously expressed and have been shown to be important for neuronal development. Moreover, knockout studies in mice have demonstrated that $G\alpha_{13}$ is essential for blood vessel formation[9,47]. Analysis of their signalling capacities has been challenging since specific inhibitors are not available[6,9]. Traditionally, they have been linked to activation of RhoA leading to cytoskeletal re-arrangements such as membrane ruffling. However, it has recently been shown that the $G\alpha_{q/11}$ family are strong activators of RhoA[30,31,48,49]. Specific effectors for $G\alpha_{12/13}$ are the GEFs p115 and pdz[6,9].

1.1.6 G beta gamma

Initially, the Gβγ subunit was regarded as a passive partner of the Gα subunit. However, it is now established that it can also activate numerous downstream effectors such as ion channels and certain forms of ACs, PLCs and G protein-coupled receptor kinases (GRKs)[50-53]. These signalling events are often attributed to $G\alpha_{i/o}$ subunits because of

their relatively high endogenous abundance compared to members of other Gα families. When activated, they release high levels of Gβγ, therefore resulting in a large number of Gβγ mediated signalling events. This is particularly relevant for $G\alpha_o$: most signalling events attributed to $G\alpha_o$ have been reported to be mediated by Gβγ[50,54].

Unlike Gα subunits, major differences in signalling between the various Gβγ subunits have not been found[6,50,55]. One exception is $G\beta_5$, which does not function like a traditional Gβ subunit: it only weakly associates with the Gγ subunit and its primary function is binding of RGS proteins[56,57].

1.2 G protein-coupled receptors (GPCRs)

1.2.1 Signalling and trafficking

Heterotrimeric G proteins are activated by the largest family of membrane receptors: G protein-coupled receptors (GPCRs). Many of the 800 GPCRs encoded in the genome are widely expressed, and are involved in a plethora of physiological and pathophysiological processes, which make them prime drug targets. Indeed, >30% of prescription drugs act directly on GPCRs[28,58,59]. Agonist-activated GPCRs predominantly interact with 3 protein families: heterotrimeric G proteins, β-arrestins and GRKs[60]. GPCRs induce intracellular responses primarily via G proteins, which were reviewed in section 1.1. In contrast, β-arrestins and GRKs have evolved as negative feedback mechanisms, causing receptor desensitisation and endocytosis. However, we now know that β-arrestins can also participate in signal transduction and activate a distinct set of effectors, such as MAPKs, phosphoinositide 3-kinase (PI3K) and the serine/threonine kinase AKT[6,60-63].

1.2.2 Structure

Based on evolutionary conservation, GPCRs are divided into six main classes: class A (rhodopsin), class B1 (secretin), class B2 (adhesion), class C (glutamate), class F (frizzled) and class T2 (taste)[28,61,64,65].

All GPCRs share a conserved transmembrane domain (TMD) which is composed of seven membrane spanning helices, hence they are sometimes referred to as seven-transmembrane (7-TM) or heptahelical receptors[2]. In contrast, the intra- and extracellular domains (ICD and ECD, respectively) are characteristic for each family. Recent advancements in protein crystallography have led to a dramatic increase in the number of characterised receptor structures[66]. Example structures of class A, B, C and F receptors are shown in Figure 1.12.

Class A contains by far the largest number of receptors (719 in humans) and has been extensively studied. Approximately half of the class A receptors are sensory GPCRs which are activated by smell or vision. Non-sensory class A receptors are typically activated by small molecule ligands such as nucleotides or neurotransmitters[67], and are characterised by a relatively short N terminus. Examples of prototypical class A receptors include the muscarinic acetylcholine receptors M_1-M_5 and the ß2 adrenergic receptor (B2AR).

Class B1 receptors such as the parathyroid hormone receptor (PTHR) are activated by peptides, which are bound by the relatively large N terminus[64,68]. The class B2 (adhesion) GPCRs are believed to be involved in cell adhesion and migration[69]. They have exceptionally large N termini (up to 2800 amino acids long)[65,70], which has so far prevented their structural characterisation.

While many other GPCRs can function as monomers, class C GPCRs such as the metabotropic glutamate receptor 5 (mGluR5) and the Calcium-sensing receptor (CaSR) are obligatory dimers[71,72]. Their characteristic is a large extracellular domain (ECD) which binds agonists. The ECD is composed of a bilobed venus flytrap domain (VFT) and a cysteine rich domain (CRD)[73].

Class F receptors have a cysteine rich N terminus. They include smoothened (SMO), which is activated by steroids, such as epoxycholesterol, and acts as an oncoprotein[74,75].

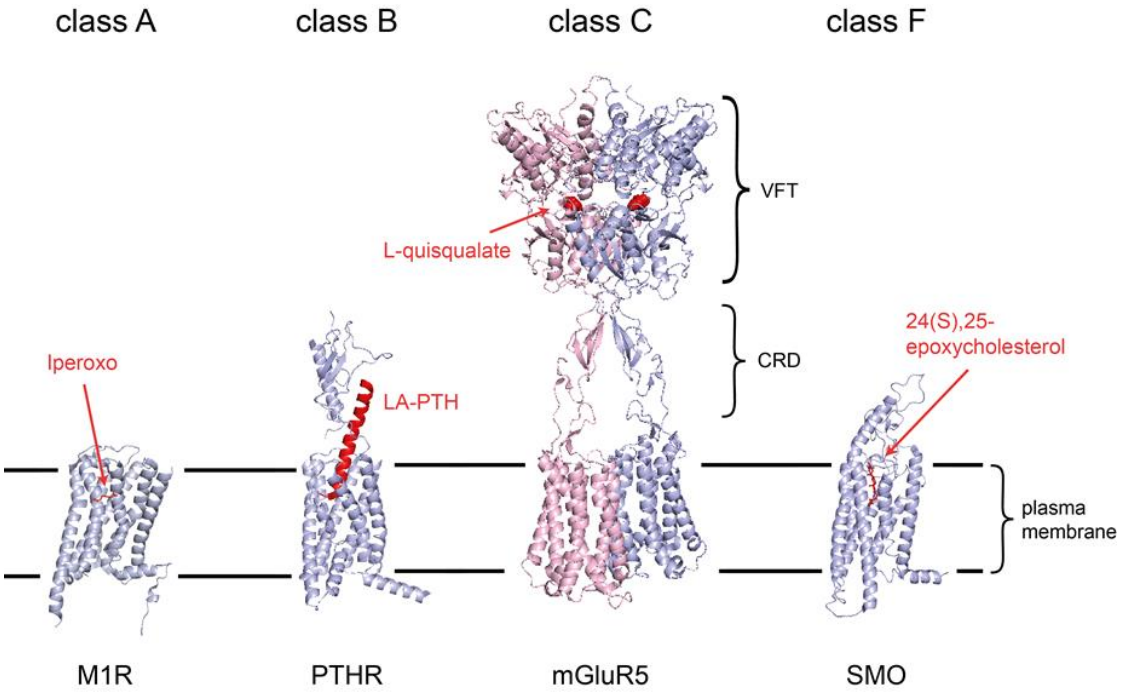


Figure 1.12 Crystal structures of class A, B, C and F GPCRs in complex with ligands. Class A is represented by the muscarinic acetylcholine receptor M1 (M1R) (light blue) in complex with the agonist iperoxo (red). (PDB code 6OIJ). Class B is represented by the parathyroid hormone receptor (PTHR) in complex with long-acting PTH (LA-PTH) (red) (PDB code 6nbf). Class C is represented by the metabotropic glutamate receptor 5 (mGluR5) in complex with the agonist L-quisqualate (red). The two protomers of the mGluR5 dimer are shown in light blue and light pink. The extracellular domain (ECD) is composed of the bilobed venus flytrap domain (VFT) and the cysteine rich domain (CRD) (PDB code 6n51). Class F is represented by smoothened (SMO) in complex with the agonist 24(S),25-epoxycholesterol (red) (PDB code 6ot0).

1.2.3 The Calcium-Sensing receptor (CaSR)

A GPCR that has been shown to be particularly important for signalling via $G\alpha_{11}$ is the Calcium-sensing receptor (CaSR), as demonstrated by germline mutations in $G\alpha_{11}$ causing abnormalities of CaSR signalling and related disorders[76] (see section 1.4). The CaSR is a member of the class C (or glutamate-like) family and shows the highest sequence homology with the orphan receptor GPRC6. It is also evolutionarily related to the taste type 1 receptors (TAS1R1-3), the metabotropic glutamate receptors (mGluR1-8) and the γ-aminobutyric acid type B receptors (GABAB1-2) (Figure 1.13)[77,78].

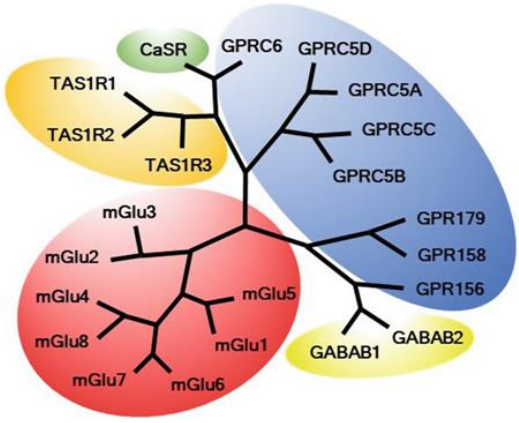


Figure 1.13 Classification of Class C GPCRs according to evolutionary conservation, comprising: the Calcium-Sensing receptor (CaSR) (green), the taste 1 receptors (TAS1R1-3) (orange), the metabotropic glutamate (mGlu) receptors (red), the gamma-aminobutyric acid receptors (GABAB1-2) (yellow) and the class C orphan receptors (blue). Adapted from Chavez-Abiega, et al.[77]

The human *CASR* gene maps to chromosome 3q13.3-21 and comprises 8 exons, of which exons 2-7 encode the 1078 amino acid long CaSR protein[79].

Analysis of 483 tissue samples obtained from the Human Protein Atlas (HPA)[80,81] RNA-Seq analysis (Figure 1.14) shows that the CaSR has by far the highest expression in the parathyroid glands, followed by the kidneys. It is therefore unsurprising that most of the physiological effects of the CaSR have been linked to calcium metabolism[76,82].

The non-calcitropic tissue with the highest CaSR mRNA expression is the pancreas[81,82], and it has been proposed that the CaSR has a role in glucose homeostasis and pancreatic islet physiology (reviewed in section 1.5).

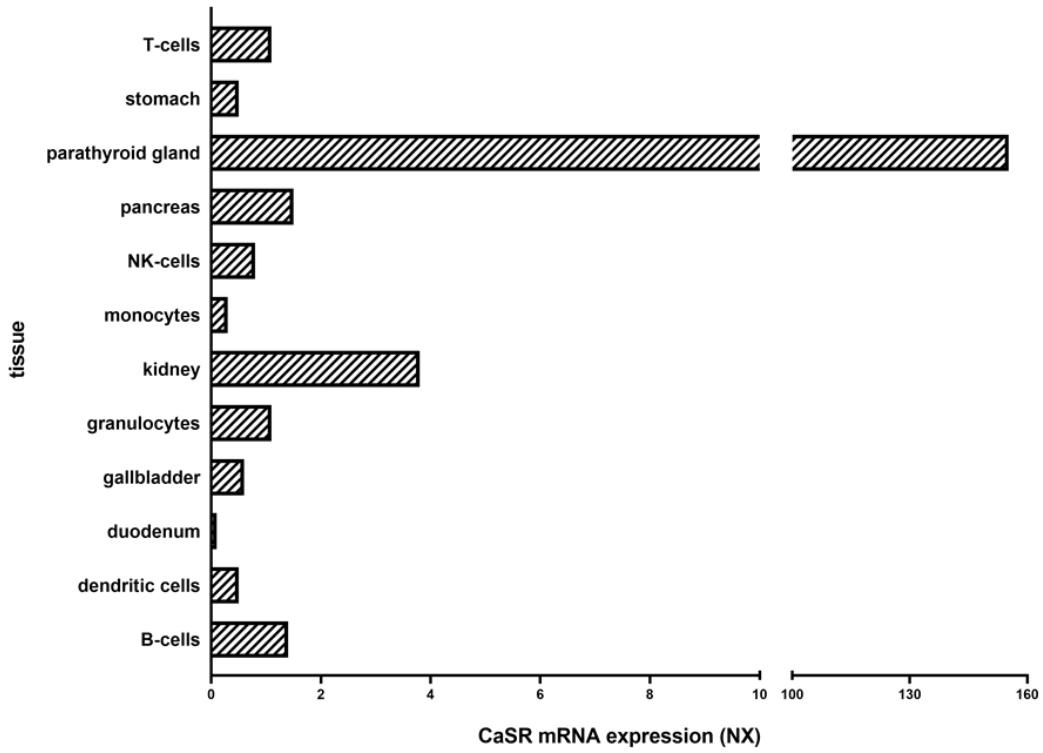


Figure 1.14 CaSR expression across a range of tissues. Normalised (NX) mRNA expression data from 483 tissue samples was obtained from the Human Protein Atlas (HPA) RNA-Seq analysis[81].

1.3 The CaSR as a regulator of extracellular calcium homeostasis

The CaSR is unique amongst GPCRs in that its main agonist is a cation: Ca^{2+}. As a result, it plays a critical role in maintaining extracellular calcium (Ca^{2+}_e) homeostasis.

Ca^{2+}_e concentrations are tightly regulated (ionised Ca^{2+}_e = 1.1-1.2 mmol/l and total Ca^{2+}_e = 2.2–2.4 mmol/l[83]) to ensure that a variety of biological processes including neuromuscular excitability, bone mineralisation, and blood coagulation occur correctly[82,84]. The main tissues involved in maintaining Ca^{2+}_e homeostasis are: the

skeleton, the parathyroid glands, the kidneys, and the intestines. Approximately half of the Ca^{2+}_e is available as free, ionised calcium, and the rest is bound to plasma albumin.

When ionised Ca^{2+}_e levels drop below 1.2 mM, the parathyroid glands secrete PTH[77]. PTH then acts on: bone to release calcium from skeletal calcium stores, the kidneys to increase renal tubular calcium reabsorption, and the 1-alpha hydroxylase to stimulate production of 1,25-dihydroxyvitamin D ($1,25(OH)_2D$), leading to an increase in dietary calcium absorption (Figure 1.15)[85-87]. Taken together, these mechanisms result in an increase in Ca^{2+}_e. This is antagonised by the calcium-sensing receptor (CaSR), which acts as a molecular feedback mechanism by detecting minor increases in Ca^{2+}_e. The CaSR elicits most of its calcitropic functions in the parathyroid glands and the kidneys[83,88], as detailed in the following section.

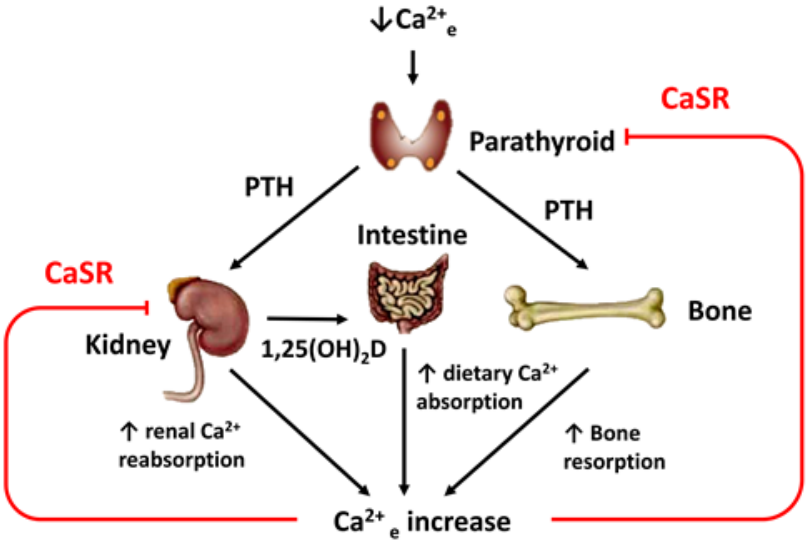


Figure 1.15 Overview of extracellular calcium (Ca^{2+}_e) homeostasis. Decreases in Ca^{2+}_e trigger parathyroid hormone (PTH) secretion from the parathyroid glands, which stimulates calcium reabsorption from bone, activation of 25(OH)D to $1,25(OH)_2D$ to increase calcium absorption from the intestine, and increases renal tubular calcium reabsorption. These mechanisms are antagonised by the calcium-sensing receptor (CaSR), which is activated by Ca^{2+}_e and decreases PTH secretion in the parathyroid glands and inhibits renal tubular calcium reabsorption. Adapted from Sigl et al, 2016[89].

1.3.1 CaSR actions in the parathyroid glands

The CaSR is highly expressed in the chief cells of the parathyroid glands, and to a lesser degree in the oxyphil cells[90,91]. It is activated by increasing concentrations of Ca^{2+}_e, which leads to signalling cascades (reviewed in section 1.6.2). These changes in signalling induce transcriptional changes which result in acute suppression of PTH secretion. In addition, CaSR activation also inhibits synthesis of preproparathyroid hormone (PreProPTH) and cell proliferation[92]. Both the $G\alpha_{q/11}$ and $G\alpha_{i/o}$ families have been shown to be critical mediators of CaSR function in the parathyroids[93,94]. However, the downstream mechanisms by which the CaSR controls PTH secretion are poorly understood[83,95]. Paradoxically, in parathyroid chief cells increases in Ca^{2+}_i lead to decreased exocytosis of secretory vesicles and thus decreased hormone secretion, whereas the opposite is true for most other secretory cells[92]. It has been suggested that this is partly mediated by Ca^{2+}_i-dependent inhibition of adenylate cyclase, which would result in inhibition of $G\alpha_s$-coupled GPCRs (e.g. B2AR) that mediate PTH secretion[83]. The central role of the parathyroid glands in Ca^{2+}_e homeostasis is highlighted by studies in mice with parathyroid-specific ablations of the CaSR, which develop severe elevations of both PTH and Ca^{2+}_e from birth[96].

1.3.2 CaSR actions in the kidneys

CaSR activation has indirect and direct effects on the kidneys. Examples of the former include CaSR-mediated suppression of PTH secretion in the parathyroid glands which leads to decreased activity of the renal PTHR, resulting in decreased Ca^{2+} reabsorption in the thick ascending limb of the loop of Henle (TAL), decreased phosphate excretion and reduced synthesis of 1,25(OH)2D by the proximal renal tubule[82]. CaSR also exhibits PTH-independent renal effects. Studies in thyroparathyroidectomised rats demonstrated that chronic CaSR inhibition increases renal tubular calcium absorption

independently of PTH secretion and intestinal calcium absorption[97]. Moreover, predialysis patients treated with cinacalcet exhibited a significantly higher number of hypocalcaemic events compared to dialysis patients, suggesting direct action of cinacalcet on renal CaSRs[98].

Renal CaSR expression is highest in the basolateral membrane of the TAL, and it has been suggested that CaSR promotes Ca^{2+} excretion in the TAL via functional interaction with tight junction proteins of the claudin family (CLDN), specifically CLDN14. CaSR mRNA and protein expression have also been confirmed in the proximal tubule, the distal convoluted tubule, the cortical collecting duct, and the outer medullary and inner medullary collecting ducts. In the glomerulus, CaSR protein but not mRNA expression has been detected.[88] Although the TAL seems to be the predominant mediator of CaSR-induced Ca^{2+} excretion, CaSRs in other regions of the kidney may be involved in fine-tuning mineral metabolism[99].

1.4 Calcitropic disorders of the CaSR signalling pathway

The importance of the CaSR in calcium homeostasis is highlighted by germline mutations of both the receptor and components of its signalling pathway (see section 1.6.2 for a detailed description of CaSR signalling)[86]. Thus, loss-of-function mutations of the *CASR*, *GNA11* and *AP2S1* (which encodes the Adaptor Related Protein Complex 2 Subunit Sigma 1) cause hypercalcaemic disorders. Conversely, gain-of-function mutations of the *CASR* and *GNA11* cause hypocalcaemic disorders[82,87,93,100-103]. An overview of calcitropic disorders caused by mutations of the CaSR signalling pathway is provided in Figure 1.16. Notably, some patients with familial hypercalcaemia/hypocalcaemia do not have mutations in the above-mentioned genes, suggesting a role for additional genes in the pathogenesis of calcitropic disorders.

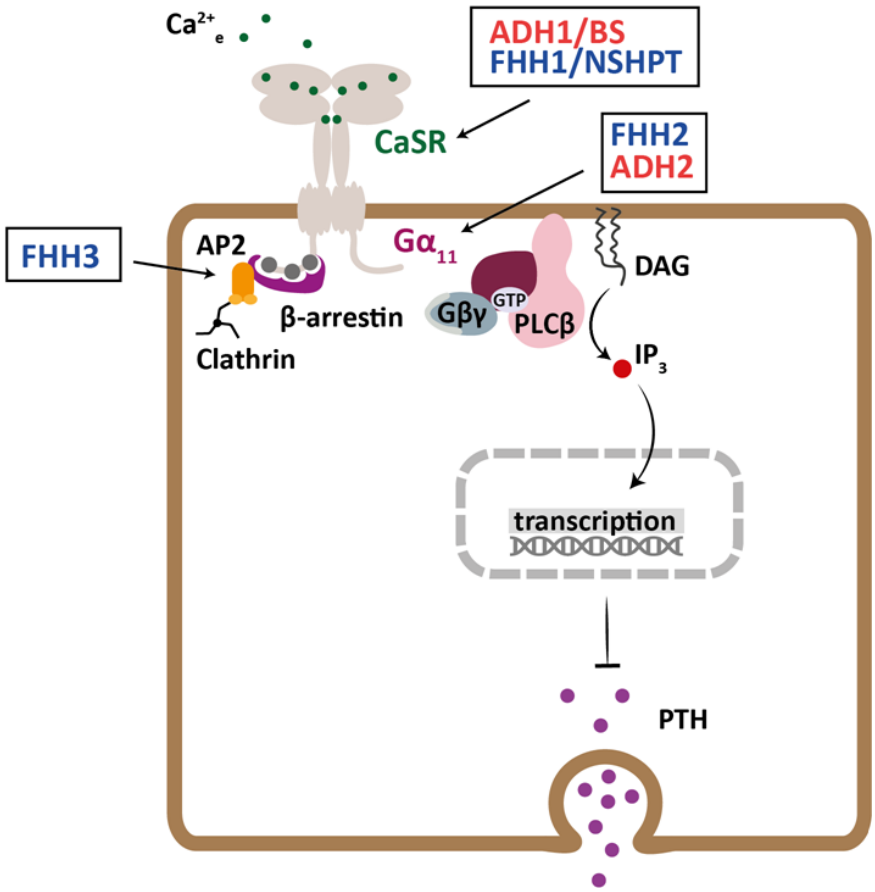


Figure 1.16 Overview of CaSR signalling in the chief cells of the parathyroid gland, and associated disorders. Stimulation of the calcium-sensing receptor (CaSR) by extracellular calcium (Ca^{2+}_e) leads to GTP binding by $G\alpha_{11}$ which results in dissociation from Gβγ. GTP-bound $G\alpha_{11}$ activates Phospholipase C beta (PLCβ) which subsequently catalyses hydrolysis of Phosphatidylinositol 4,5-bisphosphate (PIP_2) to diacylglycerol (DAG) and Inositol trisphosphate (IP_3). Transcriptional changes lead to inhibition of parathyroid hormone (PTH) secretion. Clathrin-mediated CaSR endocytosis requires β-arrestin and the Adaptor Related Protein Complex 2 Subunit Sigma (AP2). Loss- and gain-of-function CaSR mutations cause familial hypocalciuric hypercalcaemia type-1 (FHH1) and neonatal severe hyperparathyroidism (NSHPT), and autosomal dominant hypocalcaemia (ADH1) and Bartter syndrome Type 5 (BS), respectively. Moreover, loss- and gain-of-function *GNA11* mutations cause FHH2 and ADH2, respectively, and loss-of-function mutations in AP2S1 cause FHH3.

1.4.1 Hypercalcaemic disorders

1.4.1.1 Familial hypocalciuric hypercalcaemia type-1 (FHH1)

Familial hypocalciuric hypercalcaemia type-1 (FHH1) (OMIM 145980) is an autosomal dominant disorder which is caused by heterozygous loss-of-function CaSR mutations. It is characterised by elevations in Ca^{2+}_e, decreased urinary calcium, and high or high normal PTH levels. Two hundred and thirty-two FHH1-causing mutations have been reported, of which ~80% are missense mutations and the rest are nonsense mutations, deletions, insertions, insertion-deletions and intronic mutations. The majority of missense mutations are located in the ECD (152) and the TMD (67) of the CaSR, and only 13 are located in the ICD[104]. FHH1 is generally a benign disorder; however, a subset of patients may develop symptoms such as nephrolithiasis, pancreatitis, osteoporosis, muscle cramps, nausea and vomiting, headaches, fatigue or constipation[82,104]. Cinacalcet treatment has been shown to effectively lower Ca^{2+} levels in patients with symptomatic hypercalcaemia[105]. FHH1 was previously considered to be a rare disorder; however, recent studies of large population datasets have shown that FHH1 is a common cause of hypercalcaemia and has a similar prevalence as primary hyperparathyroidism[106].

1.4.1.2 Neonatal severe hyperparathyroidism (NSHPT)

Neonatal severe hyperparathyroidism (NSHPT) (OMIM 239200) is a severe, life-threatening disorder which is characterised by severe hypercalcaemia (3.5–5.0 mmol/l) due to homozygous or compound heterozygous, and in rare cases heterozygous, loss-of-function CaSR mutations. Further symptoms include bone demineralisation, hypotonia, respiratory distress and failure-to-thrive[107]. Although cinacalcet has been shown to lower Ca^{2+} and PTH in some individuals with NSHPT, parathyroidectomy is often required[104].

1.4.1.3 Familial hypocalciuric hypercalcaemia type-2 (FHH2)

Familial hypocalciuric hypercalcaemia type-2 (FHH2) (OMIM 145981) is caused by loss-of-function mutations in *GNA11.* Only 4 FHH2-causing mutations (3 missense and 1 inframe deletion) have been reported to date[93,108,109]. They cause a phenotype that is similar to that of FHH1, with mild (2.55-2.8 mmol/l) elevations of Ca^{2+}_e and low urinary calcium excretion. FHH2 may be associated with a milder phenotype than FHH1, which could be due to compensation by the related $G\alpha_q$ protein[109].

1.4.1.4 Familial hypocalciuric hypercalcaemia type-3 (FHH3)

Familial hypocalciuric hypercalcaemia type-3 (FHH3) (OMIM 600740) is caused by loss-of-function mutations in AP2S1 which is required for clathrin-mediated endocytosis of the CaSR. The vast majority (>98%) of reported FHH3 cases are caused by mutations of the Arg15 residue[86]. Paradoxically, impaired CaSR endocytosis causes a reduction of Ca^{2+} induced CaSR signalling. This is likely due to an impairment in sustained CaSR signalling[110]. FHH3 is associated with more severe hypercalcaemia than FHH1 and FHH2[76]. Moreover, some patients with FHH3 may develop cognitive impairment[111]. Finally, cinacalcet has been shown to be effective for the treatment of symptomatic FHH3[112].

1.4.2 Hypocalcaemic disorders

1.4.2.1 Autosomal Dominant Hypocalcaemia type-1 (ADH1)

Autosomal Dominant Hypocalcaemia type-1 (ADH1) (OMIM 601198) is caused by gain-of-function CaSR mutations. To date, 100 ADH1-causing CaSR mutations have been reported, of which 95 are missense mutations, 4 are deletions and 1 is a nonsense mutation. The majority of missense mutations are located in the CaSR ECD (52), and in the TMD (41). Only 2 mutations are located in the ICD. ADH1 is characterised by

mild-to-moderate hypocalcaemia, low-to-normal PTH levels, high normal-to-high urinary calcium excretion, mild hypomagnesaemia and hyperphosphataemia[86,104]. In contrast to FHH1, the majority (>70%) of patients with ADH1 develop symptoms including seizures, tetany, carpopedal spasms, paraesthesia, nephrocalcinosis and basal ganglia calcifications[104,113]. A subset of ADH1 patients (predominantly those with severe gain-of-function and constitutively active CaSR mutations) develops Bartter's syndrome type 5, which is characterised by hypokalaemia, a metabolic alkalosis, hypomagnesaemia and hyperaldosteronaemia[114,115]. Current treatments for ADH1 include oral calcium supplements, active analogues of vitamin D (e.g. calcitriol), thiazide diuretics and recombinant human PTH in patients who have not responded to treatment with calcium and vitamin D. However, calcilytics which have been shown to normalise the effects of certain CaSR mutations *in vitro* and in mouse models may constitute a more targeted treatment for ADH1[116].

1.4.2.2 Autosomal Dominant Hypocalcaemia type-2 (ADH2)

Autosomal Dominant Hypocalcaemia type-2 (ADH2) (OMIM 615361) is caused by gain-of-function *GNA11* mutations[93]. ADH2 patients have similar phenotypes to ADH1 patients; however, individuals may present with milder hypocalcaemia and less pronounced hypercalciuria than patients with ADH1[113]. Additionally, an association with short stature has been reported for 2 ADH2-causing mutations[117,118]. To date, 8 ADH2-causing *GNA11* mutations have been identified which cluster within regions of the Gα subunit that are critical for GPCR-G protein coupling, nucleotide binding and downstream effector activation[137,158,160-162].

1.4.3 Disorders arising from CaSR Autoantibodies

In rare cases, patients can develop the clinical features of FHH and ADH due to autoantibodies which inhibit or stimulate the CaSR, respectively. These are called

autoimmune hypocalciuric hypercalcaemia (AHH) and autoimmune hypoparathyroidism, respectively[82]. Notably, an AHH-causing autoantibody shows the most extreme example of biased signalling that has been reported for the CaSR[119] (section 1.6.3.4).

1.4.4 Mouse models for inherited disorders of the CaSR signalling pathway

A number of mouse models which recapitulate the phenotypes of human inherited disorders of the CaSR signalling pathway have been developed. These provide important insights into the pathogenesis of FHH and ADH and facilitate the development of novel therapeutics. An overview is provided in Table 1.1.

Table 1.1 Mouse models for inherited disorders of the CaSR signalling pathway

Human disorder	Mutation	reference
FHH1	CASR +/-	Ho, et al.[120]
NSHPT	CASR -/-	Ho, et al.[120]
FHH2	*GNA11* Asp195Gly	Howles, et al.[121]
FHH3	*AP2S1* Arg15Leu	Hannan, et al.[122]
ADH1	*CASR* (Nuf)	Hough, et al.[123]
ADH1	*CASR* Cys129Ser	Dong, et al.[116]
ADH1	*CASR* Ala843Glu	Dong, et al.[116]
ADH2	*GNA11* Arg60Cys	Roszko, et al.[124]
ADH2	*GNA11* Ile62Val (Dsk)	Gorvin, et al.[125]

1.4.4.1 FHH mouse models

The first insights into the mechanisms by which CaSR mutations cause calcitropic disorders were provided by a mouse model with disruption of the *CASR* gene (CaSR null mice)[120]. Mice with heterozygous deletion of one allele had mild hypercalcaemia and hypocalciuria as seen in FHH1 patients. Moreover, mice with deletion of both alleles of *CASR* (homozygous) had a phenotype which resembled NSHPT, with severe hypercalcaemia, moderate hypermagnesaemia and increased PTH concentrations. They

also showed significant growth retardation and died between 3 and 30 days of age (Figure 1.17). Similarly, mice with loss-of-function *GNA11* (Asp195Gly) and *AP2S1* (Arg15Leu) mutations recapitulate the phenotypes of FHH2 and FHH3, respectively[122,125].

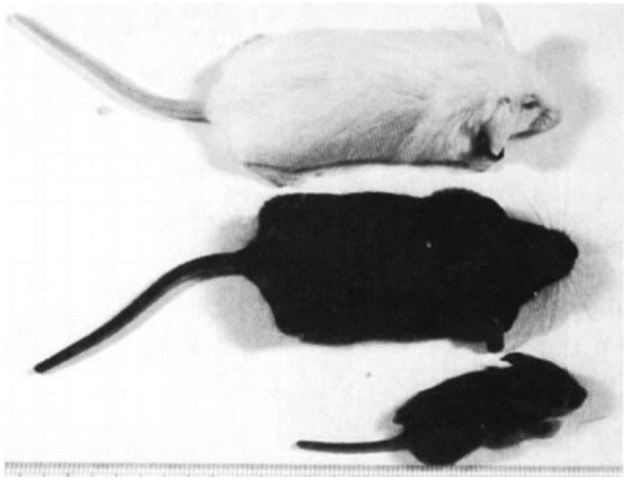


Figure 1.17 Appearance of CASR +/+ (top), +/- (middle) and -/- (bottom) mice at 23 days of age. Adapted from Ho, et al.[120].

1.4.4.2 ADH mouse models

A genetic screen using the chemical mutagen isopropyl methane sulphonate (iPMS) revealed mice with a Leu723Gln CaSR mutation which developed opaque flecks in the nucleus of the lens, and were therefore called "Nuf" mice[123]. Subsequent analysis revealed that they are a model of ADH1, i.e. they have hypocalcaemia, hyperphosphataemia, low PTH concentrations and ectopic calcifications. Moreover, when expressed *in vitro*, CaSR Leu723Gln caused gain-of-function in calcium mobilisation assays[123].

Similarly, mice with a gain-of-function *GNA11* mutation (Ile62Val) established by N-ethyl-N-nitrosourea (ENU), known as Dsk7 due to their dark skin[36], were found to be a

model for ADH2[125]. A second mouse model for ADH2 was developed by CRISPR/CAS9 knock-in of the human mutation *GNA11* Arg60Cys[124].

Interestingly, some ADH mouse models also have non-calcitropic phenotypes, which will be detailed in section 1.5.2.

1.5 Non-calcitropic effects of the CaSR

Even though systemic calcium homeostasis is regulated predominantly by calcitropic tissues such as the parathyroids and the kidneys, Ca^{2+}_e as a signalling mechanism is crucial for all cells[82].

The CaSR is expressed in a wide range of tissues[79,126] (see section 1.2.3) and in recent years it has been reported that, in addition to being critical for extracellular calcium homeostasis, it may also be involved in the pathogenesis of several non-calcitropic disorders[79,125]. Examples include: colon cancer[168], breast cancer[127-129], Alzheimer's disease[130-133], asthma[169] and abnormalities in glucose metabolism[134].

1.5.1 Systemic glucose homeostasis

In order to ensure sufficient energy supply to all organs, blood glucose must be maintained between 4 and 6 mM[135]. This is particularly critical for the brain: if glucose levels fall below 3mM for a few minutes, it can have fatal consequences[136]. Conversely, chronic hyperglycaemia causes macrovascular and microvascular pathologies, such as atherosclerosis and neuropathies, respectively[137,138]. An overview of glucose homeostasis is shown in Figure 1.18.

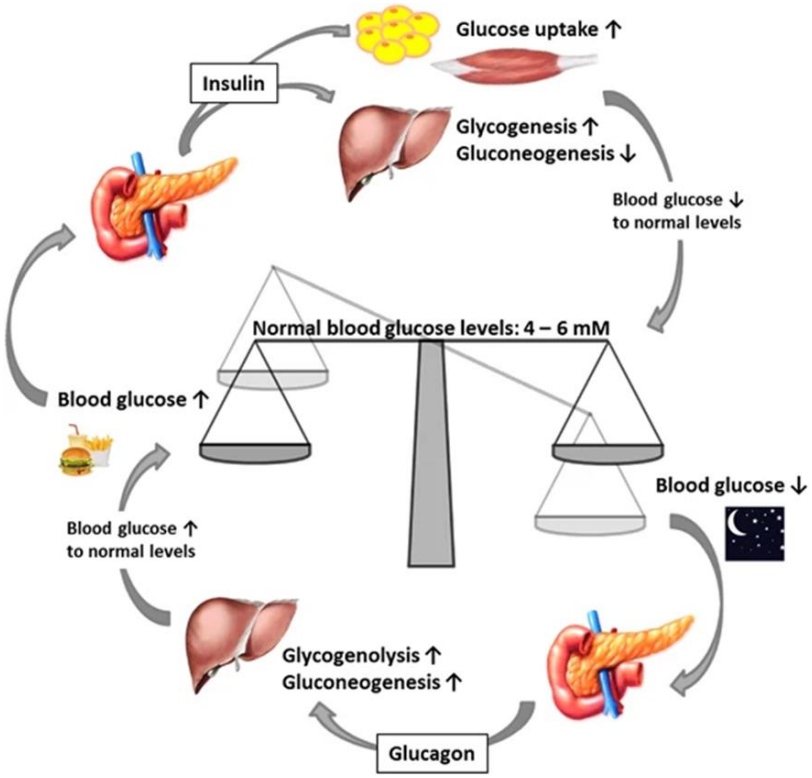


Figure 1.18 Overview of systemic glucose homeostasis. In response to increasing blood glucose concentrations, the pancreas secretes insulin which stimulates glucose uptake into muscle and adipocytes, promotes hepatic glycogenesis and inhibits gluconeogenesis. This leads to a drop in glucose levels, which triggers glucagon secretion from the pancreas. Glucagon promotes glycogenolysis and gluconeogenesis, thereby increasing glucose levels. Taken together, these mechanisms ensure that blood glucose levels are permanently kept between 4 and 6mM. Adapted from Roder, et al.[135].

The key regulators of systemic glucose metabolism are clusters of endocrine cells within the pancreas called the "islets of Langerhans" (Figure 1.19A). Pancreatic islets consist of α, ß and δ cells which produce glucagon, insulin and somatostatin, respectively, and constitute approximately 1% of pancreatic tissue (Figure 1.19B)[139].

Pancreatic ß cells express ATP-sensitive potassium (K_{ATP}) channels, which are open at low glucose concentrations. This permits K^+ efflux (due to an outwards gradient) and keeps the cell hyperpolarised. When blood sugar levels rise (e.g. after a meal), glucose

is taken up into ß cells (Figure 1.19C), which is facilitated by the glucose transporters GLUT1-3[140]. Subsequently, glucose undergoes glycolysis and mitochondrial oxidation, resulting in an increase of adenosine triphosphate (ATP). ATP causes K_{ATP} channels to close, triggering opening of T type Ca^{2+} channels and ß cell depolarisation. This leads to activation of voltage-gated Ca^{2+} and Na^{+} channels[139,141-143].

Subsequently, intracellular calcium (Ca^{2+}_i) concentrations increase due to an inward gradient. Ca^{2+}_i triggers the fusion of insulin-containing vesicles with the plasma membrane, thereby promoting insulin release into the bloodstream.

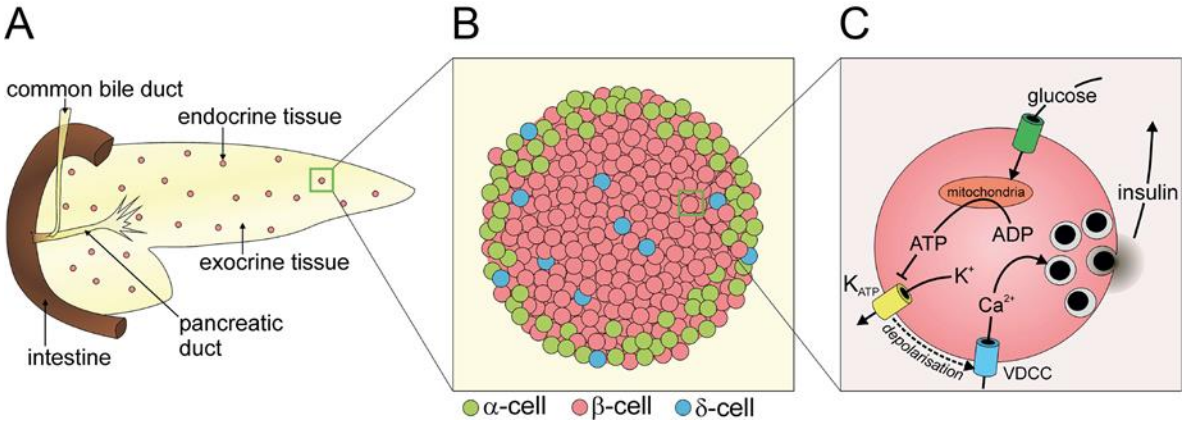


Figure 1.19 Schematic representation of pancreas histology. (A) The pancreas is located adjacent to the intestine (brown) and the common bile duct. Approximately 1% of pancreatic tissue consists of endocrine tissue (red) and the rest is exocrine tissue (pale yellow). (B) Endocrine cells are organised into clusters ("islets of Langerhans") which are composed of α (green), ß (red) and δ (blue) cells. (C) After a meal, glucose is taken up into ß cells via glucose transporters (green). Subsequently, glucose undergoes glycolysis and oxidation in mitochondria (orange), resulting in conversion of adenosine diphosphate (ADP) to adenosine triphosphate (ATP). ATP causes K_{ATP} channels (yellow) to close, triggering depolarisation and opening of voltage-dependent calcium channels (VDCCs). This leads to an influx of Ca^{2+}, which induces fusion of insulin-containing vesicles with the plasma membrane, thereby promoting insulin release into the bloodstream. Adapted from MacDonald and Rorsman[139].

This process involves a number of GPCRs which are expressed in the membrane of islet cells[144]. For example, insulin secretion is potentiated by neurotransmitters and hormones that are released in response to food, such as the incretin glucagon-like peptide-1 (GLP-1) which is released from the gut post-prandially and binds the $G\alpha_s$-coupled GLP-1 receptors expressed at the ß cell membrane[135,136,139,141,145,146].

Circulating insulin stimulates uptake of glucose into adipose and muscle tissue though the insulin sensitive glucose transporter 4 (GLUT4). Moreover, insulin acts on the liver to inhibit gluconeogenesis and promote glycogenesis, and adipose tissue to stimulate lipogenesis. Taken together, these effects lead to a decrease in glucose levels[135,142,143].

The effects of insulin are counter-balanced by its opponent glucagon, which is secreted from pancreatic α cells when glucose levels drop below 3.5mM. Glucagon drives lipolysis, glycogenolysis, and gluconeogenesis, thereby increasing glucose levels[135,144].

1.5.2 The role of the CaSR in systemic glucose homeostasis

Studies have shown that the CaSR is highly expressed in rodent[147-149] and human[91,150,151] pancreatic α and ß cells, but not in δ cells. Moreover, *CASR* mRNA was found to be one of the most abundant GPCR mRNAs in human islets[144]. However, the role of the CaSR function in pancreatic islet physiology and systemic glucose homeostasis is unclear[152].

An association study of renal transplant patients reported a common coding region CaSR variant to be an independent determinant of plasma glucose concentrations[153]. In contrast, studies in FHH patients showed no association between CaSR loss-of-function mutations and alterations in glucose tolerance or insulin secretion[154].

In isolated human pancreatic islets and the insulin-secreting cell line (MIN6), CaSR stimulation by the positive allosteric modulator (PAM) R-568 caused marked increases in insulin secretion, which was partially blocked by PLC inhibitors[150]. Moreover, R-568

treatment also caused significantly increased glucagon secretion from human pancreatic islets[150]. Another PAM, R-467, stimulated insulin secretion in mouse islets and the ßHC9 cell line, which was suggested to be independent of $G\alpha_i$, $G\alpha_o$, $G\alpha_{q/11}$ and $G\alpha_s$[155].

Notably, insulin-containing granules of the pancreatic ß cell are rich in calcium, and local concentrations of Ca^{2+}_e have been shown to increase in the millimolar range following insulin secretion, suggesting a role for calcium-sensing by the CaSR in autocrine/paracrine communication within the islet[156]. A model has been proposed in which the CaSR enhances functional coupling of pancreatic ß cells by sensing glucose-induced release of calcium from neighbouring ß cells. The resulting mobilisation of Ca^{2+} from intracellular stores stimulates further insulin and Ca^{2+} secretion, thereby propagating the signal through the islet (Figure 1.20)[152].

In contrast to the above described studies in isolated islets which suggest that CaSR activation promotes insulin secretion, Nuf mice which harbour a germline CaSR gain-of-function mutation and are a model for ADH1 have impaired glucose tolerance in combination with reduced insulin secretion and increased glucagon secretion[134]. These effects were normalised upon treatment with the NAM Ronacaleret[134]. Nuf mice also have significantly reduced pancreatic islet size and number, and analysis of individual islets revealed that the ratio of α and ß cells was shifted towards α cells. Moreover, the proportion of proliferating ß cells was significantly decreased, and the proportion of proliferating α cells was significantly increased. Abnormalities in ß cell membrane depolarisation were not found; however, Nuf mice had impaired α cell membrane depolarisation. Taken together these findings indicate that the CaSR may have different roles in acute glucose regulation compared to pancreatic islet development[134].

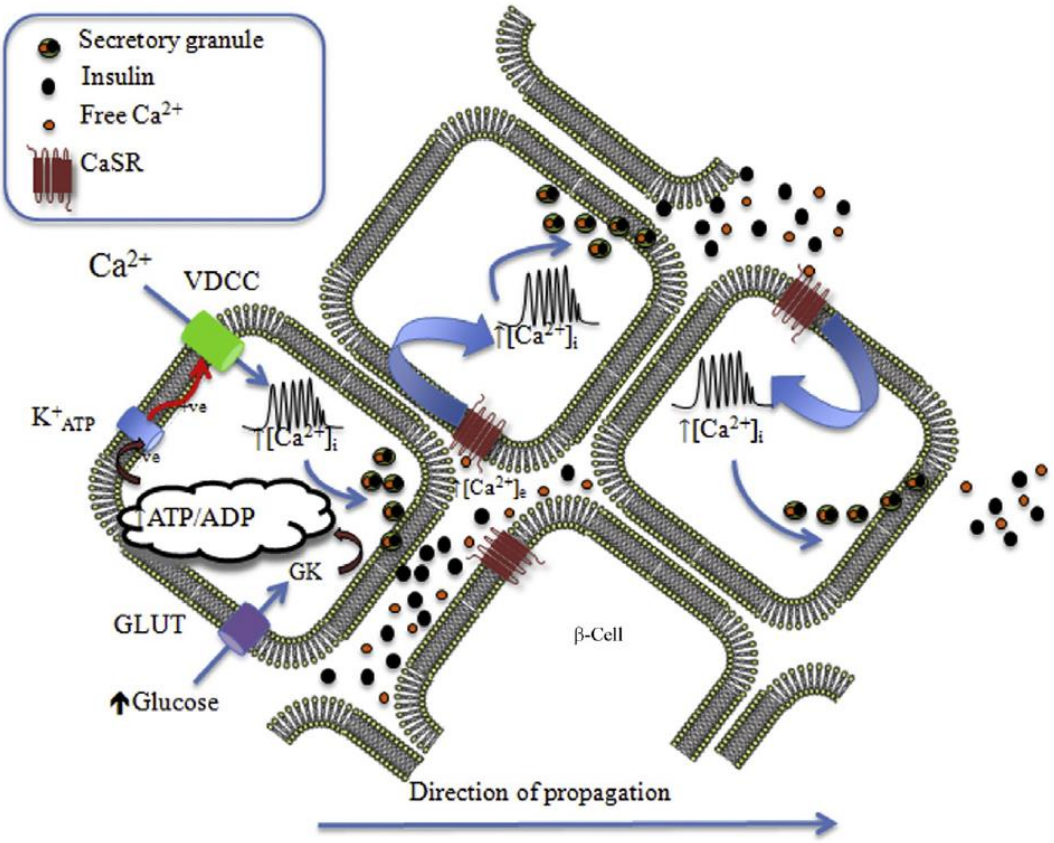


Figure 1.20 Proposed model for CaSR-mediated functional coupling of pancreatic ß cells. Increases in blood glucose result in uptake of glucose into pancreatic ß cells by GLUT transporters and glucokinase (GK) mediated glucose metabolism. The resulting increase in ATP over ADP closes K_{ATP} channels and causes activation of voltage dependent calcium channels (VDCCs). Subsequently, membrane depolarisation and Ca^{2+} influx occur. This stimulates release of secretory granules containing insulin and free Ca^{2+}. CaSRs expressed in the membrane of adjacent cells are activated by the local increase in Ca^{2+}_e, triggering mobilisation of Ca^{2+} from intracellular stores and subsequent signal propagation through the islet. Adapted from Squires, et al.[152]

Interestingly, the Dsk7 mice, which are a model for ADH2[125], mirror the calcitropic phenotype of Nuf mice. However, it is not known whether Dsk7 mice also have abnormal glucose metabolism (Table 1.2). Investigation of glucose metabolism in Dsk7 mice may

elucidate the molecular mechanism behind the impaired glucose tolerance phenotype of the Nuf mice.

Table 1.2 Comparison of phenotypes between human ADH patients, Nuf mice (model for ADH1) and Dsk7 mice (model for ADH2).

Feature	ADH patients	Nuf mice	DSK7 mice
Hypocalcaemia	✓	✓ HOM 1.62 mmol/L	✓ HOM 1.72 mmol/L
Activating CaSR mutation	✓ (ADH1)	✓, Leu723Gln	X
Activating $G\alpha_{11}$ mutation	✓ (ADH2)	X	✓, Ile62Val
Impaired glucose tolerance	?	✓	?
Reduced islet mass	?	✓	?
Abnormal α to ß cell ratio	?	✓	?
Reduced ß cell proliferation	?	✓	?
Increased α cell proliferation	?	✓	?
Membrane depolarisation defects	?	✓	?

1.6 CaSR structure and signalling

In order to understand the phenotypic effects described above it will be crucial to elucidate the fundamental signalling properties and structure-function of the CaSR. In the following section I will give an overview of the current knowledge of CaSR structure and signalling.

1.6.1 Crystal structure of the extracellular domain

The structure of the CaSR ECD homodimer has recently been solved[157,158]. It consists of 612 amino acids which form the bilobed venus flytrap domain (VFT) and the cysteine

rich domain (CRD) which are both characteristic for class C GPCRs (see section 1.2)[59,89,77].

The main endogenous agonist of the CaSR is Ca^{2+}_e. Additionally, the CaSR can also interact with a wide range of organic and inorganic molecules which will be reviewed in section 1.6.3.

In the reported crystal structures of the ECD, four calcium-binding sites have been identified in the active conformation: three in the VFT and one in the CRD (Figure 1.21). Additionally, 2 phosphate (PO_4^{3-}) molecules and one L-Tryptophan (L-Trp) molecule have been observed to bind to each protomer[158].

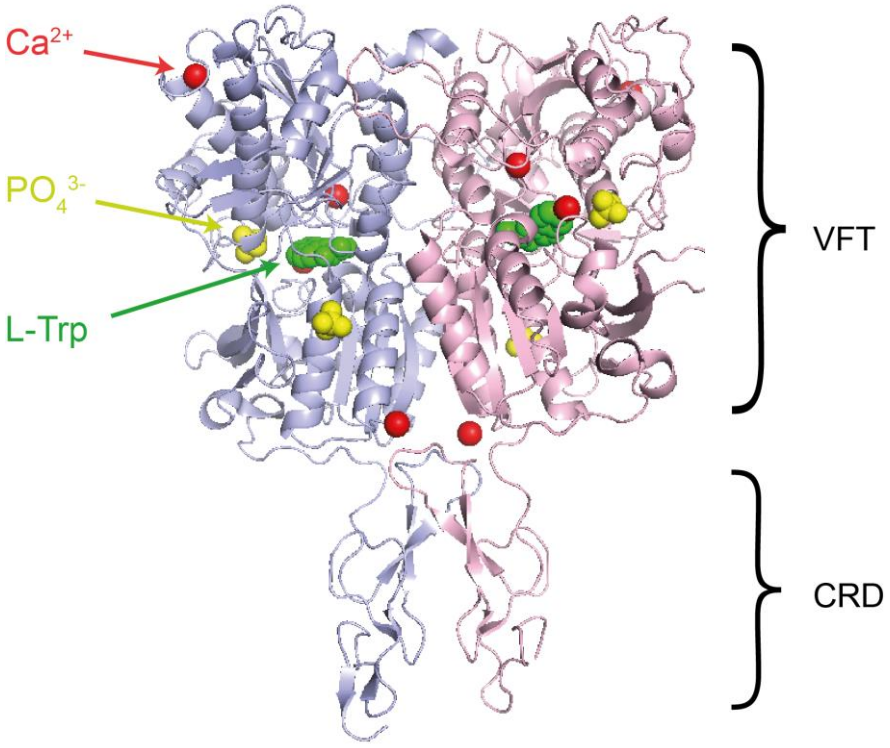


Figure 1.21 Structure of the active CaSR extracellular domain (ECD) (PDB code 5k5s). The two protomers are shown in light blue and light pink, respectively. The ECD consists of the bilobed venus flytrap domain (VFT) and the cysteine rich domain (CRD). Also shown for each protomer are: the four Ca^{2+} binding sites (red), the two PO_4^{3-} binding sites (yellow) and the L-Tryptophan (L-Trp) binding site (green).

1.6.2 Cell signalling and trafficking

The CaSR has been reported to activate multiple downstream effectors attributed to the $G\alpha_{q/11}$, $G\alpha_{i/o}$ and potentially $G\alpha_{12/13}$ subunits[77,82,94]. In addition, it has also been shown to signal via ß arrestin 1 and 2[159]. This pluripotency is remarkable because most other class C GPCRs such as the GABA B receptor[160] and the mGluRs[161] predominantly signal through one G protein family. However, this complex signalling network makes CaSR function difficult to study[77].

An overview of CaSR signalling pathways is presented in Figure 1.22. For some pathways, the responsible G protein family has been established. For example, IP_3 production and mobilisation of calcium from intracellular stores (Ca^{2+}_i mobilisation) are predominantly mediated by $G\alpha_{q/11}$[26], and inhibition of cAMP production is predominantly mediated by $G\alpha_{i/o}$[9]. Other pathways are less definitive: ERK1/2 phosphorylation can be induced by ß arrestins, $G\alpha_{q/11}$ and $G\alpha_{i/o}$; and plasma membrane ruffling can be mediated by ß arrestins, $G\alpha_{q/11}$ and $G\alpha_{12/13}$[77,94]. Moreover, it has been reported that G protein subtypes of the same family can cause differences in signalling, making the identification of G protein subtype to pathway a fraught endeavour[162].

To further complicate matters, signalling may be influenced by the subcellular compartments in which the receptors are located (e.g. plasma membrane, caveolae, endosomes) and the timescales at which they occur (fast versus slow kinetics)[60,63,163-166]. Indeed, ERK1/2 activation[110,167] and parathyroid hormone-related protein (PTHrP) secretion have been reported to be influenced by CaSR trafficking[168].

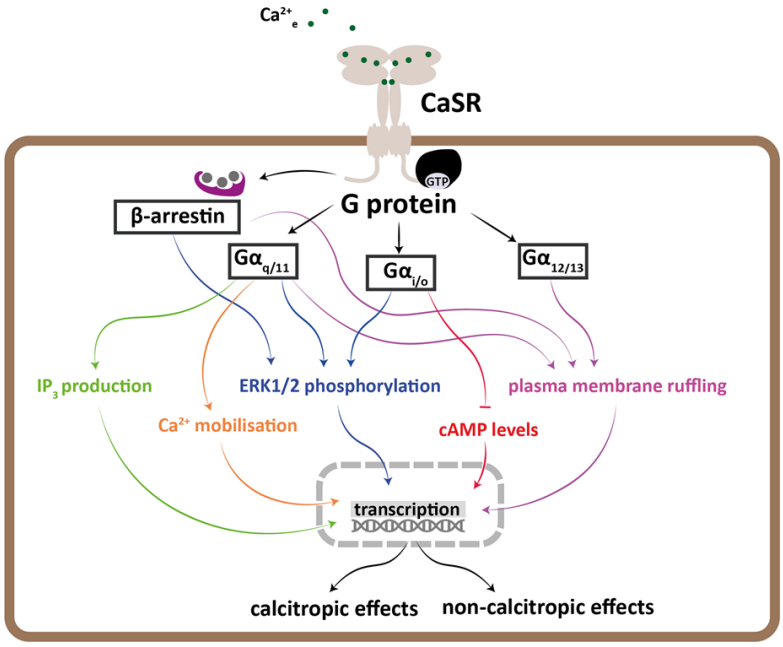


Figure 1.22 Overview of CaSR signalling pathways and cross-talk. CaSR (beige) activation by Ca^{2+}_e stimulates downstream readouts (indicated by arrows) of: β-arrestin (ERK1/2 phosphorylation, plasma membrane ruffling); $G\alpha_{q/11}$ (IP_3 production, Ca^{2+} mobilisation, ERK1/2 phosphorylation, plasma membrane ruffling); $G\alpha_{i/o}$ (ERK1/2 phosphorylation, inhibition of cAMP production); and $G\alpha_{12/13}$ (plasma membrane ruffling). These signalling events result in transcriptional changes which mediate calcitropic and non-calcitropic effects.

1.6.3 Calcimimetics and calcilytics

CaSR downstream signalling is modulated by a variety of ligands which are frequently referred to as calcimimetics and calcilytics. The terms refer to molecules which imitate or antagonise the effects of Ca^{2+} on the CaSR, respectively[98]. Calcimimetics are divided into two types. Type 1 calcimimetics are orthosteric agonists which are capable of activating the CaSR. Type 2 calcimimetics are positive allosteric modulators which require an orthosteric agonist to be present to elicit their function. Although more recent studies have shown that many allosteric modulators can also act as agonists under certain conditions, the concentrations at which this is observed are typically several orders of magnitude higher than what is physiologically relevant[74,102,103].

1.6.3.1 Orthosteric agonists

Orthosteric agonists are typically organic or inorganic polycations. An overview is provided in Table 1.3. Their EC_{50} ranges from 4nM for poly-L-arginine 100 kDa to 8mM for triethylenetetramine. The main physiological ligand, Ca^{2+}, has a medium potency with an EC_{50} of approximately 1.2 mM. In *in vitro* assays the hill coefficient of Ca^{2+}_e to activate the CaSR is between 3-5, suggesting that the multiple Ca^{2+} binding sites of the CaSR which are observed in the ECD (see Figure 1.21) are allosterically coupled[98,158].

Table 1.3 Orthosteric CaSR agonists (type 1 calcimimetics). Endogenous ligands are highlighted in red.

Chemotype	Compound	EC50 (µM)	reference
Aminoglycosides	Neomycin B	20.000	Nemeth, et al.[98]
Aminoglycosides	Gentamycin	150.000	Nemeth, et al.[98]
Aminoglycosides	Bekanamycin	200.000	Nemeth, et al.[98]
Aminoglycosides	Streptomycin	600.000	Nemeth, et al.[98]
Arylamine spider toxins	α-agatoxin 489	6.000	Nemeth, et al.[98]
Arylamine spider toxins	α-agatoxin 505	22.000	Nemeth, et al.[98]
Arylamine spider toxins	R,15 Argiotoxin 636	240.000	Nemeth, et al.[98]
Trivalent cations	Tb^{3+}	0.890	Brown, et al.[169]
Trivalent cations	Gd^{3+}	2.200	Brown, et al.[169]
Trivalent cations	Eu^{3+}	2.300	Brown, et al.[169]
Trivalent cations	Yt^{3+}	15.000	Brown, et al.[169]
Divalent cations	Ba^{2+}	1120.000	Brown, et al.[169]
Divalent cations	Ca^{2+}	1180.000	Brown, et al.[169]
Divalent cations	Sr^{2+}	1180.000	Brown, et al.[169]
Polyamines	Hexacyclen	20.000	Nemeth, et al.[98]
Polyamines	Spermine	150.000	Nemeth, et al.[98]
Polyamines	Pentaethylenhexamine	600.000	Nemeth, et al.[98]
Polyamines	Spermidine	2000.000	Nemeth, et al.[98]
Polyamines	Tetraethylenepentamine	2500.000	Nemeth, et al.[98]
Polyamines	Triethylenetetramine	8000.000	Nemeth, et al.[98]
Polycation	Poly-L-arginine 100 kDa	0.004	Nemeth, et al.[98]
Polycation	Poly-L-arginine 40 kDa	0.015	Nemeth, et al.[98]
Polycation	Poly-L-Lysine 27 kDa	0.030	Nemeth, et al.[98]
Polycation	Poly-L-Lysine 14 kDa	1.000	Nemeth, et al.[98]
Polycation	Poly-L-Lysine 27 kDa	3.000	Nemeth, et al.[98]

1.6.3.2 Positive allosteric modulators (PAMs)

A number of CaSR positive allosteric modulators (PAMs) have been identified (Table 1.4), and 3 compounds which have reached clinical approval for the treatment of secondary hyperparathyroidism are Cinacalcet, Etelcalcetide and Evocalcet[98,170].

The majority of PAMs (including cinacalcet and evocalcet) are Phenyl- and Naphthylalkylamines which bind to the TMD of the CaSR. The structure of cinacalcet is shown in Figure 1.23. Notably, cinacalcet was the first PAM of a GPCR to achieve clinical approval[98]. It is currently used to treat: secondary hyperparathyroidism due to chronic kidney disease; hypercalcaemia in adult patients with parathyroid carcinoma; and patients with primary hyperparathyroidism who are unable to undergo a parathyroidectomy[98]. However, its use is limited by gastrointestinal side-effects such as nausea and vomiting which are likely due to pharmacodynamic effects[98]. Moreover, cinacalcet is a strong inhibitor of the liver enzyme cytochrome P450 2D6 (CYP2D6)[171]. Therefore there is continuing interest to develop novel, improved calcimimetics[172].

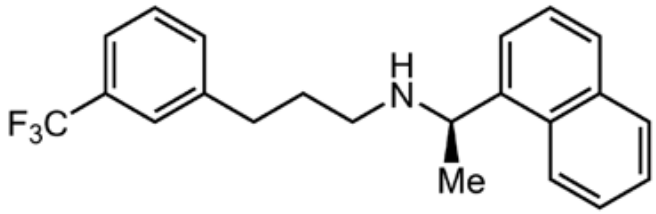


Figure 1.23 Chemical structure of the CaSR positive allosteric modulator cinacalcet[98].

Table 1.4 Positive allosteric CaSR modulators (type 2 calcimimetics). Endogenous ligands are highlighted in red, and compounds approved for clinical use are shown in green.

Chemotype	Compound	EC50 (μM)	reference
Phenyl-and Naphthylalkylamines	Cinacalcet	0.049	Nemeth, et al.[98]
Phenyl-and Naphthylalkylamines	NPS 609	0.055	Nemeth, et al.[98]
Phenyl-and Naphthylalkylamines	NPS 1457	0.085	Nemeth, et al.[98]
Phenyl-and Naphthylalkylamines	Evocalcet	0.093	Nemeth, et al.[98]
Phenyl-and Naphthylalkylamines	NPS 646	0.110	Nemeth, et al.[98]
Phenyl-and Naphthylalkylamines	NPS 1466	0.120	Nemeth, et al.[98]
Phenyl-and Naphthylalkylamines	NPS R-568	0.220	Nemeth, et al.[98]
Phenyl-and Naphthylalkylamines	NPS 1440	0.320	Nemeth, et al.[98]
Phenyl-and Naphthylalkylamines	Leo 27847	0.500	Nemeth, et al.[98]
Phenyl-and Naphthylalkylamines	NPS 610	0.590	Nemeth, et al.[98]
Phenyl-and Naphthylalkylamines	NPS R-467	2.700	Nemeth, et al.[98]
Phenyl-and Naphthylalkylamines	NPS 551	3.400	Nemeth, et al.[98]
Phenyl-and Naphthylalkylamines	NPS 467	4.100	Nemeth, et al.[98]
Phenyl-and Naphthylalkylamines	Fendiline	15.000	Nemeth, et al.[98]
Phenyl-and Naphthylalkylamines	NPS 459	30.000	Nemeth, et al.[98]
Phenyl-and Naphthylalkylamines	Prenylamine	50.000	Nemeth, et al.[98]
Other Arylalkylamines	Calcimimetic B	0.017	Nemeth, et al.[98]
Other Arylalkylamines	NPS 1410	0.020	Nemeth, et al.[98]
Other Arylalkylamines	AMG 641	0.027	Nemeth, et al.[98]
Other Arylalkylamines	NPS 1377	0.044	Nemeth, et al.[98]
Other Arylalkylamines	GSK3004774	0.050	Nemeth, et al.[98]
Other Arylalkylamines	NPS 1166	1.200	Nemeth, et al.[98]
Other Arylalkylamines	NPS 592	2.000	Nemeth, et al.[98]
Other Arylalkylamines	NPS 594	6.000	Nemeth, et al.[98]
Other Arylalkylamines	NPS 567	7.000	Nemeth, et al.[98]
Other Arylalkylamines	NPS 566	17.000	Nemeth, et al.[98]
D-peptides	KP-2067	18.400	Alexander, et al.[173]
D-peptides	Etelcalcetide	25.000	Walter, et al.[174]
1-(Benzothiazol-2-yl)phenylethanols	AC-(S)265347	0.010	Gustafsson, et al.[175]
1-(Benzothiazol-2-yl)phenylethanols	AC-265347	0.025	Gustafsson, et al.[175]
Naturally occurring peptides	γ-Glu-Abu-Gly	0.025	Nemeth, et al.[98]
Naturally occuring L-amino acids	Glutathione	0.700	Nemeth, et al.[98]
Naturally occuring L-amino acids	L-Phe	3500.000	Nemeth, et al.[98]
Naturally occuring L-amino acids	L-Trp	3500.000	Nemeth, et al.[98]

One such candidate may be AC-265347, which has high potency (EC50 = 25 and 10nM for the racemate and S-enantiomer, respectively), and does not inhibit CYP2D6 activity[176]. This may be because of its 1-(Benzothiazol-2-yl)phenylethanol chemotype, which differs significantly from the phenyl- and naphthylalkylamines because it lacks a positive charge (Figure 1.24).

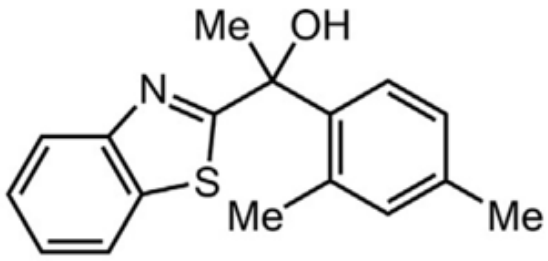


Figure 1.24 Chemical structure of the CaSR positive allosteric modulator AC-265347[98].

Recently, the first "second generation calcimimetic"[98], Etelcalcetide (also Amg 416 or Velcalcetide), has been approved for the treatment of secondary hyperparathyroidism in adult patients on dialysis[172,177,178]. In contrast to the aforementioned compounds, Etelcalcetide is an octapeptide which consists of a linear chain of seven D-amino acids with the N-terminal D-cysteine linked to an L-cysteine by a disulphide bond (Figure 1.25). It has been shown that Etelcalcetide, and the related KP-2067, have a different mechanism of action to small molecule PAMs: in contrast to small molecule PAMs which bind in the TMD, the peptides bind to the ECD of the CaSR and rely on interaction with Cys482 of the CaSR[173]. The functional effects of this different mechanism of action remain to be elucidated[98].

Naturally occurring aromatic L-amino acids, such as L-Phe and L-Trp, have also been proposed to be CaSR PAMs because they potentiate the effects of Ca^{2+}_e on CaSR

signalling[179]. However, based on the recent crystal structure of the CaSR ECD they may be more accurately classified as co-agonists[157,158].

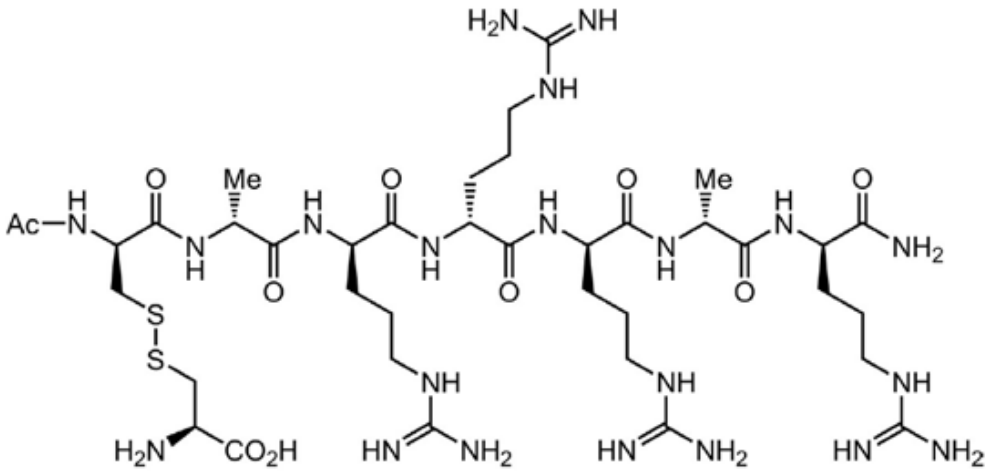


Figure 1.25 Chemical structure of the CaSR positive allosteric modulator Etelcalcetide[98].

1.6.3.3 Negative allosteric modulators (NAMs) and anabolic treatments for bone

Compared to the large number and diversity of CaSR agonists and PAMs, surprisingly few molecules have been shown to inhibit the CaSR[98]. Inhibition of the CaSR leads to increased PTH secretion[98,180]. Whereas chronically elevated levels of PTH lead to bone loss, transient elevations in plasma PTH have a net anabolic effect on the skeleton and lead to new bone formation[181].

Indeed, peptide analogues of PTH (teriparatide) or PTH-related peptide (abaloparatide) are used as bone anabolic therapies for treating osteoporosis[181]. However, these peptides are expensive and require daily subcutaneous injections[98]. Small molecule calcilytics were therefore investigated as potentially more cost-effective treatments for osteoporosis in postmenopausal women[98]. This led to the discovery of amino alcohol calcilytics such as NPS-2143 (Figure 1.26) and Ronacaleret, and later quinazolinones and diaminocyclohexanes, which bind the CaSR TMD in a similar location to small

molecule calcimimetics[95,98]. However, these compounds lacked efficacy in clinical trials, and development was therefore terminated[98]. Despite this, calcilytics were generally safe and well tolerated and therefore potentially could be repurposed for other indications, such as ADH and hypoparathyroidism[76,82,98]. More recently, inorganic phosphate has also been shown to inhibit CaSR signalling, resulting in increased PTH secretion[182].

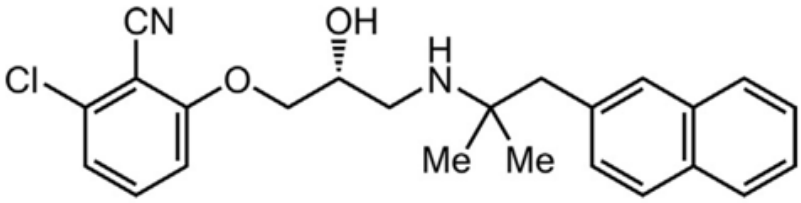


Figure 1.26 Chemical structure of the CaSR positive allosteric modulator NPS-2143[98].

Table 1.5 Negative allosteric CaSR modulators (calcilytics). Endogenous ligands are highlighted in red.

Chemotype	Compound	IC50 (μM)	reference
Amino alcohols	JTT-305 (Encaleret)	0.012	Nemeth, et al.[98]
Amino alcohols	SB751689 (Ronacaleret)	0.030	Nemeth, et al.[98]
Amino alcohols	NPS-2143	0.043	Nemeth, et al.[98]
Amino alcohols	SB423562 (NPSP795)	0.073	Nemeth, et al.[98]
Amino alcohols	SB222338	11.000	Nemeth, et al.[98]
Quinazolinones	AFT936	0.001	Nemeth, et al.[98]
Quinazolinones	AXT914	0.001	Nemeth, et al.[98]
Diaminocyclohexanes	Calhex 231	0.330	Nemeth, et al.[98]
Phosphates	Inorganic phosphate	1200.000	Centeno, et al.[182]

Interestingly, Sr^{2+} (as a ranelate salt), which is an orthosteric agonist of the CaSR, stimulates bone formation, and this has been proposed to be mediated by CaSRs expressed on osteoclasts and osteocytes[183-188]. It has therefore been postulated that calcilytics may fail to increase BMD because any bone anabolic effects induced by increased PTH secretion are antagonised by inhibition of CaSR actions in bone[98].

1.6.3.4 Ligand biased signalling

It is assumed that the majority of GPCR-targeting drugs have a similar effect on all pathways that are activated by an endogenous reference ligand. However, some compounds are so-called "biased" or functionally selective drugs. This is because they cause the receptor to adopt specific confirmations which preferentially stimulate certain pathways over others, and in some instances can even stimulate one pathway while inhibiting another[61,77,162,189,190]. This has completely changed our understanding of GPCR biology from a model of a two-state switch to one with unique, multifaceted signalling profiles[191,192]. Recent studies have linked these distinct molecular pathways to clinical presentations. For example, patients with $G\alpha_{q/11}$ biased thyrotropin receptor (TSHR) mutations have increased iodide trapping, a clinical phenotype not observed for TSHR mutations that cause loss-of-function of $G\alpha_s$[193]. This has opened new avenues for drug development, with the aim of designing biased drugs which preferentially activate desired intracellular pathways, leading to improved efficacy and reduced side effects[28]. Several biased drugs have shown promising results in clinical trials[59]; most notably, opioids which activate G protein but not ß-arrestin signalling to promote analgesia with fewer side effects than balanced agonists[194-202].

As a promiscuous receptor, the CaSR has the potential to elicit biased signalling. This has been confirmed by a study in which a CaSR-targeting autoantibody isolated from a patient with acquired hypocalciuric hypercalcaemia potentiated Ca^{2+}_e induced IP_1 accumulation but diminished Ca^{2+}_e induced ERK1/2 phosphorylation[119].

In addition, some orthosteric and allosteric CaSR ligands have also been suggested to be biased[203,204]. This conclusion largely relies on the difference in potencies measured between downstream assays[205]. For example, in HEK293 cells expressing CaSR, Ca^{2+} preferentially inhibits cAMP production and stimulates IP_3 accumulation[159], and

Cinacalcet increases Ca^{2+}_i mobilisation more than phosphorylation of ERK1/2[204]. However, sensitivity of downstream readouts is often assay dependent and may lead to false conclusions[162]. Moreover, the specific CaSR effectors underpinning these phenomena are unclear[77].

The complexity highlighted above is illustrative of GPCR function as a whole, which has led to an increasing interest in studying signalling at a more multidimensional level[162]. This has been advanced by the development of novel techniques such as: Förster resonance energy transfer (FRET)[206]; Bioluminescence Resonance transfer (BRET)[162]; and split luciferase assays (such as NanoBiT[207]). They are based on direct protein-protein interactions and therefore allow the investigation of GPCR signalling at the level of specific effectors, such as individual Gα subunits and ß arrestins[28,162,166,189].

2 THESIS OBJECTIVES

The goal of my thesis is to elucidate $G\alpha_{11}$ signalling and its role in calcium and glucose homeostasis. To this end, it has the following objectives:

1. Identification and characterisation of rare *GNA11* variants

Identify and characterise novel *GNA11* variants in large exome-datasets and determine their effects on human plasma calcium homeostasis and signalling by the CaSR and other GPCRs *in vitro*.

2. Investigation of glucose metabolism in Dsk7 mice

Investigate the glucose metabolism of Dsk7 mice which harbour a gain-of-function $G\alpha_{11}$ mutation (Ile62Val).

3. Differences between $G\alpha_{11}$ and $G\alpha_{q}$

Study the diversity within the $G\alpha_{q/11}$ family and its impact on CaSR signalling.

4. CaSR functional selectivity

Explore the role of $G\alpha_{11}$ in the context of CaSR functional selectivity and allosteric modulation using BRET biosensors.

3 MATERIALS AND METHODS

3.1 Buffer and stock solutions

3.1.1 For DNA-based techniques

3.1.1.1 TRIS/EDTA (T/E) buffer

For 100ml TRIS/EDTA (T/E) buffer, 1 ml 1M TRIS (pH 8.5) (Sigma-Aldrich) was combined with 1ml of 0.1M Ethylenediaminetetraacetic acid (EDTA) (Sigma-Aldrich) and 98ml of dH_2O to obtain a final concentration of 10mM TRIS and 1mM EDTA. Subsequently, the pH was adjusted to 8.

3.1.1.2 Lysogeny broth (LB)

Lysogeny broth (LB) was obtained by dissolving 10g Bacto™ Tryptone (BD, ref. 211705), 5g select yeast extract (G-Biosciences) and 5g NaCl (Sigma-Aldrich, ref. S3014-1KG) in 1L dH_2O and was subsequently sterilised in an autoclave. For LB agar, 15g agar per litre of LB broth was added.

3.1.2 For analysis of protein expression

3.1.2.1 CAPS

A 10x stock solution was obtained by dissolving 22.1g N-cyclohexyl-3-aminopropanesulfonic acid (CAPS) (Sigma-Aldrich, C2632-1KG) in 1L of dH_2O. Then, the pH was adjusted to 11 with NaOH.

For western blot transfers, 100ml of 10 CAPS was combined with 100ml of 100% methanol (LP Chemicals, ref. ME33204-235) to make 1x CAPS.

3.1.2.2 Phosphate-Buffered saline (PBS)

A 10x Phosphate-Buffered saline (PBS) was prepared as shown in Table 3.1 and diluted 1:10 in dH_2O to derive 1x PBS. The osmolarity of the solution was confirmed to be 0.28

osmol/kg (+/- 0.02) using an Osmomat 030 osmometer (Genotec). The pH of 1x PBS was adjusted to 7.4 using NaOH/HCl. Alternatively, 1x PBS was obtained by dissolving one PBS tablet (Thermo Fisher Scientific, ref. 18912014) in 500ml of dH_2O.

For PBS-T, 1ml of TWEEN® 20 (Sigma-Aldrich, ref. T2700-500ML) was added to 1L of 1x PBS.

Table 3.1 Reagents for 10x Phosphate-Buffered saline (PBS). All reagents were obtained from Sigma-Aldrich.

Reagent	Molecular weight	Amount required	Final concentration
NaCl	58.44	80g	1.37M
KCl	74.55	2g	27mM
$Na_2HPO_4.2H_2O$	177.99	18.1g	100mM
KH_2PO_4	136.09	2.4g	18mM
dH_2O		1L	

3.1.2.3 NP40 lysis buffer

NP40 lysis buffer was prepared as shown in Table 3.2 and stored at 4°C for up to 4 weeks. Reagents were obtained from Sigma-Aldrich.

Table 3.2 Reagents for NP40 lysis buffer.

Reagent	Stock solution	Amount used (ml)	Final concentration
TrisHCl pH 7.4	1M	0.5	50mM
EDTA	0.5M	0.02	1mM
NaCl	2M	0.75	150mM
NP40 (IGEPAL)	10% (v/v)	1	1%
cOmplete™ Protease Inhibitor		1 Tablet	1x
dH_2O		7.73	

3.1.2.4 Paraformaldehyde (PFA) solution

Paraformaldehyde (PFA) 4% (w/v) solution was obtained by dissolving 4g PFA (Sigma-Aldrich, ref. 158127) in 100ml of 1x PBS at 42°C. 10ml aliquots were stored at -20°C.

3.1.2.5 Citrate buffer

For preparation of citrate buffer, 8.5 ml of citric acid stock solution (0.1M) was combined with 41.5ml of trisodium citrate stock solution (0.1M).

Citric acid stock solution (0.1M) was prepared by dissolving 2.1g of citric acid monohydrate (Sigma-Aldrich) in 100ml of dH_2O.

Trisodium citrate stock solution (0.1M) was obtained by dissolving 2.94g of trisodium citrate dihydrate (Sigma-Aldrich) in 100ml of dH_2O.

3.1.3 For functional assays

3.1.3.1 Starvation media

Starvation media (0.45mM $CaCl_2$, 0.01% FBS, 25mM HEPES) was obtained by mixing 400µl high glucose Dulbecco's Modified Eagle Medium (DMEM) (Thermo FisherScientific, ref 41965-039) containing 10% fetal bovine serum (Thermo FisherScientific, ref. 10091148) with 10ml of high glucose DMEM (Thermo Fisher Scientific, ref 41965-039) and 30ml of calcium-free DMEM containing 25mM HEPES (both Thermo Fisher Scientific).

3.1.3.2 Complete imaging buffer

A 5x complete imaging buffer was prepared as shown in Table 3.3.

Table 3.3 Reagents for 5x complete imaging buffer

Reagent	Molecular weight	Amount required	Final concentration
NaCl	58.44	43.83 g	750 mM
KCl	74.55	969.15 mg	13 mM
$MgCl_2$	95.21	561.74 mg	5.9 mM
HEPES	238.3	11.92 g	50 mM
$CaCl_2$	147.01	73.51 mg	0.5 mM
dH_2O		1L	

To begin, 250mM Probenecid stock solution was prepared as follows: 5g of probenecid (Santa Cruz, ref. sc-202773A) were dissolved in 30 ml 1M NaOH, then a further 40ml of dH_2O was added. Subsequently, 5ml aliquots were prepared and stored at -20°C for up to 6 months.

To obtain 1x complete imaging buffer, 100ml of 5x imaging buffer was prepared as shown in Table 3.4 and the pH was adjusted to 7.4 using NaOH.

Table 3.4 Preparation of 1x complete imaging buffer

Reagent	Amount required	Final concentration
5x complete imaging buffer	100ml	150 mM NaCl, 2.6 mM KCl, 1.18 mM $MgCl_2$, 10 mM HEPES, 0.1 mM 10mM $CaCl_2$
G-glucose	0.9g	10mM
Probenecid (250 mM stock)	5ml	2.5mM
dH_2O	350ml	

3.1.3.3 Fluo-4 AM solution

Fluo-4 acetoxymethyl ester (AM) stock solution (4mM) was obtained by adding 11µl DMSO (Thermo Fisher Scientific) to a vial containing 50µg Fluo-4 AM (Thermo Fisher Scientific, ref. F14201).

Pluronic 20% w/v stock solution was obtained by dissolving 1g of Pluronic F-127 (Sigma-Aldrich, ref. P2443) in 5ml DMSO for 20 minutes at 42°C.

Fluo-4 AM working solution was prepared as shown in Table 3.5.

Table 3.5 Preparation of Fluo-4 AM working solution. N.B.: Fluo-4 and pluronic were combined first and then the other components were added.

Reagent	Stock solution	Amount used	Final concentration
Fluo-4	4mM	1µl	1µM
Pluronic	20% w/v	2µl	0.01%
Fatty-acid free BSA		20mg	0.5%
1x complete imaging buffer		4ml	

3.1.3.4 Ionomycin solution

To obtain a 15mM ionomycin stock solution, 450µl 100% ethanol was added to 5mg of ionomycin (Cambridge Bioscience, ref. 11932-5mg-CAY).

To obtain 50µM ionomycin working solution, 10µl of ionomycin stock solution was added to 3ml of dH_2O.

3.1.3.5 Tyrode's buffer

A 10x Tyrode's buffer[208] was prepared according to a modified recipe, shown in Table 3.6. Reagents were obtained from Sigma-Aldrich.

Table 3.6 Reagents for 10x Tyrode's buffer.

Reagent	Molecular weight	Amount required	Final concentration
NaCl	58.44	81.2	1400 mM
KCl	74.55	2.03	27 mM
$NaHCO_3$	84.01	10.08	120 mM
D-glucose.H_2O	198.17	11.10	56 mM
$MgCl_2.6H_2O$	203.30	1.02	5 mM
NaH_2PO_4	119.98	0.44	3.7 mM
HEPES	238.30	59.50	250 mM
dH_2O		1L	

A 1x Tyrode's buffer was obtained by adding 100ml of 10x Tyrode's buffer and 1ml $CaCl_2$ (1M) to 899ml of dH_2O (final concentrations: 140 mM NaCl, 2.7 mM KCl, 12 mM

$NaHCO_3$, 5.6 mM D-glucose, 0.37 mM NaH_2PO_4, 0.5 mM $MgCl_2$, 0.1 mM $CaCl_2$, 25 mM HEPES). Subsequently, the solution was sterile filtered (0.22µM) and the pH was adjusted to 7.4.

3.1.3.6 Prolume purple stock solution

Prolume Purple stock solution (2mM) was obtained by reconstitution of a 500µg vial of Prolume Purple (NanoLight Technology, ref. 369) in 540µl Nanofuel solvent (NanoLight Technology, ref. 399) and stored at -20°C in a plastic receptacle containing desiccant (Drierite, 8 mesh, ref. 23005) for up to 4 weeks.

3.1.3.7 Polyethylenamine (PEI) stock solution

Polyethylenamine (PEI) stock solution was prepared, as follows. PEI 25kDa linear (PolyScience, ref. 239666) was diluted in dH_2O to a final concentration of 1mg/ml. Subsequently, the solution was incubated and stirred overnight using a magnetic stirrer. The next day, the pH was lowered to 7.2 using HCl (0.1M). Finally, the solution was sterile filtered (0.22µm) and 2ml aliquots were frozen at -20°C.

3.2 Compounds

The GPCR-targeting compounds (agonists and modulators) used in this thesis are shown in Table 3.7. Etelcalcetide and KP-2067 were synthesised by Ashok Khatri at the Massachusetts General Hospital (MGH) Endocrine Unit. Compounds were dissolved in dH_2O, DMSO (Sigma-Aldrich), 10mM acetic acid (Sigma-Aldrich) or methyl acetate (Cayman chemical).

Table 3.7 GPCR-targeting compounds used in this thesis.

Compound	ref.	solvent	target
$CaCl_2$	C7902	dH_2O	CaSR
L-Phe	P5030	dH_2O	CaSR
Cinacalcet	SML2012	DMSO	CaSR
AC-265347	SML0129	DMSO	CaSR
NPS-2143	SML0362	DMSO	CaSR
Etelcalcetide	Synthesis by Ashok Khatri (MGH)	10mM acetic acid	CaSR
KP-2067	Synthesis by Ashok Khatri (MGH)	10mM acetic acid	CaSR
Acetylcholine	102073474	dH_2O	M_2R, M_3R
(-)Isoproterenol	16604	dH_2O	B2AR
U46619	16450	methyl acetate	TPα

3.3 Primers

3.3.1 Sequencing primers

All sequencing primers (Table 3.8) were obtained from Sigma-Aldrich. and diluted in dH_2O to a concentration of 100μM stock and 10μM working solution.

Table 3.8 *GNA11* sequencing primers.

Exon	forward primer	reverse primer
1	CCAGCCTGCTAGGTTGTCC	ACTCACCGAGCAGCAGCAG
2	GCAGGGTCTGGGTAAGAGG	ATGGATGACCAGGGGTAGC
3	CGAGCTCTCGACGTCTCC	CCTTCCCGAAGGGTCCCA
4	GTGCTGTGTCCCTGTCCTG	GGGCAAATGAGCCTCTCAG
5	GCCAGGTGGCTGAGTCCT	CACTGCACACAGCCCAAG
6	CTTGGGCTGTGTGCAGTG	ATGAGCCCCTCTCCCATATC
7	ACAAAGGGGCCCACGAGT	GTGTCTCCATCCCGTCTC

3.3.2 Site-directed mutagenesis primers

Site-directed mutagenesis (SDM) primers (Table 3.9 and Table 3.10) were PAGE purified and obtained from Sigma-Aldrich. They were diluted in dH_2O to a 100μM stock solution and used as a 10μM working solution.

Table 3.9 Site-directed mutagenesis (SDM) primers to introduce *GNA11* variants found in dbSNP.

Mutation		primer
c.393G>A (p.Gly51Arg)	F	GGCACGGGCGAGAGCAGGAAGAGCACGTTCA
	R	TGAACGTGCTCTTCCTGCTCTCGCCCGTGCC
c.439 G>A (p.Gly66Asp)	F	TCATCCACGGCGCCGACTACTCGGAGGAGGA
	R	TCCTCCTCCGAGTAGTCGGCGCCGTGGATGA
c.682 C>T (p.Arg147Cys)	F	CAGGAATGCTACGACTGCAGGCGCGAGTACC
	R	GGTACTCGCGCCTGCAGTCGTAGCATTCCTG
c.698 G>C (Gln152His)	F	CAGGCGCGAGTACCACCTCTCCGACTCTGCC
	R	GGCAGAGTCGGAGAGGTGGTACTCGCGCCTG
c.679 C>T (p.Arg213trp)	F	GGCCAGCGGTCGGAGTGGAGGAAGTGGATCC
	R	GGATCCACTTCCTCCACTCCGACCGCTGGCC
c.933 G>A (p.Ala231Thr)	F	ATCATGTTTCTCGTCACCCTCAGCGAATACG
	R	CGTATTCGCTGAGGGTGACGAGAAACATGAT
c 970 A>G (p.Asp243Gly)	F	TCCTGGTGGAGTCGGGCAACGAGAACCGGAT
	R	ATCCGGTTCTCGTTGCCCGACTCCACCAGGA
c.1249A>G (p.Asn336Ser)	F	CCACCGACACGGAGAGCATCCGCTTCGTGTT
	R	AACACGAAGCGGATGCTCTCCGTGTCGGTGG
c.1254C>T (p.Arg288Cys)	F	GACACGGAGAACATCTGCTTCGTGTTCGCGG
	R	GCCGCGAACACGAAGCAGATGTTCTCCGTGT

Table 3.10 Site-directed mutagenesis (SDM) primers to introduce *GNA11* variants found in the DiscovEHR cohort.

Mutation		primer
c.110G>T (p.Arg37Leu)	F	ACAAGCGCGACGCCCTGCGCGAGCTCAAGCT
	R	AGCTTGAGCTCGCGCAGGGCGTCGCGCTTGT
c.175A>T (p.Met59Leu)	F	ACGTTCATCAAGCAGCTGCGCATCATCCACG
	R	CGTGGATGATGCGCAGCTGCTTGATGAACGT
c.577C>A (p.Pro193Thr)	F	GGCATCATCGAGTACACTTTCGACCTGGAGA
	R	TCTCCAGGTCGAAAGTGTACTCGATGATGCC
c.578C>A (p.Pro193His)	F	GCATCATCGAGTACCATTTCGACCTGGAGAA
	R	TTCTCCAGGTCGAAATGGTACTCGATGATGC
c.628C>T (p.Arg210Trp)	F	GATGTGGGGGGCCAGTGGTCGGAGCGGAGGA
	R	TCCTCCGCTCCGACCACTGGCCCCCCACATC

3.4 Antibodies

Antibodies used in this thesis are outlined in Table 3.11, Table 3.12, Table 3.13 and Table 3.14.

Table 3.11 Primary antibodies used for Western blot analysis.

Antigen	organism	dilution	company	identifier
$G\alpha_{11}$	Mouse	1:1000	Santa Cruz	sc-390382
Gαq	Mouse	1:500	Santa Cruz	Sc-136181
CaSR (ADD)	Mouse	1:1000	Invitrogen	MAI-934
Calnexin	Rabbit	1:5000	Millipore	Ab2301
GAPDH	Rabbit	1:5000	Sigma-Aldrich	A8592-2MG

Table 3.12 Primary antibodies used for Immunofluorescence Microscopy.

Antigen	organism	dilution	company	identifier
Insulin	Guinea pig	1:50	Abcam	ab7842
Glucagon	Rabbit	1:200	Abcam	ab92517
Ki-67	Rabbit	1:100	Abcam	ab15580

Table 3.13 Horseradish peroxidase (HRP) conjugated secondary antibodies used for Western blot analysis.

Antigen	organism	dilution	company	identifier
Mouse IgG	goat	1:2000	Jackson ImmunoResearch	115-035-003
Rabbit IgG	goat	1:2000	Jackson ImmunoResearch	111-035-003

Table 3.14 Secondary antibodies used for Immunofluorescence Microscopy.

Antigen	organism	fluorophore	dilution	company	identifier
Guinea pig IgG	Goat	Cy2	1:100	Jackson ImmunoResearch	706-225-148
Rabbit IgG	Donkey	Alexa 568	1:100	ThermoFisher Scientific	A10042

3.5 Cell culture

3.5.1 Cell lines

HEK293A-$G\alpha_{q/11}$-KO cells[209] were a gift from Asuka Inoue (Tohoku University). HEK293-Flp-In-Flag-CaSR cells were generated by Mie Kronborg Olesen (University of Oxford). HEK293-Flp-In-TREX-CaSR wild type (WT) and mutant cells were developed by Dr. Sara Falcone (University of Oxford).

3.5.2 Media & Culture Conditions

All cells were grown in 80cm^2 flasks (Corning, ref. 178905) maintained in high glucose DMEM (Thermo Fisher Scientific, ref 41965-039) containing 10% fetal bovine serum (Thermo Fisher Scientific) (DMEM-FBS), at 37°C, 5% CO_2, with the addition of: 400µg/ml Geneticin™ (Thermo Fisher Scientific) for HEK293A-$G\alpha_{q/11}$-KO-cells, HEK293A-$G\alpha_{q/11}$-KO-CaSR-SRE cells, and HEK293A-$G\alpha_{q/11}$-KO-CaSR-NFAT-RE cells; 100µg/ml hygromycin for HEK293A-$G\alpha_{q/11}$-KO-CaSR-SRE cells, HEK293A-$G\alpha_{q/11}$-KO-CaSR-NFAT-RE cells and HEK293-Flp-In-Flag-CaSR cells; and 100µg/ml Hygromycin and 10µg/ml Blasticidin, as previously described[134,210].

When cells reached 80-90% confluency they were passaged using 0.05% Trypsin-EDTA with phenol red (Thermo Fisher Scientific, ref. 25300054). Only cells up to passage 30 were used for functional assays, as previously described[210].

To ensure sufficient supply of cells, early passages were expanded in 175cm^2 flasks (Corning, ref. 1743601) and detached after they reached 80% confluency. Subsequently cells were centrifuged, resuspended in 3ml freezing media (DMEM-FBS containing 10% dimethyl sulfoxide (DMSO)) and split into 3 cryovials (Thermo Fisher Scientific). The vials were placed at -80°C in a receptacle containing 100% isopropanol (AnalaR NORMAPUR). The following day, cells were transferred to liquid nitrogen tanks.

3.5.3 Generation of stable cell lines

To establish the HEK293A-G$\alpha_{q/11}$-KO-CaSR cell line, HEK293A-G$\alpha_{q/11}$-KO-cells were stably transfected with pcDNA3.1-*CASR* as described[93], using Lipofectamine 2000 (Thermo FisherScientific) and selected with 400µg/ml Geneticin™ (Thermo FisherScientific).

To establish the HEK293A-G$\alpha_{q/11}$-KO-CaSR-SRE and HEK293A-G$\alpha_{q/11}$-KO-CaSR-NFAT-RE cell lines, HEK293A-G$\alpha_{q/11}$-KO-CaSR cells were transfected with pGL4.33[luc2P/SRE/Hygro] and pGL4.30[luc2P/NFAT-RE/Hygro] (Promega), respectively, using Lipofectamine 2000, and selected with 100µg/ml hygromycin (Thermo FisherScientific).

HEK293-Flp-In-flag-CaSR cells were generated by Mie Kronborg Olesen (University of Oxford). WT *CASR-FLAG* was cut from an existing pFLAG-N1-CASR vector, cloned into the pcDNA5/FLP recombination target (FRT) expression vector (Life Technologies) and transfected into HEK293-Flp-In cells (Life Technologies) using Lipofectamine 2000. Cells expressing the CaSR protein were selected with 100µg/ml hygromycin.

WT and mutant HEK293-Flp-In-TREX-CaSR cell lines were generated by Dr. Sara Falcone (University of Oxford). WT *CASR* was cut from an existing pEGFP-N1 vector and cloned into the pcDNA5/FLP recombination target (FRT) expression vector (Life Technologies) and mutations were introduced using site-directed mutagenesis (see section 3.6.1), as described[134,211]. Subsequently, WT and mutant constructs were transfected into HEK293-Flp-In-TREX cells (Life Technologies) using Lipofectamine 2000, as described[211]. Stably transfected cells were selected with 100µg/ml hygromycin and 10µg/ml Blasticidin.

3.6 DNA-based techniques

3.6.1 Site-directed mutagenesis

Mutant pBI-CMV2-*GNA11* constructs were generated using the QuikChange Lightning Site-directed Mutagenesis (SDM) kit (Agilent Technologies) and gene-specific primers (Sigma-Aldrich), as described[211]. It comprises three steps: mutant strand synthesis using a WT template and primers containing the desired mutation; *DPNI* digestion of the template; and transformation of competent cells with mutated molecules[212]. A list of all SDM primers that were used is provided in section 3.3.2.

For the SDM reaction, 1µl of dsDNA template (pBI-CMV2-*GNA11*-WT) was mixed with 5µl of reaction buffer, 1.25µl of each primer, 1µl of dNTP mix and 1.5µl of QuikSolution reagent. Next, 39µl of dH_2O were added and the solution was mixed. Subsequently, 1µl of QuikChange Lightning enzyme was added.

Then, the reaction was placed in a Tetrad Thermal Cycler (Biorad) and the reaction was performed as shown in Table 3.15. Finally, 2µl of Dpn1 restriction enzyme was added to the completed reaction, which was then mixed and incubated for 5 minutes at 4°C.

Table 3.15 QuikChange Lightning site-directed mutagenesis reaction

Segment	cycles	temperature	time
1	1	95°C	2 minutes
2	18	95°C	20 seconds
		60°C	10 seconds
		68°C	2.44 minutes (0.5 per kb of plasmid)
3	1	68°C	5 minutes

3.6.2 Transformation of ultracompetent bacteria

XL10-Gold ultracompetent bacteria were thawed and 20µl were added to a 14ml round bottom polypropylene tube (Falcon, ref 352059). Next, 2µl of the Dpn1 treated reaction

was added to the ultracompetent bacteria and the tube was placed on ice for 10 minutes. Subsequently, the tubes were heat-pulsed in a 42°C water bath for 30 seconds, then placed on ice for 2 minutes. 500µl of sterile Lysogeny broth (LB) (see 3.1.1.2) was added to the tubes and they were incubated for 30 minutes at 37°C with 225-250rpm shaking.

Next, 20µl of broth was smeared onto agar plates containing 50µg/ml ampicillin and the plates were incubated at 37°C overnight. The following day, single colonies were picked and incubated overnight in LB containing 50µg/ml ampicillin. The day after that, the cell suspension was centrifuged at 2000xg for 10 minutes and the supernatant was discarded.

3.6.3 Plasmid DNA extraction

Plasmid DNA was extracted using a Wizard® Plus SV Miniprep DNA Purification System (Promega), according to the manufacturer's instructions. Pellets obtained from overnight cultures were resuspended in 250µl of cell resuspension solution and moved to 1.5ml tubes. Next, 250µl of cell lysis solution was added and the tubes were inverted. After 3 minutes of incubation, 10µl of Alkaline Protease solution was added and the tubes were inverted. After a further 3 minutes of incubation, 250µl of neutralisation solution was added and the tubes were inverted.

Then, tubes were spun at 14,000xg for 10 minutes. Subsequently, the spin columns were inserted into the collection tubes. The supernatants from the 1.5ml tubes were added to the spin columns and the pellets were discarded. Then, the samples were spun at 14,000xg for 1 minute. The flow-through was discarded and the spin column was re-inserted into the collection tube.

Next, 750µl of Wash solution was added and the samples were spun at 14,000xg for 1 minute. The flow-through was discarded and the spin column was re-inserted into the

collection tube. Then, 250µl of wash solution was added and the samples were spun at 14,000xg for 2 minutes. The flow-through was discarded and the spin column was re-inserted into the collection tube. Subsequently, the spin column was transferred to a sterile 1.5ml tube and 60µl of nuclease-free water was added. Finally, the tubes with spin columns were spun at 14,000xg for 1 minute, and the spin column was discarded.

The obtained DNA was quantified using a Nanodrop Spectrophotometer (Thermo Fisher Scientific).

3.6.4 Sanger sequencing

DNA sequence changes were confirmed by Sanger DNA sequencing using the BigDye Terminator v3.1 Cycle Sequencing Kit (Life Technologies), as described[211]. Sanger sequencing is based on the incorporation of 2′, 3′-dideoxynucleotides, that lack the 3′-hydroxyl group which is essential for chain extension, thereby terminating DNA elongation. This results in the production of fragments of different lengths which can be separated by electrophoresis. For BigDye sequencing, each of the four dideoxynucleotide terminators is tagged with a different fluorophore which permits sequencing in a single reaction[213]. For DNA amplification, primers (3.3.1) were diluted 1:15 to a concentration of 0.67µM and Big Dye master mix (MM) was prepared as shown in Table 3.16.

Table 3.16 BigDye master mix components (per well).

Big Dye	0.5µl
Big dye buffer	1.75µl
dH_2O	1.75µl

To start, 4µl of diluted primer was dispensed per well of a 0.2ml 96-well PCR plate (Thermo fisher Scientific) and 4µl of MM and 2µl of DNA was added. Next, the plates were sealed and mixed by vortexing. Then, the plate was paced in a Tetrad Thermal

Cycler (Biorad) and the following cycles were performed 30 times: 10 seconds at 96°C, 5 seconds at 50°C and 60 seconds at 60°C.

Subsequently, 7ml of 100% Ethanol was mixed with 280µl of 3M NaOAc pH 5.2 (Sigma-aldrich, ref. S7899-100ML), and 52µl of this mixture was added to each well of the completed reaction. Then, plates were sealed, vortexed and centrifuged at 2750xg for 30 minutes. Immediately after spinning, plates were inverted onto tissue paper and 150µl of 70% ethanol were added to the wells. Next, plates were spun at 2750xg for 10 minutes, and as before, plates were inverted onto tissue paper immediately after spinning. Subsequently, plates were spun upside-down for 2 minutes at 100xg, air dried and sealed.

Finally, the DNA pellets were analysed using an automated detection system (ABI3730 Automated capillary sequencer, Applied Biosystems)[109] by sequencing technicians at the University of Oxford Department of Zoology.

3.7 Analysis of protein expression

3.7.1 Western blot analysis

Western blot analysis is a widely used technique which allows to conserve and detect specific proteins in a sample via antibody staining[214]. It comprises three main steps: separation of proteins by molecular weight using sodium dodecyl sulfate (SDS) polyacrylamide gel electrophoresis; vertical transfer of proteins to and fixation on a polymer membrane; and antibody driven staining to elucidate protein identity.

3.7.1.1 Transfection

To analyse $G\alpha_{11}$ and $G\alpha_{q}$ protein expression, 200,000 HEK293A-$G\alpha_{q/11}$-KO-CaSR or HEK293-Flp-In-Flag-CaSR cells per well in 1ml DMEM-FBS were transiently

transfected in 12-well plates (CytoOne, ref. CC7682-7512) with 500ng of WT and mutant pBI-CMV2-*GNA11/GNAQ* construct and 2.5µl Lipofectamine 20000 (Thermo Fisher Scientific, ref 11668019) in 100µl 1x PBS.

3.7.1.2 Cell lysis

48 hours after transfection, each well was lysed in 100µl NP40 lysis buffer (see 3.1.2.3) for 10 minutes at 4°C, transferred to 1.5ml microtubes (Corning, re. MCT-15-C) and centrifuged for 10 minutes at 14,000xg at 4°C. Subsequently, the supernatant (containing the soluble fraction of proteins) was transferred to a new tube and the pellet was discarded.

3.7.1.3 Bradford assay

Protein content was quantified using Bradford assays, based on the colour change of the coomassie brilliant blue dye from brown to blue upon protein binding in an acidic medium[215]. Two microlitres of a 1:10 dilution of cell lysate was transferred to a clear 96 well plate (flat bottom, Sarstedt) and 200µl of Quick Start™ Bradford 1x Dye Reagent (Biorad, ref. 5000205) was added. Moreover, protein standards containing 0, 0.25, 0.5, 0.75, 1, 1.25, 1.5, 1.75 and 2mg/ml bovine serum albumin (BSA) were prepared using Pierce™ Bovine Serum Albumin Standard (2 mg/ml) (Thermo Fisher Scientific, ref. 23209) and added to the plate. Subsequently, the plate was placed in a PHERAstar plate reader (Bmg Labtech) and absorption at 595nm was read. The standard curve was fitted using linear regression, and the protein concentration of the sample was inferred.

3.7.1.4 Sample preparation

Cell lysates were diluted to a concentration of 10mg/ml total protein and diluted 1 in 2 in 2x Laemmli sample buffer (Biorad, ref. 1610737) containing 10% ß-Mercaptoethanol

(Sigma, ref. M3148) to obtain a final protein concentration of 0.2mg/ml. Subsequently, samples were denatured at 80°C for 5 minutes.

3.7.1.5 SDS-PAGE gel preparation

SDS-PAGE gels (0.75mm thick) were prepared using the Mini-PROTEAN® system (Biorad). All components of the apparatus were washed with 70% ethanol, dried and assembled. Subsequently, running gel mixtures were prepared and poured in between the two glass plates (a ~2cm gap was left at the top) and approximately 1ml of isopropanol (AnalaR NORMAPUR) was added immediately. For analysis of $G\alpha_{11}$ and $G\alpha_q$, 10% acrylamide running gels were used (Table 3.17), and for analysis of CaSR 6% acrylamide running gels were used (Table 3.18), as previously described[211]. Alternatively, TruPAGE™ 4-12% precast gradient gels (Sigma, ref. PCG2003) were used for simultaneous analysis of all proteins of interest.

Table 3.17 Reagents for 10ml of 10% SDS-PAGE running gel.

Reagent	Stock concentration	Amount required (ml)	Final concentration
Acrylamide 37:1	30%	3.3	10%
TRIS pH 8.8	1.5M	2.5	0.375M
SDS	10%	0.1	0.1%
Ammonium persulfate (APS)	10%	0.1	0.1%
Tetramethylethylenediamine (TEMED)	99%	0.01	0.1%
dH_2O		4	

Table 3.18 Reagents for 10ml of 6% SDS-PAGE running gel.

Reagent	Stock concentration	Amount required (ml)	Final concentration
Acrylamide 37:1	30%	2	6%
TRIS pH 8.8	1.5M	2.5	0.375M
SDS	10%	0.1	0.1%
Ammonium persulfate (APS)	10%	0.1	0.1%
Tetramethylethylenediamine (TEMED)	99%	0.01	0.1%
dH_2O		5.3	

After the running gels had dried (approximately 10 minutes), isopropanol was removed, and the gels were washed twice with dH_2O. Subsequently, a 5% stacking gel (Table 3.19) was added and 10-well combs were placed at the top in order to form pockets.

Table 3.19 Reagents for 10ml of 5% SDS-PAGE stacking gel

Reagent	Stock concentration	Amount required (ml)	Final concentration
Acrylamide 37:1	30%	1.5	6%
TRIS pH 6.8	0.5M	6.8	0.375M
SDS	10%	90	0.1%
Ammonium persulfate (APS)	10%	90	0.1%
Tetramethylethylenediamine (TEMED)	99%	30	0.3%
dH_2O		0.6	

3.7.1.6 Electrophoresis

To perform electrophoresis, SDS-PAGE gels were taken out of the frame and placed in Mini-PROTEAN® gel tanks (Biorad) filled with TRIS/Glycine/SDS (TGS) running buffer (Invitrogen, ref. LC2675-5). Subsequently, 10µl (equivalent to 5µg protein) of sample were added to each well. As a molecular weight marker, Precision Plus ProteinTM Dual Color standard (Biorad, ref. 161-0374) was used. Subsequently, gels were run at 100V for 1-2 hours[214,216].

3.7.1.7 Transfer

In preparation for the transfer, Immuno-Blot® 0.2µM Polyvinylidene fluoride (PVDF) membranes (Biorad, ref. 1620177) were cut into 7x9 cm pieces, and 3MM cellulose chromatography paper (Whatman, 3030-335) was cut into 10x10cm pieces. PVDF membranes were activated in 100% methanol (Sigma) for 1 minute in order to prevent unspecific hydrophobic effects and then placed in water. Next, 1x CAPS transfer buffer was prepared (see 3.1.2.1) and PVDF membranes and chromatography paper were

soaked in transfer buffer for 10 minutes. Subsequently, the gels were taken out of the electrophoresis tank and the stacking gel was removed. The running gels were briefly immersed in transfer buffer[216].

In the following step, filter papers, gels and membranes were assembled in the Criterion™ Blotter (Biorad) as follows (positive to negative pole): sponge - filter paper – membrane – running gel – filter paper - sponge. Subsequently, eventually trapped air bubbles were expelled using a transfer-stack roller (Biorad). Thereafter, the lid of the blotter was closed, and protein transfer was performed at 100V for 60 minutes[217].

3.7.1.8 Probing with antibodies

Membranes were taken out of the blotter and incubated with blocking buffer (5% Marvel dry skimmed milk in PBS-T) for 60 minutes in order to cover unspecific binding sites. Primary antibodies (list see 3.4) were diluted in blocking buffer. Membranes were briefly drained and placed in plastic film. Antibody solution (~2ml/membrane) was added and the film was sealed shut using a foil welding apparatus (Hulme Martin). The membranes were incubated with primary antibody overnight[218].

The next day, primary antibody solutions were removed, and the membranes were washed with PBS-T (3x5 minutes). Subsequently, membranes were incubated with horseradish peroxidase conjugated secondary antibodies: goat anti-rabbit IgG-HRP (Jackson ImmunoResearch, 111-035-003) or goat anti-rabbit IgG-HRP (Jackson Immuno Research, 115-035-003) at a dilution of 1:2000 in blocking buffer. After that, the membrane was again washed with PBS-T (5x5 minutes)[211,219].

3.7.1.9 Detection

For each membrane, 2ml of chemiluminescence reagent (Clarity Western ECL Substrate (BioRad) was prepared by mixing the enhancer and peroxide solution in a

ratio of 1:1. Next, the membranes were placed on plastic wrap and incubated with the chemiluminescence reagent for 3 minutes. Excess of detection solution was removed using a paper towel and the membranes were placed in plastic wrap. Subsequently, Western blots were visualised using on a Chemidoc XRS+ system with Image Lab 6.0.1 software (BioRad), as described[211,220].

3.7.1.10 Re-probing of blots

If necessary, membranes could be re-probed after removal of primary and secondary antibodies with RestoreTM Western Blot Stripping buffer (Thermo fisher Scientific, ref. 21063) for 10 minutes, and the procedure was repeated from step 3.7.1.8.

3.7.2 Immunocytochemistry

To visualise GFP expression in cells, glass coverslips (Menzel™) were placed in 12-well plates (CytoOne, ref. CC7682-7512) and coated with Poly-d-Lysine (Sigma) and 250,000 HEK293A-G$\alpha_{q/11}$-KO-CaSR or HEK293-Flp-In-Flag-CaSR cells in 1ml DMAM-FBS were added per well. Next, cells were transfected with 500ng of WT and mutant pBI-CMV2-*GNA11/GNAQ* construct and 2.5µl Lipofectamine 20000 (Thermo Fisher Scientific, ref 11668019) in 100µl 1x PBS[109,211].

After 48 hours, cell media was removed, and cells were fixed in 5% PFA/PBS for 10 minutes. Then, cells were washed once with 1x PBS and permeabilised with 1% triton-X100 (BDH, ref. 306324N) in 1x PBS for 10 minutes. Subsequently, cells were washed once with 1x PBS and stained with DAPI (5mg/ml, Sigma, ref. D9542) at a 1:2500 dilution (final concentration 2µg/ml) for 5 minutes.

Then, cells were washed with 1x PBS and mounted using VECTASHIELD Antifade Mounting Medium with DAPI (LSBio, ref. IVDH-1200). Finally, fluorescence was visualised on an Eclipse E400 fluorescence microscope with a Y-FL Epifluorescence

attachment and a triband 4,6-diamidino-2-phenylindole-FITC-Rhodamine filter in combination with a DXM1200C digital camera and NIS Elements software (Nikon)[124,221].

3.7.3 Haematoxylin and Eosin (H&E) staining

Haematoxylin and Eosin (H&E) staining was performed by Dr. Valerie Babinsky (University of Oxford). Formalin-fixed, paraffin-embedded Dsk7 pancreas 4.5 µM sections from +/+, Dsk7/+ and Dsk7/Dsk7 mice were rehydrated and stained with Harris hematoxylin solution (Sigma Aldrich) for 2.5 minutes and Eosin (0.02%) for 12 minutes.

3.7.4 Immunohistochemistry

3.7.4.1 Rehydration and antigen retrieval

Formalin-fixed, paraffin-embedded Dsk7 pancreas 4.5µM sections were obtained from Dr. Sian Piret (for a full list see Appendix Table 9.1). Each slide contained 3 serial sections, which were stained for insulin and glucagon, insulin and Ki67, and negative control, respectively.

To remove paraffin and rehydrate the sections, slides were placed in Histoclear (National Diagnostics) and different concentrations of ethanol, according to the scheme shown in Table 3.20. Subsequently, slides were washed with dH_2O.

Table 3.20 Dewaxing and rehydration steps for paraffin-embedded pancreas sections.

Histoclear 1	5 minutes
Histoclear 2	3 minutes
Histoclear 3	3 minutes
Ethanol 100% 1	3 minutes
Ethanol 100% 2	3 minutes
Ethanol 95% 1	3 minutes
Ethanol 95% 2	3 minutes
Ethanol 80% 1	3 minutes
Ethanol 80% 2	3 minutes

For antigen retrieval, a cuvette filled with citrate buffer pH 6 (for preparation see 3.1.2.5) was pre-heated in a food steamer. Next, the slides were placed in the boiling solution for 20 minutes. After the antigen retrieval solution with slides had cooled down for 20 minutes at room temperature, the slides were taken out of the cuvette and washed with tap water for 5 minutes, dH_2O for 2 minutes, and twice with 1x PBS for 5 minutes. Tissue spots were encircled with a hydrophobic dako pen (Agilent Technologies, Inc., ref. S2002) to reduce the surface area for antibody incubation. N.B. from this point, slides were kept in a wet chamber.

3.7.4.2 Antibody binding

Slides were covered with blocking and permeabilisation buffer (10% donkey serum with 0.05% saponin in 1x PBS) for 30 minutes at room temperature. The primary antibodies were diluted 1:50 (guinea pig anti-insulin), 1:100 (rabbit anti-Ki67) and 1:200 (rabbit anti-glucagon) in blocking buffer. 100µl of dilution was added to the section (except for the negative controls) for 3 hours. Then, the slides were washed twice for 10 minutes in 1x PBS. The secondary antibodies (Alexa 568-conjugated goat anti-rabbit and Cy2-conjugated donkey anti-guinea pig) were diluted 1:100 with blocking buffer and added to the slides (including the negative controls) for one hour at room temperature (N.B. from this point on, the slides were kept in the dark to prevent bleaching).

Subsequently, the slides were washed twice for 10 minutes in 1x PBS. Nuclei were stained using 4',6-diamidino-2-phenylindole (DAPI) which was diluted 1:2000 in 1x PBS and added to the sections for 10 minutes at room temperature. Then, the slides were washed twice for 10 minutes in 1x PBS and placed in dH_2O for 5minutes.

3.7.4.3 Mounting

Subsequently, water was removed from the slides using a paper towel, and each section was coated with two drops of Fluoromount-G (SouthernBiotech, ref. 0100-01) and

covered with 24x60mm cover slips (Menzel-Gläser). Any encased bubbles were expelled with a needle. After that, the slides were dried in a chamber with silica gel overnight at room temperature. For longer storage, the slides were placed in a box and kept at 4°C.

3.7.4.4 Image acquisition

Images of the slides were acquired using an automated microscope (TissueFAXS Inverted PLUS system in combination with automated TissueFAXS 4.2.6245.1032 scanning software and a Hamamatsu Photonics K.K., Hamamatsu, JP, type C11440-22C camera), as described[218]. Previews of the entire slides were first taken using a 2.5x objective on the DAPI channel and subsequently images were taken with 20x magnification on the DAPI, Alexa 568 and Cy2 channels. For each Field of View (FOV), individual monochrome images were captured separately for all selected pixel shift-free filter sets. For presentation, false colours replace the monochrome image. For quantification, raw images were transferred to StrataQuest 5.0.1.317 software (see section 3.11.2).

3.8 Functional assays

3.8.1 Luciferase reporter assays

3.8.1.1 Assay principle

Luciferase reporter assays were used to detect CaSR-mediated changes in gene transcription[210]. Stimulation of the MAPK pathway activates the transcription factor serum response factor (SRF) which binds to the serum response element (SRE) in the promoter region of many genes involved in cell growth, such as c-fos[222-225]. Similarly, intracellular calcium (Ca^{2+}_i) mobilisation activates the transcription factor nuclear factor of activated T cells (NFAT) which binds to NFAT response element (NFAT-RE)[6].

The pGL4.30 and pGl4.33 luciferase reporter constructs (Promega) contain NFAT-RE and SRE cloned upstream of a luciferase reporter gene, respectively. The pGL4.33[luc2P/SRE/Hygro] vector is shown as an example in Figure 3.1. It is a high copy number plasmid which contains SRE cloned upstream of a synthetic firefly luciferase (Luc2P). Additionally, it contains genes encoding for hygromycin B phosphotransferase which provides hygromycin resistance in mammalian cells (HygR), and for ß-lactamase which confers ampicillin resistance in bacteria (AmpR). When cells transfected with pGl.4.33 activate the MAPK pathway, SRF will bind to SRE, thus promoting luciferase transcription. This can then be detected using luciferase substrates which, in the presence of luciferase, will emit light. Thus, transcription factor activity of the cells is translated into luminescence[226,227].

The pGL4.30[luc2P/NFAT-RE/Hygro] and pGL4.33[luc2P/SRE/Hygro] constructs were stably transfected into HEK293A-$G\alpha_{q/11}$-KO-CaSR cells to generate the HEK293A-$G\alpha_{q/11}$-KO-CaSR-SRE and HEK293A-$G\alpha_{q/11}$-KO-CaSR-NFAT-RE cell lines (section 3.5.3).

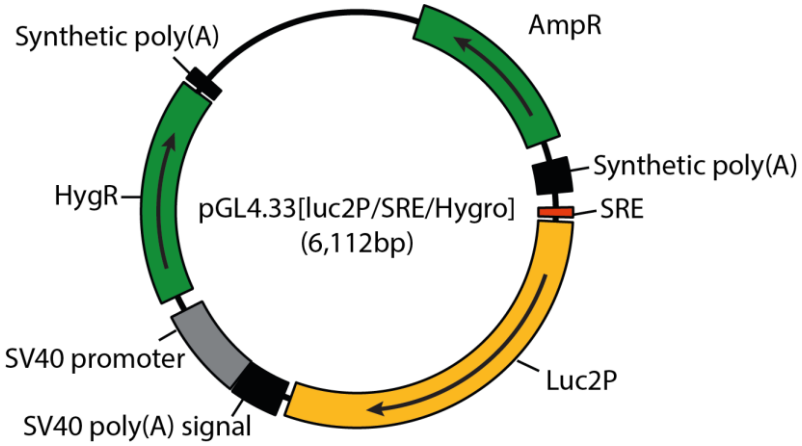


Figure 3.1 pGL4.33[luc2P/SRE/Hygro] vector map. Serum response element (SRE) (red) is cloned upstream of a synthetic luciferase (Luc2P) (yellow). The ampicillin (AmpR) and hygromycin (HygR) resistance genes are shown in green. The latter is under the control of an SV40 promoter (grey). Poly(A) signals (black) are present to reduce background signals. Adapted from PromegaCorporation[228].

3.8.1.2 Protocol

Day 1

T75 flasks containing healthy, 80% confluent HEK293A-$G\alpha_{q/11}$-KO-CaSR-SRE and HEK293A-$G\alpha_{q/11}$-KO-CaSR-NFAT-RE cells were washed once with 1x PBS and 2ml of 0.05% Trypsin-EDTA with phenol red (Thermo Fisher Scientific, ref. 25300054) were added. After the cells had detached (~1min), 4ml DMEM-FBS was added. Subsequently, cells were counted using a haemocytometer (bright line, Neubauer). The cell suspension was diluted to 100,000 cells/ml, and 100µl were plated in clear 96 well plates (flat bottom, Sarstedt Inc.) using a multichannel pipette.

Day 2

The next day, the following transfection solutions were prepared (per well): 50ng WT or mutant pBI-CMV2-*GNA11*/*GNAQ* constructs in 10µl DMEM and 0.2µl Lipofectamine 2000 (Thermo Fisher Scientific, ref 11668019) in 10µl DMEM. Subsequently, the solutions were mixed and incubated for 5 minutes at room temperature, and 20µl of the mix was added to each well of plated cells.

Day3

24 hours after transfection, cell growth media was removed using an aspirator (Vacusafe, Integra) and replaced with 100µl starvation media (composition see section 3.1.3.1).

Day 4

After 18 hours of starvation, cell media was replaced with 50µl of 0.1, 1, 2.5, 4, 5, 6, 7.5, 10 mM $CaCl_2$ (≥99.0%, Sigma-Aldrich) in calcium free DMEM containing 25mM HEPES (Thermo Fisher Scientific). Cells were treated for 4 hours at 37°C to induce SRE/NFAT-RE luciferase reporter expression. Subsequently, treatment media was removed, and

cells were lysed in 50µl passive lysis buffer (PLB) (Promega, ref. E194A). Cell lysates were incubated for 10 minutes at 4°C and subsequently frozen at -80°C.

Day 5

Cell lysates were thawed for 20 minutes at 4°C and 10 minutes at room temperature. Next, 20µl lysate of each well was transferred to 96-well white assay plates with opaque bottom (Corning, ref. 3917). Luciferase assay reagent (LAR) (Promega, ref. E1501) was freshly prepared by dissolving one aliquot of dry reagent in 10ml of buffer. Subsequently, one of the injectors of the PHERAstar FS plate reader (Bmg Labtech) was washed with water and 70% ethanol and primed twice with LAR. Assay plates were placed in the plate reader, and 30µl of LAR was injected into each well, followed by 3 seconds of light collection. Gain values of 2000 and 4000 were used for SRE and NFAT-RE assays, respectively. Data was exported from MARS software (Bmg Labtech) and analysed using Microsoft Excel 2004 and GraphPad Prism 8. All responses were normalised to baseline (0.1 mM $CaCl_2$).

3.8.2 NanoBiT assays

3.8.2.1 Assay principle

NanoBiT[207] assays (Promega) are split luciferase assays which allow measurement of direct protein-protein interactions. They constitute two fragments of the NanoLuc luciferase: a 15 kDA large bit (lgBiT) and a 1.3 kDa small bit (smBiT). The two bits do not self-associate and have no luciferase activity by themselves; however, when they are in direct contact they act as a bright luciferase enzyme. This means that two proteins of interest can be independently tagged with the bits, and if they interact, the LgBit and SmBiT will complement and a luciferase signal is observed (Figure 3.2A).

For PLC NanoBit assays, $G\alpha_q$ and $G\alpha_{11}$ were tagged with the large bit between amino acids 97 and 98 (97,98-Lg), or between amino acids 123 and 124 (123,124-Lg)[207,209]. The $G\alpha_{q/11}$ effectors Phospholipase C (PLC) β_2 and β_3 were tagged N-terminally with the small bit (Figure 3.2B). Upon CaSR-mediated activation, the Gα subunit and PLC are expected to interact[27], thus leading to an increase in luciferase activity.

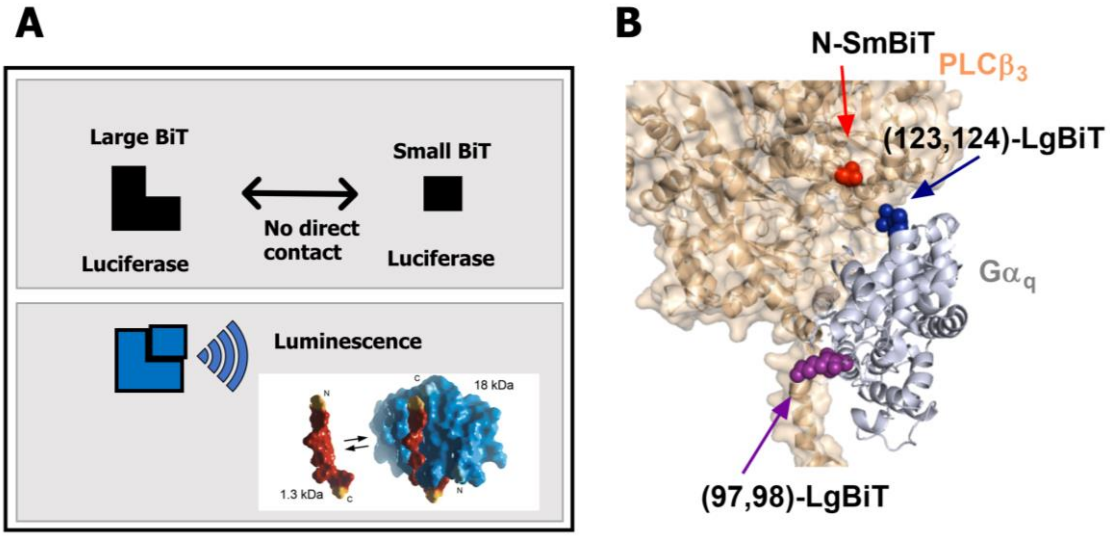


Figure 3.2 Illustration of NanoBiT assays. (A) NanoLuc luciferase is split into 2 parts: SmBiT and LgBiT. When the two parts form a complex, they produce luminescence. (B) For NanoBiT PLC assays, the SmBiT is N-terminally fused to PLCß$_{2/3}$ and the LgBiT is placed in different positions of the $G\alpha_{q/11}$ subunit. When $G\alpha_{q/11}$ and PLC interact, the SmBiT and the LgBiT are brought into close proximity and luminescence can be detected[207]. PDB code 3OHM.

3.8.2.2 Protocol

Day 1

Per well, 20ng of LgBiT DNA and 20ng of SmBiT DNA (see Table 3.21), and 0.2µl Lipofectamine 2000 (Thermo Fisher Scientific, ref 11668019) were diluted separately in 10µl DMEM, then mixed together and incubated for 5 minutes at room temperature, and dispensed into opaque, white 96 well assay plates (Corning, ref. 3610).

Table 3.21 NanoBiT split luciferase constructs.

LgBiT plasmids	SmBiT plasmids
pcDNA3.1-*GNA11*-(97,98)-LgBiT	pCAGGS-PLCβ2(N)SmBiT
pcDNA3.1-*GNA11*-(123,124)-LgBiT	pCAGGS-PLCβ3(N)SmBiT
pcDNA3.1-*GNAQ*-(97,98)-LgBiT	
pcDNA3.1-*GNA1Q*(123,124)-LgBiT	

Next, T75 flasks containing healthy, 80% confluent HEK293A-$G\alpha_{q/11}$-KO-CaSR cells were washed once with 1x PBS and detached with 2ml of 0.05% Trypsin-EDTA with phenol red (Thermo Fisher Scientific, ref. 25300054). Subsequently, 4ml of DMEM-FBS were added and cells were counted using a haemocytometer (bright line, Neubauer). The cell suspension was diluted to 200,000 cells/ml, and 80µl were added to the wells containing transfection reagents using a multichannel pipette.

Day 3

Forty-eight hours after transfection, cell growth media was replaced with Ca^{2+} and Mg^{2+}-free HBSS (Thermo Fisher Scientific) supplemented with: 0.1 mM $CaCl_2$, 1.18 mM $MgCl_2$, and 5mM HEPES for 4 hours. Next, live cells were incubated with NanoGlo® live cell substrate (Promega, ref N1110) for 120 minutes at room temperature. Following this, one of the injectors of the PHERAstar FS plate reader (Bmg Labtech) was washed with water and 70% ethanol and primed twice with 100mM $CaCl_2$ stock solution. Plates were placed in the plate reader and a baseline luciferase reading was taken. Increasing concentrations of $CaCl_2$ (0.1 to 15 mM) were injected, and changes in Luminescence were recorded at 2.5, 5 and 10 minutes post injection. Data was exported from MARS software (Bmg Labtech) and analysed using Microsoft Excel 2004 and GraphPad Prism 8. All responses were normalised to baseline luminescence 0.1 mM $CaCl_2$.

3.8.3 GTPase activity assays

3.8.3.1 Assay principle

The intrinsic GTPase activity of WT and mutant $G\alpha_{11}$ was measured using the GTPase-Glo™ assay (Promega, ref V7681). The GTPase-Glo™ reagent converts GTP to ATP which is required for firefly luciferase reactions (Figure 3.3). In the presence of a GTPase, some GTP will be hydrolysed to GDP and will therefore not be converted to ATP. Thus, higher GTPase activity causes a decrease in luminescence[229].

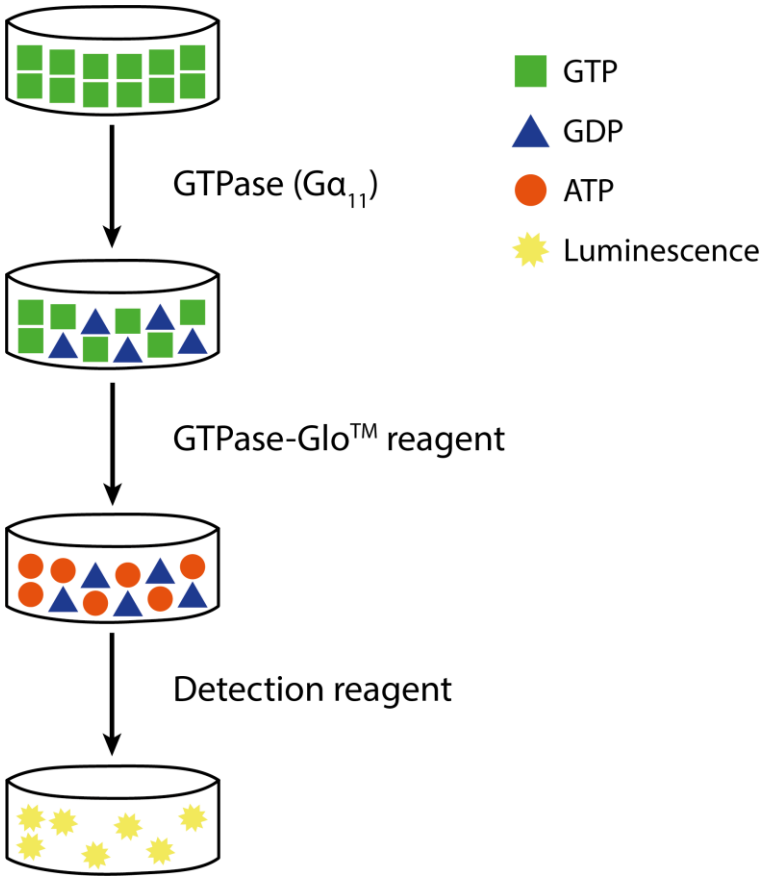


Figure 3.3 Glo™ assay principles. GTP (green) is hydrolysed to GDP (blue) by GTPases such as $G\alpha_{11}$. Remaining GTP is converted to ATP (red) by the GTPase-Glo™ reagent. ATP is required for firefly luminescence (yellow) which is detected using detection reagent.

3.8.3.2 Protocol

Day 1

On day 1, T75 flasks containing healthy, 80% confluent HEK293A-$G\alpha_{q/11}$-KO-CaSR cells were washed once with 1x PBS and detached with 2ml of 0.05% Trypsin-EDTA with phenol red (Thermo Fisher Scientific, ref. 25300054). Next, 4ml DMEM-FBS was added and cells were counted using a haemocytometer (bright line, Neubauer). The cell suspension was diluted to 200,000 cells/ml in DMEM-FBS. Subsequently, 3ml cell suspension were added to 6-well plates (Sarstedt, ref. 83.3920) containing 2µg WT or mutant pBI-CMV-*GNA11* and 4µl Lipofectamine 2000 (Thermo Fisher Scientific, ref 11668019) in 200µl DMEM.

Day 3

48 hours after transfection, cells were washed and lysed in 200µl PLB (Promega, ref. E194A) for 10 minutes at 4°C. Next, cell lysates were centrifuged at 14,000xg for 10 minutes at 4°C, then the supernatant was moved to a new tube. Meanwhile, the GTPase solution was prepared (10µM GTP and 1mM DTT in GTPase/GAP buffer).

30µl cell lysate were placed in a 96-well clear bottom plate (Sarstedt). 50µl of GTP solution was added to initiate the GTPase reaction and incubated at room temperature overnight on a rocker.

Day 4

The next day, the completed GTPase reaction was briefly centrifuged (1 minute at 10,000xg) and 25µl of supernatant from each reaction were transferred to two wells of a white assay plate with opaque bottom (Corning, ref. 3917) to obtain technical duplicates. Next, the thawed GTPase-Glo™ reagent (500X) was mixed by inversion and

immediately before use reconstituted GTPase-Glo™ reagent was prepared as shown in Table 3.22.

Table 3.22 Reagents for 1 ml GTPase-Glo™ reagent.

GTPase-Glow Reagent 500x	2 ul
ADP, 10mM	0.5 ul
GTPase-Glo buffer	998 ul

Subsequently, 25µl of reconstituted GTPase-Glo™ Reagent was added to the 96 well plate containing the complete GTPase reaction, mixed briefly and incubated for 30 minutes at room temperature with shaking. Then, 50µl of detection reagent was added to each well and the plate was incubated for 10 minutes at room temperature. Luminescence was measured using a PHERAstar FS plate reader with MARS software (Bmg Labtech).

3.8.4 Fluo-4 calcium mobilisation assay

3.8.4.1 Assay principle

Activation of $G\alpha_{q/11}$ triggers intracellular calcium (Ca^{2+}_i) mobilisation. This increase was measured using the fluorescent Ca^{2+} indicator Fluo-4. When bound to Ca^{2+}, Fluo-4 responds to excitation from 485nm light by emitting light of 520nm wavelength. To selectively measure intracellular Ca^{2+}, Fluo-4 was added to the buffer as an acetoxymethyl ester (AM) (Figure 3.4) in which it is unable to bind any extracellular calcium[230,231]. After penetration into the cell, the AM is cleaved by intracellular esterases, and Fluo-4 is revealed, leading to fluorescence. Ionomycin which promotes Ca^{2+} influx was used as a positive control[231].

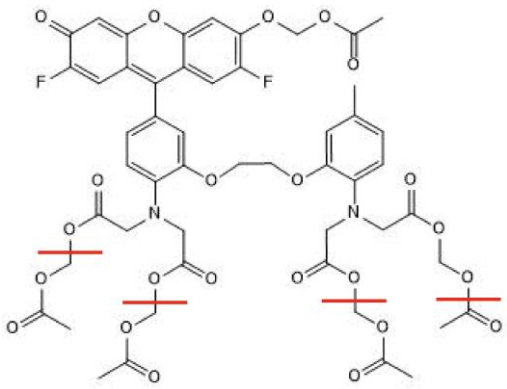


Figure 3.4 Structure of Fluo-4 acetoxymethyl ester (AM). Cleavage sites are indicated in red. Structure obtained from Tocris[230].

3.8.4.2 Protocol

Day 1

On day 1, HEK293A-$G\alpha_{q/11}$-KO-CaSR cells were detached and diluted in DMEM-FBS to a concentration of 200,000 cells/ml. Subsequently, 3ml cell suspension was plated in 6-well plates (Sarstedt, ref. 83.3920).

Day 2

24 hours after plating, each well was transfected with 1µg WT or mutant pBI-CMV-*GNA11*/*GNAQ* and 2µl Lipofectamine 2000 (Thermo Fisher Scientific, ref 11668019). Each of these were prepared separately in 100µl DMEM, combined and incubated for 15 minutes at room temperature and added to the cells.

Day 3

24 hours after transfection, cells were re-seeded from 6-well plates into black 96-well plates (flat, clear bottom, Corning) coated with poly-l-lysine (Thermo Fisher Scientific).

Day 4

At 48h post transfection, cell media was removed, and cells were washed with 100µl Complete Imaging Buffer (for composition see 3.1.3.2). Next, cells were loaded with Fluo-4 working solution (see 3.1.3.3) and incubated for 60 minutes at room temperature. Cells were washed again before the addition of a further 100µl of Complete Imaging Buffer. Subsequently, cells were incubated for 30 min at room temperature in the dark. Meanwhile, the two injectors of a PHERAstar FS microplate reader (BMG Labtech), were washed and primed with stock solutions of 20mM $CaCl_2$ in complete imaging buffer, and complete imaging buffer, respectively. Finally, microplates containing live cells were placed in the plate reader (at 37 °C), and increasing concentrations of either calcium chloride (0.05 to 10 mM) or 50µM ionomycin (positive control) working solution (3.1.3.4) were injected into wells as shown in Table 3.23.

Table 3.23 Treatment solutions used for Fluo-4 assays.

Well	Injector 1 (20mM $CaCl_2$) (µl)	Injector 2 (complete imaging buffer) (µl)	Injector 2 (50µM ionomycin)	Final $CaCl_2$ concentration (mM)	Final ionomycin concentration (µM)
1	0	0	50	0	25
2	0.5	99.5	0	0.05	0
3	1	99	0	0.1	0
4	2	98	0	0.2	0
5	4	96	0	0.4	0
6	6	94	0	0.6	0
7	8	92	0	0.8	0
8	10	90	0	1	0
9	50	50	0	2	0
10	100	0	0	10	0

Changes in Ca^{2+}_i concentrations were recorded via detection of fluorescence for 30s with an excitation filter of 485nm and an emission filter of 520nm. The peak mean fluorescence ratio of the transient response following each individual stimulus was measured using MARS data analysis software (Bmg Labtech). Relative fluorescence

units were normalised to the fluorescence stimulated by ionomycin, to account for differences in cell number and loading efficiency, and then further normalised to the maximum response observed for cells transfected with WT constructs[210].

3.8.5 AlphaScreen assays

3.8.5.1 Assay principle

Amplified Luminescent Proximity Homogeneous Assay (Alpha) Screen technology (Perkin Elmer) is a "sandwich assay" based on energy transfer from donor to acceptor beads (Figure 3.5)[232]. Upon excitation at 680nm, each donor bead produces up to 60,000 singlet oxygen molecules per second. If an acceptor bead is present within a 200nm radius, it will react with the singlet oxygen and emit light of 520-620 nm. The donor-bead is coated with streptavidin and the acceptor bead is conjugated to Protein A. Donor- and acceptor beads do not self-associate and are only brought into close proximity if analyte and anti-analyte antibodies are present. For example, if the analyte is p-Erk, biotinylated anti-p-Erk binds to Erk. Moreover, the donor bead binds to biotinylated anti-p-Erk. Similarly, the acceptor bead detects anti-p-Erk IgGs. Thus, a signal is only observed in the presence of p-Erk[232].

GAPDH, total ERK, p-ERK1/2 and p-JNK1/2/3 AlphaScreen kits were purchased from PerkinElmer, and have previously been used to investigate CaSR signalling via the MAPK pathway[211,219].

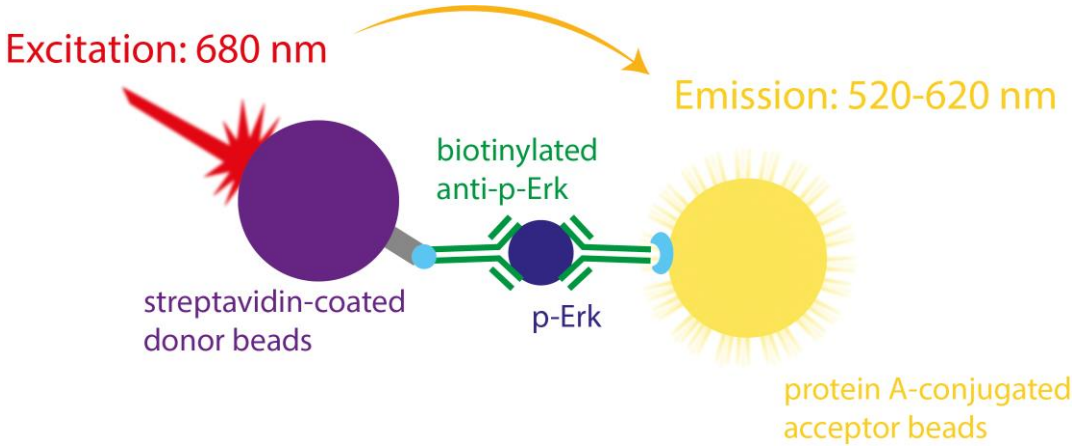


Figure 3.5 Schematic illustration of AlphaScreen technology[232] Upon excitation at 680nm, donor beads (purple) transfer energy to acceptor beads (yellow) if the analyte p-Erk (blue) is present. P-Erk is detected by biotinylated anti-p-Erk antibodies which are recognised by the donor-and acceptor beads.

3.8.5.2 Protocol

Day 1

Per well, 50ng WT or mutant pBI-CMV2-*GNA11* construct, and 0.2µl Lipofectamine 2000 (Thermo Fisher Scientific, ref 11668019) were diluted separately in 10µl DMEM, then mixed together and incubated for 5 minutes at room temperature and dispensed into clear 96 well assay plates (flat bottom, Sarstedt).

Next, T75 flasks containing healthy, 80% confluent HEK293A-$G\alpha_{q/11}$-KO-CaSR cells were washed once with 1x PBS and detached with 2ml of 0.05% Trypsin-EDTA with phenol red (Thermo Fisher Scientific, ref. 25300054). Then, 4ml DMEM-FBS was added and the cells were counted using a haemocytometer (bright line, Neubauer). The cell suspension was diluted to 200,000 cells/ml, and 80µl were added to the wells containing transfection reagents using a multichannel pipette.

Day 3

48 hours after transfection, cell growth media was removed using an aspirator (Vacusafe, Integra) and replaced with 50µl calcium-free DMEM containing 25mM HEPES (both Thermo Fisher Scientific). Subsequently, 2x treatment solutions of $CaCl_2$ (≥99.0%, Sigma-Aldrich) were prepared in calcium-free DMEM (0.2,1,2,5,8,10,15,20mM).

After 4 hours of starvation, cells were treated with 50µl 2x treatment solutions to achieve final Ca^{2+}_e concentrations of 0,1,2.5,4,5,7.5,10mM. After 2.5 minutes, treatment media was removed, and cells were lysed in 50µl SureFire lysis buffer (PerkinElmer) and frozen at -20°C.

Day 4

Plates containing cell lysates were thawed for 20 minutes at 4°C and 10 minutes at room temperature (RT). Meanwhile, the activation buffer was diluted in reaction buffer at a ratio of 1 to 5. Donor beads were added in low light conditions at a ratio of 1 to 50.

Next, 5µl of cell lysate was transferred to 385-well AlphaPlates (PerkinElmer) and 5µl of acceptor bead solution were added per well. Subsequently, plates were sealed and incubated for 2 hours at RT in the dark (covered by aluminium foil).

Subsequently, donor beads were diluted 1 in 20 in dilution buffer in the dark, and 2µl were added per well of the 385-well plate. Thereafter, plates were sealed and incubated for 2 hours at RT in the dark (covered by aluminium foil).

Finally, plates were placed in a PHERAstar FS plate reader (Bmg Labtech) and fluorescence ratios were measured using a PHERAstar FS plate reader equipped with an AlphaScreen module (Bmg Labtech) (excitation: 680 nm, emission: 570 nm). Data was exported from MARS software (Bmg Labtech) and analysed using Microsoft Excel

2004 and GraphPad Prism 8. P-Erk responses were normalised to total Erk and GAPDH and expressed as fold change over baseline (0.1 mM $CaCl_2$).

3.8.6 Bioluminescence Resonance Energy Transfer (BRET)

3.8.6.1 Assay principle

Bioluminescence Resonance Energy Transfer (BRET) refers to the transfer of energy from a luciferase donor (e.g. firefly) to a fluorescent acceptor, e.g. green fluorescent protein (GFP)[233,234]. The luciferase and activated GPF emit light of different wavelengths (400 and 515nm, respectively) which can be detected separately (Figure 3.6). BRET only occurs if the energy donor and acceptor are within 10nm of each other, and the light intensity of the fluorescent acceptor is inversely proportional to the sixth power of distance. Cellular re-arrangements occur in the same order of magnitude distance-wise (the average protein size is approximately 5nm), and therefore BRET-based techniques have been used extensively in recent years to characterise protein-protein interactions in living cells.[34,35]

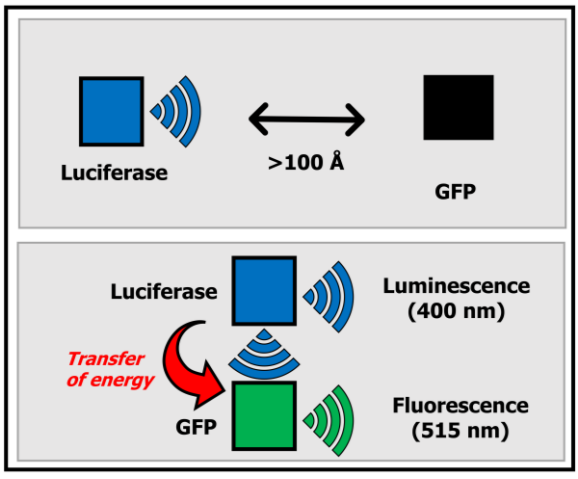


Figure 3.6 Overview of BRET. Luciferase (blue) transfers energy to GFP (green) when they are in close proximity.

A disadvantage of BRET is that it requires proteins of interest to be fused to the BRET partners, which can affect their function. Moreover, BRET pairs that are optimised to minimise self-association often lack efficiency, resulting in a poor background-to-noise ratio.

These drawbacks are overcome by enhanced bystander (eb) BRET[166]. EbBRET uses a BRET pair that occurs naturally in *Renilla reniformis*: the luciferase Rluc (or the brighter mutant form RlucII) and rGFP. They have near perfect (almost 100%) transfer efficiency, compared to 20-40% for conventional BRET[166,235]. Rluc and rGFP self-associate when in close contact, hence they are activated by random interactions. This can be harnessed to study cell trafficking: for example, rGFP can be immobilised in a specific subcellular compartment (e.g. plasma membrane (PM) or endosomes) and used to detect the presence of Rluc-tagged proteins of interest. To study G protein activation, rGFP was directed to the PM by fusion with polybasic and prenylation CAAX-motif of Kras4b, and RlucII was fused with effectors (GEFs/GAPs) that are recruited to the Gα subunit upon activation (Figure 3.7). This allows assessment of direct activation of untagged G protein activity. The specific effectors and their G proteins partners are shown in Table 3.24. Comparison of individual G protein subunits within a family was possible because the upstream effectors used are non-amplified (meaning endogenous activity is low) and therefore the contribution of individual G proteins could be determined by overexpression of native subunits. Additionally, ß-arrestin 1 and 2 recruitment to the PM upon GPCR activation was measured directly using RlucII-tagged ß-arrestin 1/2[162,165,166].

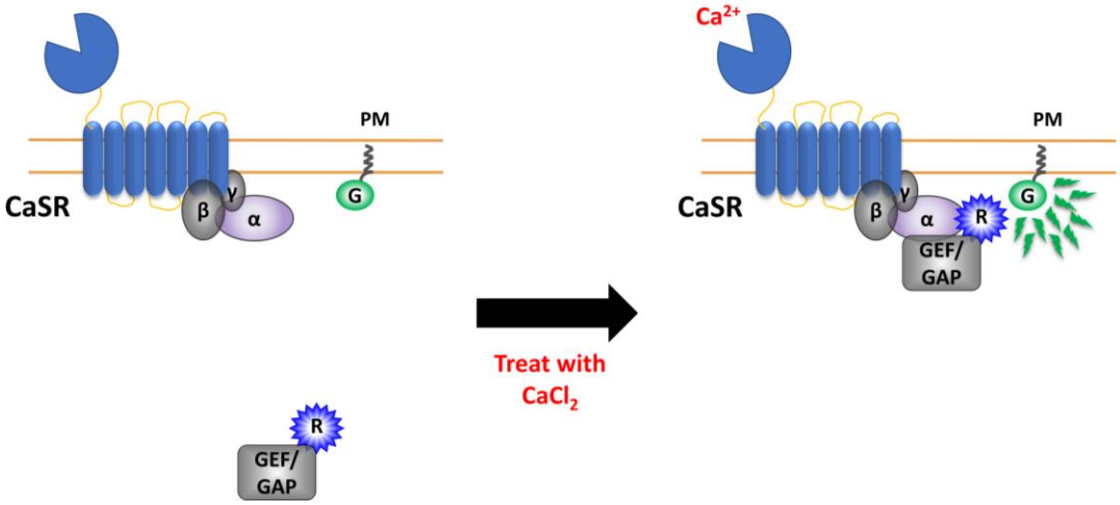


Figure 3.7 Schematic representation of ebBRET. In the basal state, rGFP-CAAX (G) is bound to the membrane and GEF or GAP-RlucCII (R) is in the cytoplasm. Upon CaSR activation, GEF/GAP-RlucII gets recruited to the Gα subunit and a BRET signal occurs.

3.8.6.2 Protocol

Day 1

For studies of G protein signalling, 35,000 HEK293-Flp-In-Flag-CaSR cells/well of a white 96 well assay plate (Corning, ref. 3610) were transiently transfected with: 300ng/ml pcDNA3.1(+)_rGFP-CAAX, RlucII-effector, and native G proteins (GenScript). Transfection amounts for effector and G protein constructs were optimised and are shown in Table 3.24. For ß-arrestin studies, HEK293-Flp-In-Flag-CaSR cells were transiently transfected with: 300ng/ml pcDNA3.1(+)_rGFP-CAAX pcDNA3.1(+) and 20ng/ml pcDNA3.1(+)_ß-arrestin1-RlucII or 10ng/ml pcDNA3.1(+)_ß-arrestin2-RlucII. The total DNA concentration was adjusted to 1000ng/ml using UltraPure™ Salmon Sperm DNA (SSD) (Thermo Fisher Scientific, ref. 15632-011). As a transfection reagent, 3µl PEI stock solution (preparation see 3.1.3.7) was used per ml of cell suspension.

Table 3.24 Enhanced bystander (eb) BRET effectors and native G proteins used.

Gα subunit	ng DNA/ml	effector	ng DNA/ml
$G\alpha_q$	100	p63RhoGEF-RlucII	10
$G\alpha_{11}$, $G\alpha_{15}$	10	p63RhoGEF-RlucII	10
$G\alpha_{14}$	50	p63RhoGEF-RlucII	10
$G\alpha_{i1}$, $G\alpha_{i2}$, $G\alpha_{i3}$, $G\alpha_{oA}$, $G\alpha_{oB}$, $G\alpha_z$	100	rap1gap-RlucII	3
$G\alpha_{12}$, $G\alpha_{13}$	50	pdzRhoGEF-RlucII	5
$G\alpha_{12}$, $G\alpha_{13}$	50	p115RhoGEF-RlucII	5

For positive control experiments, HEK293-Flp-In-Flag-CaSR cells were transfected as above, with the addition of 300ng/ml GPCR (pcDNA3.1-M_2R/M_3R/TPα/B2AR). Where appropriate, empty vector (EV) or salmon sperm DNA were used as negative controls.

For studies of CaSR mutants, HEK293-Flp-In-TREX-CaSR-WT, HEK293-Flp-In-TREX-CaSR-Arg185Gln and HEK293-Flp-In-TREX-CaSR-Ser657Cys were transfected as above with the addition of 1µg/ml tetracyclin (Sigma, ref. T7660-5G) to induce CaSR expression.

Day 3

Cell growth media was removed 48 hours after transfection, washed once with a modified Tyrode's buffer[208] (for formulation see 3.1.3.5) containing 0.1 mM $CaCl_2$. Next, 80µl Tyrode's buffer was added per well and the plates were incubated for 60 minutes at 37°C. Subsequently, 2mM Prolume Purple stock solution (see 3.1.3.6) was diluted 1:200 in Tyrode's buffer and 10µl were added to each well using a repeat dispenser (Eppendorf) (final concentration: 1µM). Then, cells were incubated with 1µM of for 8 minutes at 37°C. 10x $CaCl_2$ solutions (1.0, 8.8, 13.2, 19.8, 29.6, 44.4, 66.7, 100.0 mM) or positive control agonists were prepared in Tyrode's buffer and 10µl were added to each well (final $CaCl_2$ concentrations: 0.1, 0.88, 1.32, 1.98, 2.96, 4.44, 6.67, 10 mM). Cells were incubated for a further 2 min at 37°C. For studies with allosteric modulators,

compounds were added to the Prolume Purple working solution. A list of all GPCR-targeting compounds is provided in section 3.2.

Luminescence measurements were performed using a Mithras LB940 Microplate Reader (Berthold Technologies), equipped with BRET2 filters (donor: 400/70 nm, acceptor: 515/20 nm). The BRET2 ratio was determined by calculating the ratio of the light intensity emitted by rGFP over the light intensity emitted by the RlucII.

3.8.7 IP-One assays

3.8.7.1 Assay principle

The IP-One Gq kit (Cisbio, ref. 62PAPEB) is a competitive immunoassay which allows indirect detection of Inositol 1 phosphate (IP_1), a metabolite of IP_3. It is based on the homogeneous Time Resolved Fluorescence (HTRF®) technique[236]. The kit contains an anti-IP_1 antibody conjugated to an energy donor (Terbium cryptate) and a fluorescent acceptor (d2) conjugated to IP_1. If added together, energy is transferred from the donor to the acceptor, and a FRET signal is observed (Figure 3.8). However, when cells produce IP_1 through activation of the PLC pathway, this unlabelled IP_1 competes for the anti-IP_1 antibody, thereby decreasing the FRET signal. Hence, cell signalling is inversely proportional to fluorescence intensity. IP_1 accumulation in cells is facilitated by LiCl which inhibits its degradation to Myo-Inositol[237].

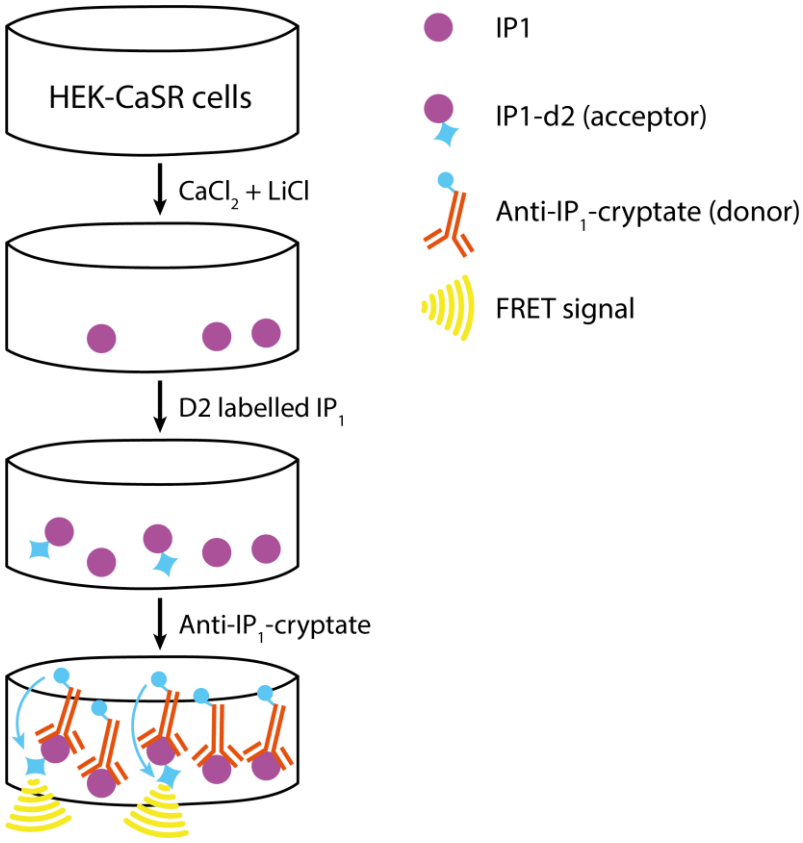


Figure 3.8 Schematic representation of IP-One assays. In the presence of $CaCl_2$ and LiCl IP_1 accumulates in the cell and competes with d2-labelled acceptor (purple) for binding of the anti-IP_1 (red) cryptate donor (blue). Thus, increasing concentrations of IP_1 produced by the cell lead to a decrease in FRET signal (yellow).

3.8.7.2 Protocol

Day 1

Per well, 50ng WT or mutant pBI-CMV2-*GNA11* construct, and 0.2µl Lipofectamine 2000 (Thermo Fisher Scientific, ref 11668019) were diluted separately in 10µl DMEM, then mixed together and incubated for 5 minutes at room temperature and dispensed into clear 96 well assay plates (flat bottom, Sarstedt).

Next, T75 flasks containing healthy, 80% confluent HEK293A-$G\alpha_{q/11}$-KO-CaSR cells were washed once with 1x PBS and detached with 2ml of 0.05% Trypsin-EDTA with

phenol red (Thermo Fisher Scientific, ref. 25300054). Subsequently, 4ml DMEM-FBS was added and the cells were counted using a haemocytometer (bright line, Neubauer). The cell suspension was diluted to 200,000 cells/ml, and 80µl were added to the wells containing transfection reagents using a multichannel pipette.

Day 3

Forty-eight hours after transfection, cell growth media was removed using an aspirator (Vacusafe, Integra) and replaced with assay buffer (HBSS with 0.1 mM $CaCl_2$, 1.18 mM $MgCl_2$, 5mM HEPES) for 4 hours. Next, 2x treatment solutions of $CaCl_2$ (≥99.0%, Sigma-Aldrich) were prepared in calcium-free DMEM (0.2,1,2,5,8,10,15,20mM).

Then, cells were treated with 50µl 2x treatment solutions to achieve final Ca^{2+}_e concentrations of 0,1,2.5,4,5,7.5,10mM for 30 minutes at 37°C in the presence of 40 mM LiCl. Following stimulation, cells were lysed in 50µl lysis and detection buffer (Cisbio) for 30 minutes at room temperature and plates were frozen at -20°C.

Day 4

Plates containing cell lysates were thawed for 20 minutes at 4°C and 10 minutes at room temperature. Next, 5µl lysate of each well was transferred to 385-well white low volume assay plates with opaque bottom (Corning). IP_1-d2 and anti IP_1-cryptate solutions (Cisbio) were diluted at a ratio of 1 in 20 in assay buffer. Subsequently, 5µl of IP_1-d2 and anti IP_1-cryptate working solution was prepared per well of cell lysate. Plates were sealed and incubated for 60 minutes in the dark. Finally, fluorescence ratios were detected using a PHERAstar FS plate reader equipped with an HTRF® module (Bmg Labtech) (excitation: 340 nm, emission: 615 and 665 nm).

3.9 *In vivo* studies

Dsk7 mice[125] were rederived on a C3H strain background (C3H.C3HeB/FeJ-Gna11Mhdadsk7/IegH) by *in vitro* fertilisation using sperm obtained from the European Mutant Mouse Archive (EMMA). Mice were housed at the MRC Harwell Institute in accordance with MRC and UK Home Office welfare guidelines, and approved protocols from project license PPL 3003271 were used. Mice had free access to water and were fed ad libitum on a commercial diet (RM3, Special Diet Services) that contained 1.15% calcium, 0.58% phosphate, and 4089 IU/kg of vitamin D. All biochemical assays, including IPGTTs were performed by technical staff at MRC Harwell.

3.9.1 Plasma Biochemistry

To obtain terminal blood samples for plasma biochemistry, 14 weeks old WT and Dsk7 mice were fasted for 4 hours and terminal anaesthesia was performed using 4% isoflurane[125]. Next, blood was obtained from the retro-orbital vein and separated by centrifugation at 5,000xg for 10 minutes. Subsequently, plasma biochemical analysis was undertaken using a Beckman Coulter AU680 automated analyser[125].

3.9.2 Intraperitoneal Glucose tolerance tests (IPGTTs)

Intraperitoneal glucose tests (IPGTTs) were performed in 14-week-old WT and Dsk7 mice, as described[134]. After 18 hours of fasting (overnight), mice were weighed, and the amount of glucose stock solution (0.2mg/µl) needed to obtain 2g/kg was calculated. Then, a local anaesthetic (Emla cream) was applied to the tails of the mice. Twenty minutes later, mice were restrained, the tail was massaged and 30µl of blood were collected from the lateral tail vein and placed on ice. Subsequently, the previously calculated volume of glucose solution was injected into the peritoneum. Blood sample collection was repeated at 30, 60 and 90 minutes (Figure 3.9)[134]. The samples were stored at -20°C.

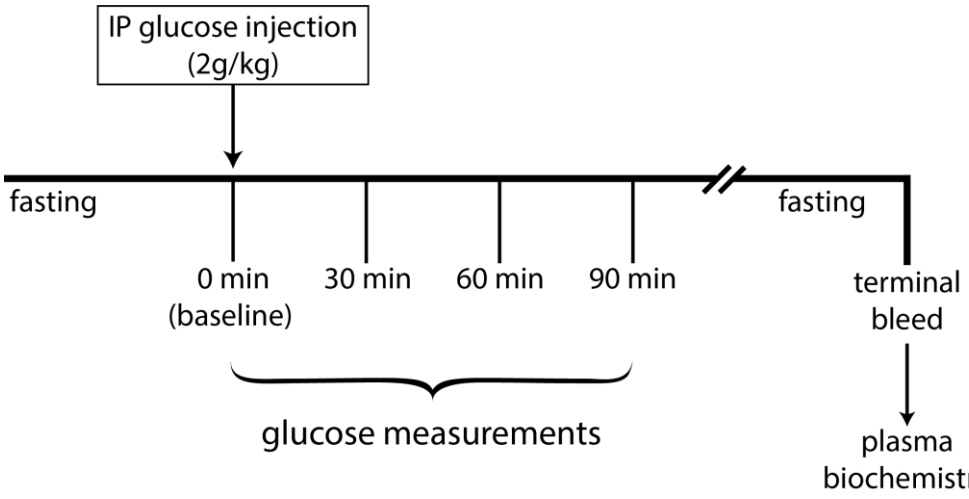


Figure 3.9 Protocol for Dsk7 intraperitoneal glucose tolerance tests (IPGTTs) and terminal bleeds.

Plasma glucose concentrations were measured using an Analox Glucose Analyser which was calibrated by using 0, 8 and 25mM glucose solutions as a reference. Plasma samples from the IPGTTs were thawed in batches and 5µl of each sample were injected into the machine. Every few samples, the 8mM glucose reference was retested, and the machine was recalibrated as necessary.

3.9.3 Tissue preparation and embedding

Tissue preparation and embedding was performed by Dr. Sian Piret (University of Oxford). Pancreata from +/+, Dsk7/+ and Dsk7/Dsk7 mice were harvested at 14 weeks of age and immediately fixed in 10% formalin. After 24 hours, they were transferred to 70% ethanol and embedded in paraffin using a semi-enclosed benchtop tissue processor (Leica Biosystems). Subsequently, 4.5µM sections were cut using a fully automated rotary microtome (Leica Biosystems) and serial sections were transferred to glass slides.

3.10 Bioinformatics analysis

3.10.1 Evolutionary conservation

Amino acid sequences of $G\alpha_{q/11}$ orthologs and $G\alpha$ paralogs were aligned using ClustalOmega[17]. Amino acids were grouped according to similarity (one letter code): GAVLI, FYW, CM, ST, KRH, DENQ, P.

3.10.2 Prediction of pathogenicity

Variant pathogenicity was analysed using the following prediction software: polyphen-2[238], SIFT[239], CADD[240], REVEL[241] and metaLR[242].

3.10.3 Three-dimensional homology modelling

All crystal structures were obtained from RCSB PDB [243] and analysed using the PyMOL Molecular Graphics System, v2 (Schrödinger, Inc.). A full list of structures that are shown in this thesis is provided in Table 3.25.

The $G\alpha_{11}$ homology model was built using SWISS-MODEL[244-249] based on the nucleotide-bound structure of $G\alpha_q$[38] which is 90% identical to $G\alpha_{11}$[9].

Table 3.25 Crystal structures used in this thesis with corresponding PDB codes.

Structure	PDB code
Structure of heterotrimeric G protein Galpha-q beta gamma in complex with an inhibitor YM-254890	3AH8
Crystal structure of wild-type KRAS bound to GDP and Mg	6MBt
Structure of regulator of G protein signaling 8 (RGS8) in complex with AlF4-activated Galpha-q	5DO9
The structure of a membrane adenylyl cyclase bound to an activated stimulatory G protein	6R3Q
Crystal structure of Galphaq in complex with full-length human PLCbeta3	4gnk
Crystal Structure of p63RhoGEF complex with Galpha-q and RhoA	2RGN
Muscarinic acetylcholine receptor 1-G11 protein complex	6OIJ
Cryo-EM structure of parathyroid hormone receptor type 1 in complex with a long-acting parathyroid hormone analog and G protein	6nbf
Metabotropic Glutamate Receptor 5 bound to L-quisqualate and Nb43	6n51
Structure of human Smoothened-Gi complex	6ot0
Crystal structure of the active form of human calcium-sensing receptor extracellular domain	5k5S
Crystal structure of the inactive form of human calcium-sensing receptor extracellular domain	5K5T
Crystal structure of the extracellular domain of human calcium sensing receptor	5FBK
Crystal structure of the extracellular domain of human calcium sensing receptor with bound Gd3+	5FBH
Crystal structure of the beta2 adrenergic receptor-Gs protein complex	3sn6

3.11 Data analysis

3.11.1 Western blot quantification

Densitometry analysis of Western blots was performed using imageJ software. Pixel density of bands of interest was calculated, corrected for background signal, and normalised to the density of the corresponding reference band (i.e. calnexin), as described[210].

3.11.2 Tissue cytometry

Images obtained from pancreatic islet staining were quantified using Tissuegnostics StrataQuest 5.0.1.317 image analysis software[250,251]. In collaboration with Stefan Sarbu

at Tissuegnostics I developed an algorithm for semi-automated detection of α, ß, and proliferating cells within pancreatic islets (Figure 3.10). In order to detect islets, the software first performs nuclear segmentation based on DAPI (blue) staining, and then finds areas around the nuclei that are positive for insulin (Cy2, green). From this information a density map is built, which enables identification of islet candidates. Clusters of auto-fluorescent erythrocytes (false positives) are removed, and areas of hypo-density within islet candidates are filled to select the final islet structure. Insulin and glucagon are present in the cytoplasm and Ki-67 is present in the nucleus. Therefore, two protocols were established for the automated detection of cells that are positive for insulin or glucagon (Alexa 568, red) in the cytoplasm and areas within the nucleus that are positive for Alexa568 (Ki-67).

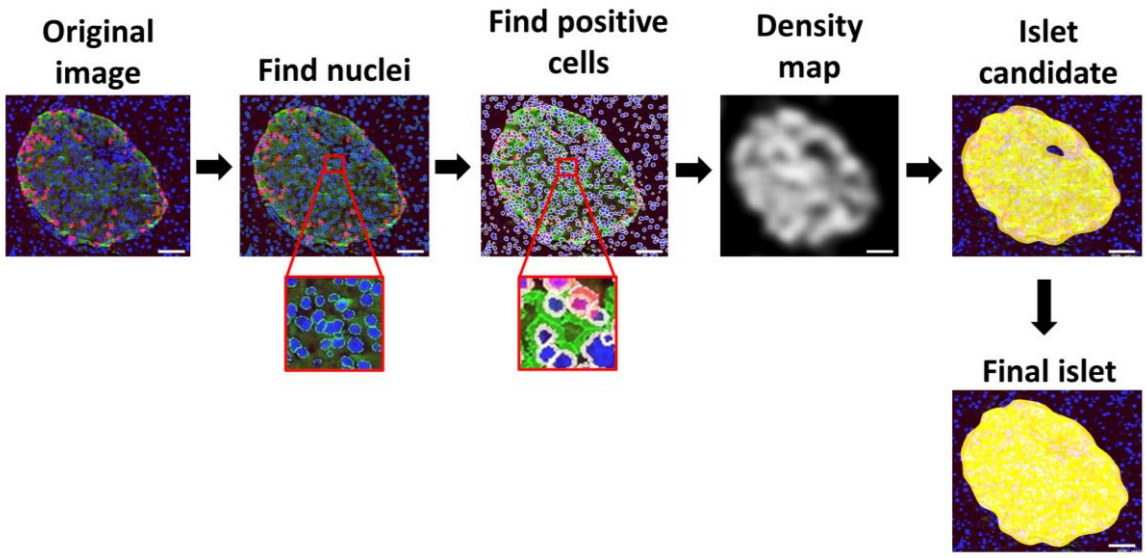


Figure 3.10 Overview of semi-automated detection of α, ß, and proliferating cells within pancreatic islets using StrataQuest. Starting with the original image, nuclei and positively stained areas around them are detected. From that a density map is obtained, which equates to an islet candidate. Subsequently, areas of low density within the islets are filled to obtain a final islet. Scale bar = 50µM.

3.11.3 Statistical analyses

Data analysis was performed in Microsoft Excel 2004 and GraphPad Prism 8.4.1. Data obtained from the IUPHAR/BPS Guide to PHARMACOLOGY[252] and GPCRdb[253] databases were analysed with Python 3.7.4 using the NumPy, pandas and matplotlib packages. Statistical tests were performed in GraphPad Prism 8.4.1. The specific analysis undertaken for each experiment is stated in the corresponding figure legend.

3.12 Patients and ethics

Informed consent was obtained from all persons with the use of protocols approved by local and national ethics committees (MREC /02/2/93).

Mutational analysis of samples obtained from FHH patients negative for mutations in *CASR*, *GNA11* and *AP2S1* was performed using leukocyte DNA. The seven exons, exon-intron boundaries and untranslated regions of *GNAQ* were examined for mutations by sequence analysis (see 3.6.4 for procedure) by Manesh Modi (University of Oxford).

The DiscovEHR cohort[254] consisted of 50,726 Geisinger Health System (GHS) patients within the MyCode Community Health Initiative, who underwent whole exome sequencing[254]. Informed consent was obtained from all persons with the use of protocols approved by local and national ethics committees. All clinical data and unique International Classification of Disease-9 (ICD9) codes for the DiscovEHR cohort were obtained from the electronic health records (EHR) in a de-identified manner through an approved data broker, in accordance with Institutional Review Board approvals[2].

dbSNP[255,256] is a publicly available (https://www.ncbi.nlm.nih.gov/snp/) repository for single-base nucleotide substitutions and short deletion and insertion polymorphisms. Build 153 contains 695,448,618 references SNPs from over 2 billion submissions.

Information from gnomAD v2.1.1[257-259] is publicly available (https://gnomad.broadinstitute.org) and contains genetic variation from 125,748 exomes and 15,708 genomes from unique unrelated individuals with high-quality sequence data, spanning 6 global and 8 sub-continental ancestries. Data were obtained primarily from case-control studies of adult-onset common diseases, including cardiovascular disease, type 2 diabetes, and psychiatric disorders. Each dataset was uniformly processed, and joint variant calling was performed using a standardised BWA-Picard-GATK pipeline. Samples with inadequate consent for release of aggregate data, and individuals known to have a severe childhood onset disease as well as their first-degree relatives were removed.

4 IDENTIFICATION AND CHARACTERISATION OF RARE *GNA11* VARIANTS

4.1 Aims

To date, 4 FHH2-causing[93,108,109] and 8 ADH2-causing[93,117,211,220,260] mutations in *GNA11* have been reported (see section 1.4). They cause loss-of-function and gain-of-function of CaSR mediated signalling, respectively. Disease-causing CaSR mutations have also been shown to promote biased signalling of downstream pathway readouts[261,262]; however, such effects have not been reported for *GNA11* or *AP2S1* mutations. Notably, despite the fact that $G\alpha_{11}$ is a ubiquitously expressed G protein and interacts with multiple GPCRs[6,39,67], patients with reported germline *GNA11* mutations develop disorders of calcium metabolism as their predominant phenotype[82], and patients with somatic, constitutively active *GNA11* mutations develop uveal melanoma (see section 1.1.2)[33]. In addition, mice with a gain-of-function *GNA11* mutation (Dsk7)[35,125] develop calcium abnormalities and dark skin (see 1.4.4.2)[125,36]. The aim of this chapter was to investigate whether rare *GNA11* variants found in large exome-datasets, many of which do not report clinical phenotypes, could represent pathogenic mutations and affect signalling by the CaSR and other GPCRs, such as the muscarinic acetylcholine receptor M_3 (M_3R) and the ß2 adrenergic receptor (B2AR).

4.2 Results

4.2.1 Identification of *GNA11* variants in large-scale sequence databases.

4.2.1.1 Single Nucleotide Polymorphism Database (dbSNP)

To identify novel *GNA11* variants, I examined the publicly available (online) Single Nucleotide Polymorphism Database (dbSNP)[255,256] for variants in *GNA11.* To assess variant frequencies, I used the subset of dbSNP variants that were obtained from gnomAD v2.1.1[257,258], which comprises sequencing data from 125,748 exomes and 15,708 genomes (see methods section 3.12). However, this database does not contain any

information on the associated phenotypes of the patients. It contains data from unrelated individuals sequenced as part of various disease-specific and population genetic studies, excluding individuals known to be affected by severe paediatric disease and their first-degree relatives[259].

This analysis revealed a total of 314 previously uncharacterised germline *GNA11* single nucleotide variants (SNVs). Of these, 170 were synonymous variants (Appendix Table 9.2) and 144 were missense variants (Appendix Table 9.3). All *GNA11* missense variants were rare (minor allele frequency (MAF) < 0.01)[263,264] and observed in the heterozygous state, with the exception of rs147528229 (p.Ala65Thr), which was rare overall (minor allele frequency of 0.00172 in gnomAD) (Table 9.4) but occurred in 3.6% of the African/African-American population, and two African/African-American individuals were homozygous for *GNA11* Ala65Thr. The observed number of missense *GNA11* variants in the gnomAD database was significantly lower than estimated based on the sequence (χ^2 test, $p<0.0001$) (Figure 4.1B). A similar effect was seen for *GNAQ* (Figure 4.1A) and *GNA15* (Figure 4.1D) but not *GNA14* (Figure 4.1C). This indicates that the $G\alpha_{11}$ amino acid sequence is highly conserved and that its alteration is likely to be deleterious for cellular functions[259,265].

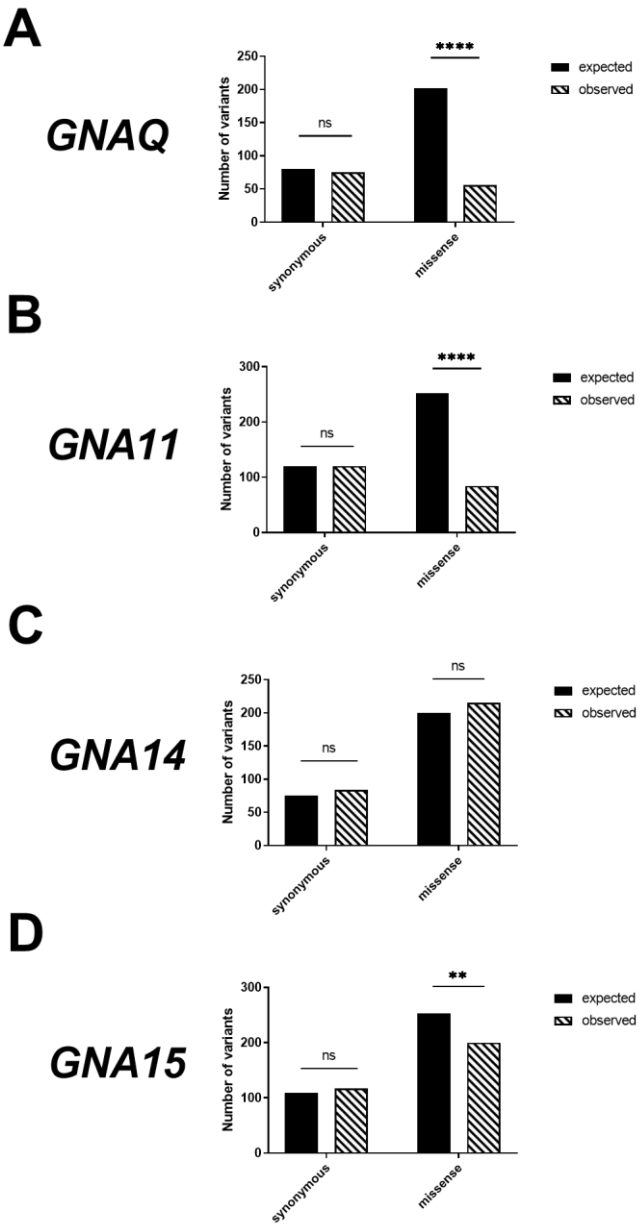


Figure 4.1 Comparison of expected (shown in black) versus observed (diagonal lines) synonymous and missense (A) *GNAQ* (B) *GNA11* (C) *GNA14 and (D) GNA15* variants in the gnomAD database[259]. Significantly more missense *GNAQ*, *GNA11 and GNA15* variants were expected than observed, whereas there was no significant difference for synonymous variants (χ^2 test, $p<0.0001$). In contrast, no significant differences were observed for missense and synonymous *GNA14* variants.

The rare missense variants were further assessed for possible pathogenicity by examining scores from prediction software: polyphen-2[238], SIFT[239], CADD[240], REVEL[241] and metaLR[242]. Seventy-nine variants were predicted to be deleterious in two or more of the tools and subsequently were assessed for evolutionary conservation (Figure 4.2). This revealed that 43 variants were evolutionarily conserved in all orthologs and at least 3 paralogs. I selected a subset of 9 variants spanning different exons for *in vitro* validation.

4.2.1.2 DiscovEHR cohort

I additionally investigated the DiscovEHR cohort[254], which has the advantage of containing phenotyping data that is matched to genotype data obtained from exomes of 51,289 patients. In this database I identified an additional 29 *GNA11* variants and selected 5 for *in vitro* analysis because they had at least one plasma calcium reading that was outside the normal range. Of those, individuals carrying the Arg37Leu, Arg210Trp had mean plasma calcium values outside the normal range (Table 4.1).

Table 4.1 Genotypes and Phenotypes of selected *GNA11* variants from the DiscovEHR cohort (n=5)

Nucleotide change	Amino acid change	Total serum calcium (mg/dl)[a]
c.110G>T	p.Arg37Leu	10.23 (9-11.3)
c.175A>T	p.Met59Leu	8.80 (7.9-10)
c.175A>T	p.Met59Leu	8.77 (7.6-9.6)
c.577C>A	p.Pro193His	8.80 (7.9-9.5)
c.578C>A	p.Pro193Thr	10.10 (10.1-10.1)
c.628C>T	p.Arg210Trp	10.44 (9.9-11.1)

[a]Mean serum calcium values. Normal range=8.30–10.00 mg/dL, which is defined as the mean±2 standard deviations.

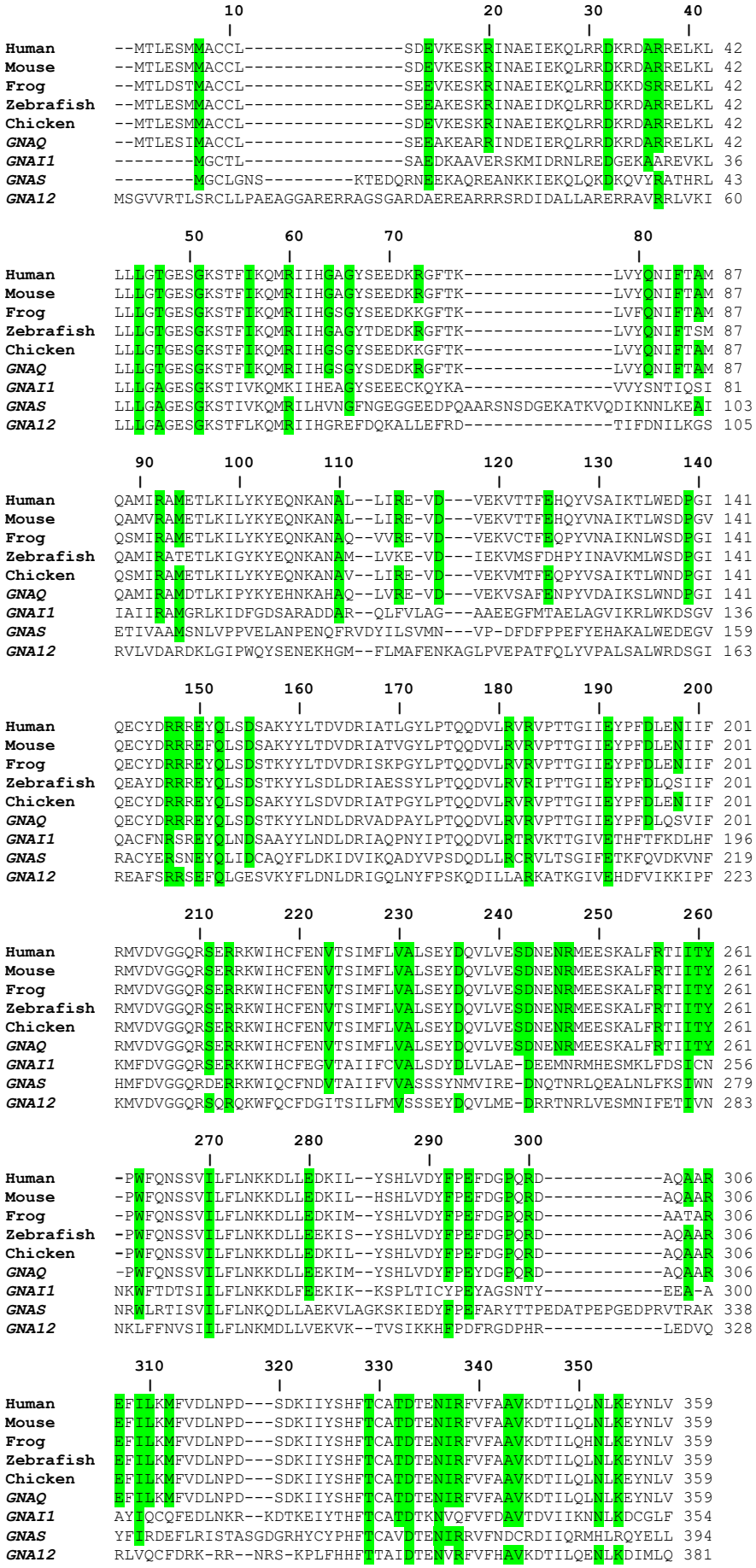

Human --MTLESMMACCL----------SDEVKESKRINAEIEKQLRRDKRDARRELKL 42
Mouse --MTLESMMACCL----------SDEVKESKRINAEIEKQLRRDKRDARRELKL 42
Frog --MTLDSTMACCL----------SEEVKESKRINAEIEKQLRRDKKDSRRELKL 42
Zebrafish --MTLESMMACCL----------SEEAKESKRINAEIDKQLRRDKRDARRELKL 42
Chicken --MTLESMMACCL----------SDEVKESKRINAEIEKQLRRDKRDARRELKL 42
GNAQ --MTLESIMACCL----------SEEAKEARRINDEIERQLRRDKRDARRELKL 42
GNAI1 --------MGCTL----------SAEDKAAVERSKMIDRNLREDGEKAAREVKL 36
GNAS --------MGCLGNS---------KTEDQRNEEKAQREANKKIEKQLQKDKQVYRATHRL 43
GNA12 MSGVVRTLSRCLLPAEAGGARERRAGSGARDAEREARRRSRDIDALLARERRAVRRLVKI 60
Human LLLGTGESGKSTFIKQMRIIHGAGYSEEDKRGFTK----------LVYQNIFTAM 87
Mouse LLLGTGESGKSTFIKQMRIIHGAGYSEEDKRGFTK----------LVYQNIFTAM 87
Frog LLLGTGESGKSTFIKQMRIIHGSGYSEEDKKGFTK----------LVFQNIFTAM 87
Zebrafish LLLGTGESGKSTFIKQMRIIHGAGYTDEDKRGFTK----------LVYQNIFTSM 87
Chicken LLLGTGESGKSTFIKQMRIIHGSGYSEEDKKGFTK----------LVYQNIFTAM 87
GNAQ LLLGTGESGKSTFIKQMRIIHGSGYSDEDKRGFTK----------LVYQNIFTAM 87
GNAI1 LLLGAGESGKSTIVKQMKIIHEAGYSEEECKQYKA----------VVYSNTIQSI 81
GNAS LLLGAGESGKSTIVKQMRILHVNGFNGEGGEEDPQAARSNSDGEKATKVQDIKNNLKEAI 103
GNA12 LLLGAGESGKSTFLKQMRIIHGREFDQKALLEFRD----------TIFDNILKGS 105
Human QAMIRAMETLKILYKYEQNKANAL--LIRE-VD---VEKVTTFEHQYVSAIKTLWEDPGI 141
Mouse QAMVRAMETLKILYKYEQNKANAL--LIRE-VD---VEKVTTFEHQYVNAIKTLWSDPGV 141
Frog QSMIRAMETLKILYKYEQNKANAQ--VVRE-VD---VEKVCTFEQPYVNAIKNLWSDPGI 141
Zebrafish QAMIRATETLKIGYKYEQNKANAM--LVKE-VD---IEKVMSFDHPYINAVKMLWSDPGI 141
Chicken QSMIRAMETLKILYKYEQNKANAV--LIRE-VD---VEKVMTFEQPYVSAIKTLWNDPGI 141
GNAQ QAMIRAMDTLKIPYKYEHNKAHAQ--LVRE-VD---VEKVSAFENPYVDAIKSLWNDPGI 141
GNAI1 IAIIRAMGRLKIDFGDSARADDAR--QLFVLAG---AAEEGFMTAELAGVIKRLWKDSGV 136
GNAS ETIVAAMSNLVPPVELANPENQFRVDYILSVMN---VP-DFDFPPEFYEHAKALWEDEGV 159
GNA12 RVLVDARDKLGIPWQYSENEKHGM--FLMAFENKAGLPVEPATFQLYVPALSALWRDSGI 163
Human QECYDRRREYQLSDSAKYYLTDVDRIATLGYLPTQQDVLRVRVPTTGIIEYPFDLENIIF 201
Mouse QECYDRRREFQLSDSAKYYLTDVDRIATVGYLPTQQDVLRVRVPTTGIIEYPFDLENIIF 201
Frog QECYDRRREYQLSDSTKYYLTDVDRISKPGYLPTQQDVLRVRVPTTGIIEYPFDLENIIF 201
Zebrafish QEAYDRRREYQLSDSTKYYLSDLDRIAESSYLPTQQDVLRVRIPTTGIIEYPFDLQSIIF 201
Chicken QECYDRRREYQLSDSAKYYLSDVDRIATPGYLPTQQDVLRVRVPTTGIIEYPFDLENIIF 201
GNAQ QECYDRRREYQLSDSTKYYLNDLDRVADPAYLPTQQDVLRVRVPTTGIIEYPFDLQSVIF 201
GNAI1 QACFNRSREYQLNDSAAYYLNDLDRIAQPNYIPTQQDVLRTRVKTTGIVETHFTFKDLHF 196
GNAS RACYERSNEYQLIDCAQYFLDKIDVIKQADYVPSDQDLLRCRVLTSGIFETKFQVDKVNF 219
GNA12 REAFSRRSEFQLGESVKYFLDNLDRIGQLNYFPSKQDILLARKATKGIVEHDFVIKKIPF 223
Human RMVDVGGQRSERRKWIHCFENVTSIMFLVALSEYDQVLVESDNENRMEESKALFRTIITY 261
Mouse RMVDVGGQRSERRKWIHCFENVTSIMFLVALSEYDQVLVESDNENRMEESKALFRTIITY 261
Frog RMVDVGGQRSERRKWIHCFENVTSIMFLVALSEYDQVLVESDNENRMEESKALFRTIITY 261
Zebrafish RMVDVGGQRSERRKWIHCFENVTSIMFLVALSEYDQVLVESDNENRMEESKALFRTIITY 261
Chicken RMVDVGGQRSERRKWIHCFENVTSIMFLVALSEYDQVLVESDNENRMEESKALFRTIITY 261
GNAQ RMVDVGGQRSERRKWIHCFENVTSIMFLVALSEYDQVLVESDNENRMEESKALFRTIITY 261
GNAI1 KMFDVGGQRSERKKWIHCFEGVTAIIFCVALSDYDLVLAE-DEEMNRMHESMKLFDSICN 256
GNAS HMFDVGGQRDERRKWIQCFNDVTAIIFVVASSSYNMVIRE-DNQTNRLQEALNLFKSIWN 279
GNA12 KMVDVGGQRSQRQKWFQCFDGITSILFMVSSSEYDQVLME-DRRTNRLVESMNIFETIVN 283
Human -PWFQNSSVILFLNKKDLLEDKIL--YSHLVDYFPEFDGPQRD----------AQAAR 306
Mouse -PWFQNSSVILFLNKKDLLEDKIL--HSHLVDYFPEFDGPQRD----------AQAAR 306
Frog -PWFQNSSVILFLNKKDLLEDKIM--YSHLVDYFPEFDGPQRD----------AATAR 306
Zebrafish -PWFQNSSVILFLNKKDLLEEKIS--YSHLVDYFPEFDGPQRD----------AQAAR 306
Chicken -PWFQNSSVILFLNKKDLLEDKIL--YSHLVDYFPEFDGPQRD----------AQAAR 306
GNAQ -PWFQNSSVILFLNKKDLLEEKIM--YSHLVDYFPEYDGPQRD----------AQAAR 306
GNAI1 NKWFTDTSIILFLNKKDLFEEKIK--KSPLTICYPEYAGSNTY----------EEA-A 300
GNAS NRWLRTISVILFLNKQDLLAEKVLAGKSKIEDYFPEFARYTTPEDATPEPGEDPRVTRAK 338
GNA12 NKLFFNVSIILFLNKMDLLVEKVK--TVSIKKHFPDFRGDPHR----------LEDVQ 328
Human EFILKMFVDLNPD---SDKIIYSHFTCATDTENIRFVFAAVKDTILQLNLKEYNLV 359
Mouse EFILKMFVDLNPD---SDKIIYSHFTCATDTENIRFVFAAVKDTILQLNLKEYNLV 359
Frog EFILKMFVDLNPD---SDKIIYSHFTCATDTENIRFVFAAVKDTILQHNLKEYNLV 359
Zebrafish EFILKMFVDLNPD---SDKIIYSHFTCATDTENIRFVFAAVKDTILQLNLKEYNLV 359
Chicken EFILKMFVDLNPD---SDKIIYSHFTCATDTENIRFVFAAVKDTILQLNLKEYNLV 359
GNAQ EFILKMFVDLNPD---SDKIIYSHFTCATDTENIRFVFAAVKDTILQLNLKEYNLV 359
GNAI1 AYIQCQFEDLNKR--KDTKEIYTHFTCATDTKNVQFVFDAVTDVIIKNNLKDCGLF 354
GNAS YFIRDEFLRISTASGDGRHYCYPHFTCAVDTENIRRVFNDCRDIIQRMHLRQYELL 394
GNA12 RLVQCFDRK-RR--NRS-KPLFHHFTTAIDTENVRFVFHAVKDTILQENLKDIMLQ 381

Figure 4.2 Evolutionary conservation of 79 *GNA11* variants found in the dbSNP database in $G\alpha_{11}$ orthologs (mouse, frog, zebrafish, chicken) and Gα paralogs (*GNAQ*, *GNAI1*, *GNAS2*, *GNA12*). Identical residues are highlighted in green. Variants that were identical in all orthologs and at least 3 paralogs were considered to be conserved.

4.2.2 Structural characterisation using PyMOL

In order to assess the location of the variants, the 14 selected variants from the dbSNP and DiscovEHR databases were mapped to the sequence of *GNA11*. This showed that 4 variants were located in exon 5; 3 variants in exon 2; 2 variants in exons 3, 4 and 7, respectively; and 1 variant in exon 1 (Figure 4.3).

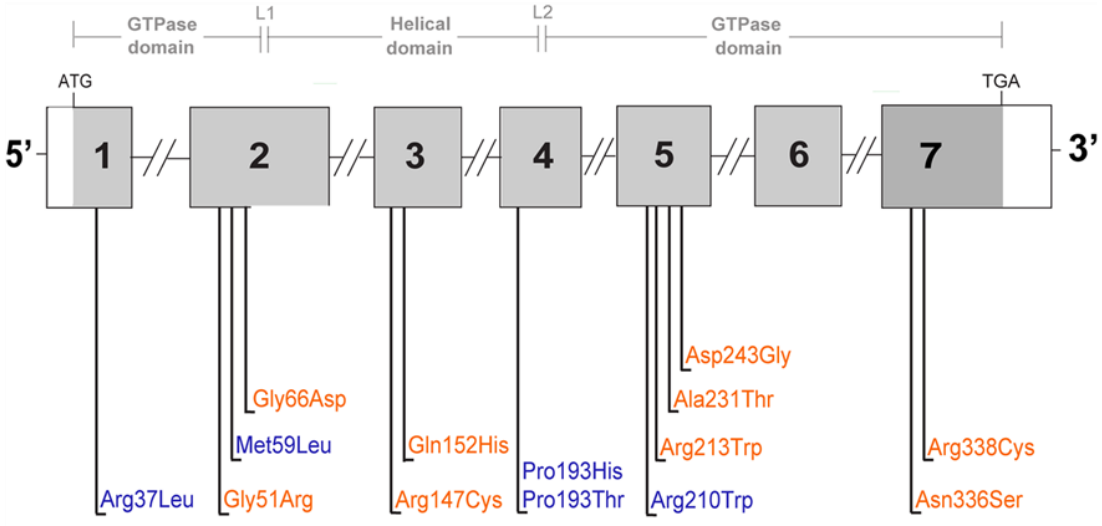


Figure 4.3 Rare *GNA11* variants selected from dbSNP (shown in orange) and the DiscoveEHR cohort (shown in blue) mapped to the 7 exomes of *GNA11*. The locations of the GTPase domain, helical domain, linker 1 (L1) and linker 2 (L2) are indicated.

Three-dimensional homology modelling in PyMOL (see methods section 4.2.2) was used to predict the effects of the *GNA11* variants on the structure of $G\alpha_{11}$ and its interaction with effectors. A full length crystal structure of $G\alpha_{11}$ is not available and I therefore built

a homology model based on the nucleotide-bound structure of the closely related $G\alpha_q$[38] which is 90% identical to $G\alpha_{11}$ (see 1.1.2.1)[9] using SWISS-MODEL[244-249]. This revealed that Gly51 forms hydrogen bonds with GDP, Thr54 (which is a known FHH2 residue[108]) and Phe55 in the α1 helix (Figure 4.4A). Arg51 is larger and predicted to form additional contacts with Asn274 and Thr329 in the ß5 sheet (Figure 4.4B). This indicates that Gly51Arg may disrupt G protein interaction with guanine nucleotides.

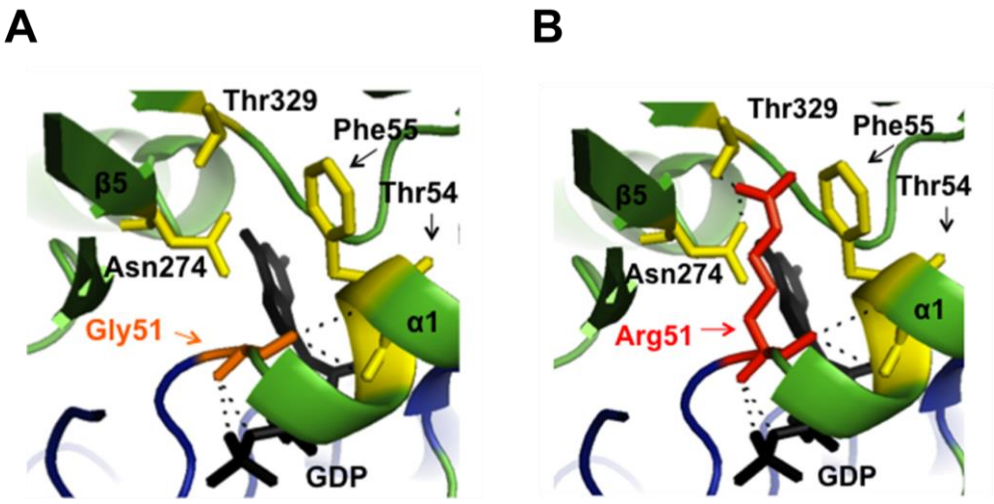


Figure 4.4 (A) Gly51 (orange) is forming hydrogen bonds with GDP (black), Thr54 and Phe55 in the α1 helix. (B) Arg51 (red) is larger and predicted to form additional contacts (shown in black dotted lines) with Asn274 and Thr329 in the ß5 sheet.

To further characterise the potential of the variants to disrupt downstream effector, GPCR and βγ function I analysed structures in complex with related G alpha subunits: $G\alpha_s$ in complex with B2AR[266] (Figure 4.5A) and $G\alpha_q$ in complex with $PLC\beta_3$[267] (Figure 4.5B) using PyMOL 2.3. These were used because structures of $G\alpha_{11}$ in complex with these effectors are not currently available. This revealed that the 14 selected *GNA11* variants were located in key regions of the Gα subunit: 4 variants (Gly51Arg, Met59Leu, Gly66Asp and Ala231Thr) were located in the interdomain interface that binds GDP and GTP; 3 variants (Arg147Cys, Gln152His, Asp243Gly) were located close to the flexible switch 3 region of the interdomain interface; 3 variants (Asn336Ser, Arg338Cys,

Arg37Leu) were located in the α5 and αN helices which are important for GPCR interaction; and 4 variants (Pro193His, Pro193Thr, Arg210Trp, Arg213Trp) were located at the Gα-Gβγ and PLC interaction sites.

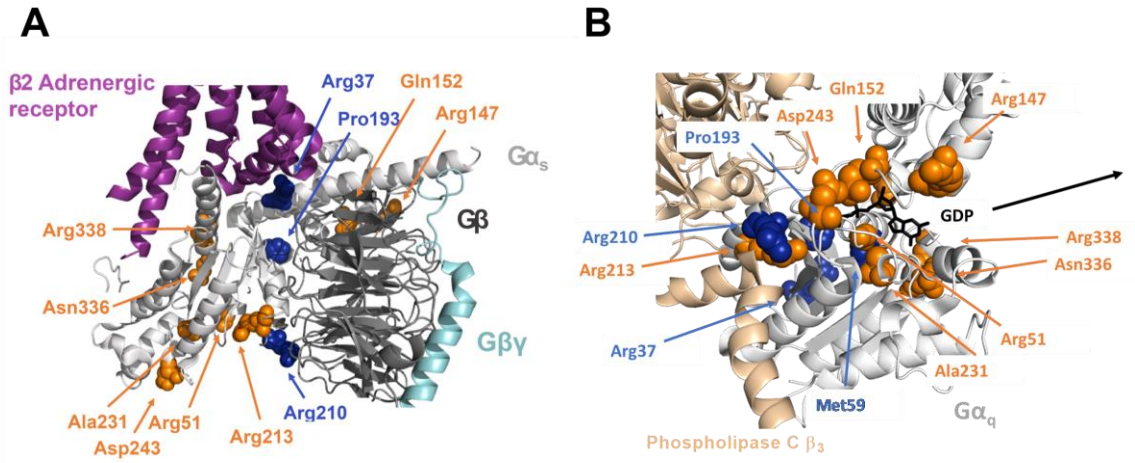


Figure 4.5 (A) Crystal structure (PDB code 3sn6) of B2AR (purple) in complex with $G\alpha_s$ (light grey) Gβ (dark grey) and Gγ (turquoise). Selected $G\alpha_{11}$ variants are shown as their equivalent residues in $G\alpha_s$. (B) Crystal structure (PDB code 4gnk) of $PLC\beta_3$ (beige) in complex with $G\alpha_q$ (light grey). Selected $G\alpha_{11}$ variants are shown as their equivalent residues in $G\alpha_q$. Variants found in dbSNP are shown in orange, DiscovEHR variants are shown in blue, GDP is shown in black.

The structure of the GTPase domain of $G\alpha_{11}$ in complex with the M_1R has recently been solved[67]. Analysis of variants that are located in this domain revealed that Arg37 forms hydrogen bonds with Arg134 and Ala135 in the intracellular loop 2 (ICL2) of the receptor (Figure 4.6A). This interaction is predicted to be disrupted by Leu37 (Figure 4.6B). Moreover, in the structure of $G\alpha_q$ in complex with $PLC\beta_3$[267] the Arg210 and Arg213 form hydrogen bonds with Asn861 and Leu859 of PLC, respectively (Figure 4.6C), and these interactions are predicted to be lost for Trp210 and Trp213 (Figure 4.6D). Taken together these data indicate that the identified variants are likely to disrupt $G\alpha_{11}$ function.

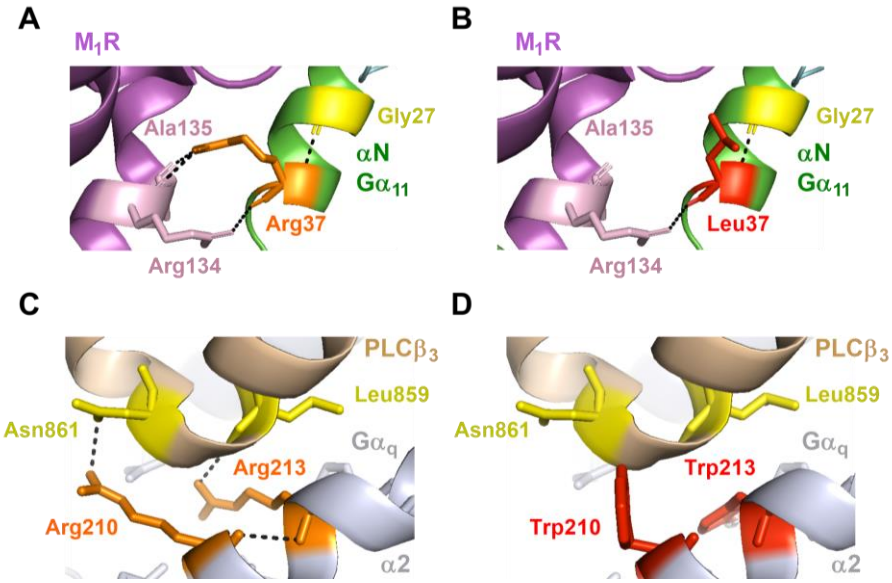


Figure 4.6 (A) Arg37 (orange) in the αN helix of Gα11 (green) forms polar contacts (black, dashed lines) with Arg134 and Ala135 (light pink) of M_1R (purple) (PDB code 6OIJ). (B) This interaction is predicted to be disrupted for Leu37 (red). (C) Arg210 and Arg213 (orange) in the α2 helix of $G\alpha_q$ (grey), which are equivalent to Arg210 and Arg213 in Gα11, form polar contacts (black, dashed lines) with Asn861 and Leu859 (light pink) of PLCß3 (beige), respectively (PDB code 4gnk). (D) The interactions are predicted to be disrupted for Trp210 and Trp213 (red).

4.2.3 Expression of selected $G\alpha_{11}$ variants.

To study the consequences of the 14 selected *GNA11* missense variants (Arg37Leu, Gly51Arg, Met59Leu, Gly66Asp, Arg147Cys, Gln152His, Pro193His, Pro193Thr, Arg210Trp, Arg213Trp, Ala231Thr, Asp243Gly, Asn336Ser, and Arg338Cys) *in vitro*, I performed site-directed mutagenesis (see methods 3.6.1) using an existing pBI-CMV2-*GNA11* bidirectional vector which allows simultaneous expression of green fluorescent protein (GFP) and Gα11[93]. I confirmed successful transfection of WT and mutant constructs using Immunofluorescence microscopy (Figure 4.7E) (methods section 3.7.2). Moreover, I assessed protein expression using Western blot analysis (Figure 4.7A,B) (methods 3.7.1). Quantification of 3 independent Western blots (Figure 4.7C,D) showed that all 14 variants were expressed at similar levels to WT Gα11.

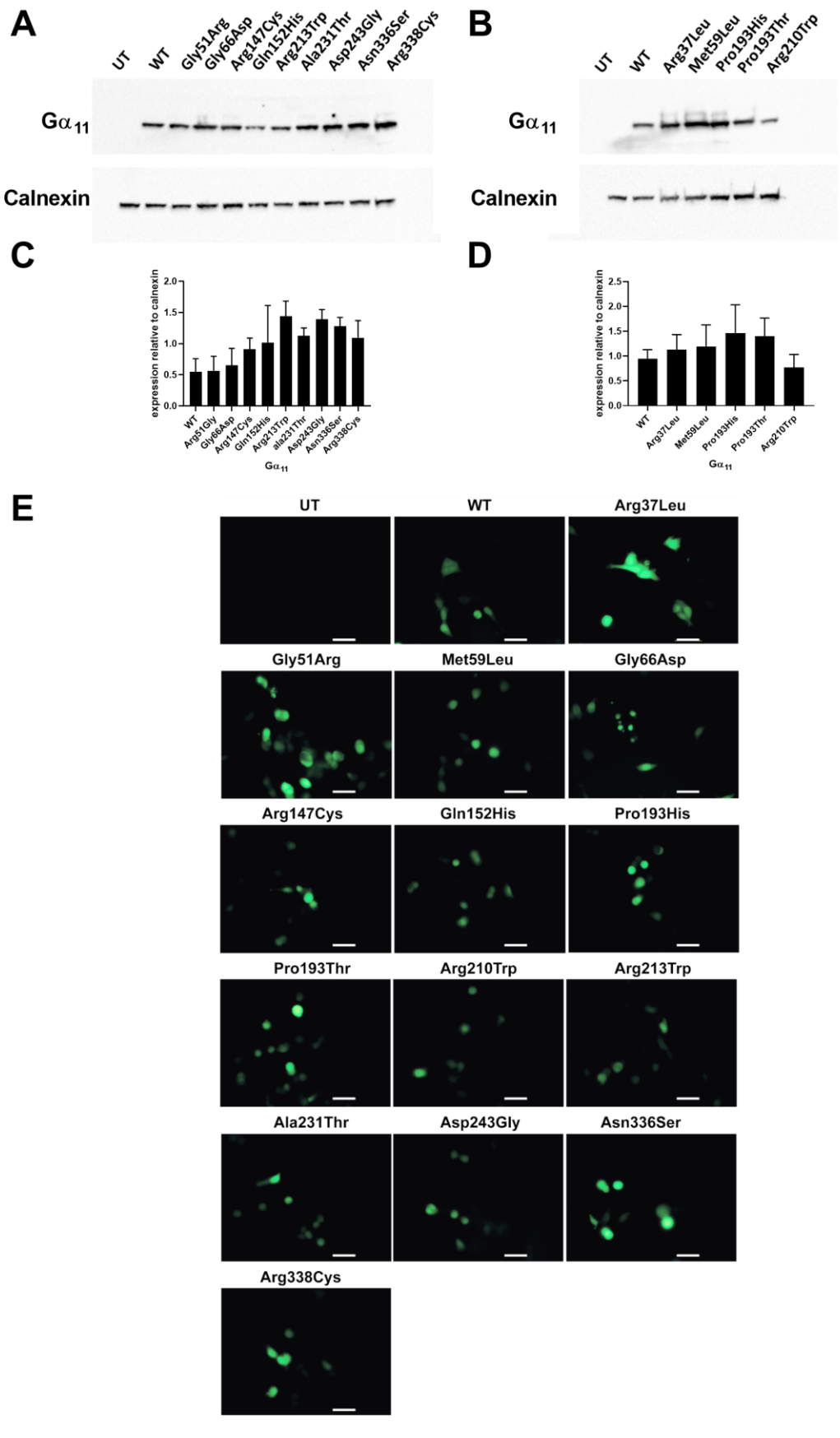

A
UT
WT
Gly51Arg
Gly66Asp
Arg147Cys
Gln152His
Arg213Trp
Ala231Thr
Asp243Gly
Asn336Ser
Arg338Cys
Gα11
Calnexin
B
UT
WT
Arg37Leu
Met59Leu
Pro193His
Pro193Thr
Arg210Trp
Gα11
Calnexin
C
expression relative to calnexin
2.0
1.5
1.0
0.5
0.0
WT
Arg51Gly
Gly66Asp
Arg147Cys
Gln152His
Arg213Trp
ala231Thr
Asp243Gly
Asn336Ser
Arg338Cys
Gα11
D
expression relative to calnexin
2.5
2.0
1.5
1.0
0.5
0.0
WT
Arg37Leu
Met59Leu
Pro193His
Pro193Thr
Arg210Trp
Gα11
E
UT
WT
Arg37Leu
Gly51Arg
Met59Leu
Gly66Asp
Arg147Cys
Gln152His
Pro193His
Pro193Thr
Arg210Trp
Arg213Trp
Ala231Thr
Asp243Gly
Asn336Ser
Arg338Cys

Figure 4.7 (A) Protein expression of selected *GNA11* variants from dbSNP, assessed by Western blot analysis. (B) Protein expression of selected *GNA11* variants from the DiscovEHR cohort, assessed by Western blot analysis. (C) Quantification of n=3 Western blots of dbSNP variants, represented as mean+/-SEM. (D) Quantification of n=3 Western blots of DiscovEHR cohort variants. (E) Immunofluorescence microscopy of untransfected (UT) cells and cells transfected with wild-type (WT) and variant pBI-CMV2-*GNA11* constructs. GFP expression (green) shows successfully transfected cells. Scale bar = 20 μM.

4.2.4 Effects of rare $G\alpha_{11}$ variants on CaSR signalling

The effects of the variants on CaSR-mediated signalling were assessed using Serum Response Element (SRE) and Nuclear Factor of Activated T-cells Response Element (NFAT-RE) luciferase reporter assays (see methods 3.8.1), which are downstream readouts of calcium mobilisation and MAPK (illustrated in Figure 4.8). To exclude any contributions of endogenous $G\alpha_{q/11}$, luciferase reporter assays were performed in HEK293A cells, modified by CRISPR/CAS9 to lack expression of endogenous $G\alpha_q$ or $G\alpha_{11}{}^{209}$, and stably express the CaSR (HEK293A$G\alpha_{q/11}$-KO-CaSR cells). WT or variant $G\alpha_{11}$ were transiently transfected into HEK293A$G\alpha_{q/11}$-KO-CaSR cells, and luciferase reporter activity in response to increasing concentrations of $Ca^{2+}{}_e$ was measured.

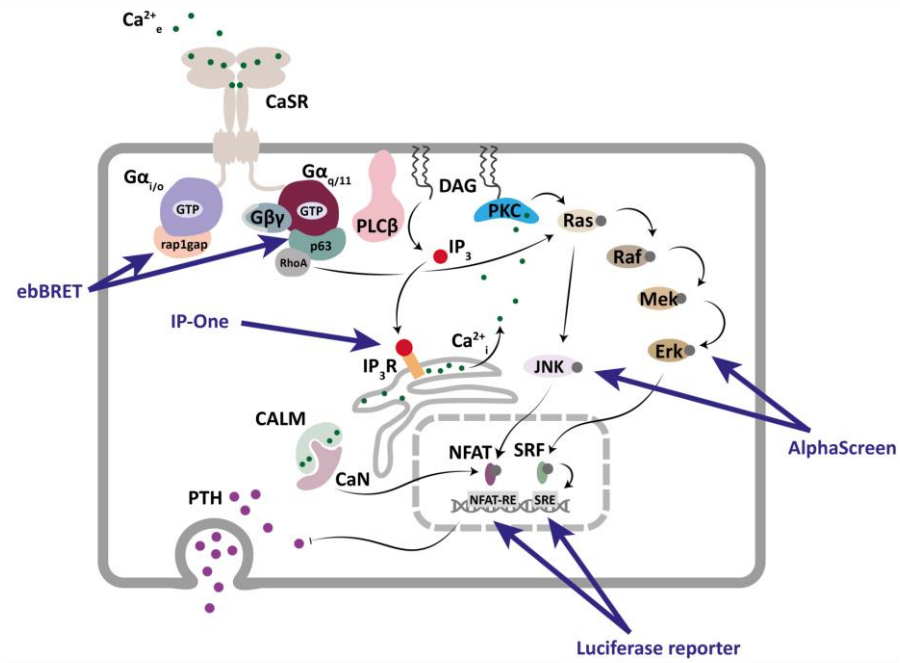


Figure 4.8 Overview of CaSR-mediated signalling and downstream assays[28,77,227]. Stimulation of the calcium-sensing receptor (CaSR) by extracellular calcium (Ca^{2+}_e) leads to GTP binding by $G\alpha_{q/11}$, which leads to dissociation of Gα from Gβγ. $G\alpha_{q/11}$ then interacts with phospholipase C beta (PLCß) which catalyses hydrolysis of Phosphatidylinositol 4,5-bisphosphate (PIP_2) to diacylglycerol (DAG) and Inositol trisphosphate (IP_3), which is then further hydrolysed to IP_1 and was measured using IP-One assays. IP_3 binds IP_3 receptors (IP_3R) to release calcium from intracellular stores. Both calcium and DAG activate Proteinkinase C (PKC), which leads to phosphorylation of Ras, Raf, Mek, and Erk. Calcium also induces calcineurin (CaN) binding of calmodulin (CALM) which induces the transcription factor Nuclear Factor of Activated T-cells (NFAT) which binds to Nuclear Factor of Activated T-cells Response Element (NFAT-RE). GTP-bound $G\alpha_{q/11}$ and $G\alpha_{i/o}$ also recruit p63 and rap1gap, respectively, which can be measured using ebBRET assays. P63 interacts with RhoA which activates the Ras-JNK pathway. Phosphorylated Erk and JNK were detected using AlphaScreen assays. Moreover, JNK and Erk can activate NFAT-RE and Serum Response Element (SRE), respectively, which were detected using luciferase reporter assays. Transcriptional changes lead to inhibition of parathyroid hormone (PTH) secretion.

4.2.4.1 Benign Variants

Three variants from dbSNP (Asp243Gly, Asn336Ser and Arg338Cys) and 3 variants from the DisvovEHR cohort (Met59Leu, Pro193His, Pro193Thr) showed no differences in CaSR mediated SRE and NFAT luciferase reporter activity (Figure 4.9). Moreover, mean plasma calcium values of individuals with Met59Leu, Pro193His and Pro193Thr variants in the DiscovEHR cohort were in the normal range (Table 4.1). These findings indicate that the variants are benign polymorphisms.

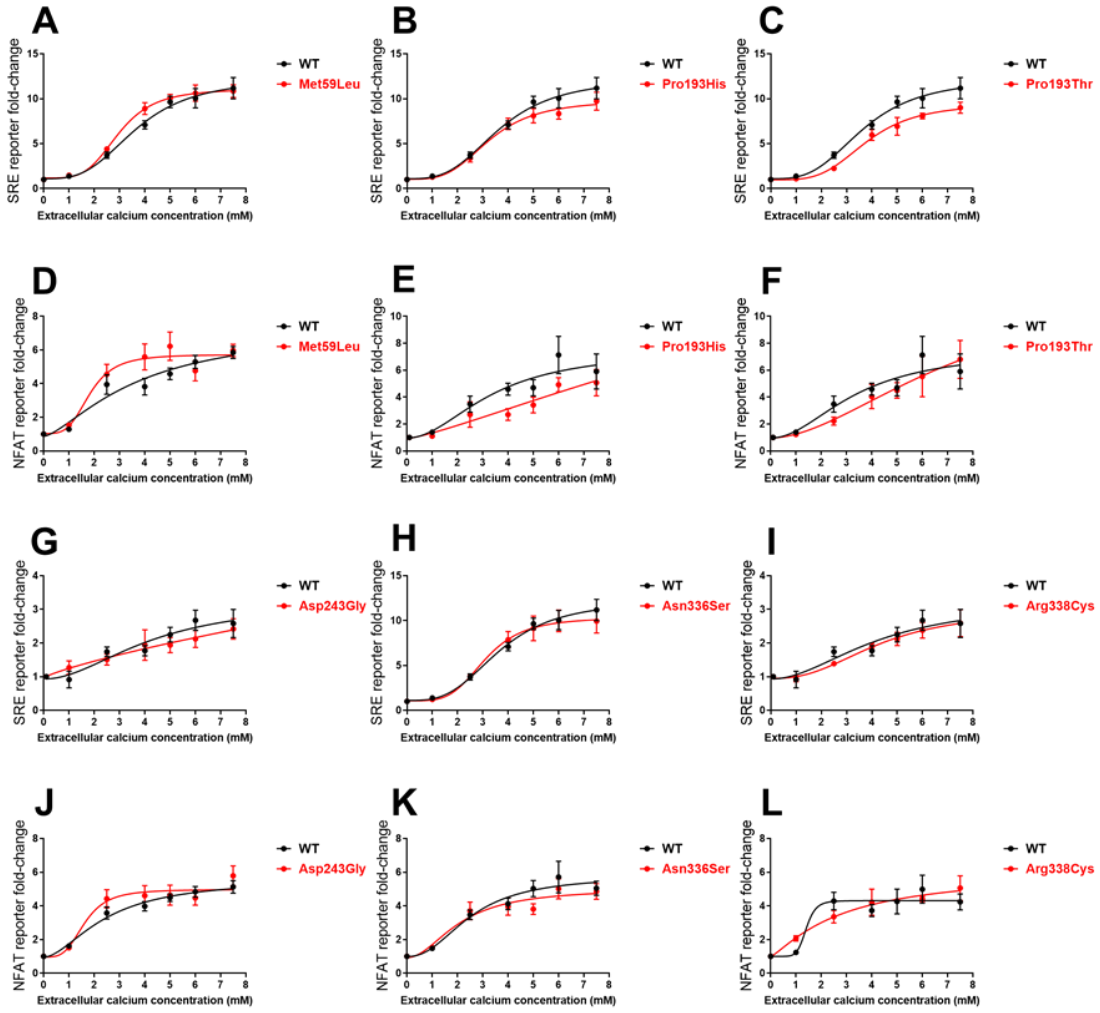


Figure 4.9 Six *GNA11* variants did not affect CaSR signalling in SRE and NFAT-RE luciferase reporter assays: (A,D) Met59Leu, (B,E) Pro193His, (C,F) Pro193Thr, (G,J) Asp243Gly, (H,K) Asn336Ser and (I,L) Arg338Cys. Values are shown as mean±SEM of 3-4 independent transfections.

4.2.4.2 Loss-of-function variants in the DiscovEHR cohort

$G\alpha_{11}$ Arg37Leu and Arg210Trp were associated with mild hypercalcaemia (mean plasma calcium >10mg/dL) (Table 4.1) in the DiscovEHR cohort and resulted in significantly decreased responses in SRE (Figure 4.10A,D) and NFAT-RE luciferase reporter assays (Figure 4.10B,E) of up to 2.8-fold ($p<0.0001$), and 6.5-fold ($p<0.0001$), respectively. The variants were further characterised in ebBRET assays (see methods 3.8.6), which measure the recruitment of p63 to the membrane (tagged with rGFP-CAAX) upon $G\alpha_{11}$ activation[166] (Figure 4.10C,F). EbBRET assays were performed in HEK293-Flp-In-Flag-CaSR cells which endogenously express $G\alpha_{q/11}$, thereby approximating the heterozygous situation in the patient.

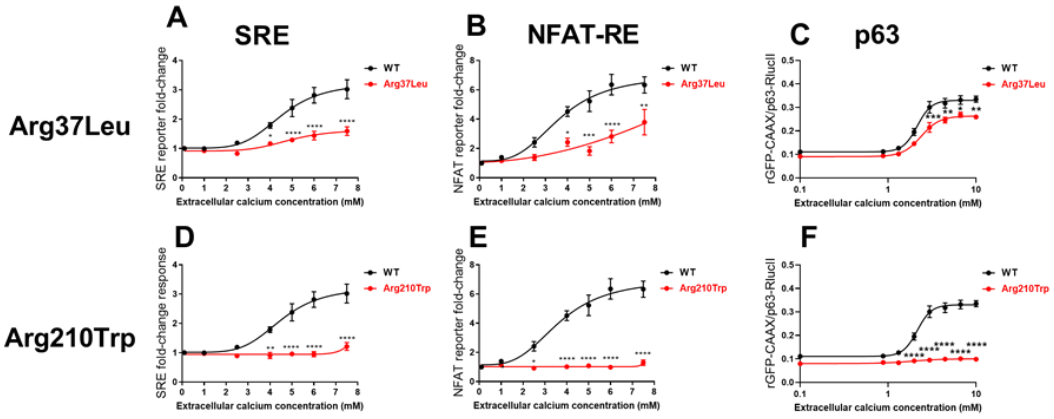


Figure 4.10 Dose-response curves of HEK293AG$\alpha_{q/11}$-KO-CaSR cells (A,B,D,E) and (C,F) HEK293-Flp-In-Flag-CaSR cells transiently transfected with either WT (black) or variant (red) $G\alpha_{11}$. Arg37Leu shows significantly lower calcium-induced responses compared to WT in (A) SRE luciferase reporter assays, (B) NFAT-RE luciferase reporter assays and (C) ebBRET p63 recruitment assays. Similarly, Arg210Trp shows significantly lower calcium-induced responses compared to WT in (D) SRE luciferase reporter assays, (E) NFAT-RE luciferase reporter assays and (F) p63 recruitment ebBRET assays. Values are shown as mean±SEM of 3-4 independent transfections. Two-way ANOVA with Sidak correction for multiple comparisons was performed using GraphPad Prism 8.4.1. *$p<0.05$, **$p<0.01$, ***$p<0.001$, ****$p<0.0001$.

In these assays, the Arg37Leu and Arg210Trp also resulted in significantly reduced responses (up to 1.4-fold, p<0.001, and up to 3.4-fold, p<0.0001, respectively), compared to WT $G\alpha_{11}$. Together these data indicate that *GNA11* Arg37Leu and Arg210Trp likely represent novel FHH2-causing mutations.

4.2.4.3 Loss-of-function variants in dbSNP

$G\alpha_{11}$ Gly51Arg and Arg213Trp showed decreased luciferase reporter activity in SRE and NFAT-RE luciferase reporter assays compared to WT $G\alpha_{11}$ (Figure 4.11A,B,D,E) of up to 3.5-fold (p<0.0001) and 4.2-fold (p<0.0001), respectively. Moreover, they showed significantly reduced responses (up to 3.6-fold, p<0.0001, and up to 3.4-fold, p<0.0001, respectively) in p63 ebBRET assays compared to WT $G\alpha_{11}$ (Figure 4.11C,F). This indicates that Gly51Arg and Arg213Trp are likely FHH2-causing mutations, however confirmatory phenotype data of the patients in this database is not available.

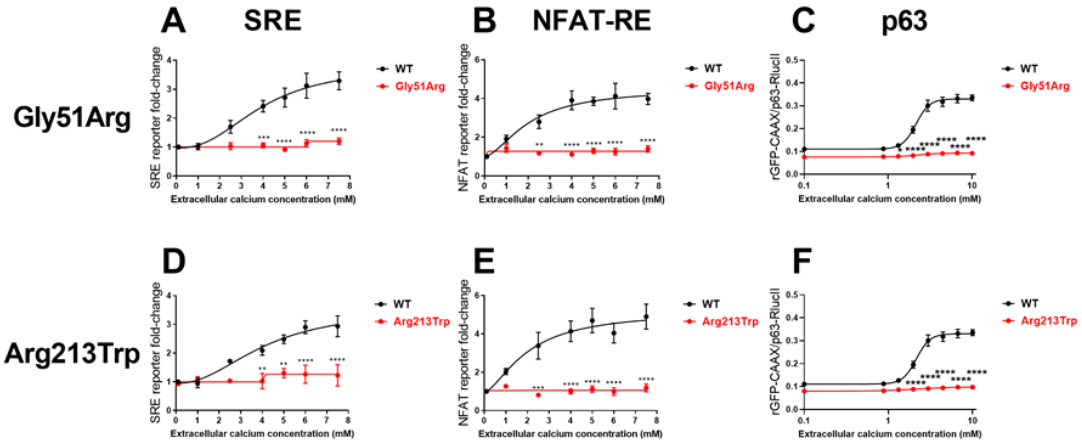


Figure 4.11 Dose-response curves of HEK293AG$\alpha_{q/11}$-KO-CaSR cells (SRE, NFAT-RE) and HEK293-Flp-In-Flag-CaSR cells (p63) expressing either WT (black line) or variant (red line) $G\alpha_{11}$. Gly51Arg and Arg213Trp show significantly decreased responses compared to WT in (A,D) SRE, (B,E) NFAT-RE assays and p63 recruitment ebBRET assays (C,F). Values are shown as mean±SEM of 3-4 independent transfections. Two-way ANOVA with Sidak correction was performed using GraphPad Prism 8.4.1. **p<0.01, ***p<0.001, ****p<0.0001.

Additionally, I assessed the effects of Gly51Arg LOF in GTPase Glo assays (see methods section 3.8.3), because this variant is predicted to disrupt Gα interaction with guanine nucleotides. This revealed that Gly51Arg resulted in significantly reduced GTPase activity compared to WT $G\alpha_{11}$ (Figure 4.12).

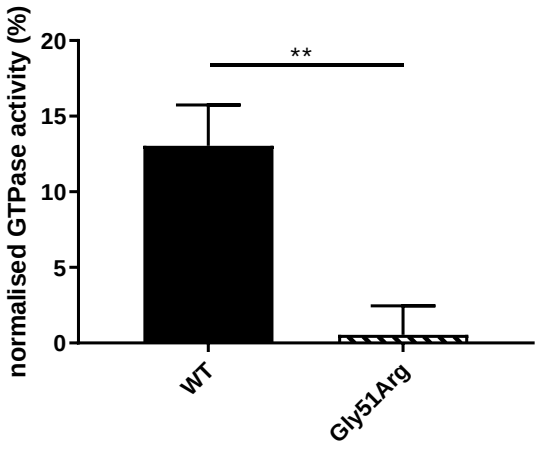


Figure 4.12 GTPase activity of $G\alpha_{11}$ Gly51Arg was significantly reduced, compared to WT $G\alpha_{11}$. Values are shown as mean±SEM of 4 independent transfections. An unpaired t-test was performed using GraphPad Prism 8.4.1. **p<0.01.

4.2.4.4 Gain-of-function variants in dbSNP

One variant, Gln152His, resulted in significantly increased SRE and NFAT-RE luciferase reporter activity (Figure 4.13A,B) by up to 1.6-fold ($p<0.05$). However, responses were not significantly different from WT in ebBRET assays which were conducted in cells expressing endogenous $G\alpha_{q/11}$ (Figure 4.13C). This indicates that Gln152His is probably benign, though it may be pathogenic if it occurs in a homozygous state, as represented in the SRE and NFAT-RE assays. The phenotypic information of the participant is not available in the database.

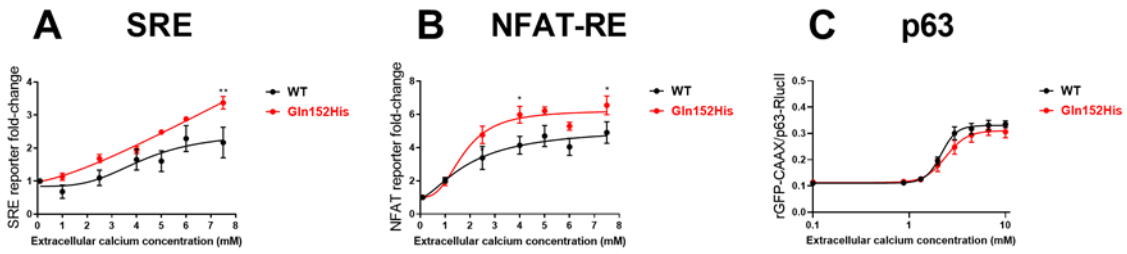


Figure 4.13 Gln152His (red line) shows significantly increased calcium-induced responses compared to WT (black line) in (A) SRE and (B) NFAT-RE luciferase reporter assays. In contrast, no significant difference was observed in (C) ebBRET p63 recruitment assays, indicating it is may be a mild gain-of-function mutation. Values are shown as mean±SEM of 3-4 independent transfections. Two-way ANOVA with Sidak correction for multiple comparisons was performed using GraphPad Prism 8.4.1. *p<0.05, **p<0.01.

4.2.4.5 Biased variants

Three of the variants found in dbSNP/gnomAD online databases (Gly66Asp, Arg147Cys, Ala231Thr) were found to have different effects on CaSR-mediated Ca^{2+}_e induced SRE and NFAT-RE transcription (Figure 4.14). Ala231Thr (Figure 4.14C) significantly reduced (by up to 2.3-fold ($p<0.01$)) SRE luciferase response activity, while Gly66Asp and Arg147Cys (Figure 4.14A-B) did not significantly affect SRE luciferase response activity. However, all 3 variants significantly increased NFAT-RE luciferase reporter activity, by up to 1.6-fold ($p<0.0001$), up to 1.7-fold ($p<0.0001$) and up to 2.4-fold ($p<0.001$), respectively (Figure 4.14A-C).

I hypothesised that these variants might promote biased signalling upstream of SRE and NFAT-RE, and therefore undertook 5 additional CaSR signalling assays to further characterise the effects of these variants in response to increasing concentrations of Ca^{2+}_e: ebBRET (p63 recruitment), ebBRET (rap1gap recruitment), p-ERK1/2 AlphaScreen, p-JNK1/2/3 AlphaScreen, and IP-One (HTRF®) (illustrated in Figure 4.7).

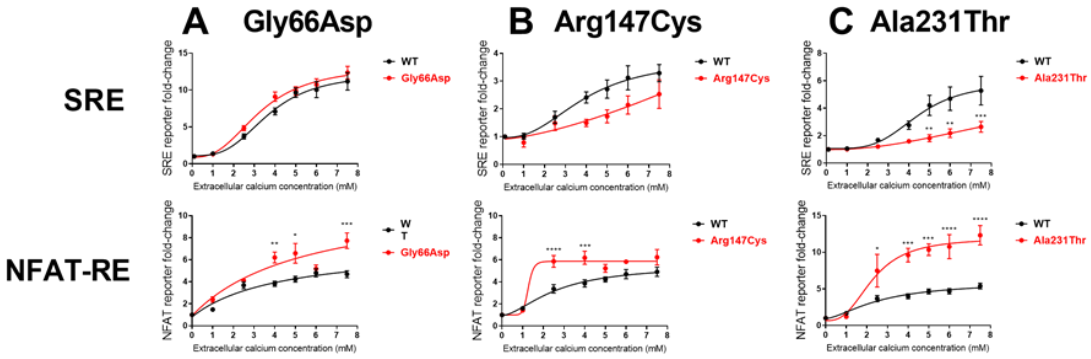


Figure 4.14 (A) CaSR-mediated signalling responses of $G\alpha_{11}$ Gly66Asp. NFAT-RE responses were significantly increased. In contrast, no significant difference was observed for SRE luciferase reporter assays. (B) CaSR-mediated signalling responses of $G\alpha_{11}$ Arg147Cys. NFAT-RE responses were significantly increased whereas no significant change was observed for SRE assays. (C) CaSR-mediated signalling responses of $G\alpha_{11}$ Ala231Thr. NFAT-RE responses were significantly increased. In contrast, SRE luciferase reporter assays were significantly decreased. Values are shown as mean±SEM of 3-12 independent transfections. Two-way ANOVA with Sidak correction for multiple comparisons was performed using GraphPad Prism 8.4.1. *p<0.05, **p<0.01, ***p<0.001, ****p<0.0001.

This revealed distinct molecular phenotypes for each variant. $G\alpha_{11}$ Gly66Asp significantly increased p63 recruitment by up to 1.4-fold ($p<0.05$) compared to WT, and p-ERK1/2 by up to 1.7-fold ($p<0.001$) (Figure 4.15A). $G\alpha_{11}$ Arg147Cys significantly decreased p63 recruitment by up to 1.7-fold ($p<0.0001$), and increased p-ERK1/2 by up to 1.6-fold ($p<0.001$) (Figure 4.15B). $G\alpha_{11}$ Ala231Thr significantly decreased p63 recruitment by up to 3.0-fold ($p<0.0001$), and decreased IP_1 by up to 1.4-fold ($p<0.001$), but increased p-JNK1/2/3 by up to 2.2-fold ($p<0.0001$) (Figure 4.15C). Moreover, $G\alpha_{11}$ Gly66Asp, Arg147Cys and Ala231Thr increased rap1gap recruitment, which reflects $G\alpha_{i/o}$-mediated signalling, by up to 1.2-fold ($p<0.001$), 1.2-fold ($p<0.05$) and 1.2-fold ($p<0.01$) compared to WT $G\alpha_{11}$, respectively. Notably, $G\alpha_q$ Gly66Asp (which is equivalent to $G\alpha_{11}$ Gly66Asp and was used as a control) also caused gain-of-function (Figure 4.16).

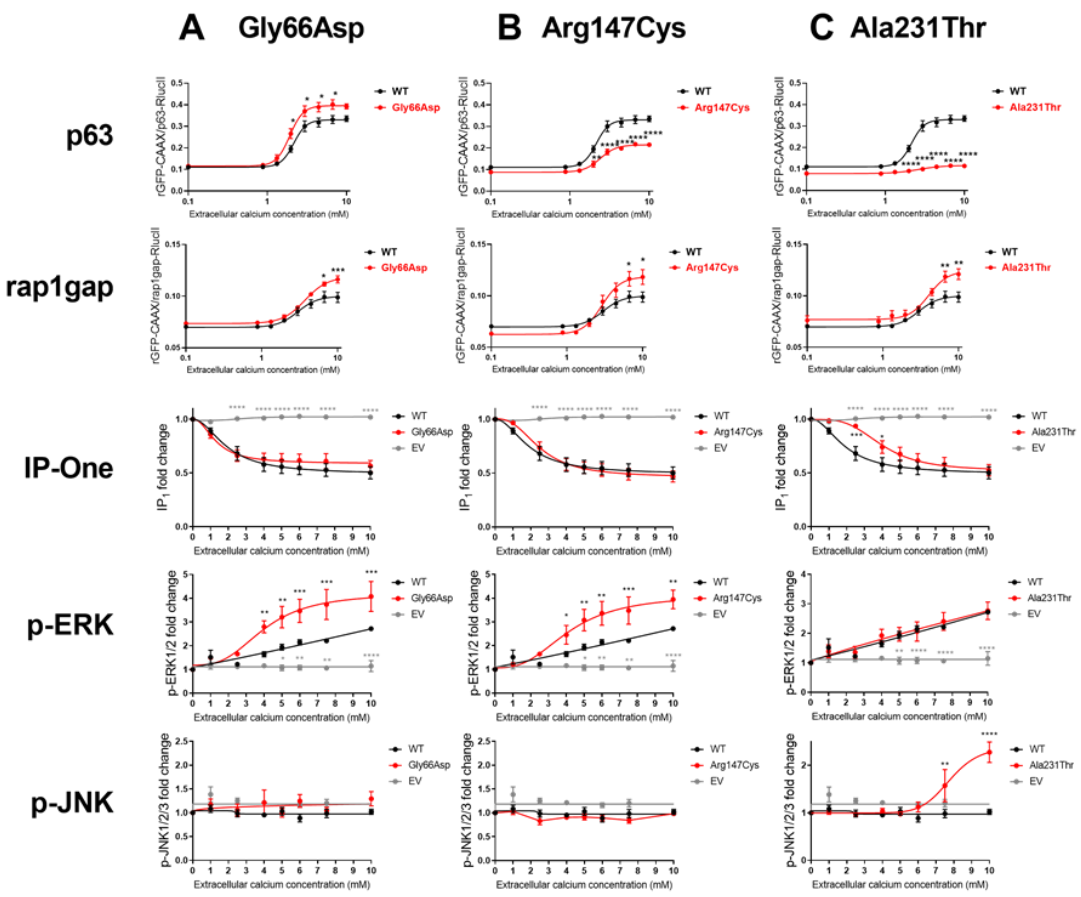


Figure 4.15 (A) CaSR-mediated signalling responses of $G\alpha_{11}$ Gly66Asp. P63 and rap1gap ebBRET assays, and p-ERK AlphaScreen responses were significantly increased. In contrast, no significant difference was observed for IP-One (HTRF®) assays and p-JNK AlphaScreen assays. (B) CaSR-mediated signalling responses of $G\alpha_{11}$ Arg147Cys. Rap1gap, and p-ERK AlphaScreen responses were significantly increased. In contrast, p63 responses were significantly decreased. No significant change was observed for IP-One assays and p-JNK AlphaScreen assays. (C) CaSR-mediated signalling responses of $G\alpha_{11}$ Ala231Thr. Rap1gap and p-JNK AlphaScreen responses were significantly increased. In contrast, p63 assays and IP-One assay were significantly decreased. No significant difference was observed for p-ERK AlphaScreen assays. Values are shown as mean±SEM of 3-4 independent transfections. For assays that show high variability (IP-One, p-ERK, p-JNK) an empty vector (EV) control was included in each experiment. Two-way ANOVA with Sidak correction for multiple comparisons was performed using GraphPad Prism 8.4.1. *p<0.05, **p<0.01, ***p<0.001, ****p<0.0001.

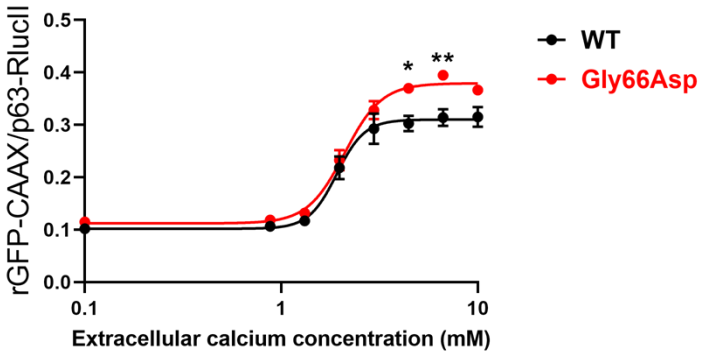


Figure 4.16 CaSR-mediated P63 ebBRET responses of $G\alpha_q$ Gly66Asp were significantly increased. Values are shown as mean±SEM of 3 independent transfections. Two-way ANOVA with Sidak correction for multiple comparisons was performed using GraphPad Prism 8.4.1. *p<0.05, **p<0.01.

4.2.5 Effects on GPCRs other than CaSR

Due to the ubiquitous expression of $G\alpha_{11}$ and its interaction with many GPCRs[6,9], I hypothesised that the identified CaSR-disrupting $G\alpha_{11}$ mutations may also disrupt signalling by other GPCRs. I therefore investigated the IUPHAR/BPS Guide to PHARMACOLOGY[252] and GPCRdb[253] databases for receptors that may be affected. This revealed a total of 94 receptors that have been reported to couple primarily to $G\alpha_{q/11}$ and a further 28 receptors for which secondary coupling to $G\alpha_{q/11}$ has been observed (Figure 4.17A). Of the primarily $G\alpha_{q/11}$ coupled receptors, the majority (85) were class A receptors, 6 were class B receptors and one was a class F receptor. They cover a broad range of endogenous ligands, including peptides, lipids, aminergic neurotransmitters, nucleotides and ions (Figure 4.17B). I selected the muscarinic acetylcholine receptor M_3 (M_3R) as a primarily $G\alpha_{q/11}$ coupled receptor, which, like $G\alpha_{11}$, is widely expressed in the central nervous system (CNS) and the periphery, whereas the M_1 and M_5 receptors are predominantly expressed in the CNS[81,268,269].

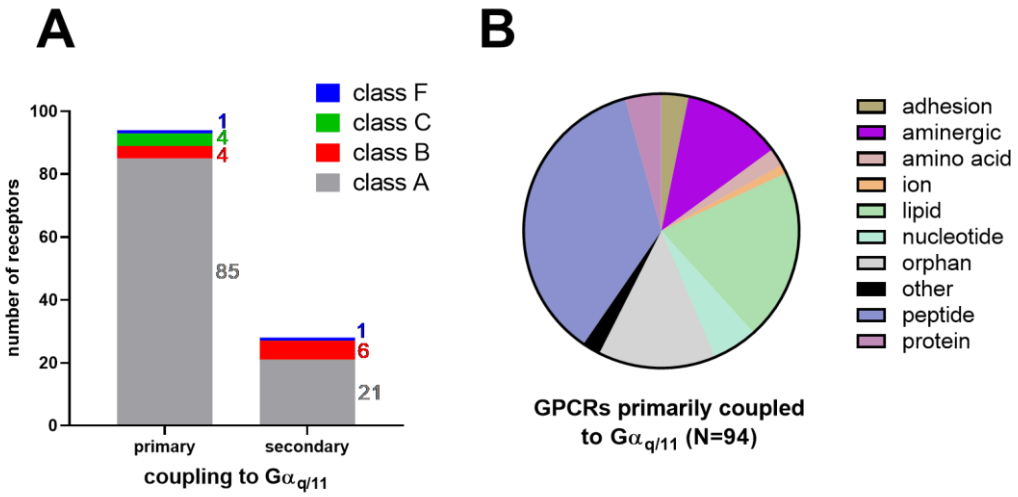


Figure 4.17 (A) Analysis of $G\alpha_{q/11}$ coupled receptors in the IUPHAR/BPS Guide to PHARMACOLOGY/GPCRdb[252,253]. Class F receptors are shown in blue. Class C receptors are shown in green. Class B receptors are shown in red. Class A receptors are shown in grey. (B) Endogenous ligands of primarily $G\alpha_{q/11}$ coupled receptors in the IUPHAR/BPS Guide to PHARMACOLOGY.

4.2.5.1 M_3R mediated signalling

I used acetylcholine as a ligand to study the effects of the identified $G\alpha_{11}$ mutants on M_3R signalling using p63 recruitment ebBRET assays. This revealed that the $G\alpha_{11}$ mutations Gly51Arg, Arg210Trp and Arg213Trp, which disrupt CaSR signalling, also disrupt signalling by the M_3R compared to WT $G\alpha_{11}$ by up to 4.5-fold ($p<0.0001$), up to 3.8-fold ($p<0.0001$), and up to 4.1-fold ($p<0.0001$), respectively (Figure 4.18A-C). In contrast, $G\alpha_{11}$ Arg37Leu, which disrupts CaSR signalling, had no effect on M_3R-mediated ebBRET responses (Figure 4.18D).

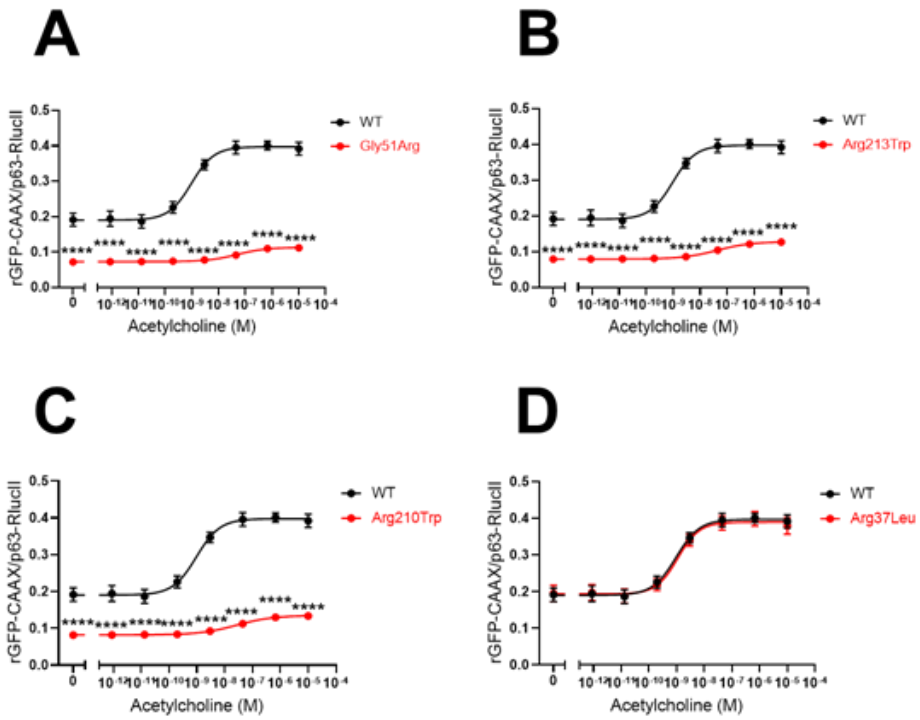


Figure 4.18 M_3R mediated p63 recruitment in response to acetylcholine was significantly decreased for (A) $G\alpha_{11}$ Gly51Arg (B) $G\alpha_{11}$ Arg213Trp and (C) $G\alpha_{11}$ Arg210Trp. In contrast, no significant difference was observed for (D) $G\alpha_{11}$ Arg37Leu. Values are shown as mean±SEM of 4 independent transfections. Two-way ANOVA with Sidak correction for multiple comparisons was performed using GraphPad Prism 8.4.1. ****p<0.0001.

Moreover, the Gln152His variant, which shows increased CaSR-mediated SRE and NFAT-RE luciferase reporter activity in HEK293AGq/11-KO-CaSR cells but not in CaSR-mediated p36 ebBRET assays, was not significantly different from WT $G\alpha_{11}$ (Figure 4.19).

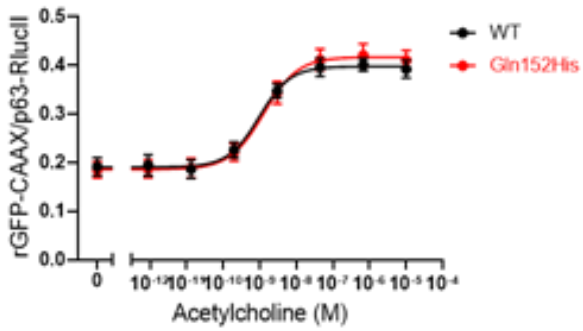


Figure 4.19 M_3R-mediated p63 recruitment in response to acetylcholine of $G\alpha_{11}$ Gln152His. No significant differences compared to WT were observed. Values are shown as mean±SEM of 4 independent transfections.

In addition, $G\alpha_{11}$ Arg147Cys and Ala231Thr significantly decreased M_3R-mediated p63 recruitment by up to 1.8-fold ($p<0.001$) and up to 3.8-fold ($p<0.0001$), respectively, which was similar to the changes observed for CaSR (Figure 4.20B,C). In contrast, $G\alpha_{11}$ Gly66Asp and the control $G\alpha_q$ Gly66Asp, which caused gain-of-function CaSR signalling, did not significantly alter M_3R responses (Figure 4.20A,D).

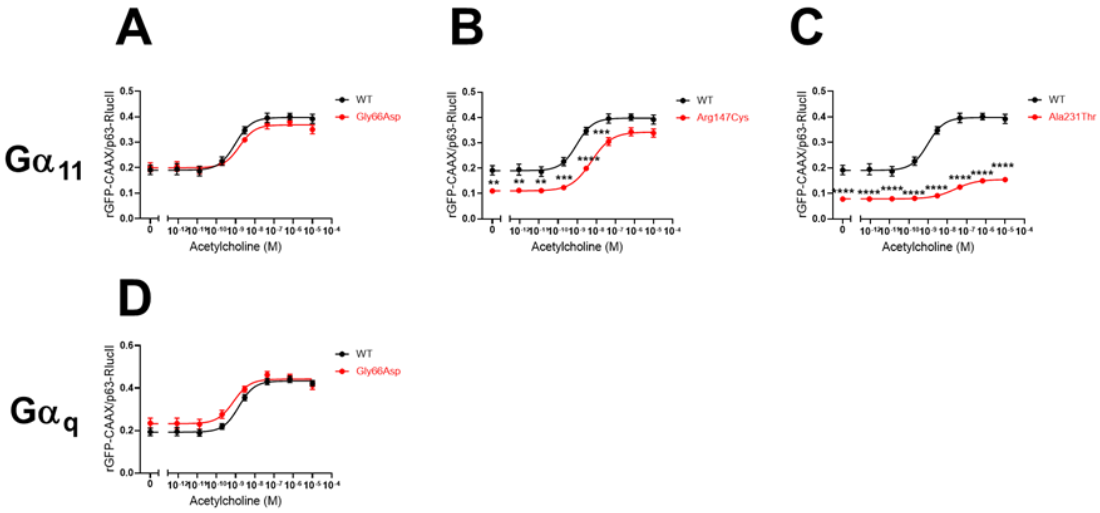


Figure 4.20 M_3R mediated p63 recruitment in response to acetylcholine of (A) $G\alpha_{11}$ Gly66Asp (B) $G\alpha_{11}$ Arg147Cys (C) $G\alpha_{11}$ Ala231Thr and (D) $G\alpha_q$ Gly66Asp. Values are shown as mean±SEM of 4 independent transfections. Two-way ANOVA with Sidak correction for multiple comparisons was performed using GraphPad Prism 8.4.1. **p<0.01, ***p<0.001, ****p<0.0001.

4.2.5.2 Promiscuous properties of "biased" variants

$G\alpha_q$ Gly66Asp, which is equivalent to $G\alpha_{11}$ Gly66Asp, has previously been reported to make the G protein alpha subunit promiscuous[23]. I therefore studied the effects of $G\alpha_{11}$ mutations on p63 recruitment mediated by the ß2 adrenergic receptor (B2AR), which does not normally couple to $G\alpha_{q/11}$, using isoproterenol as a ligand. As expected, no isoproterenol-induced recruitment of p63 was observed with WT $G\alpha_{11}$, however, significant increases were observed for $G\alpha_{11}$ Gly66Asp and Ala231Thr (up to 1.4-fold and 1.3-fold increase compared to WT $G\alpha_{11}$, $p<0.0001$) (Figure 4.21E,G), thereby indicating they are promiscuous.

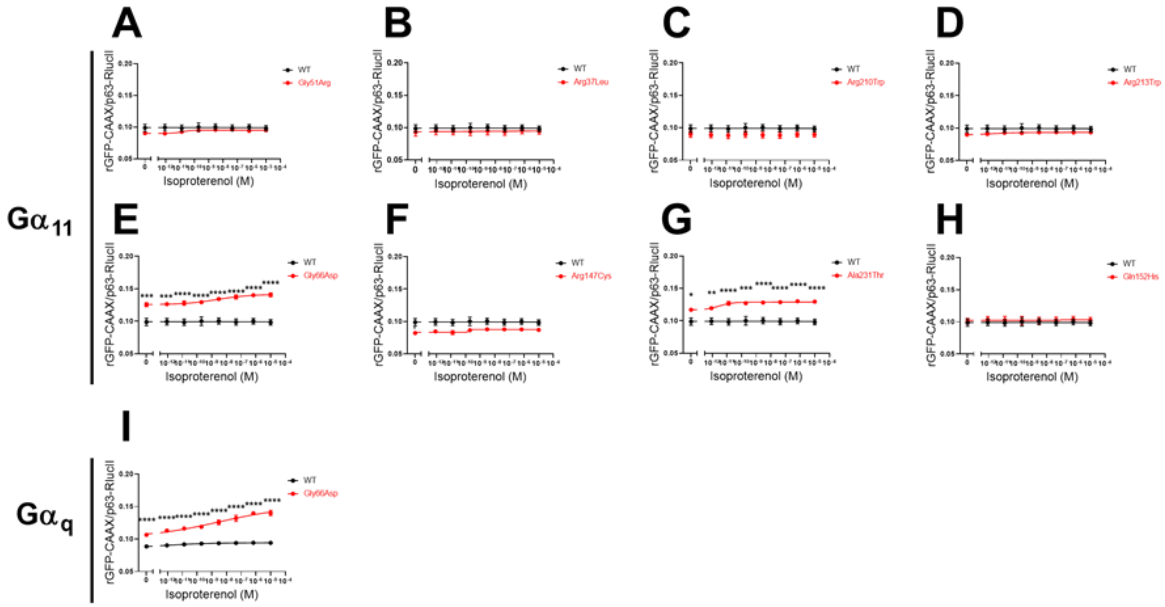


Figure 4.21 B2AR-mediated p63 recruitment in response to isoproterenol of (A) $G\alpha_{11}$ Gly51Arg (B) $G\alpha_{11}$ Arg37Leu (C) $G\alpha_{11}$ Argg210Trp (D) $G\alpha_{11}$ Arg213Trp (E) $G\alpha_{11}$ Gly66Asp (F) $G\alpha_{11}$ Arg147Cys (G) $G\alpha_{11}$ Ala231Thr (H) $G\alpha_{11}$ Gln152His and (I) $G\alpha_q$ Gly66Asp. Values are shown as mean±SEM of 4 independent transfections. Two-way ANOVA with Sidak correction for multiple comparisons was performed using GraphPad Prism 8.4.1. *p<0.05, **p<0.01, ***p<0.001, ****p<0.0001.

Similarly, $G\alpha_q$ Gly66Asp (previously reported to be promiscuous and therefore used as a positive control[23]), which is equivalent to $G\alpha_{11}$ Gly66Asp, showed significantly increased (up to 1.5-fold, $p<0.0001$) responses when compared to WT $G\alpha_q$ (Figure 4.21I). In contrast, $G\alpha_{11}$ Arg147Cys showed significantly decreased p63 recruitment at baseline (1.2-fold decrease compared to WT $G\alpha_{11}$, $p<0.05$) (Figure 4.21F). None of the other (non-biased) variants had an effect on B2AR-mediated recruitment of p63 (Figure 4.21A-D,H).

4.3 Discussion

In this chapter, I identified novel, rare, germline $G\alpha_{11}$ mutations that disrupt CaSR and M_3R function and promote biased signalling through G protein promiscuity.

4.3.1 Prevalence of FHH2- and ADH2-causing mutations

Two of the variants (Arg37Leu, Arg210Trp) caused CaSR loss-of-function and were associated with mild hypercalcaemia, similarly to previously reported FHH2-causing *GNA11* mutations, thus indicating that they likely represent novel FHH2-causing mutations. Based on a total number of 51,289 patients in the DiscovEHR database[254], I estimate that the prevalence of FHH2 is 3.9 per 100,000 individuals. In comparison, in the same database, FHH1 had a prevalence of 74.1 per 100,000, ADH1 had a prevalence of 3.9 per 100,000[106], and FHH3 had a prevalence of 7.8 per 100,000 individuals[106]. My observations agree with previous studies which concluded that FHH2 is less common than FHH1 and FHH3[270-272]. CaSR loss-of-function was also observed for Gly51Arg and Arg213Trp variants, suggesting they may be FHH2-causing; however, these variants were found in dbSNP and therefore phenotype data was not available.

I did not observe any variants associated with hypocalcaemia in this study, indicating the prevalence of ADH2 is likely <1.9 per 100,000 individuals. Moreover, out of the 14

variants that were functionally characterised, only one was a gain-of-function in both SRE and NFAT-RE luciferase reporter assays. However, this gain-of-function was not observed in p63R ebBRET assays, which were performed in cells containing endogenous WT $G\alpha_{q/11}$, indicating that this mutation may only be a gain-of-function when present in a homozygous state. Conversely, the majority (8) of reported disease-causing $G\alpha_{11}$ mutations have been heterozygous, autosomal dominant gain-of-function mutations as opposed to only 4 observed FHH2-causing mutations. This ratio is in contrast to CaSR mutations, where 232 FHH1-causing missense mutations have been reported and 95 ADH1-causing mutations[104]. One explanation may be that some $G\alpha_{11}$ loss-of-function mutations are partly compensated by WT $G\alpha_{11}$ and other G proteins, and therefore cause mild, subclinical forms of FHH2. This is supported by the fact that the loss-of-function mutations that I observed in the DiscovEHR cohort[254] were only associated with mild hypercalcaemia (mean plasma calcium values between 10mg/dL and 11mg/dL), which may not cause symptoms.

4.3.2 $G\alpha_{11}$ structure-function

My analysis of rare *GNA11* variants in large exome datasets reveals an additional 8 novel $G\alpha_{11}$ mutations that affect CaSR signalling. It shows that $G\alpha_{11}$ is highly conserved, and amino acid substitution is likely to be deleterious. This is highlighted by the significantly reduced numbers of missense variants that are observed, compared to the expected number. $G\alpha_{11}$ shares this feature with other members of the $G\alpha_{q/11}$ family: $G\alpha_{q}$ and $G\alpha_{15}$. Interestingly, for $G\alpha_{14}$ the expected number of variants was not different from the observed number, suggesting some members of the family are more conserved than others.

The Arg37Leu mutation, which disrupts CaSR signalling and is associated with hypercalcaemia in the DiscovEHR cohort, but also appears in dbSNP, demonstrates that

pathogenic mutations may be present in sequencing cohorts that are often used as a reference for normal genetic variation. Structural characterisation using PyMol showed that identified mutations are located in 4 key regions of the Gα subunit: the interdomain interface that binds GDP and GTP (Gly51Arg, Gly66Asp, Ala231Thr); the flexible switch 3 region (Arg147Cys, Gln152His); the αN helix which is important for GPCR interaction (Arg37Leu), and the Gα-Gβγ and PLC interaction site (Arg210Trp, Arg213Trp). Interestingly, the Gly51Arg mutation is in close proximity to the previously reported FHH2-causing mutation Thr54Met[108]. Based on structure of the closely related $G\alpha_q$ in complex with PLC-β3[267], the loss-of-function mutations Arg210Trp and Arg213Trp are predicted to disrupt $G\alpha_{11}$ interaction with its effector PLC. Moreover, they are located in close proximity to the ADH2-causing mutation Ser211Trp[260] and the constitutively active, uveal melanoma-causing somatic mutation Gln209Leu[33]. This shows that this part of $G\alpha_{11}$ can harbour three different types of mutations (loss-of-function, gain-of-function, and constitutively active). Interestingly, Arg37Leu is the first reported mutation in the αN helix, which has been shown to be important for Gα interactions with GPCRs[18,266]. This is further supported by the recent structure of the GTPase domain of $G\alpha_{11}$ in complex with the muscarinic acetylcholine receptor M_1[67]. In this structure, Arg134 and Ala135 in the intracellular loop 2 (ICL2) of the receptor form hydrogen bonds with Arg37 of $G\alpha_{11}$. This interaction was not present in the complex of the M2 receptor and $G\alpha_{oB}$. This suggests that Arg37Leu may specifically disrupt $G\alpha_{11}$ interaction with GPCRs. Interestingly, Arg37Leu did not disrupt M_3R-mediated signalling, providing a possible explanation of why reported FHH2/ADH2-causing *GNA11* mutations, although present in every tissue of the patient, are predominantly associated with disorders of calcium metabolism[93].

4.3.3 Effects on GPCRs other than CaSR

Previously, germline $G\alpha_{11}$ mutations in humans had only been reported to disrupt signalling by the CaSR, a class C GPCR, and cause disorders of calcium homeostasis, with 4 loss-of-function mutations causing FHH2[93,108,109] and 8 gain-of-function mutations causing ADH2[93,117,211,220,260]. My analysis of rare *GNA11* variants in large population datasets reveals an additional 8 novel $G\alpha_{11}$ mutations that affect CaSR signalling. I show that while some of the identified $G\alpha_{11}$ mutations are CaSR-specific, the majority also disrupted signalling of prototypical class A receptors, the most prominent group of GPCRs (see introduction section 1.2.2)[59]. Out of 7 $G\alpha_{11}$ variants that disrupted p63 recruitment by the CaSR, 5 also affected M_3R signalling, and 3 affected B2AR signalling.

Because GPCRs are widely expressed and involved in a plethora of physiological and pathophysiological processes, they are prime drug targets with >30% of prescription drugs acting directly on GPCRs (see introduction section 1.2.1)[58]. My analysis of the IUPHAR/BPS Guide to PHARMACOLOGY[252] and GPCRdb[253] databases revealed a total of 94 receptors that have been reported to be primarily coupled to $G\alpha_{q/11}$. Based on the present study it is likely that the identified loss-of-function, gain-of-function, and promiscuous $G\alpha_{11}$ mutations affect the signalling of multiple GPCRs and may therefore have potential implications for diseases that are associated with these receptors. One such phenotype may be short stature which has previously been observed in patients[117,260] and mice[36,124,125] with gain-of-function $G\alpha_{11}$, but not CaSR mutations (see 1.4). Moreover, the Ile62Val mutation also causes dark skin in mice[36]. Additionally, individuals with rare $G\alpha_{11}$ mutations may show altered response to drugs that target these receptors. Such differences in pharmacogenomics have been observed for several GPCR variants[58].

4.3.4 Biased and promiscuous mutations

Recently, there has been great interest in studying biased signalling of GPCRs, i.e. the ability to activate specific signalling cascades to elicit distinct cellular signalling profiles (see section 1.6.3.4)[28,162,194]. Strikingly, I observed "biased" signalling for three $G\alpha_{11}$ variants (Gly66Asp, Arg147Cys, Ala231Thr), which did not significantly affect (Gly66Asp, Arg147Cys) or significantly reduced (Ala231Thr) SRE luciferase response activity but significantly increased NFAT-RE luciferase reporter activity. This was associated with unique molecular phenotypes for each variant in 7 CaSR signalling assays upstream of SRE and NFAT-RE (summarised in Figure 4.22).

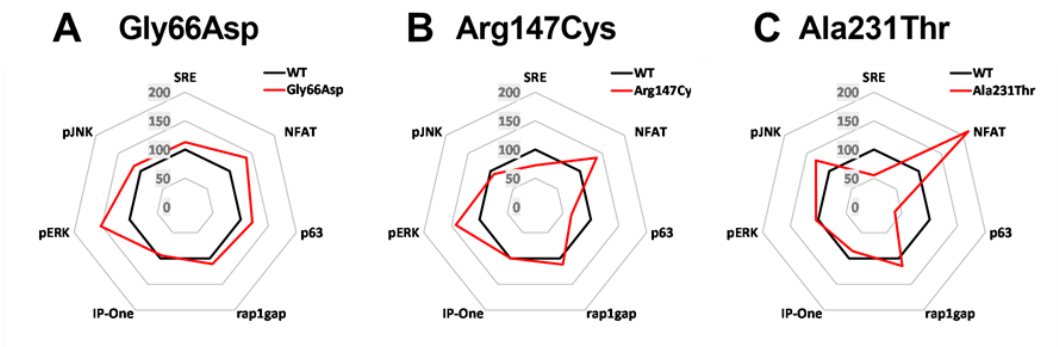


Figure 4.22 Radar plots show variant (black line) AUC normalised to WT (red line) of 7 different signalling assays for (A) $G\alpha_{11}$ Gly66Asp (B) $G\alpha_{11}$ Arg147Cys (C) $G\alpha_{11}$ Ala231Thr to facilitate comparison of variant effects across the 7 different assays.

Interestingly, the biased variants are all located in the flexible interdomain interface, which binds guanine nucleotides[11,38]. The $G\alpha_{11}$ Gly66 residue has previously been shown to be important for CaSR signalling: Gly66Ser causes ADH2[211]. Similarly, $G\alpha_{11}$ Arg149His, which is in close proximity to Arg147Cys, also causes ADH2[211]. Notably, Gly66Asp has been reported to be promiscuous in $G\alpha_q$, i.e. have the ability to be activated by $G\alpha_i$- and $G\alpha_s$-coupled receptors[23]. Indeed, using ebBRET assays I showed

that even though isoproterenol stimulation of the B2AR does not result in recruitment of the $G\alpha_q$ family specific effector p63[29] when co-expressed with WT $G\alpha_{11}$ or $G\alpha_q$, significant increases were observed for both $G\alpha_{11}$ Gly66Asp and $G\alpha_q$ Gly66Asp. A similar effect was seen for $G\alpha_{11}$ Ala231Thr, thereby confirming that it also causes the G protein to be promiscuous.

In contrast, the Arg147Cys variant resulted in the opposite effect, and caused a significant decrease of baseline p63 recruitment. Additionally, all three variants caused an increase in CaSR-mediated recruitment of rap1gap, which is a specific effector of the $G\alpha_{i/o}$ family[273,274]. I hypothesise that the $G\alpha_{11}$ mutants may be able to recruit rap1gap due to their promiscuity, or that the receptor is able to better engage members of the $G\alpha_{i/o}$ family when mutant $G\alpha_{11}$ is present. Interestingly, Gly66Asp, despite being promiscuous, did not affect the function of the already $G\alpha_{q/11}$ coupled M_3R. This is in agreement with a previous study[23], but different from what I observed for the CaSR, which did show significantly increased signalling responses. I observed higher basal activity and E_{max} for the M_3R than for CaSR, suggesting it is already strongly coupled to $G\alpha_{11}$ and therefore it may be that the signalling response cannot be further increased by the promiscuous mutation.

Taken together, these data suggest that the complex effects in signalling assays that I observed for Gly66Asp, Arg147Cys and Ala231Thr are likely a reflection of their promiscuity, and that each of the variants may interact with a unique set of receptors that would normally not couple to $G\alpha_{q/11}$, giving rise to distinct molecular phenotypes. Because of the complex effects of these mutants it is difficult to predict their potential pathophysiological effects, however, due to their promiscuity they may impair a wide range of physiological functions. This highlights the need for patients diagnosed with FHH2/ADH2 to be closely monitored for additional, non-calcitropic phenotypes as they may differ depending on the specific mutation.

In conclusion, this chapter highlights the evolutionary conservation of $G\alpha_{11}$ and demonstrates that receptors other than the CaSR are affected by germline *GNA11* mutations. I reveal 8 previously unreported, naturally occurring loss-of-function, gain-of-function and promiscuous $G\alpha_{11}$ mutations. This provides insights into $G\alpha_{11}$ structure-function and has potential implications for a wide range of GPCRs.

5 INVESTIGATION OF GLUCOSE METABOLISM IN DSK7 MICE

5.1 Aims

Gα11 is a major signalling partner of the CaSR[77] and its mRNA is highly expressed in the pancreas (see introduction section 1.2.3)[81,275,276]. However, the role of Gα11 in CaSR-mediated effects on glucose metabolism is not known. 102/H strain background mice with a gain-of-function CaSR mutation (referred to as Nuf), which are a model for autosomal dominant hypocalcaemia type 1 (ADH1)[123,277], have impaired glucose tolerance, reduced insulin secretion, and decreased pancreatic islet size and proliferation (see 1.5.2)[134]. This indicates a role for the CaSR in pancreatic islets.

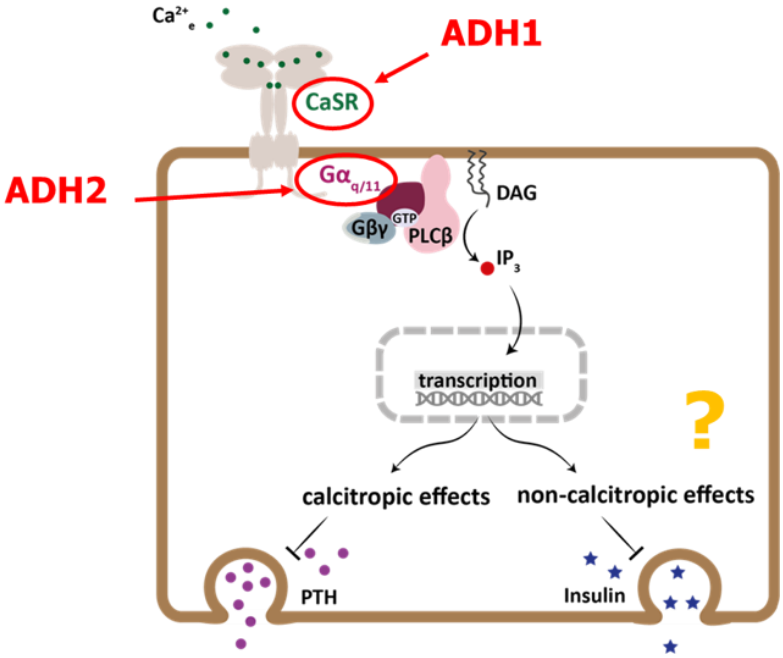


Figure 5.1 Overview of CaSR signalling via Gα11. Gain-of-function mutations of both CaSR and Gα11 cause autosomal dominant hypocalcaemia types 1 and 2, respectively (ADH1/2) in humans and mice. Mouse models for ADH1 (Nuf) also have impaired glucose homeostasis; however, the contribution of the Gα11 signalling pathway to CaSR-mediated effects on glucose metabolism is not known.

C3H strain background mice with a gain-of-function Gα11 mutation (Ile62Val) (referred to as Dsk7) develop ADH type-2 (ADH2)[125], mirroring the calcitropic phenotype of Nuf

mice. Additionally, Dsk7 mice have non-calcitropic phenotypes, such as reduced body weight and dark skin[35,36]; however, their glucose metabolism has not been investigated. I therefore hypothesised that Dsk7 mice may develop similar abnormalities of glucose homeostasis as Nuf mice (illustrated in Figure 5.1). The aims of this chapter were to assess fasted baseline plasma biochemistry of Dsk7 mice, and to investigate defects in glucose metabolism and pancreatic islet architecture.

5.2 Results

5.2.1 Viability

Mouse studies were conducted in collaboration with the Mary Lyon Centre (MRC Harwell) (see 3.9). $G\alpha_{11}$ Ile62Val results in the loss of a FokI restriction site, which was confirmed by restriction digest[125]. Analysis of genotypes bred from crosses of Dsk7/+ × Dsk7/+ mice over a two-year period revealed that the observed number of male and female homozygous (Dsk7/Dsk7) mice at >3 weeks was significantly lower than expected (Chi-square test, $p<0.001$ and $p<0.01$, respectively) (Table 5.1), indicating that Dsk7/Dsk7 mice have reduced viability.

Table 5.1 Proportion of +/+, Dsk7/+ and homozygous Dsk7/Dsk7 mice observed in a sample of 174 male and 167 female mice at >3 weeks bred between 2017 and 2019. Chi-square test was performed using GraphPad Prism 8.4.1.

Genotype	gender	expected	observed
+/+	male	43.5	61
Dsk7/+	male	87	88
Dsk7/Dsk7	male	43.5	25
+/+	female	41.75	54
Dsk7/+	female	83.5	85
Dsk7/Dsk7	female	41.75	28

In contrast, the number of heterozygous (Dsk7/+) mice did not significantly differ from the prediction of 25% WT (+/+), 50% Dsk7/+ and 25% Dsk7/Dsk7. Moreover, Dsk7/Dsk7

mice had significantly ($p<0.05$) reduced body weight at 14 weeks of age, whereas no significant difference in body weight was observed for Dsk7/+ mice (Figure 5.2).

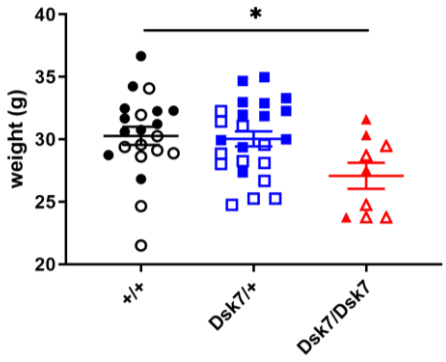


Figure 5.2 Body weight of male (solid symbols) and female (hollow symbols) of +/+ (n=21), Dsk7/+ (n=24) and Dsk7/Dsk7 (n=9) mice. Kruskal-Wallis test with Dunn's correction for multiple comparisons was performed using GraphPad Prism 8.4.1. *$p<0.05$.

5.2.2 Fasted plasma biochemistry

Differences in plasma biochemistry between WT and Dsk7 mice have been reported previously; however, these were studied in non-fasted mice (see section 1.4.4.2)[125]. Plasma samples of fasted 14-week-old Dsk7 mice were collected under terminal anaesthesia and were assessed using an automated analyser[123]. A range of commonly used biomarkers were studied, with particular emphasis on electrolytes. This revealed that both male and female Dsk7/+ and Dsk7/Dsk7 mice had normal plasma levels of potassium, urea, alkaline phosphatase (ALP), Alanine transaminase (ALT), total Cholesterol, Low-density lipoprotein (LDL), Triglycerids, Glycerol, Free Fatty Acids, total Billirubin, Lactate dehydrogenase (LDH), Iron, Amylase, Creatine kinase (CK), Uric Acid, Ketone Bodies and fructose (Table 5.2). However, abnormalities of plasma calcium, albumin, total protein, inorganic phosphorus, sodium, chloride, magnesium, creatinine, high-density lipoprotein (HDL), and Aspartate transaminase (AST) were observed.

Table 5.2 Plasma biochemistry of electrolytes and metabolites that were similar in +/+, Dsk7/+ and Dsk7/Dsk7 mice.

Females

	+/+			Dsk7/+			Dsk7/Dsk7		
	Mean	SEM	N	Mean	SEM	N	Mean	SEM	N
Urea (mmol/l)	6.060	0.196	10	7.092	0.426	12	7.460	1.105	5
ALP (U/l)	124.700	6.625	10	144.833	7.677	12	139.800	14.158	5
ALT (U/l)	26.800	0.975	10	29.333	3.587	12	33.000	7.266	5
Total Cholesterol (mmol/l)	3.097	0.122	10	3.278	0.113	12	3.482	0.070	5
LDL (mmol/l)	0.601	0.073	10	0.693	0.070	12	0.814	0.151	5
Triglycerides (mmol/l)	3.172	0.330	10	3.272	0.350	12	3.166	0.450	5
Glycerol (μmol/l)	399.800	20.366	10	384.500	25.660	12	478.600	74.972	5
Free Fatty Acids (mmol/l)	1.133	0.067	10	1.055	0.086	12	1.590	0.376	5
Total Billirubin (μmol/l)	1.940	0.067	10	1.942	0.092	12	1.820	0.180	5
LDH (U/l)	489.900	83.732	10	396.750	63.316	12	490.600	67.780	5
Iron (μmol/l)	22.050	1.047	10	24.483	1.132	12	23.240	1.888	5
Amylase (U/l)	577.000	17.317	10	585.000	17.427	12	615.400	9.978	5
CK (U/l)	123.700	23.456	10	152.333	45.403	12	108.600	15.622	5
Uric Acid (μmol/l)	62.300	6.346	10	63.091	5.731	11	48.000	8.888	3
Ketone Bodies (mmol/l)	2.240	0.183	10	2.023	0.135	12	1.986	0.342	5
FRUCT (μmol/l)	216.800	4.528	10	213.333	3.066	12	207.800	2.853	5
Potassium (mmol/l)	4.511	0.104	10	4.243	0.129	12	3.916	0.251	5

Males

	+/+			Dsk7/+			Dsk7/Dsk7		
	Mean	SEM	N	Mean	SEM	N	Mean	SEM	N
Urea (mmol/l)	8.018	0.902	11	7.567	0.227	12	8.975	1.674	4
ALP (U/l)	88.818	4.333	11	94.500	5.165	12	109.000	6.583	4
ALT (U/l)	24.909	2.016	11	26.833	1.709	12	31.000	3.109	4
Total Cholesterol (mmol/l)	3.743	0.124	11	3.918	0.189	12	3.828	0.187	4
LDL (mmol/l)	0.762	0.049	11	0.920	0.108	12	0.810	0.129	4
Triglycerides (mmol/l)	2.381	0.172	11	2.611	0.208	12	1.943	0.468	4
Glycerol (μmol/l)	283.000	9.279	11	333.167	28.344	12	318.000	26.118	4
Free Fatty Acids (mmol/l)	0.981	0.034	11	1.147	0.111	12	0.948	0.075	4
Total Billirubin (μmol/l)	2.082	0.101	11	1.950	0.087	12	1.875	0.111	4
LDH (U/l)	476.364	93.489	11	426.083	49.735	12	563.750	26.260	4
Iron (μmol/l)	19.645	1.092	11	19.442	0.515	12	19.350	0.595	4
Amylase (U/l)	595.636	17.405	11	603.333	14.054	12	554.000	25.017	4
CK (U/l)	126.091	24.192	11	85.833	9.910	12	178.000	39.875	4
Uric Acid (μmol/l)	74.500	9.478	10	73.000	10.019	9	77.750	16.342	4
Ketone Bodies (mmol/l)	1.675	0.131	11	1.415	0.078	12	1.698	0.132	4
FRUCT (μmol/l)	192.182	3.653	11	194.083	3.679	12	207.000	2.000	4
Potassium (mmol/l)	4.692	0.161	11	4.585	0.164	12	4.435	0.116	4

Plasma calcium values of Dsk7/+ and Dsk7/Dsk7 mice of both genders were significantly decreased (Figure 5.3). Notably, plasma albumin levels were significantly reduced in male Dsk7/Dsk7 mice ($p<0.01$), female Dsk7/+ mice ($P<0.01$), and pooled Dsk7/Dsk7 data ($P<0.01$) (Figure 5.4A-C). In addition, total protein levels were reduced in male Dsk7/Dsk7 mice ($p<0.05$) and combined genders ($p<0.01$) (Figure 5.4D-F).

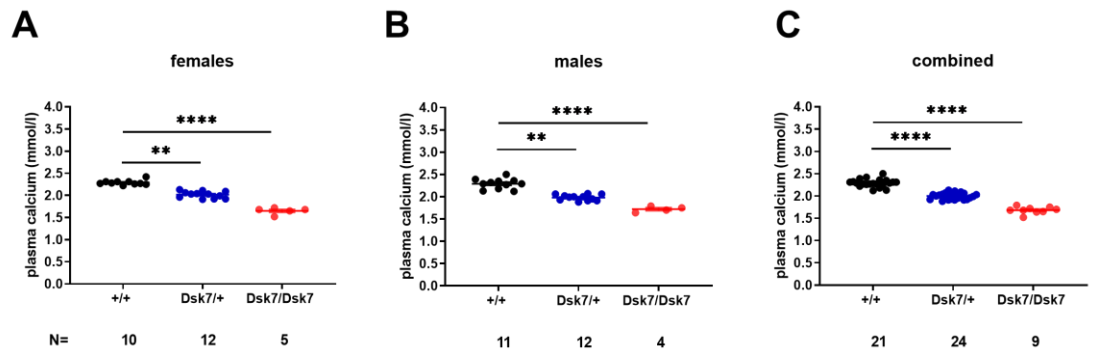


Figure 5.3 Plasma calcium values (mmol/l) of (A) female (B) male and (C) gender pooled +/+, Dsk7/+ and Dsk7/Dsk7 mice, in black, blue and red, respectively. N numbers are indicated below each graph. Kruskal-Wallis test with Dunn's correction for multiple comparisons was performed using GraphPad Prism 8.4.1. **p<0.01, ****p<0.0001.

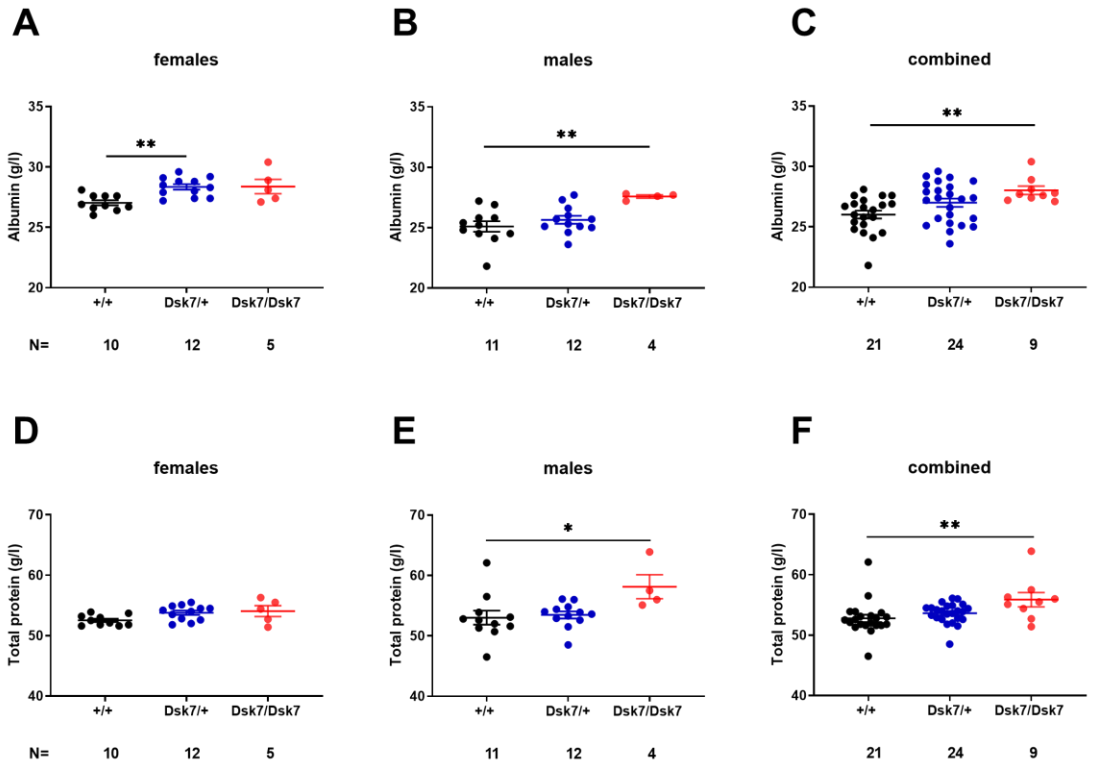


Figure 5.4 Plasma albumin levels (A-C) and total protein (D-F) of female, male and gender pooled +/+, Dsk7/+ and Dsk7/Dsk7 mice, highlighted in black, blue and red, respectively. N numbers are indicated below each graph. Kruskal-Wallis test with Dunn's correction for multiple comparisons was performed using GraphPad Prism 8.4.1. *p<0.05, **p<0.01.

Plasma calcium levels were therefore adjusted for albumin, using the following formula: (plasma calcium (mmol/l) – [(plasma albumin (g/l) – 30) × 0.02]). Albumin-corrected plasma calcium values were significantly decreased for Dsk7/+ ($p<0.01$) and Dsk7/ Dsk7 ($p<0.0001$) mice of both genders (Figure 5.5A-B) and combined gender data ($p<0.0001$) (Figure 5.5C). Average combined albumin corrected plasma calcium values were 2.06±0.08, 1.72±0.08, and 2.37±0.09 mmol/l for Dsk7/+, Dsk7/Dsk7 and +/+, respectively.

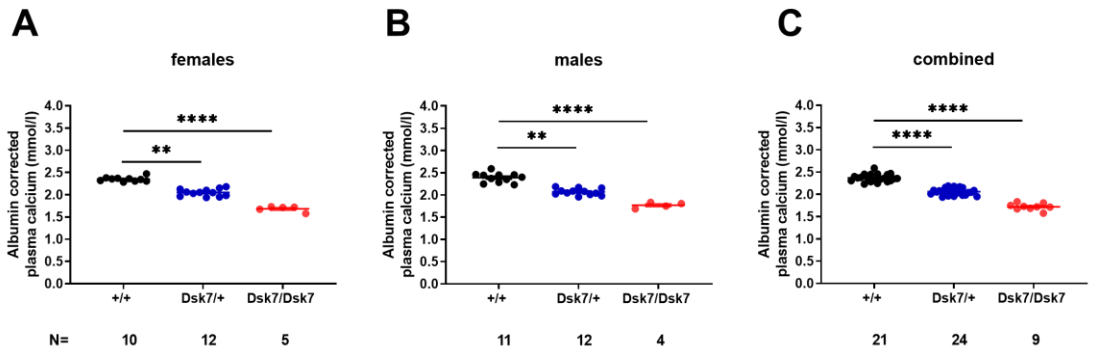


Figure 5.5 Albumin corrected plasma calcium values (mmol/l) of (A) female (B) male and (C) gender pooled +/+, Dsk7/+ and Dsk7/Dsk7 mice, highlighted in black, blue and red, respectively. N numbers are indicated below each graph. Kruskal-Wallis test with Dunn's correction for multiple comparisons was performed using GraphPad Prism 8.4.1. **$p<0.01$, ****$p<0.0001$.

Moreover, inorganic phosphate levels of Dsk7/+ and Dsk7/Dsk7 mice of both genders were significantly increased (Figure 5.6).

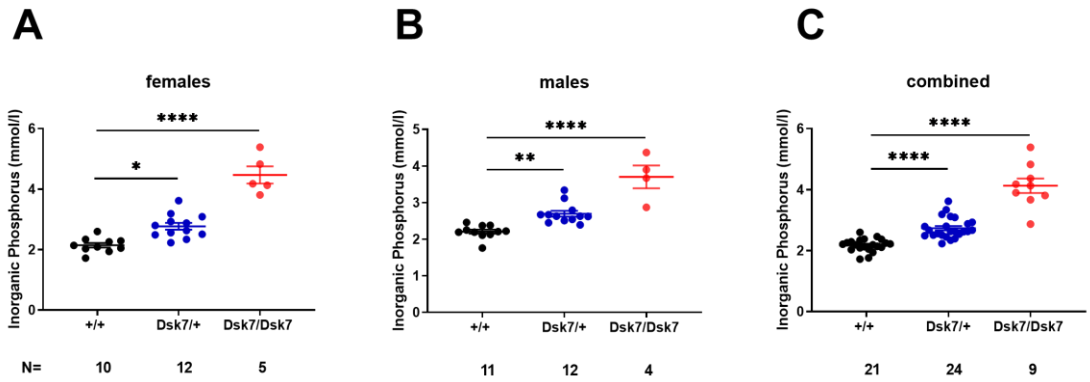


Figure 5.6 Inorganic phosphate values (mmol/l) of (A) female (B) male and (C) gender pooled +/+, Dsk7/+ and Dsk7/Dsk7 mice, highlighted in black, blue and red, respectively. N numbers are indicated below each graph. Kruskal-Wallis test with Dunn's correction was performed using GraphPad Prism 8.4.1. *p<0.05, **p<0.01, ****p<0.0001.

Additionally, sodium levels were significantly increased in female Dsk7/Dsk7 mice and pooled data (p<0.05 and p<0.01, respectively) (Figure 5.7).

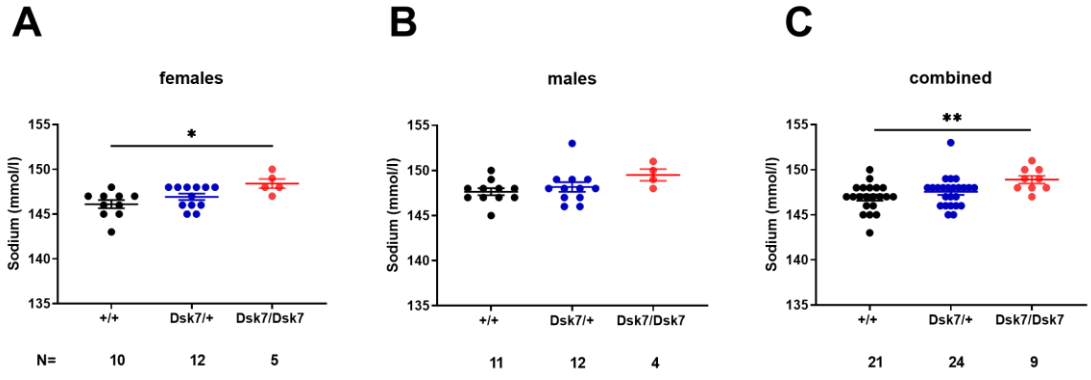


Figure 5.7 Plasma sodium values (mmol/l) of (A) female (B) male and (C) gender pooled +/+, Dsk7/+ and Dsk7/Dsk7 mice, highlighted in black, blue and red, respectively. N numbers are indicated below each graph. Kruskal-Wallis test with Dunn's correction for multiple comparisons was performed using GraphPad Prism 8.4.1. *p<0.05, **p<0.01.

In contrast, chloride levels were significantly reduced in Dsk7/Dsk7 male and female mice ($p<0.05$) (Figure 5.8A-B) and combined data ($p<0.05$) (Figure 5.8C). Moreover, magnesium levels were significantly decreased in male Dsk7/+ and Dsk7/Dsk7 mice ($p<0.05$) (Figure 5.8D-F).

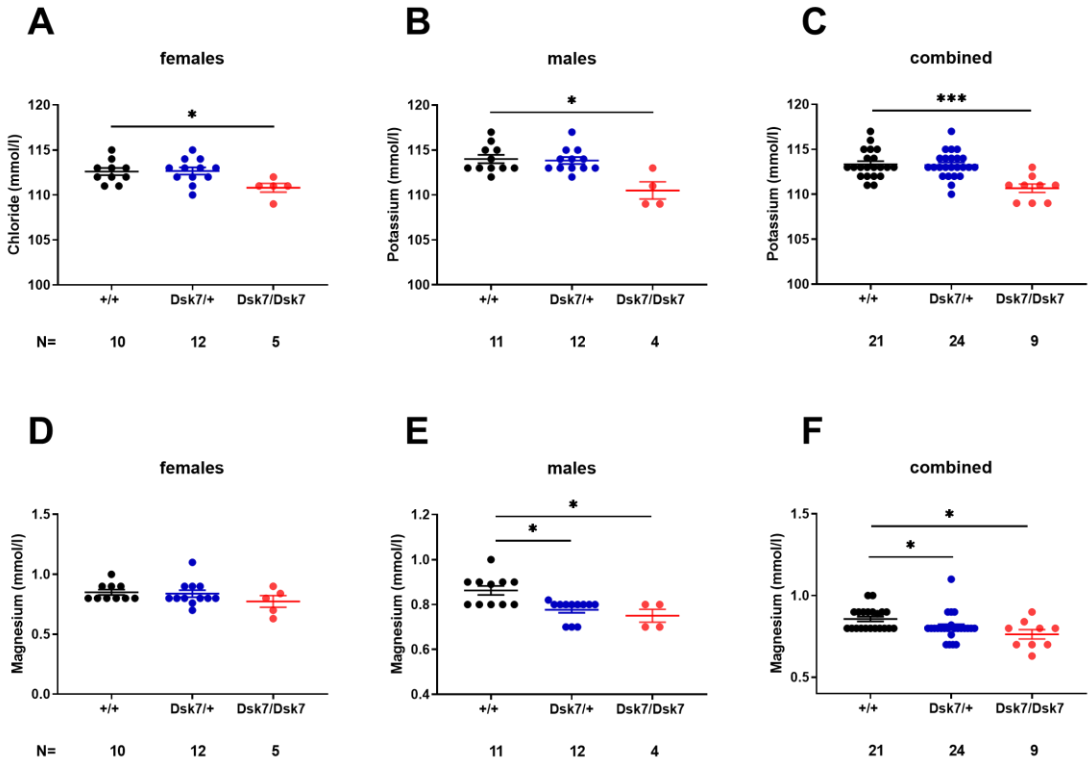


Figure 5.8 Plasma levels of chloride (A-C) and magnesium (D-F) of female, male and gender pooled +/+, Dsk7/+ and Dsk7/Dsk7 mice, highlighted in black, blue and red, respectively. N numbers are indicated below each graph. Kruskal-Wallis test with Dunn's correction for multiple comparisons was performed using GraphPad Prism 8.4.1. *$p<0.05$, ***$p<0.001$.

Furthermore, male and gender pooled Dsk7/Dsk7 mice had significantly increased plasma creatinine levels ($p<0.05$) (Figure 5.9A-C); female Dsk7/Dsk7 mice had significantly increased levels of HDL ($p<0.05$) (Figure 5.9D-F); and male Dsk7/Dsk7 mice had significantly increased levels of AST ($p<0.05$) (Figure 5.9G-I).

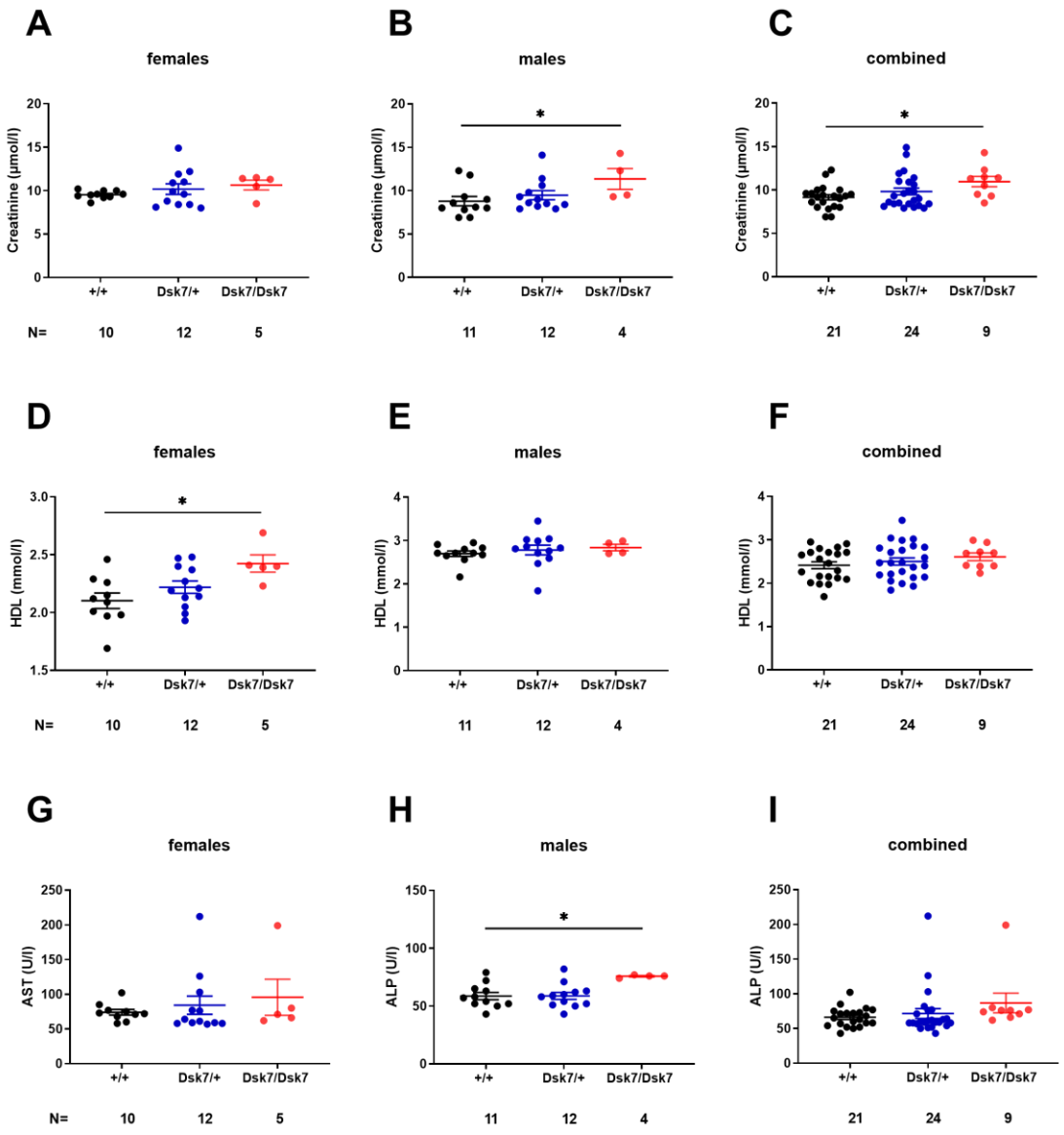


Figure 5.9 Plasma levels of creatinine (A-C), High-density lipoprotein (HDL) (D-F) and Aspartate transaminase (AST) (G-I) of female, male and gender pooled +/+, Dsk7/+ and Dsk7/Dsk7 mice, highlighted in black, blue and red, respectively. N numbers are indicated below each graph. Kruskal-Wallis test with Dunn's correction for multiple comparisons was performed using GraphPad Prism 8.4.1. *p<0.05.

5.2.3 Glucose metabolism

In order to assess the glucose metabolism of Dsk7 mice, plasma glucose concentrations of +/+, Dsk7/+ and Dsk7/Dsk7 mice were compared, both at baseline and after an intraperitoneal glucose tolerance test (IPGTT). Analysis of baseline glucose concentrations of fasted mice revealed no significant differences in female (Figure 5.10A), male (Figure 5.10B) and gender pooled (Figure 5.10C) Dsk7 mice compared to WT littermates.

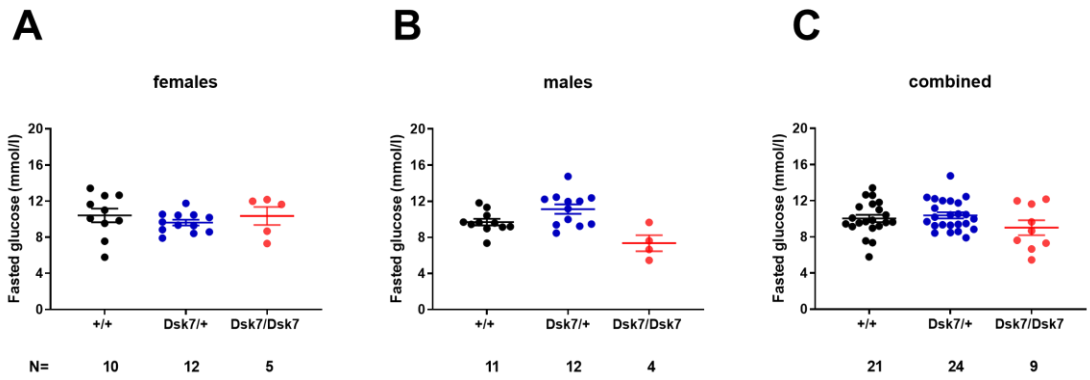


Figure 5.10 Comparison of baseline plasma glucose values between genotypes. Fasted glucose values (mmol/l) of (A) female (B) male and (C) gender pooled +/+, Dsk7/+ and Dsk7/Dsk7 mice, highlighted in black, blue and red, respectively. N numbers are indicated below each graph. Kruskal-Wallis test with Dunn's correction for multiple comparisons was performed using GraphPad Prism 8.4.1.

For the Nuf mice, gender differences in baseline glucose were observed for the different genotypes[134]. I therefore compared baseline glucose levels across genders. This showed no significant difference for +/+ and Dsk7/+ mice; however, male Dsk7/Dsk7 mice had significantly lower baseline plasma glucose levels than female Dsk7/Dsk7 mice (Figure 5.11).

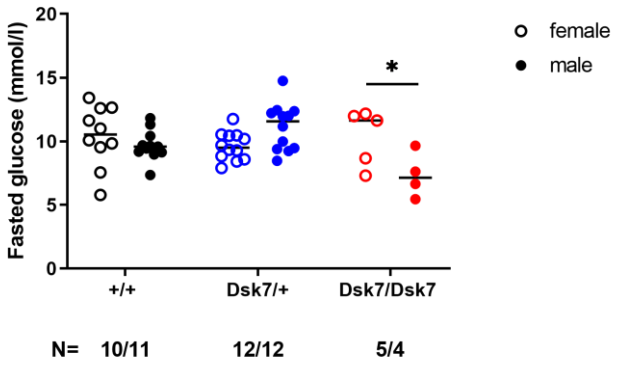


Figure 5.11 Comparison of baseline glucose values (mmol/l) between genders, of +/+ (black), Dsk7/+ (blue) and Dsk7/ Dsk7 (red) mice. Males are represented using filled symbols, females are represented using open symbols. N numbers are indicated below each graph. Two-way ANOVA with Sidak's correction for multiple comparisons was performed using GraphPad Prism 8.4.1. *p<0.05.

To assess the glucose tolerance of Dsk7 mice, IPGTTs were performed as described in section 3.9.2[134]. Analysis of plasma samples at 0, 30, 60, and 90 minutes post-glucose injection showed no differences in glucose tolerance between +/+, Dsk7/+ or Dsk7/Dsk7 mice of both genders and gender pooled data (Figure 5.12), indicating that Dsk7 mice have normal glucose tolerance.

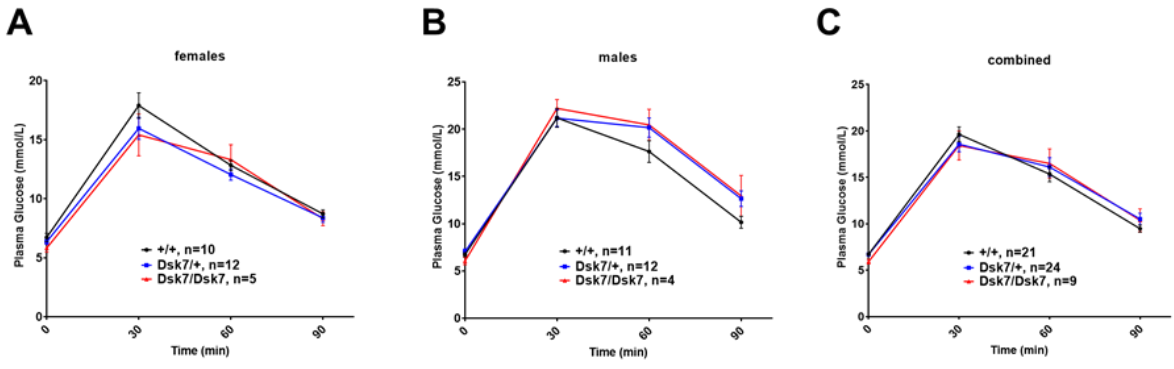


Figure 5.12 Intraperitoneal glucose tolerance tests (IPGTTs) showed no difference between +/+, Dsk7/+ and Dsk7/Dsk7 mice. Two-way ANOVA with Dunett's correction for multiple comparisons was performed using GraphPad Prism 8.4.1.

5.2.3.1 Pancreatic islet histology

Nuf mice have abnormalities in pancreatic islet histology, and I therefore investigated potential abnormalities in the pancreatic islet structure of Dsk7 mice. WT and Dsk7 mice were aged to 14 weeks and pancreata were harvested. Subsequently, paraffin-embedded tissue sections were stained with haematoxylin and eosin (H&E).

This revealed that the number of islets/mm^2 of Dsk7/+ and Dsk7/Dsk7 mice of both genders and combined data was not significantly altered compared to +/+ littermates (Figure 5.13A-C). Moreover, no significant differences in islet area were observed. These data indicate that Dsk7 mice have normal pancreatic islet histology (Figure 5.13D-F).

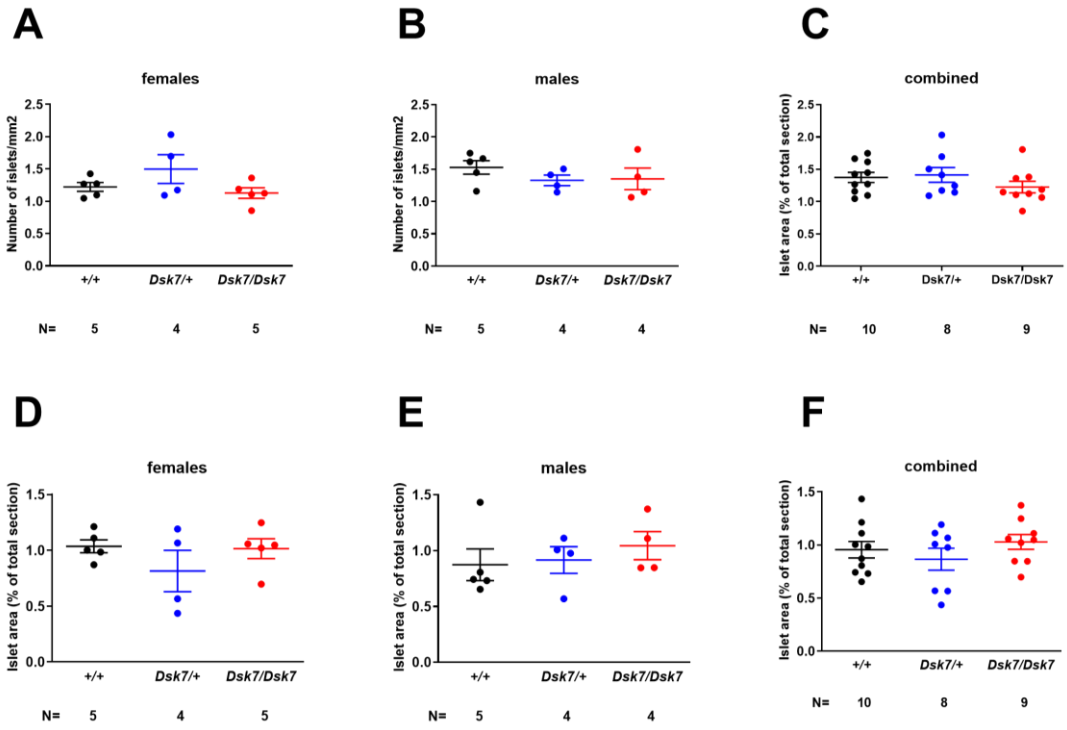


Figure 5.13 Quantification of islet area and number of H&E stain of pancreatic islet sections from Dsk7 mice. No differences between WT and Dsk7 mice were observed for (A-C) the number of islets per mm^2 and (D-F) islet area as a percentage of the total section. N numbers are indicated below each graph. Kruskal-Wallis test with Dunn's correction for multiple comparisons was performed using GraphPad Prism 8.4.1. Data generated by Dr. Valerie Babinsky (University of Oxford).

5.2.3.2 Immunofluorescence microscopy

In order to assess potential abnormalities in individual islet architecture, immunofluorescence microscopy (methods section 3.7.3) was performed on a total of 224 serial sections of pancreata from 4 +/+, 4 Dsk7/+ and 4 Dsk7/Dsk7 mice of each gender (aged 14 weeks).

Of the 224 sections, 68 were stained for DAPI, insulin (indicating ß-cells) and glucagon (indicating α-cells) (Figure 5.14A,C,E), 60 sections were stained for DAPI, insulin and Ki67 (indicating proliferating cells) (Figure 5.14B,D,F), and 96 were negative controls (DAPI and secondary antibody only).

The number of α, ß and proliferating cells per islet was quantified using Tissuegnostics StrataQuest 5.0.1.317 image analysis software (see methods section 3.11.2). This revealed that, on average, each individual islet of +/+ mice contained approximately 30% α-cells and approximately 70% ß-cells. No significant differences in α- and ß-cell number were observed for male and female Dsk7/+ and Dsk7/Dsk7 mice of both genders, and gender pooled data (Figure 5.15).

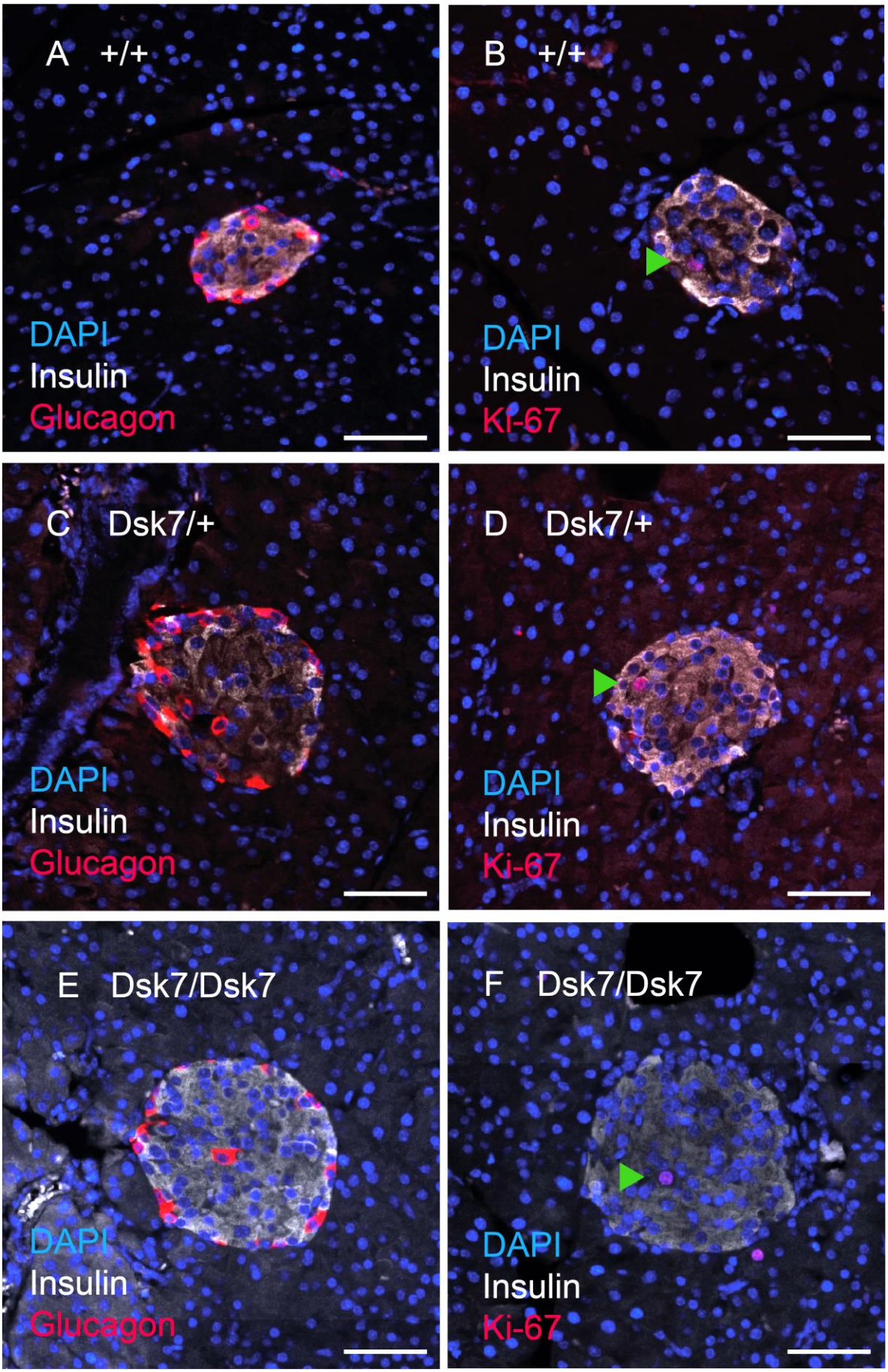

A +/+
DAPI
Insulin
Glucagon
B +/+
DAPI
Insulin
Ki-67
C Dsk7/+
DAPI
Insulin
Glucagon
D Dsk7/+
DAPI
Insulin
Ki-67
E Dsk7/Dsk7
DAPI
Insulin
Glucagon
F Dsk7/Dsk7
DAPI
Insulin
Ki-67

Figure 5.14 Immunofluorescence staining of pancreatic islet sections from +/+, Dsk7/+ and Dsk7/Dsk7 mice for DAPI (blue), insulin (white), and either glucagon (red) (A,C,E) or Ki-67 (red) (B,D,F). Ki67, which indicates proliferating cells, is co-located with DAPI and therefore appears purple. Proliferating cells within islets are indicated by a green arrow.

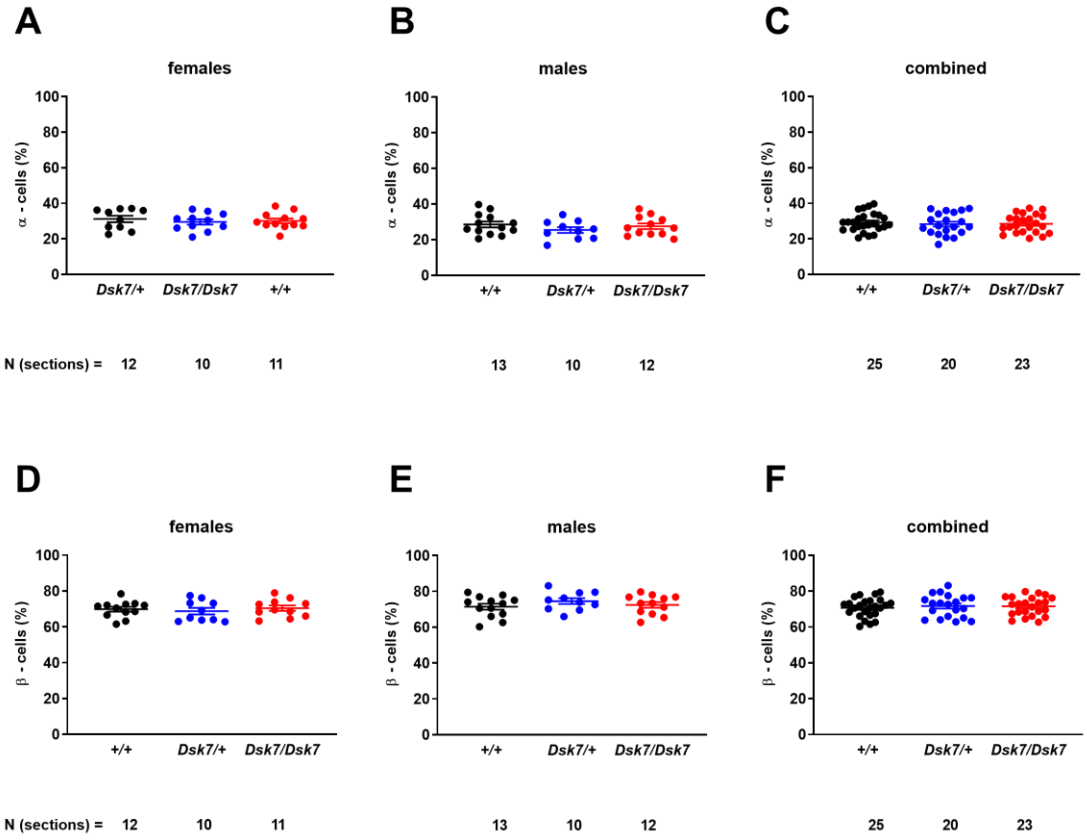


Figure 5.15 Quantification of glucagon positive (α) cells (A-C) and insulin positive (ß) cells (D-F) in pancreatic islet sections of +/+ (black), Dsk7/+ (blue) and Dsk7/Dsk7 (red) mice. N numbers are indicated below each graph. A Kruskal-Wallis test with Dunn's correction for multiple comparisons was performed using GraphPad Prism 8.4.1.

Next, potential differences in islet proliferation were investigated, using the proliferation marker Ki-67. Islets were co-stained for Ki-67 and insulin to determine the proportion of proliferating insulin-positive (ß) and insulin-negative (predominantly α)

cells. This revealed that the proportion of proliferating insulin-negative (predominantly α) cells was significantly reduced for male Dsk7/+ and Dsk7/Dsk7 mice (Figure 5.16B). In contrast, insulin-negative (predominantly α) cell proliferation of female Dsk7/+ and Dsk7/Dsk7 mice (Figure 5.16A) and combined results (Figure 5.16C) was not significantly different from +/+.

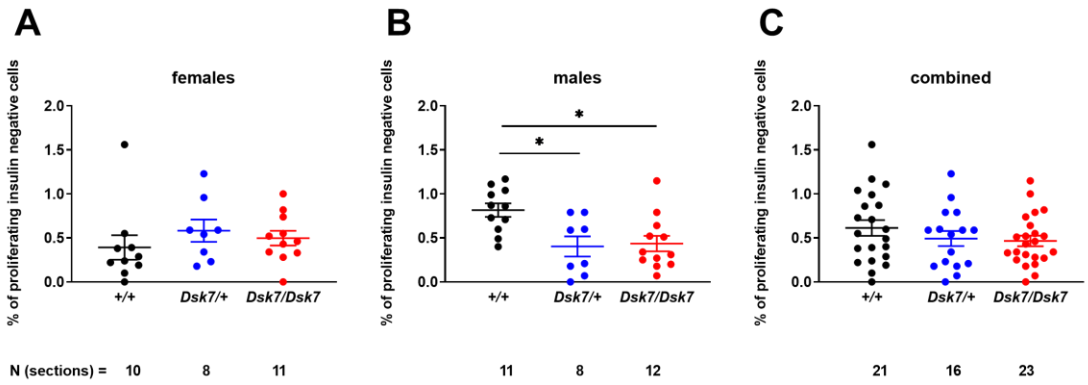


Figure 5.16 Proportion of proliferating (Ki-67 positive) insulin negative (predominantly α) cells in pancreatic islet sections of +/+ (black), Dsk7/+ (blue) and Dsk7/Dsk7 (red) mice. N numbers are indicated below each graph. Kruskal-Wallis test with Dunn's correction for multiple comparisons was performed using GraphPad Prism 8.4.1.

Moreover, the proportion of proliferating insulin positive (ß) cells was significantly reduced for male Dsk7/Dsk7 mice (Figure 5.17B). However, no significant differences compared to +/+ were observed for male Dsk7/+ mice, female mice (Figure 5.17A) and combined results (Figure 5.17C).

Taken together the immunohistochemical results indicate that female Dsk7 mice have normal pancreatic islet architecture, and male Dsk7 mice have normal α- and ß-cell number but impaired α- and ß-cell proliferation. However, islet size was normal in these mice, thereby indicating that the observed changes in proliferation are likely to be too small to have a physiological effect.

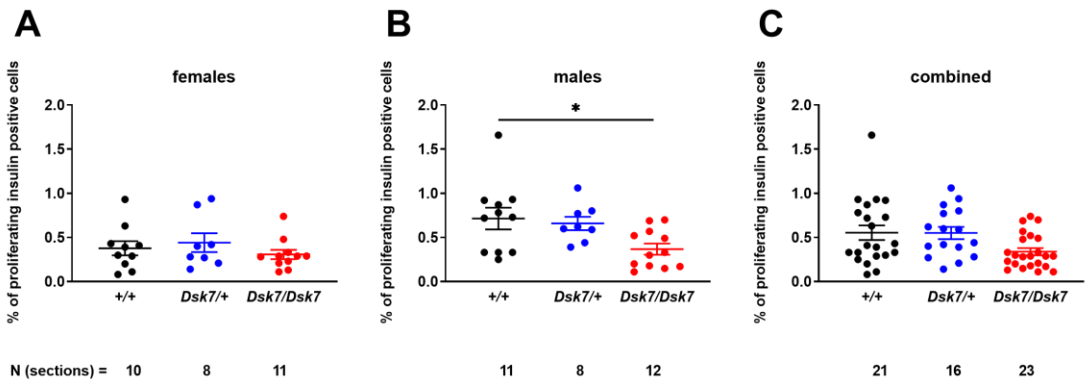


Figure 5.17 Proportion of proliferating (Ki-67 positive) insulin positive (ß) cells in pancreatic islet sections of +/+ (black), Dsk7/+ (blue) and Dsk7/Dsk7 (red) mice. N numbers are indicated below each graph. A Kruskal-Wallis test with Dunn's correction for multiple comparisons was performed using GraphPad Prism 8.4.1.

5.3 Discussion

This chapter highlights that Dsk7 mice, which are a model for ADH2[125], mirror the calcitropic phenotypes of Nuf mice (model for ADH1[277]); however, there are significant differences when it comes to non-calcitropic phenotypes, such as glucose metabolism.

5.3.1 Fasted plasma biochemistry

My analysis of fasted terminal bleed plasma biochemistry reveals differences and similarities to that reported for non-fasted Dsk7 mice[125]. Male and female fasted and non-fasted Dsk7/+ and Dsk7/Dsk7 mice had hypocalcaemia and hyperphosphataemia. These abnormalities are similar to those reported for mice with a gain-of-function CaSR mutation (Nuf)[123,277] and mice with hypocalcaemia due to an Arg60Cys $G\alpha_{11}$ mutation[124]. However, several additional abnormalities were observed for fasted Dsk7 mice compared to non-fasted: male Dsk7/+ and Dsk7/Dsk7 mice also had significantly decreased levels of magnesium, and male Dsk7/Dsk7 mice had decreased levels of chloride. In addition, male Dsk7/Dsk7 mice also had increased levels of total protein,

albumin, creatinine (which may be indicative of dehydration) and AST. Female Dsk7/+ had significantly increased plasma albumin levels, and female Dsk7/Dsk7 mice had significantly decreased levels of levels of chloride and increased levels of sodium and HDL. This indicates that fasting is important to see the full extent of biochemical abnormalities.

Starvation may have a greater effect on the biochemistry of Dsk7 mice because of the reduced viability and lower body weight of Dsk7/Dsk7 mice, which have been reported in previous studies[36,125] and were also confirmed in this chapter (Table 5.1 and Figure 5.2, respectively). Indeed, fasting studies in humans have reported decreases in magnesium and chloride levels, and increases in sodium levels[278]. Interestingly, hypomagnesaemia is present in: patients with ADH[82]; knock-in mice of the human ADH1 mutations CaSR Cys129Ser and Ala843Glu[116]; and fasted Dsk7 mice. In contrast, no significant changes were observed for non-fasted Dsk7[125] and Nuf[123] mice.

Due to the normal urinary calcium excretion of Dsk and other gain-of-function $G\alpha_{11}$ mice[124,125], and the mild urine biochemistry alterations seen in ADH2 patients[82,93,117,211,220,260], it has been suggested that in the renal tubules the CaSR couples to G proteins other than $G\alpha_{11}$[113,125]. However, fasted male and female Dsk7/Dsk7 mice had decreased plasma levels of magnesium and chloride, which have been associated with renal CaSR activation[99,279], suggesting $G\alpha_{11}$ may in fact contribute to CaSR function in the kidneys.

5.3.2 Glucose metabolism

The CaSR is highly expressed in pancreatic α- and ß-cells[91] and has been reported to be involved in insulin secretion[150,151]. However, the role of the CaSR in systemic glucose homeostasis is unclear (see section 1.5.2). Although studies in FHH patients showed no association between CaSR loss-of-function mutations and alterations in glucose

tolerance or insulin secretion[154], it has been suggested that ADH, but not FHH, may be associated with alterations in glucose metabolism because Nuf mice, which are a model for ADH1, develop severe impairment of pancreatic islet architecture and glucose homeostasis. The latter was rectified by the negative CaSR modulator Ronacaleret[134]. However, impaired glucose homeostasis has not been studied, to date, in humans with ADH.

Dsk7 mice, which harbour a gain-of-function $G\alpha_{11}$ mutation, mirror the calcitropic phenotype of the Nuf mice[125], and the aim of this chapter was to investigate whether $G\alpha_{11}$ gain-of-function causes similar abnormalities in glucose homeostasis as CaSR gain-of-function.

My findings indicate that $G\alpha_{11}$ gain-of-function does not result in baseline plasma glucose concentrations that are significantly different from WT. This is in agreement with observations in Nuf mice where such differences were also not observed[134]. Moreover, male Dsk7/Dsk7 mice had significantly greater baseline plasma glucose concentrations than female Dsk7/Dsk7 mice. Similarly, male Nuf/Nuf mice had significantly greater baseline plasma glucose values than female Nuf/Nuf littermates. However, in contrast to the Nuf mice, Dsk7 mice did not show impaired glucose tolerance in IPGTTs. Moreover, unlike Nuf mice, Dsk7 mice have normal pancreatic islet number and size. Assessment of individual islet architecture revealed no differences in α- and ß-cell number compared to WT. In contrast, Nuf/Nuf mice had significantly fewer ß-cells and significantly more α-cells compared to WT.

Some differences in Dsk7 islet proliferation (assessed by Ki-67 staining) were observed, however, these were gender specific. Thus, male Dsk7/Dsk7 and Dsk7/+ mice had significantly reduced proliferation of insulin negative (predominantly α) cells, and male Dsk7/Dsk7 mice had significantly reduced proliferation of insulin positive (ß) cells,

whereas no differences in proliferation were observed for female mice, and gender pooled data. For insulin positive cells, my data agree with studies in Nuf mice, which showed that Nuf/Nuf and Nuf/+ mice had significantly reduced ß-cell proliferation, although gender specific data were not reported[134]. However, Nuf/Nuf mice had significantly increased proliferation of insulin negative cells, which is in contrast to observations in male Dsk7/Dsk7 and Dsk7/+ mice. Because Dsk7/Dsk7 mice have reduced viability and body weight, the observed reduction in pancreatic islet proliferation is likely to be a reflection of systemic proliferation defects, rather than a pancreas specific effect. In contrast, Nuf mice have normal body weight[134], and therefore the observed growth impairment of the Dsk7 mice is likely due to interactions with receptors other than the CaSR, and highlights the importance of $G\alpha_{11}$ for normal physiology. Overall, the results of this chapter indicate that Dsk7 mice mirror the calcitropic effects of Nuf mice; however, both Nuf and Dsk7 mice have unique non-calcitropic phenotypes. (summarised in Table 5.3).

Specifically, Nuf mice have cataracts, ectopic calcifications, and impaired glucose tolerance, which is not observed in Dsk7 mice. In turn, Dsk7 mice have reduced viability, reduced body weight and dark skin, which are not observed in Nuf mice. I therefore suggest that non-calcitropic effects observed in the Dsk7 mice are likely to be mediated by GPCRs other than the CaSR. This is supported by my analysis of $G\alpha_{q/11}$ coupled GPCRs in 4.3.3 which revealed a total of 94 receptors that have been reported to be primarily coupled to $G\alpha_{q/11}$ and demonstrated that disease-causing $G\alpha_{11}$ mutations also affect signalling by the M_3R.

The increased skin pigmentation of Dsk7 mice may be mediated by the melanocortin receptor 1 (MC_1R) which is a key regulator of pigmentation[280,281] and has been reported to couple to $G\alpha_{q/11}$[207]. Moreover, constitutively activating $G\alpha_{q/11}$ mutations cause uveal

melanoma in humans[33]. Similarly, MC_1R loss-of-function mutations in humans are associated with fair skin and increased melanoma risk[280,282].

Notably, reduced viability and dark skin were also observed in mice harbouring a $G\alpha_{11}$ mutation that causes ADH2 in humans (Arg60Cys)[124] and therefore seems to be a general feature of $G\alpha_{11}$ gain-of-function. In contrast, $G\alpha_{11}$ Arg60Cys mice did not have lower body weight, suggesting this feature may be specific to $G\alpha_{11}$ Ile62Val or due to strain differences (C3H versus C57BL/6). However, in humans the gain-of-function $G\alpha_{11}$ mutations Arg60Lys and Val340Met are associated with short stature[117,118].

Table 5.3 Comparison of phenotypes between human ADH1/2 patients, Nuf mice (model for ADH1), and Dsk7 and R60C mice (models for ADH2).

Feature	Human ADH1	Human ADH2	Nuf mice	DSK7 mice	R60C mice
Hypocalcaemia	✓	✓	✓ HOM 1.62 mmol/L	✓ HOM 1.72 mmol/L	✓
Hyperphosphataemia	✓	✓	✓	✓	✓
Hypomagnesaemia	✓	✓	X	Only when fasted	✓
Activating CaSR mutation	✓	X	✓, Leu723Gln	X	X
Activating $G\alpha_{11}$ mutation	X	✓	X	✓, Ile62Val	✓ Arg60Cys
Low PTH	✓	✓	✓	✓	✓
Hypercalciuria	✓	✓	✓	X	X
Impaired glucose tolerance	?	?	✓	X	?
Reduced islet mass	?	?	✓	X	?
Abnormal α to ß-cell ratio	?	?	✓	X	?
Reduced weight/height	X	✓	X	✓	X
Reduced viability	?	?	X	✓	✓
Dark skin	?	?	X	✓	✓

Interestingly, mice lacking $G\alpha_{q/11}$ expression in the paraventricular nucleus of the hypothalamus (PVN) develop obesity due to hyperphagia[283]. The observed reduction in body weight observed for Dsk7/Dsk7 mice (which have increased $G\alpha_{11}$ activity) may therefore be associated with feeding behaviour.

Conversely, non-calcitropic effects of Nuf mice are likely to be mediated by G proteins other than $G\alpha_{11}$ or could be G protein independent. The latter is supported by a study with the PAM R-467, which stimulated insulin secretion in mouse islets and the ßHC9 cell line, and this was suggested to be independent of $G\alpha_i$, $G\alpha_o$, $G\alpha_{q/11}$ and $G\alpha_s$[155].

Moreover, the ratio of $G\alpha_{q/11}$ family member expression varies across tissues[81,93,275,276]. This indicates that in some tissues abnormal signalling by $G\alpha_{11}$ may be compensated by $G\alpha_q$, whereas it causes a phenotype in others. Interestingly, the pancreas is one of few tissues where $G\alpha_{14}$ is expressed, making it a potential mediator of CaSR functions in islets[6].

In conclusion, the findings of this chapter indicate that $G\alpha_{11}$ gain-of-function does not influence glucose homeostasis or pancreatic islet architecture. Thus, the glucose phenotype observed in the Nuf mice is likely transduced by G proteins other than $G\alpha_{11}$ or is due to G protein independent mechanisms.

6 DIFFERENCES BETWEEN *GNA11* AND *GNAQ*

6.1 Aims

In recent years, there has been increasing interest in studying G protein signalling at the level of the individual subunit (see 3.8.6)[162].

Interestingly, despite the high sequence homology of $G\alpha_q$ and $G\alpha_{11}$ (see section 1.1.2.1), loss- and gain-of function mutations in *GNA11 (and not in GNAQ)* cause FHH2[93,108,109] and ADH2[93,117,211,260] (see section 1.4). In contrast, somatic, constitutively active mutations of *GNA11* and *GNAQ* have been shown to cause both uveal melanoma[33] and congenital haemangioma[34].

The aims of this chapter were to: investigate mutations in *GNAQ* as a potential novel cause for FHH/ADH; study the mechanisms by which FHH2-causing loss-of-function $G\alpha_{11}$ mutations can be compensated by $G\alpha_q$ or positive allosteric CaSR modulators; and explore for differences between $G\alpha_q$ and $G\alpha_{11}$.

To study functional effects *in vitro*, I used a range of CaSR signalling assays (illustrated in Figure 6.1) which included: upstream assays such as ebBRET and NanoBit PLC; amplified responses like Fluo-4 calcium mobilisation; and downstream transcriptional readouts such as SRE and NFAT-RE luciferase reporter assays.

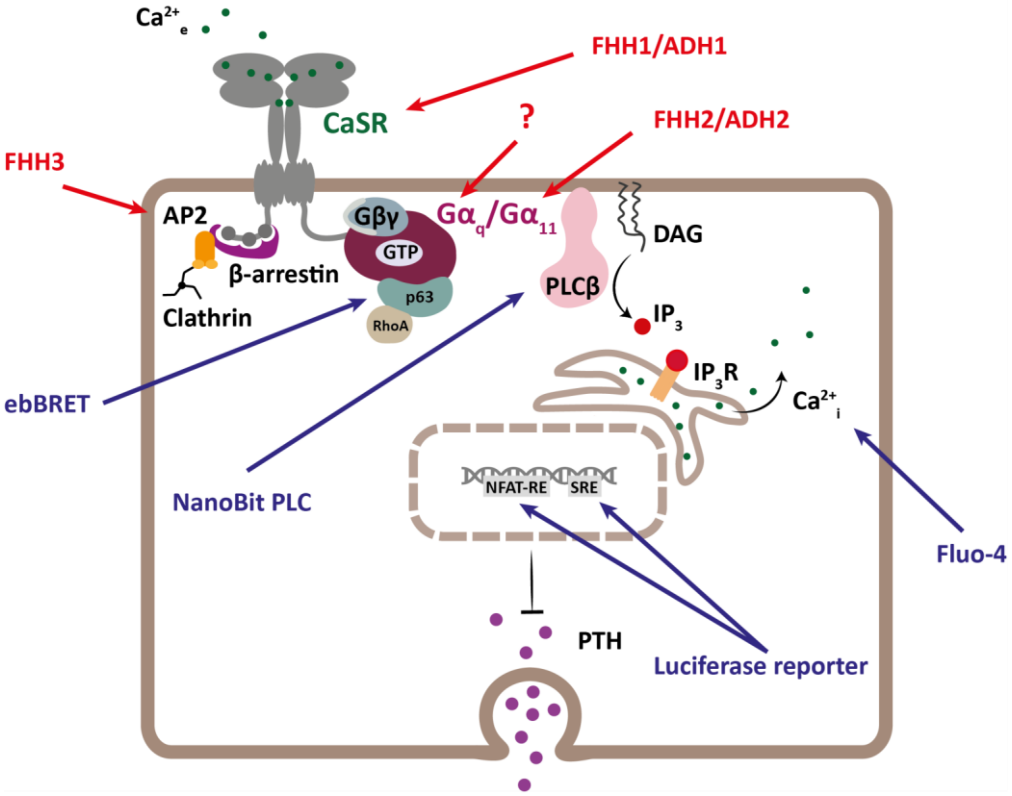


Figure 6.1 Overview of CaSR-mediated signalling and downstream assays used in this chapter[28,77,227]. Stimulation of the calcium-sensing receptor (CaSR) by extracellular calcium (Ca^{2+}_e) leads to GTP binding by $G\alpha_{q/11}$ which results in dissociation from Gßγ. GTP-bound $G\alpha_{q/11}$ recruits the p63RhoGEF (p63) which was measured using ebBRET assays. $G\alpha_{q/11}$ also activates Phospholipase C beta (PLCß) which subsequently catalyses hydrolysis of Phosphatidylinositol 4,5-bisphosphate (PIP_2) to diacylglycerol (DAG) and Inositol trisphosphate (IP_3). IP_3 binds IP_3 receptors (IP_3R) to release calcium from intracellular stores which was measured using Fluo-4 calcium mobilisation assays (Fluo-4). Moreover, calcium, DAG and p63 activate the map kinase (MAPK) pathway. Transcriptional changes downstream of MAPK were measured using a Serum Response Element (SRE) luciferase reporter assay. Calcium also induces calcineurin (CaN) binding of calmodulin (CALM) which induces the transcription factor Nuclear Factor of Activated T-cells (NFAT) which binds to Nuclear Factor of Activated T-cells Response Element (NFAT-RE). NFAT-RE was detected using luciferase reporter assays. Transcriptional changes lead to inhibition of parathyroid hormone (PTH) secretion.

6.2 Results

6.2.1 Investigation of *GNAQ* as a candidate gene for FHH/ADH

6.2.1.1 Mutational analysis of *GNAQ* in FHH and ADH patients

To investigate the possibility that *GNAQ* mutations cause FHH and/or ADH, a cohort of 20 FHH and 17 ADH patients that were negative for mutations in *CASR*, *GNA11* and *AP2S1* was examined. Patient leukocyte DNA was investigated for mutations within the seven exons, exon-intron boundaries and untranslated regions of *GNAQ* by Sanger sequence analysis (performed by Manesh Modi, University of Oxford). No mutations were identified in the coding or non-coding regions of *GNAQ*. Binomial probability analysis, as previously described[284,285], indicated that the likelihood of detecting at least one disease-causing *GNAQ* mutation was ≥98.85% and ≥97.75%, respectively, using the assumption that mutations in *GNAQ* would occur at a prevalence of 20% in FHH and ADH patients negative for mutations in *CASR*, *GNA11* and *AP2S1*. I therefore concluded that mutations in *GNAQ* are unlikely to cause FHH and ADH, and if they do, it must be rare.

6.2.1.2 Characterisation of rare *GNAQ* variants in the DiscovEHR cohort

To study the role of rare *GNAQ* variants in calcium homeostasis, I investigated the DiscovEHR cohort[254], which comprises exomes of 50,726 patients with matched clinical records (see 3.12). In this cohort, I identified six missense variants in *GNAQ*, which resulted in the following amino acid changes: Arg19Trp, Ala110Val, Gln299His, Ala302Ser, Ala331Thr and Val344Ile. All residues were conserved in $G\alpha_q$ orthologs, and all residues apart from Arg19 were also conserved in $G\alpha_{11}$ (Figure 6.2). Mean serum calcium values of the patients were within the normal range (Table 6.1).

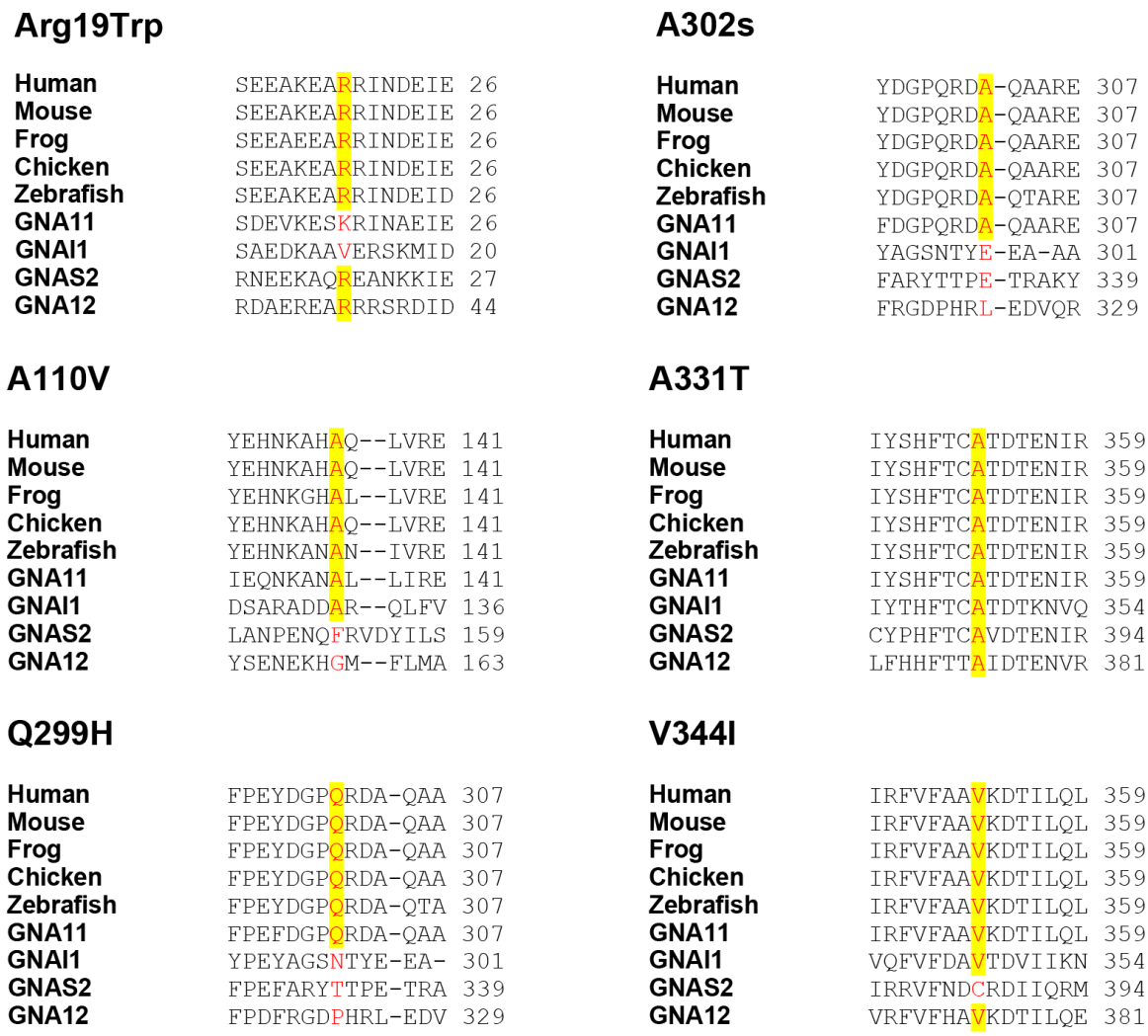


Figure 6.2 Evolutionary conservation of *GNAQ* variants found in the DiscovEHR cohort in $G\alpha_q$ orthologs and Gα paralogs. The residue of interest is highlighted in yellow. The numbers on the right-hand side indicate amino acid positions. All 6 variants are fully conserved in $G\alpha_q$ orthologs (mouse, frog, chicken, zebrafish). In addition, Ala331Thr is also conserved in Gα paralogs *(GNA11*, *GNAI1*, *GNAS2*, *GNA12)*.

Table 6.1 Genotypes and Phenotypes of patients with *GNAQ* variants from the DiscovEHR cohort

Nucleotide change	Amino acid change	Mean serum calcium (mg/dl)[b]
c.55C>T	p.Arg19Trp	8.92
c.329C>T	p.Ala110Val	9.80
c.897G>C	p.Gln299His	9.15/9.60
c.904G>T	p.Ala302Ser	9.95
c.991G>A	p.Ala331Thr	8.28
c.1030G>A	p.Val344Ile	8.88

[b] Mean serum calcium values. Normal range=8.30–10.00 mg/dL, which is defined as the mean±2 standard deviations.

To assess the functional consequences of the variants, the cDNA of WT *GNAQ* was cloned into an existing pBI-CMV2 vector[93] to allow simultaneous expression of $G\alpha_q$ and GPF (established by Dr. Mark Stevenson (University of Oxford)). Subsequently, site-directed mutagenesis to introduce the six missense mutations was performed (by Dr. Sara Falcone (University of Oxford)).

$Ga_{q/11}$ is ubiquitously expressed, therefore in order to selectively determine the effects of the variants, I used HEK293A cells that were modified by CRISPR/CAS9 to lack expression of endogenous $G\alpha_q$ or $G\alpha_{11}$[209] and stably express the CaSR (HEK293A$G\alpha_{q/11}$-KO-CaSR cells). These cells were transfected with either WT or variant $G\alpha_q$. Successful transfection was confirmed by immunofluorescence microscopy (Figure 6.3). Western blot analysis showed that all variants had similar protein expression to WT $G\alpha_q$ (Figure 6.4).

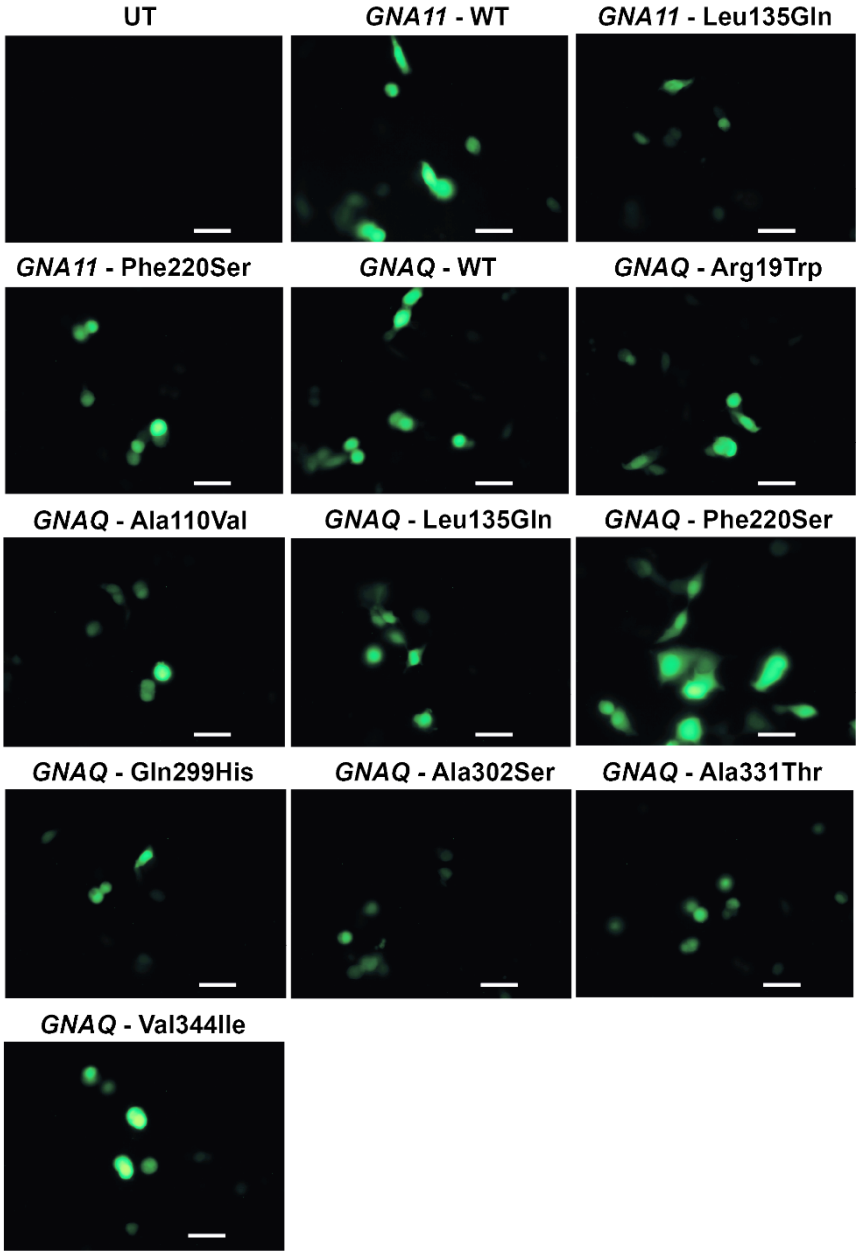


Figure 6.3 Immunofluorescence microscopy of cells transfected with pBI-CMV2 constructs. GFP expression (green) shows successfully transfected cells.

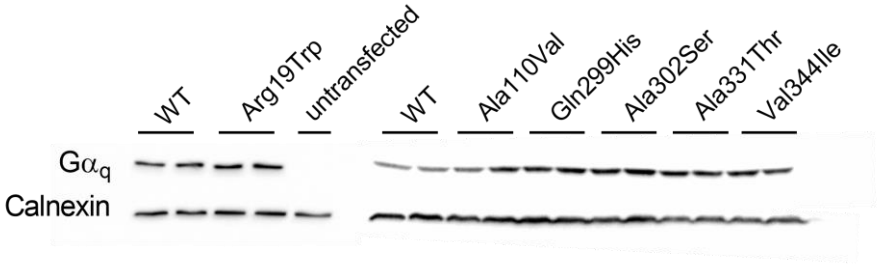


Figure 6.4 $G\alpha_q$ variants Arg19Trp, Ala110Val, Gln299His, Ala302Ser, Ala331Thr and Val344Ile are expressed at similar levels to WT $G\alpha_q$, as determined by western blot analysis of lysates from transfected HEK293A$G\alpha_{q/11}$-KO-CaSR cells. Calnexin was used as a loading control. Western blots were performed by Dr. Sara Falcone (University of Oxford).

The effect of the variants on CaSR-mediated signalling were assessed using Serum Response Element (SRE) (Figure 6.5A) and Nuclear Factor of Activated T-cells response element (NFAT-RE) (Figure 6.5B) luciferase reporter assays, and Fluo-4 calcium mobilisation assays (Figure 6.5C). HEK293A$G\alpha_{q/11}$-KO-CaSR cells were transfected with either WT or variant $G\alpha_q$, and signalling activity in response to increasing concentrations of $CaCl_2$ was measured. In all three assays, the variants showed no significant difference to WT $G\alpha_q$ responses. Therefore, I found no evidence that *GNAQ* is associated with abnormal plasma calcium, and rare *GNAQ* variants that were found in a large population database did not cause CaSR signalling abnormalities. These combined results indicate that variants in *GNAQ* are unlikely to be FHH or ADH-causing mutations.

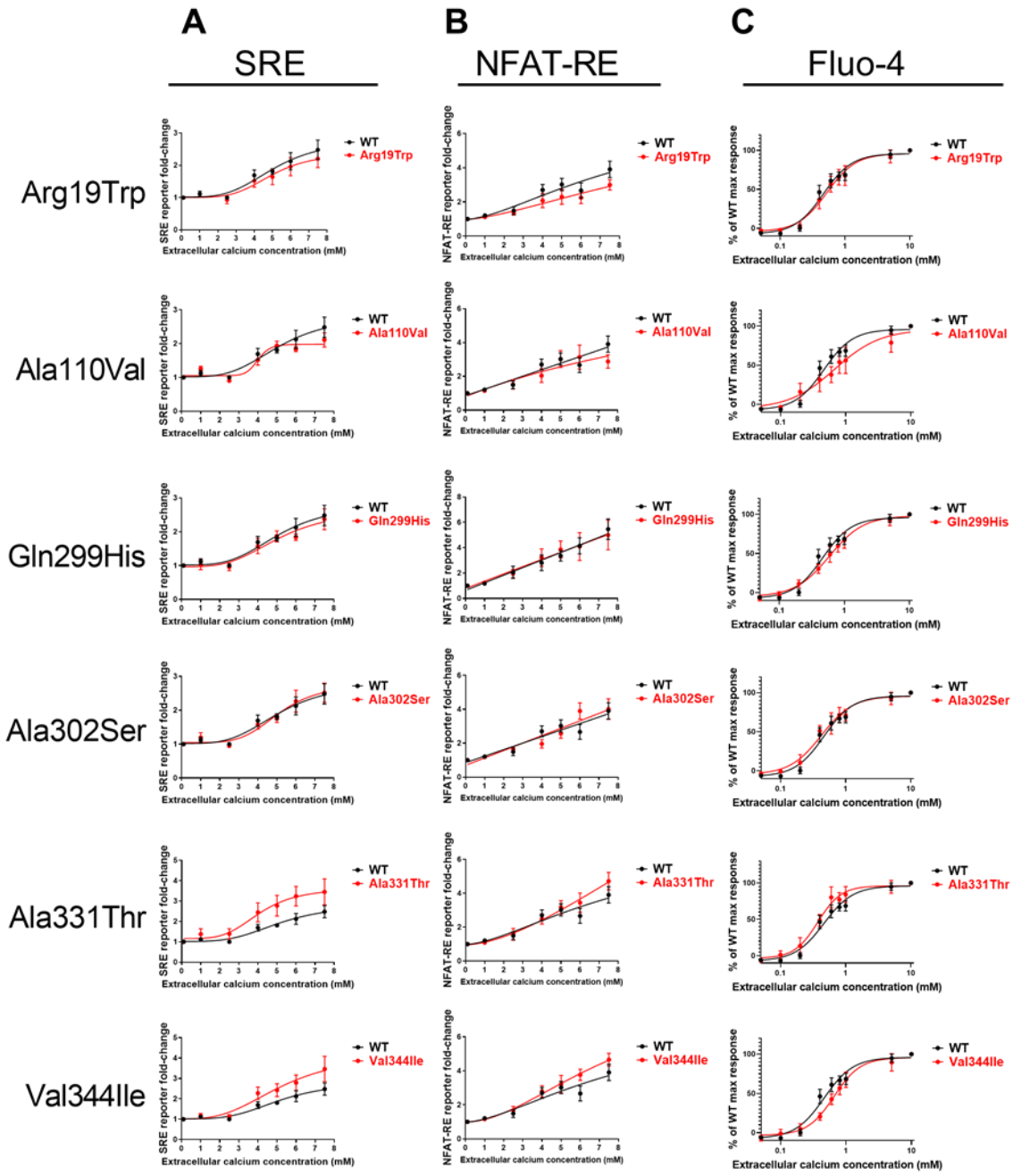


Figure 6.5 (A) SRE luciferase reporter assays, (B) NFAT-RE assays and (C) Fluo-4 calcium mobilisation assays showed no significant differences in response to increasing concentrations of extracellular calcium between variant (red line) and WT (black line) $G\alpha_q$. Values are shown as mean±SEM of 4-8 independent transfections. Two-way ANOVA with Sidak correction for multiple comparisons was performed using GraphPad Prism 8.4.1. Fluo-4 assays were performed by Dr. Mark Stevenson (University of Oxford).

6.2.2 Differences between $G\alpha_q$ and $G\alpha_{11}$

6.2.2.1 Expression across tissues

To investigate potential differences between $G\alpha_q$ and $G\alpha_{11}$ across a range of tissues, I obtained normalised mRNA expression data from three different transcriptomics datasets (FANTOM[275], GTEX[276], HPA[81]) from the human protein atlas (http://www.proteinatlas.org). I investigated a total of 21 human tissues for differences between *GNAQ* and *GNA11* mRNA expression (Figure 6.6). No tissue shows significantly lower *GNA11* expression compared to *GNAQ* expression. *GNA11* is expressed at significantly higher levels than *GNAQ* in human colon (2.6-fold, $p<0.01$), heart muscle (1.6-fold, $p<0.05$), skeletal muscle (4.7-fold, $p<0.05$), and small intestine (10-fold, $p<0.0001$). None of these tissues are primarily involved in CaSR-mediated suppression of PTH secretion. The two tissues most relevant for human calcium homeostasis are parathyroid glands and the kidneys. No significant difference between *GNAQ* and *GNA11* was observed in the kidneys. Expression data for the parathyroid glands was only available for the HPA dataset, which showed similar expression of *GNAQ* and *GNA11*. In this dataset, the CaSR was expressed approximately 40-fold higher in the parathyroid gland than in the kidneys. $G\alpha_q$ and $G\alpha_{11}$ protein expression across tissues could not be analysed because currently there are no antibodies available that selectively recognise $G\alpha_{11}$ over $G\alpha_q$, and vice versa.

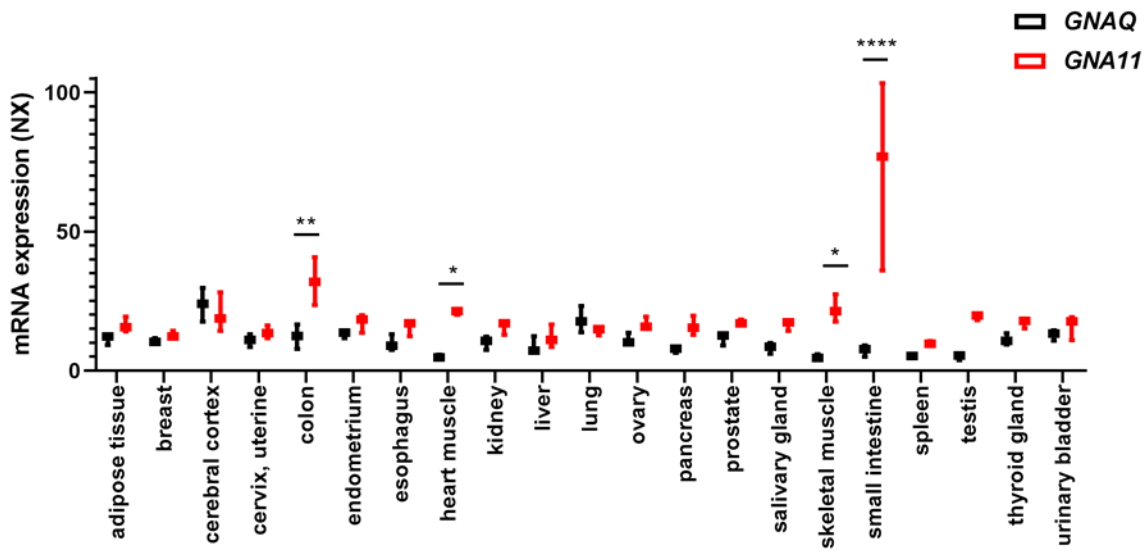


Figure 6.6 Normalised mRNA expression (NX) of *GNAQ* and *GNA11* across 21 tissues obtained from the FANTOM, GTEX and HPA RNA-Seq datasets. *GNAQ* mRNA expression is indicated in black, *GNA11* mRNA expression is indicated in red. In colon, heart muscle, skeletal muscle and small intestine *GNA11* was expressed at significantly higher levels than *GNAQ*. Ordinary one-way ANOVA with Tukey correction for multiple comparisons was performed using GraphPad Prism 8.4.1. *p<0.05, ***p<0.001, ****p<0.0001.

6.2.2.2 Functional differences

6.2.2.2.1 Functions effects of FHH2-causing mutations in $G\alpha_q$

To investigate whether equivalent mutations have the same functional effects in $G\alpha_q$ and $G\alpha_{11}$, two FHH2-causing $G\alpha_{11}$ mutations that are conserved in $G\alpha_q$ were selected and the equivalent mutations were engineered in $G\alpha_q$: Leu135Gln[93], which is located in the helical domain; and Phe220Ser[109], which is located in the GTPase domain (Figure 6.7).

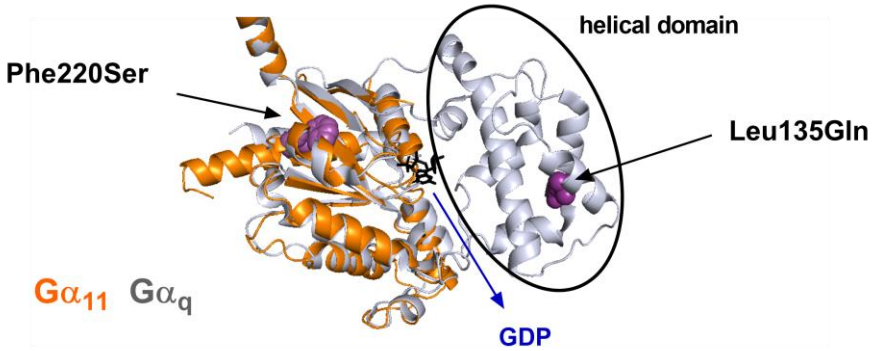


Figure 6.7 Alignment of the $G\alpha_{11}$ GTPase domain (orange) (PDB code 6OIJ) and the GDP (black) bound structure of $G\alpha_q$ (grey) (PDB code 3AH8). The helical domain is indicated by a black circle. The blue arrow shows the direction of GDP-GTP exchange during G protein activation. The Leu135Gln and Phe220Ser mutations are indicated by arrows.

To assess the effects of $G\alpha_q$ Leu135Gln and Phe220Ser on CaSR signalling, I expressed the mutants in HEK293A-$G\alpha_{q/11}$-KO-CaSR cells. Both the experimental $G\alpha_q$ and the FHH2-causing $G\alpha_{11}$ mutations were expressed at similar levels to WT, as shown by western blot analysis (Figure 6.8).

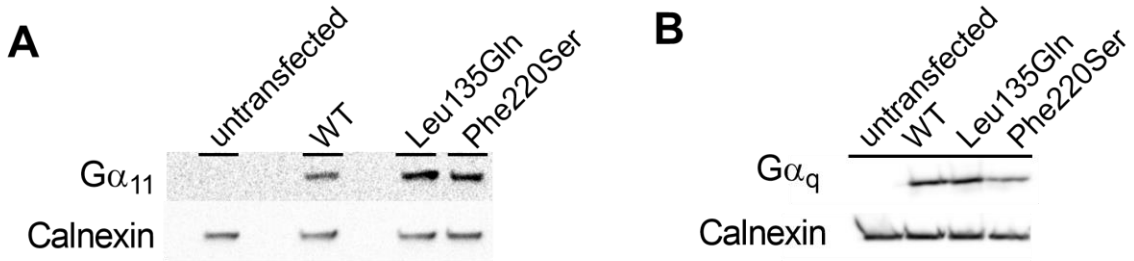


Figure 6.8 (A) FHH2-causing $G\alpha_{11}$ mutations Leu135Gln and Phe220Ser and (B) engineered $G\alpha_q$ variants Leu135Gln and Phe220Ser are expressed at similar levels to WT $G\alpha_{11}$ and $G\alpha_q$, respectively, as shown by western blot analysis of HEK293A$G\alpha_{q/11}$-KO-CaSR cells, transiently transfected with pBI-CMV2 constructs. The blot shown in panel B was generated by Dr. Sara Falcone (University of Oxford).

To assess functional effects of the mutations on CaSR signalling I treated cells with increasing concentrations of extracellular calcium (Ca^{2+}_e) and performed SRE and NFAT-RE luciferase reporter assays, and Fluo-4 calcium mobilisation assays (Figure 6.9). This revealed that $G\alpha_{11}$ Leu135Gln showed: up to 6-fold reduction in signalling response in SRE luciferase reporter assays ($p<0.0001$); up to 5.9-fold reduction in signalling response in NFAT-RE luciferase reporter assays ($p<0.0001$); and up to 4.9-fold reduction in Fluo-4 calcium mobilisation assays ($p<0.0001$) (Figure 6.9A). In contrast, $G\alpha_q$ Leu135Gln showed no significant differences in signalling responses when compared to WT $G\alpha_q$ in all three assays (Figure 6.9B).

In addition, $G\alpha_{11}$ Phe220Ser showed: up to 3.6-fold reduction in signalling response in SRE luciferase reporter assays ($p<0.0001$); up to 4-fold reduction in signalling response in NFAT-RE luciferase reporter assays at ($p<0.01$); and up to 9.6-fold reduction in Fluo-4 calcium mobilisation assays ($p<0.0001$) (Figure 6.9C). In contrast, $G\alpha_q$ Phe220Ser showed no differences in signalling responses in SRE and NFAT-RE luciferase reporter assays.

In Fluo-4 calcium mobilisation assays, $G\alpha_q$ Phe220Ser showed up to 5.7-fold reduced responses ($p<0.0001$) compared to WT $G\alpha_q$ (Figure 6.9D); however, the magnitude of the loss-of-function for $G\alpha_q$ Phe220Ser was much smaller than the loss-of-function for $G\alpha_{11}$ Phe220Ser (5.7-fold reduction for $G\alpha_q$ compared to 9.6-fold reduction for $G\alpha_{11}$), and significant differences were only observed at 0.4, 0.6 and 0.8mM Ca^{2+}_e (as opposed to 0.2, 0.4, 0.6, 0.8 and 1 mM Ca^{2+}_e for $G\alpha_{11}$). These data demonstrate that Leu135Gln is exclusively a loss-of-function mutation in $G\alpha_{11}$ but not in $G\alpha_q$. They also demonstrate that Phe220Ser has a more severe loss-of-function effect in $G\alpha_{11}$ than it does in $G\alpha_q$ and does not affect transcriptional changes downstream of CaSR signalling.

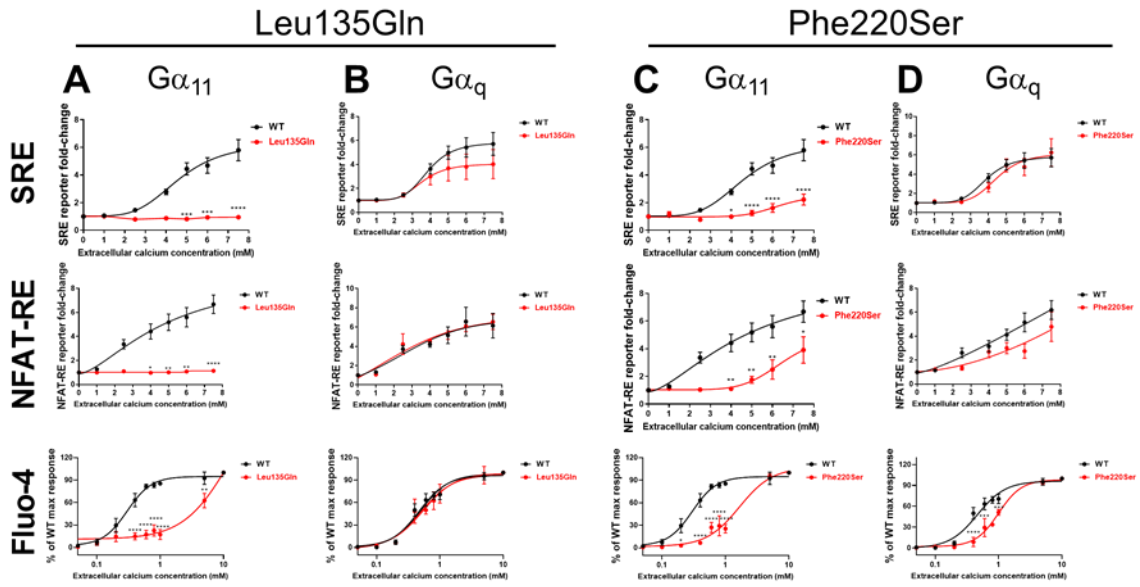


Figure 6.9 (A) $G\alpha_{11}$ Leu135Gln shows significantly lower calcium-induced responses in SRE luciferase reporter assays, NFAT-RE reporter assays, and Fluo-4 calcium mobilisation assays when compared to WT $G\alpha_{11}$. In contrast, (B) no significant differences were observed for $G\alpha_q$ Leu135Gln in SRE luciferase reporter assays, NFAT-RE reporter assays and Fluo-4 calcium mobilisation assays when compared to WT $G\alpha_q$. (C) $G\alpha_{11}$ Phe220Ser shows significantly lower calcium-induced responses compared to WT $G\alpha_{11}$ in SRE luciferase reporter assays, NFAT-RE reporter assays and Fluo-4 calcium mobilisation assays. (D) For $G\alpha_q$ Phe220Ser no significant differences were observed in SRE luciferase reporter assays and NFAT-RE reporter assays. In contrast, Fluo-4 calcium mobilisation responses were significantly reduced. WT responses are indicated by a black line and variant responses are indicated by a red line. Values are shown as mean±SEM of 3-16 independent transfections. Two-way ANOVA with Sidak correction for multiple comparisons was performed using GraphPad Prism 8.4.1. Fluo-4 assays were performed by Dr. Mark Stevenson (University of Oxford).

6.2.2.2.2 $G\alpha_q$ and $G\alpha_{11}$ interaction with the effector PLC

Phospholipase Cβ (PLCβ) is the main effector of $G\alpha_{q/11}$[286]. I therefore investigated differences between $G\alpha_q$ and $G\alpha_{11}$ in their interaction with PLCβ. I used a NanoBit split luciferase approach[207], in which the Gα subunit was tagged with the large bit, either

between amino acids 97 and 98 (97,98-Lg) or 123 and 124 (123,124-Lg), and PLCß2 and ß3 were tagged N-terminally with the small bit (see methods section 3.8.2). Upon CaSR-mediated activation of $G\alpha_q$, the large- and small bit tags complemented each other, leading to an increase in luciferase activity.

I confirmed protein expression of the tagged Gα subunits HEK293A$G\alpha_{q/11}$-KO-CaSR cells using Western blot analysis. $G\alpha_{11}$(97,98-Lg) were expressed at similar levels to $G\alpha_{11}$(123,124-Lg), and likewise $G\alpha_q$(97,98-Lg) expression was similar to that of $G\alpha_q$(123,124-Lg) (Figure 6.10).



Figure 6.10 (A) Western blot showing $G\alpha_{11}$ protein expression in HEK293$G\alpha_{q/11}$-KO-CaSR cells transfected with NanoBit sensors pcDNA3.1-*GNA11*(97,98)-LgBiT, and pcDNA3.1-*GNA11*(97,98)-LgBiT. Glyceraldehyde 3-phosphate dehydrogenase (GAPDH) was used as a loading control. (B) Western blot showing $G\alpha_q$ protein expression in HEK293$G\alpha_{q/11}$-KO-CaSR cells transfected with NanoBit sensors pcDNA3.1-*GNAQ*(97,98)-LgBiT, pcDNA3.1-*GNAQ*(123,124)-LgBiT. GAPDH was used as a loading control.

To assess the interaction between $G\alpha_{q/11}$ and PLCß2/3 upon stimulation, live cells were treated with increasing concentrations of $CaCl_2$ and changes in Luminescence signal were measured. The largest increase was observed with $G\alpha_q$(123,124-Lg) and (N-sm)-PLCß2 (Figure 6.11D) with a maximum fold change of 3.2 compared to control ($p<0.0001$). Luminescence signal was also significantly greater than control for

$G\alpha_q$(123,124-Lg) and (N-sm)-PLC ß3 (Figure 6.11H, p<0.0001), and $G\alpha_q$ (97,98-Lg) and (N-sm)-PLC ß2 (Figure 6.11C) (p<0.0001).

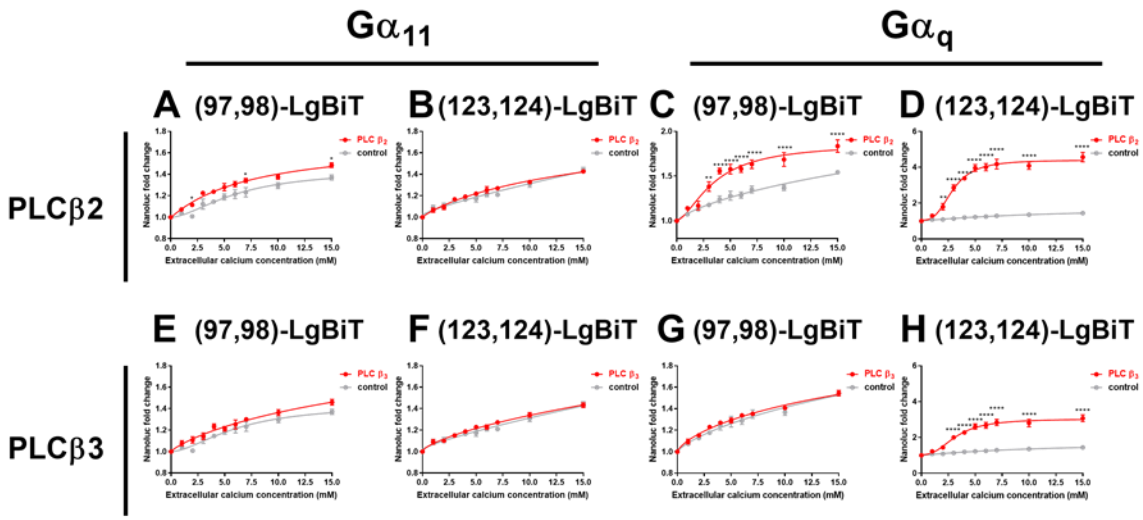


Figure 6.11 (A) Calcium-induced Nanoluc responses are significantly increased for cells transfected with $G\alpha_{11}$(97,98)-LgBiT and PLCß$_2$(N)SmBiT, compared to control. (B) Responses are not significantly different between cells transfected with $G\alpha_{11}$(123,124)-LgBiT and PLCß$_2$(N)SmBiT and control. (C) Nanoluc responses, compared to control, are significantly increased between $G\alpha_q$(97,98)-LgBiT and PLCß$_2$(N)SmBiT. (D) Calcium-induced Nanoluc responses showing significantly increased interaction between cells transfected with $G\alpha_q$(123,124)-LgBiT and PLCß$_2$(N)SmBiT, compared to control. (E) No significant difference in Calcium-induced Nanoluc response was observed between cells transfected with $G\alpha_{11}$(97,98)-LgBiT and PLCß$_3$(N)SmBiT, and control. (F) Calcium-induced Nanoluc responses showing no significant difference in interaction between cells transfected with $G\alpha_{11}$(123,124)-LgBiT and PLCß$_3$(N)SmBiT (G) Compared to control, calcium-induced Nanoluc responses show no significant difference in interaction between cells transfected with $G\alpha_q$(97,98)-LgBiT and PLCß$_3$(N)SmBiT (H) Calcium-induced Nanoluc responses showing significantly increased interaction between cells transfected with $G\alpha_q$(123,124)-LgBiT and PLCß$_3$(N)SmBiT, compared to control. Values are shown as mean±SEM of 4 independent transfections. Two-way ANOVA with Sidak correction for multiple comparisons was performed using GraphPad Prism 8.4.1. *p<0.05, **p<0.01, ***p<0.001, ****p<0.0001.

In contrast, for $G\alpha_{11}$ a significant increase was only observed for $G\alpha_{11}$ (97,98-Lg) and (N-sm)-PLC ß2 (Figure 6.11A) at 2, 7, and 15mm mM Ca^{2+}_e ($p<0.05$) and the maximum increase was only 1.1-fold, compared to control. No significant difference was seen for $G\alpha_{11}$ (123,124-Lg) with PLC ß2 (Figure 6.11B), $G\alpha_{11}$ (97,98-Lg) and (123,124-Lg) with PLC ß3 (Figure 6.11E,F) and $G\alpha q$ (97,98-Lg) with PLC ß3 (Figure 6.11G). These findings suggest that $G\alpha_q$ and $G\alpha_{11}$ interact with the effector PLC in a different orientation.

6.2.2.2.3 Stoichiometry

Recent studies have highlighted the importance of stoichiometry (i.e. the quantitative relationship between protein expression levels) for GPCR signalling[287]. I studied the effects of increasing amounts of $G\alpha_q$ and $G\alpha_{11}$ DNA, which resulted in increasing amounts of expressed protein as confirmed by western blot analysis (Figure 6.12) on CaSR signalling.

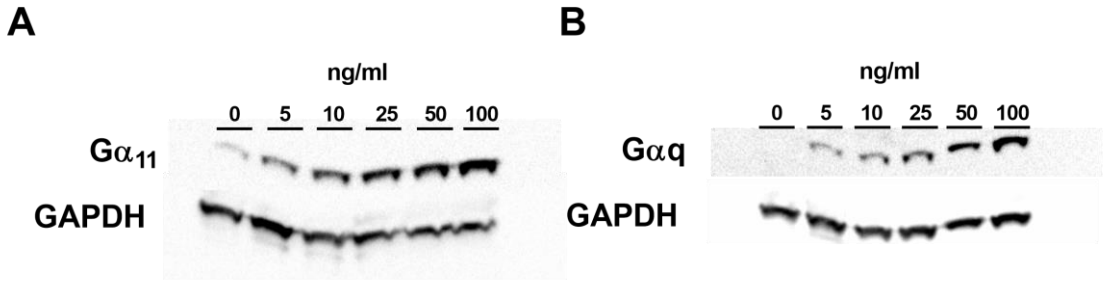


Figure 6.12 (A) Western blot showing that transfection of HEK293-Flp-In-Flag-CaSR cells with increasing amounts (ng/ml) of *GNA11* cDNA results in increased $G\alpha_{11}$ protein expression in HEK293-Flp-In-Flag-CaSR cells. GAPDH was used as a housekeeping protein. (B) Western blot showing that transfection of HEK293-Flp-In-Flag-CaSR cells with increasing amounts (ng/ml) of *GNAQ* cDNA results in increased $G\alpha_q$ protein expression. GAPDH was used as a housekeeping protein.

CaSR-mediated recruitment of p63RhoGEF, which is a specific effector of $G\alpha_{q/11}$, was assessed ebBRET assays. This revealed that increasing amounts of $G\alpha_q$ transfection resulted in higher signalling responses with the maximal response at 100ng/ml transfected DNA. In contrast, for $G\alpha_{11}$, the maximum response was reached at 10ng/ml, and higher concentrations led to a decrease in signalling despite more $G\alpha_{11}$ protein being produced (Figure 6.13).

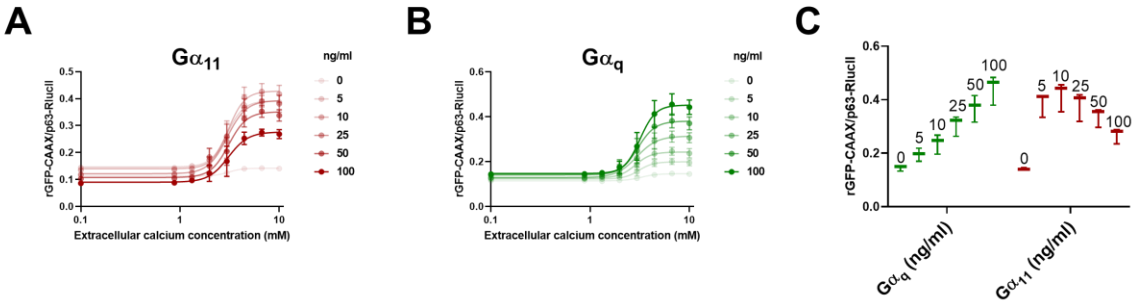


Figure 6.13 (A) Dose-response curves of BRET2 responses of increasing amounts of *GNA11* cDNA. Darker red shades indicate higher expression. (B) Dose-response curves of BRET2 responses of increasing amounts of *GNAQ* cDNA. Darker green shades indicate higher expression. (C) Maximal BRET2 responses (rGFP-CAAX signal divided by p63-RLucII) at 10mM extracellular calcium of increasing amounts of *GNAQ* (green) and *GNA11* (red) DNA. Values are shown as mean±SEM of 3 independent transfections.

6.2.3 Compensation of FHH-causing $G\alpha_{11}$ mutations

6.2.3.1 Compensation of FHH-causing $G\alpha_{11}$ mutations by $G\alpha_q$

Next, I co-expressed FHH2-causing loss-of-function $G\alpha_{11}$ mutations and WT $G\alpha_q$ and assessed functional effects in SRE and NFAT-RE luciferase reporter assays. Using HEK293A-$G\alpha_{q/11}$-KO-CaSR cells I showed that the $G\alpha_{11}$ mutations could be compensated by WT $G\alpha_q$ so that they were not significantly different from WT $G\alpha_{11}$ (Figure 6.14). Nevertheless, patients with $G\alpha_{11}$ loss-of-function mutations develop a phenotype,

indicating that stoichiometry of Gα subunits may be important for the pathogenesis of FHH2.

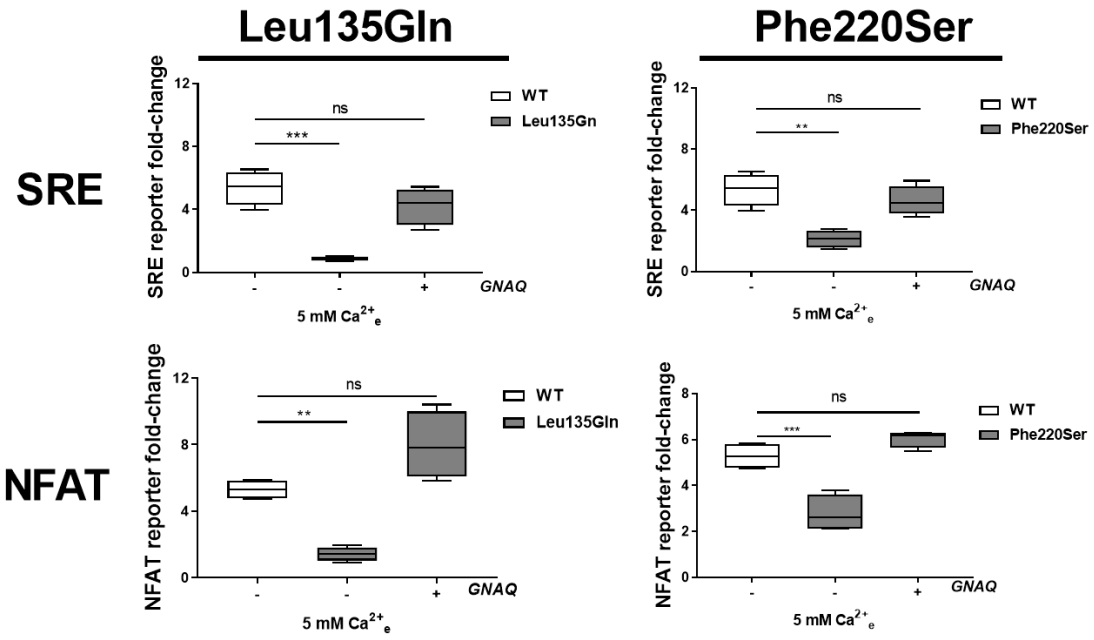


Figure 6.14 Aberrant responses of the FHH2-causing $G\alpha_{11}$ mutations Leu135Gln and Phe220Ser (grey boxes, minus sign) in HEK293$G\alpha_{q/11}$-KO-CaSR SRE (top row) and HEK293$G\alpha_{q/11}$-KO-CaSR NFAT-RE (bottom row) cells can be compensated by co-transfection with WT *GNAQ* (grey boxes, plus sign), so that the responses are not significantly different from WT $G\alpha_{11}$ (white boxes). Values are shown as mean±SEM of 4 independent transfections. Ordinary one-way ANOVA with Tukey correction for multiple comparisons was performed using GraphPad Prism 8.4.1. **p<0.01, ***p<0.001.

6.2.3.2 Compensation of FHH-causing $G\alpha_{11}$ mutations by cinacalcet

Allosteric modulators of the calcium-sensing receptor have been developed (see introduction section 1.6.3), with the positive allosteric modulator (PAM) cinacalcet being used in the clinic to treat secondary hyperparathyroidism due to renal failure[98].

Cinacalcet has also been shown to rectify hypercalcaemia *in vivo* in a patient with FHH2 caused by a germline loss-of-function mutation in *GNA11*, and rectified calcium-induced signalling abnormalities *in vitro* in HEK293-CaSR cells[109]. To investigate whether cinacalcet acts directly on the mutant $G\alpha_{11}$ or rectifies impaired signalling of the mutant $G\alpha_{11}$ by compensatory signalling via WT $G\alpha_{11}$ and/or WT $G\alpha_q$ (which is present endogenously in HEK293 cells and in the cells of the heterozygous patient), I investigated the effects of cinacalcet on the mutants in cells with no endogenous expression of $G\alpha_q$ (HEK293A-$G\alpha_{q/11}$-KO-CaSR cells). I showed that treatment with cinacalcet does not increase the signalling of loss-of-function $G\alpha_{11}$ mutants Leu135Gln and Phe220Ser at 5 mM Ca^{2+}_e (Figure 6.15). Therefore, it is likely that *in vivo*, cinacalcet rectifies signalling defects via compensatory signalling via WT $G\alpha_{11}$ and $G\alpha_q$.

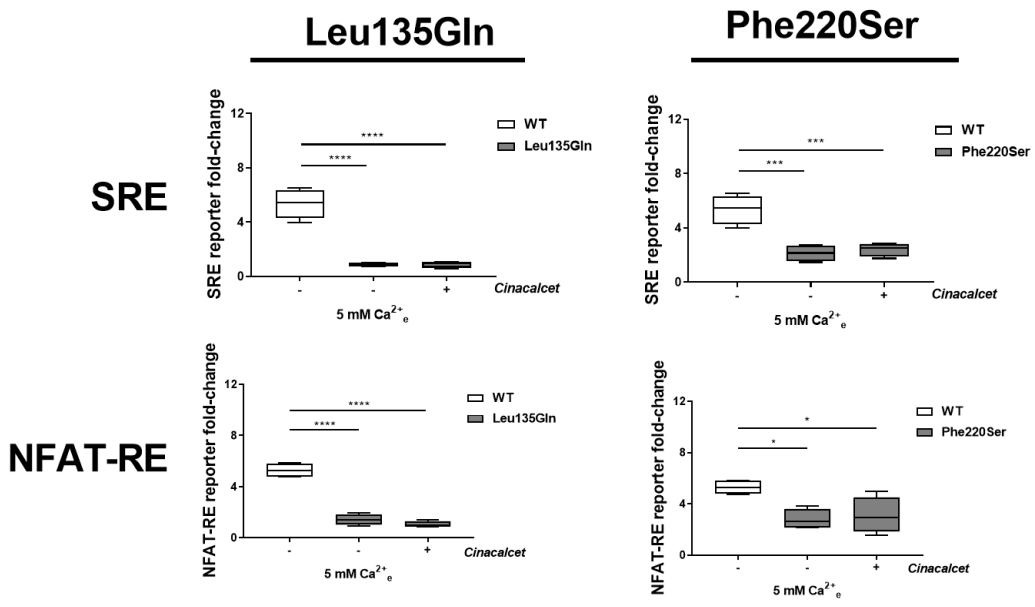


Figure 6.15 Aberrant CaSR-mediated, calcium-induced responses of the FHH2-causing $G\alpha_{11}$ mutations Leu135Gln and Phe220Ser (grey boxes, minus sign) in SRE (top row) and NFAT-RE (bottom row) assays are not compensated by cinacalcet (grey boxes, plus sign) in cells lacking endogenous $G\alpha_q$ and $G\alpha_{11}$. Values are shown as mean±SEM of 4 independent transfections. Ordinary one-way ANOVA with Tukey correction for multiple comparisons was performed using GraphPad Prism 8.4.1. *p<0.05, ***p<0.001, ****p<0.0001.

6.2.3.3 Effects of allosteric CaSR modulators

To test the ability of CaSR PAMs and NAMs to induce changes in signalling via WT $G\alpha_q$ and $G\alpha_{11}$ in the absence of other $G\alpha_{q/11}$ subunits, I used HEK293A-$G\alpha_{q/11}$-KO-CaSR cells and performed SRE and NFAT-RE luciferase reporter assays. This showed significantly increased signalling responses for both $G\alpha_q$ (up to 2.4-fold $p<0.0001$) and $G\alpha_{11}$ (up to 2.2-fold $p<0.001$) mediated responses in both assays when co-stimulated with calcium and cinacalcet as opposed to calcium alone (Figure 6.16).

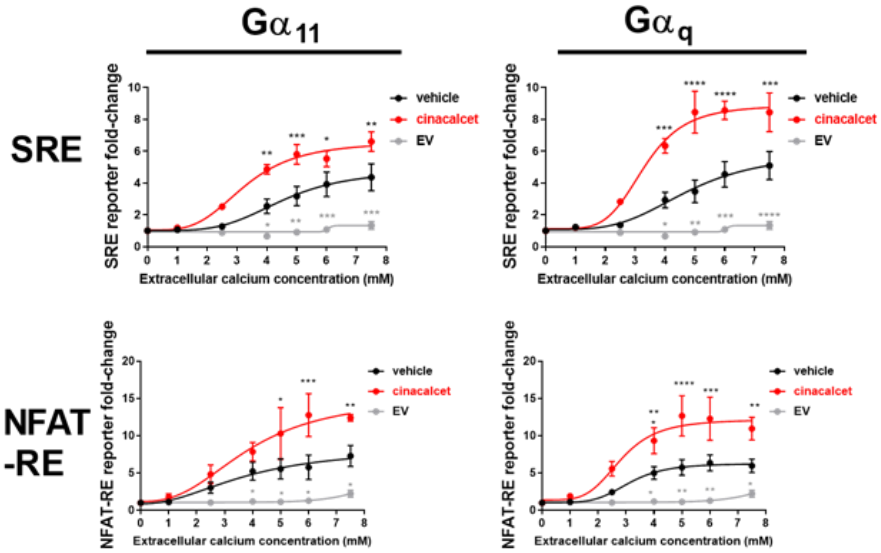


Figure 6.16 HEK293$G\alpha_{q/11}$-KO-CaSR cells transfected with SRE (top row) and NFAT-RE (bottom row) luciferase reporter constructs. Calcium-induced responses were significantly increased with addition of cinacalcet (red line), compared to vehicle (DMSO) treated cells (black line) in both cells transfected with $G\alpha_{11}$ (graphs on the left) and $G\alpha_q$ (graphs on the right). Empty vector (EV) transfected cells (grey line) were used as a negative control. Values are shown as mean±SEM of 4-8 independent transfections. Two-way ANOVA with Sidak correction for multiple comparisons was performed using GraphPad Prism 8.4.1. *p<0.05, **p<0.01, ***p<0.001, ****p<0.0001.

Likewise, CaSR-mediated signalling responses of both $G\alpha_q$ (up to 5.1-fold <0.0001) and $G\alpha_{11}$ (up to 4.8-fold <0.0001) were decreased upon treatment with the NAM NPS-2143

(Figure 6.17). This suggests that cinacalcet may rectify hypercalcaemia in FHH2 patients partly via compensatory signalling via WT $G\alpha_q$.

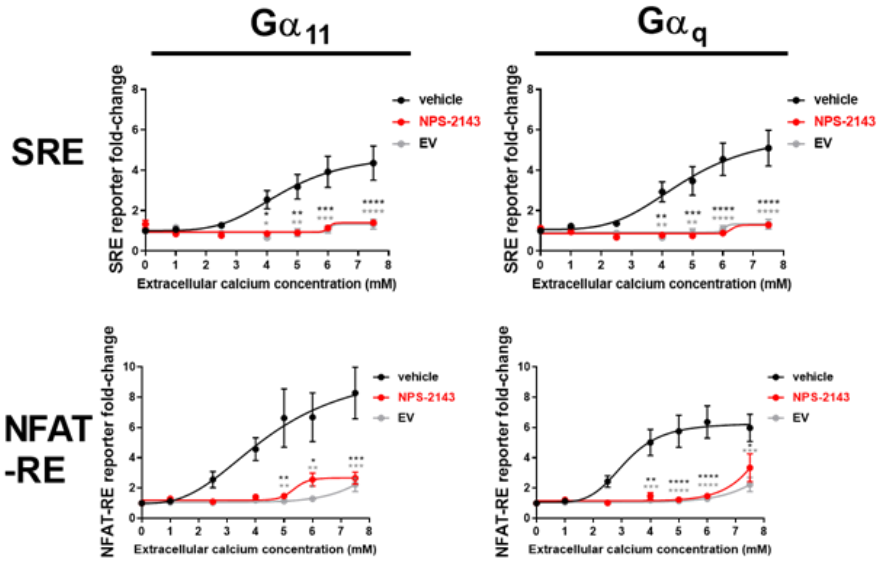


Figure 6.17 HEK293$G\alpha_{q/11}$-KO-CaSR cells transfected with SRE (top row) and NFAT-RE (bottom row) luciferase reporter constructs. Calcium-induced responses were significantly decreased with the addition of NPS-2143 (red line) compared to vehicle (DMSO) treated cells (black line) in both cells transfected with $G\alpha_{11}$ (graphs on the left) and $G\alpha_q$ (graphs on the right). Empty vector (EV) transfected cells (grey line) were used as a negative control. Values are shown as mean±SEM of 4-8 independent transfections. Two-way ANOVA with Sidak correction for multiple comparisons was performed using GraphPad Prism 8.4.1. *p<0.05, **p<0.01, ***p<0.001, ****p<0.0001.

6.3 Discussion

6.3.1 Investigation of *GNAQ* as a candidate gene for FHH/ADH

$G\alpha_q$ has been proposed as a possible novel cause of FHH and ADH due to the high sequence similarity (>90%) with $G\alpha_{11}$, which is a known cause of FHH2 and ADH2[82]. However, no *GNAQ* mutations were detected in a cohort of 20 FHH and 17 ADH patients that were negative for mutations in *CASR*, *AP2S1* and *GNA11*. Using large-scale exome

datasets linked to clinical records, in combination with three different CaSR signalling assays, I showed that in contrast to $G\alpha_{11}$, $G\alpha_q$ missense variants are not associated with abnormalities in plasma calcium and/or impaired CaSR signalling. These results indicated that variants in *GNAQ* are unlikely to be FHH or ADH-causing mutations. I therefore proceeded to studying potential differences between $G\alpha_q$ and $G\alpha_{11}$.

6.3.2 Expression studies

Previously reported differences between $G\alpha_q$ and $G\alpha_{11}$ have been linked to differences in expression. For example, $G\alpha_q$ deficiency in mice results in severe bleeding and premature death[288], which is due to a lack of compensatory $G\alpha_{11}$ expression in platelets[289]. Moreover, even though both $G\alpha_q$ and $G\alpha_{11}$ are widely expressed in the nervous system[290], only $G\alpha_q$-deficient mice develop loss of inflammation-induced hyperalgesia[290] and defects of motor control[291]. The latter may be due to the fact that Purkinje cells express at least 10-fold more $G\alpha_q$ mRNA than $G\alpha_{11}$[292].

My analysis of three independent transcriptomics datasets (FANTOM[275], GTEX[276], HPA[81]) for variations in *GNAQ* and *GNA11* mRNA revealed that *GNA11* is expressed at significantly higher levels than *GNAQ* in colon, heart muscle, skeletal muscle, and small intestine. However, in the kidneys, which are important for maintaining calcium homeostasis[88,293,294], no difference was found between *GNAQ* and *GNA11* mRNA expression. Expression data for the parathyroid glands, the main regulator of calcium homeostasis[82], was only available for the HPA dataset, which showed similar expression of *GNAQ* and *GNA11* mRNA. This is in contrast to human parathyroid adenoma, where previous studies found that *GNA11* mRNA expression was approximately three-fold higher than *GNAQ* mRNA expression[93]. However, this alone would not be a sufficient explanation for the observed differences because parathyroid-specific knockout mouse

models in which both $G\alpha_q$ and $G\alpha_{11}$ are deleted exhibit hypercalcaemia, whilst single knockout mice are normocalcaemic[295].

Comparison of $G\alpha_q$ and $G\alpha_{11}$ protein expression is hampered because antibodies that exclusively detect $G\alpha_q$ but not $G\alpha_{11}$, and vice versa, are not available. Differentiation of $G\alpha_q$ and $G\alpha_{11}$ functional effects is also difficult, because both are (with the exception of platelets[289]) ubiquitously expressed and activate similar downstream effectors[27,39,296]. For these reasons, signalling via $G\alpha_q$ and $G\alpha_{11}$ has traditionally been studied as an entity, and many $G\alpha_{q/11}$ mediated effects reported in *in vitro* assays could be mediated by $G\alpha_q$ and/or $G\alpha_{11}$. To overcome this difficulty and study the functional properties of $G\alpha_q$ and $G\alpha_{11}$ independently, I utilised HEK293A cells, modified by CRISPR/CAS9 to lack expression of endogenous $G\alpha_q$ or $G\alpha_{11}$[209].

6.3.3 Functional effects on CaSR signalling

The FHH2-causing *GNA11* loss-of-function mutations Leu135Gln and Phe220Ser, when engineered in $G\alpha_q$, caused no impairment of CaSR signalling in SRE and NFAT-RE reporter assays, and only a small decrease in response in Fluo-4 intracellular calcium mobilisation assays, despite having profound effects on $G\alpha_{11}$ mediated signalling. The resistance of $G\alpha_q$ to missense mutations suggests that the observed differences are not solely a consequence of altered G protein expression in different tissues, and this led me to hypothesise that there may be additional functional differences between $G\alpha_q$ and $G\alpha_{11}$.

Despite the functional differences, WT $G\alpha_q$ could compensate for $G\alpha_{11}$ loss-of-function mutations *in vitro* in HEK293A-$G\alpha_{q/11}$-KO-CaSR-SRE and NFAT-RE cells. This may not be representative for *in vivo* effects due to artificial overexpression of $G\alpha_q$ in these assays, however it does agree with the above mentioned studies in parathyroid-specific knockout mouse models in which $G\alpha_q$ and $G\alpha_{11}$ could compensate for each other[295]. Nevertheless, patients with $G\alpha_{11}$ loss-of-function mutations develop a phenotype,

indicating that stoichiometry of Gα subunits may be important for the pathogenesis of FHH2. Indeed, a titration of the amount of *GNAQ/GNA11* transfected (which resulted in increases in $G\alpha_q$/$G\alpha_{11}$ protein expression), revealed striking differences in Gα-mediated recruitment of p63RhoGEF in ebBRET assays. Increasing amounts of $G\alpha_q$ resulted in greater signal, with the maximal response at 100ng/ml transfected. In contrast, for $G\alpha_{11}$ the maximal response was reached at the second lowest amount (10ng/ml) after which the signal declined, so that at 100ng/ml it was not significantly different from 0ng/ml. This suggests that for $G\alpha_{11}$, conclusions should not be drawn from expression levels because expression and magnitude of response are not directly proportional. Notably, the constitutively active $G\alpha_q$ Gln209Leu mutation which causes uveal melanoma[15] and congenital Haemangioma[33,34] has been described as a "conditional oncogene", based on expression levels. When expressed at low levels, it led to transformation of fibroblasts, however, at higher levels it induced growth inhibition and apoptosis[297,298].

The structure of $G\alpha_q$ (but not $G\alpha_{11}$) in complex with PLCß3 has been solved[267], and the SmBiT and LgBiT of the split luciferase were cloned in the ideal positions to produce the maximal luminescence signal in response to $G\alpha_q$ activation. Therefore, I utilised this technology to study the differences between $G\alpha_q$ and $G\alpha_{11}$ in their interaction with effectors, using a NanoBit[207] Phospholipase C assay. However, when the same tags were used for $G\alpha_{11}$, calcium-induced increases in luminescence were not significantly different from controls, with the exception of a small increase for $G\alpha_{11}$(97,98)-LgBiT and PLCß$_2$(N)SmBiT. These results suggest that $G\alpha_q$ and $G\alpha_{11}$ interact with the effector PLC in a different orientation. This might have implications for other GPCRs that promote Gα interaction with PLCß isoforms, including the thromboxane A_2 receptor, angiotensin II receptor, histamine receptor H_1, vasopressin receptor V_1, and the muscarinic receptors M_1 and M_3[27,162,207,299]. Even though the structure of a fragment of $G\alpha_{11}$ in

complex with the M_1 receptor has recently been solved[67], studies of signalling downstream of $G\alpha_{11}$ would be greatly enhanced by the availability of full-length $G\alpha_{11}$ in complex with an effector.

6.3.4 Allosteric CaSR modulators

In this chapter, I also show that positive and negative allosteric modulators targeting the receptor affect $G\alpha_q$ and $G\alpha_{11}$ mediated signalling in a similar way, which is in agreement with previous publications[6,39,300-302], suggesting that $G\alpha_q$ and $G\alpha_{11}$ interact similarly with receptors. This is likely due to perfect conservation of the C-terminal helix, which is crucial for GPCR-G protein interaction[18] (see introduction 1.1). Interestingly, in the absence of WT $G\alpha_q$ and WT $G\alpha_{11}$, impaired signalling of $G\alpha_{11}$ loss-of-function mutations could not be "rescued" by the CaSR positive allosteric modulator cinacalcet, despite the fact that cinacalcet normalised plasma calcium levels *in vivo* in an FHH2 patient, who also had pruritus[109] and *in vitro* in cells with SiRNA knockdown of endogenous $G\alpha_{11}$[219]. However, the pruritus, from which the FHH2 patient suffered the most, did not resolve and treatment was stopped. This suggests that cinacalcet may rectify hypercalcaemia in FHH2 patients via compensatory stimulation of WT $G\alpha_q$ but subtle differences in signalling downstream of G proteins may affect clinical outcomes.

6.3.5 Implications for FDA approved drugs

GPCRs are the target of approximately one third of prescription drugs[58], and I hypothesised that in patients with LOF $G\alpha_{11}$ mutations compensation by $G\alpha_q$ (and potentially other G protein alpha subunits) and the associated changes in downstream signalling may also have implications for receptors other than the CaSR, and lead to lack of efficacy and/or change in clinical outcomes of GPCR-targeting drugs that these patients may be taking. My analysis of IUPHAR/BPS Guide to PHARMACOLOGY[252] and GPCRdb[253] databases revealed a total of 156 FDA-approved drugs that target

receptors coupling primarily to $G\alpha_{q/11}$. They act on a wide range of GPCRs with the largest group being class A aminergic receptors (Figure 6.18).

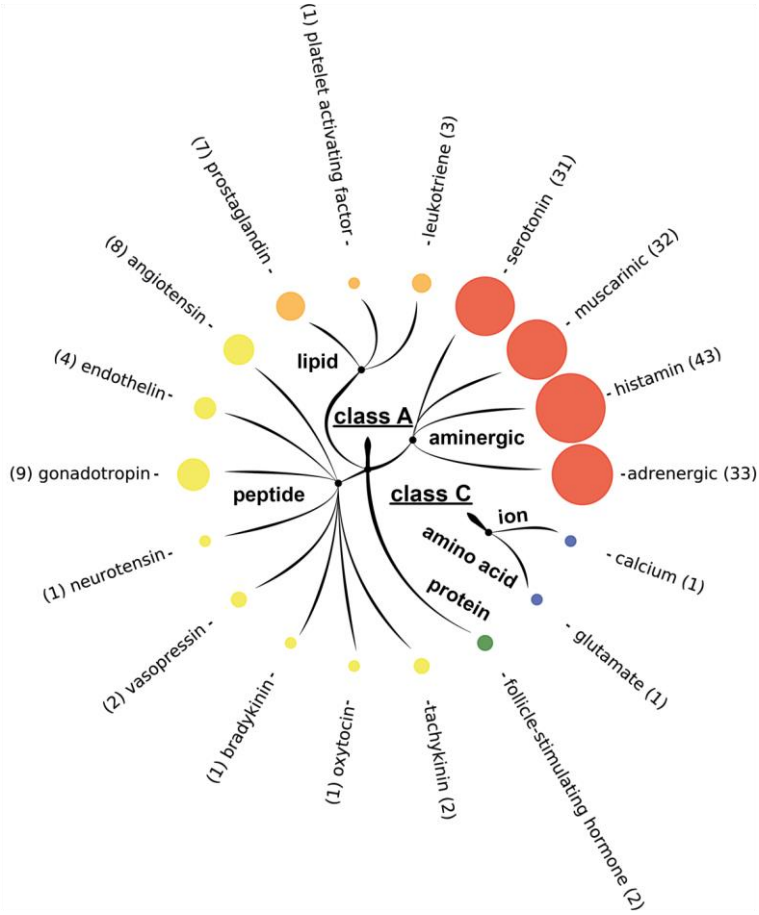


Figure 6.18 Number of FDA approved drugs (in brackets) that target receptors which primarily signal via $G\alpha_{q/11}$ mediated pathway. The size of the circles is proportional to the number of compounds for each group. Class A aminergic receptors are shown in red, class A lipid receptors are shown in orange, class A peptide receptors are shown in yellow, class A protein receptors are shown in green, and class C receptors are shown in blue.

Analysis of Anatomical Therapeutic Chemical (ATC) classification revealed that the most prevalent indication of these drugs was related to diseases of the nervous system (41) followed by diseases related to the alimentary tract and metabolism (34) (Figure 6.19). I predict that tissue specific differences between $G\alpha_q$ and $G\alpha_{11}$ function, and their

tissue specific interaction with GPCRs, could provide an additional source of bias, similar to the tissue-specific effects of opioids[200,303].

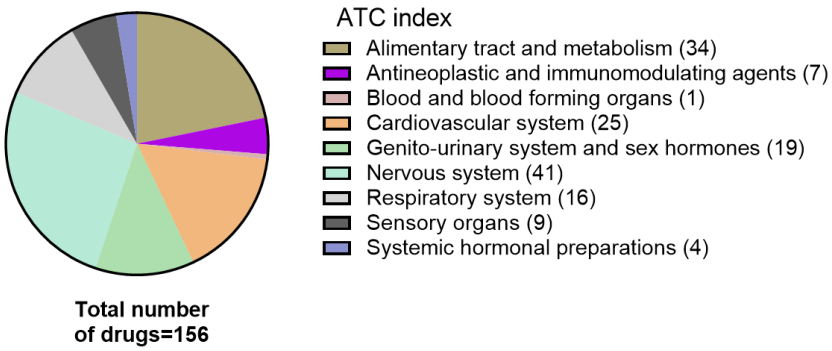


Figure 6.19 Number of FDA approved drugs (shown in brackets) that target receptors which primarily signal via $G\alpha_{q/11}$ mediated pathway, grouped by anatomical main group (ATC index).

In conclusion, this chapter demonstrates that there are functional differences between the $G\alpha_q$ and $G\alpha_{11}$ subunits at the level of human pathology, G protein activation, effector interaction, and transcription. Moreover, I highlight the importance of stoichiometry for GPCR signalling. My findings shed light on the biological significance of diversity within the $G\alpha_{q/11}$ family, which is still disputed[6,32]. Although I used the CaSR as a model GPCR, the differences identified are downstream of G protein signalling and therefore likely receptor independent. Due to the high degree of conservation of GPCR-G protein interaction, my findings may have wider implications and could potentially affect other GPCRs as well as a number of clinically approved and pre-clinical drugs.

7 CASR FUNCTIONAL SELECTIVITY

7.1 Aims

Recent studies of GPCR functional selectivity have linked distinct molecular pathways to clinical benefits, or side effects[193]. This has led to the development of so-called biased drugs, which are able to selectively modulate certain intracellular pathways. For instance, G protein biased opioids provide analgesia with fewer side effects than unbiased opioids[194] (see introduction 1.6.3.4).

The CaSR is a pluripotent GPCR which can activate multiple intracellular signalling pathways, attributed to the $G\alpha_{q/11}$, $G\alpha_{i/o}$ and potentially $G\alpha_{12/13}$ subunits[77,94]. Additionally, it is has been reported to signal via ß arrestin[77] (for a detailed description of CaSR signalling see introduction 1.6).

Cinacalcet, a positive allosteric CaSR modulator, is currently used to treat: secondary hyperparathyroidism due to chronic kidney disease; hypercalcaemia in adult patients with parathyroid carcinoma; and patients with primary hyperparathyroidism who are unable to undergo parathyroidectomy[98]. However, its use is limited by gastrointestinal side-effects such as nausea and vomiting which are likely due to pharmacodynamic effects of cinacalcet[98]. Notably, it has been suggested that CaSR modulators can promote biased signalling (see 1.6.3.4)[204,262].

The aim for this chapter was to investigate biased signalling and functional selectivity of the CaSR by assessing its preferred G protein and ß arrestin signalling pathways, and the effects of CaSR allosteric modulators and disease-causing mutations.

7.2 Results

7.2.1 CaSR functional selectivity

To study CaSR functional selectivity, I used enhanced bystander Bioluminescence Resonance Transfer (ebBRET) assays (see 3.8.6)[166]. The main advantages of this technique are that it is a direct measurement of protein-protein interactions in living cells, and that it allows comparison of individual G protein subunits within a family. This enabled me to determine the contribution of 12 individual G protein alpha subunits of the $G\alpha_{q/11}$, $G\alpha_{i/o}$, $G\alpha_{12/13}$ families, and ß-arrestin 1 and 2 to CaSR signalling in response to increasing concentrations of extracellular calcium Ca^{2+}_e.

7.2.1.1 $G\alpha_{q/11}$ family

To assess activation of $G\alpha_q$, $G\alpha_{11}$, $G\alpha_{14}$, and $G\alpha_{15}$ (which are members of the $G\alpha_{q/11}$ family), I measured recruitment of the p63-RlucII ebBRET sensor[162] to rGFP-CAAX. As a positive control, I used the muscarinic acetylcholine receptor M_3 (M_3R), a prototypical $G\alpha_{q/11}$ coupled class A GPCR[304]. This showed that the M_3R signals through members of the $G\alpha_{q/11}$ family both constitutively and in response to its agonist acetylcholine. Constitutive activation was observed for $G\alpha_q$ (up to 2.5-fold, $p<0.0001$) (Figure 7.1A), $G\alpha_{11}$ (up to 2.6-fold, $p<0.0001$) (Figure 7.1B), and $G\alpha_{14}$ (up to 1.9-fold, $p<0.0001$) (Figure 7.1C), but not $G\alpha_{15}$ (Figure 7.1D). In addition, agonist-mediated signalling was observed for all members of the $G\alpha_{q/11}$ family: $G\alpha_q$ (up to 3.1-fold, $p<0.0001$) (Figure 7.1A), $G\alpha_{11}$ (up to 2.9-fold, $p<0.0001$) (Figure 7.1B), $G\alpha_{14}$ (up to 2.3-fold, $p<0.0001$) (Figure 7.1C), and $G\alpha_{15}$ (up to 1.6-fold, $p<0.0001$).

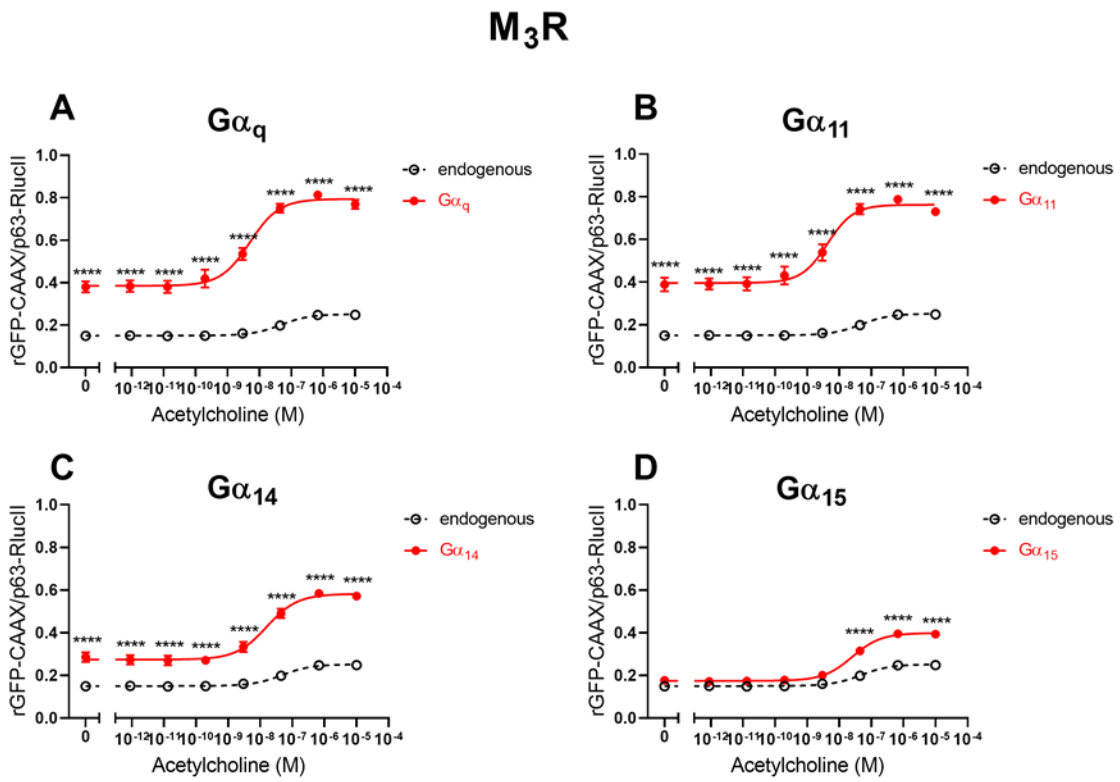


Figure 7.1 Acetylcholine-induced activation of (A) $G\alpha_q$, (B) $G\alpha_{11}$, (C) $G\alpha_{14}$ and (D) $G\alpha_{15}$ in HEK293 cells transiently transfected with the Muscarinic acetylcholine receptor M_3. Values are shown as mean±SEM of 4 independent transfections. Two-way ANOVA with Sidak's correction for multiple comparisons was performed using GraphPad Prism 8.4.1.****p<0.0001.

In comparison, the CaSR did not show any constitutive activation of the $G\alpha_{q/11}$ family. However, in response to Ca^{2+}_e stimulation, a significant increase over endogenous activity was observed for cells transfected with $G\alpha_q$ (up to 2.3-fold, p<0.0001) (Figure 7.2A), $G\alpha_{11}$ (up to 2.2-fold, p<0.0001) (Figure 7.2B), $G\alpha_{14}$ (up to 1.9-fold, p<0.0001) (Figure 7.2C), but not $G\alpha_{15}$ (Figure 7.2D).

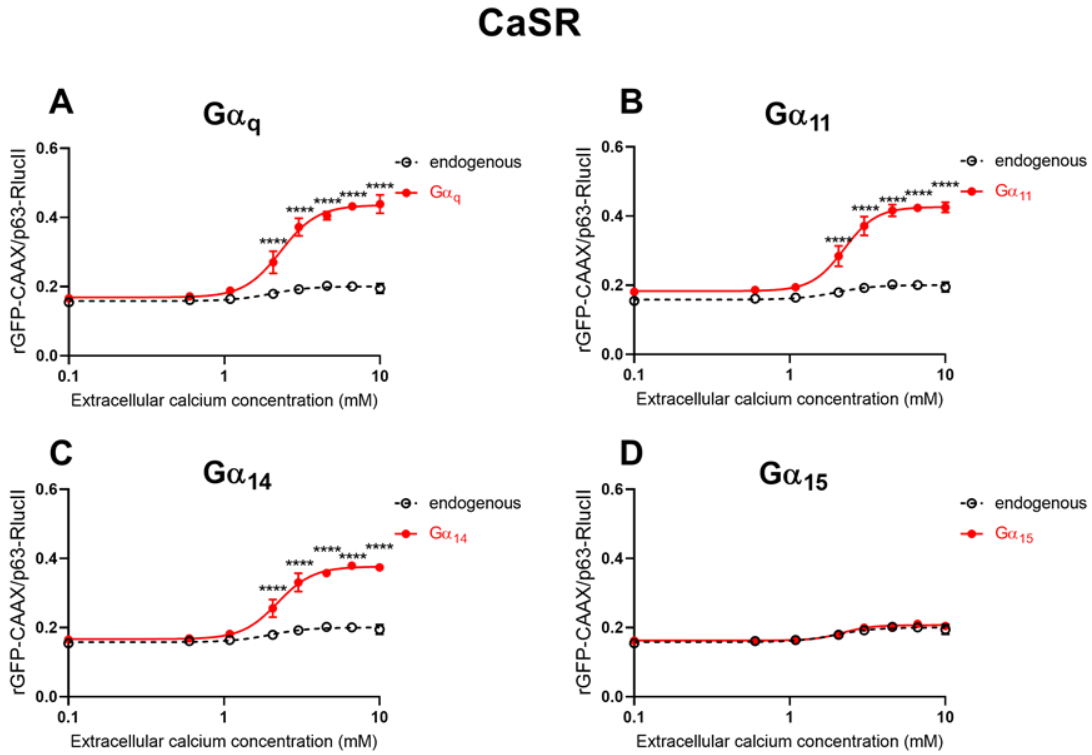


Figure 7.2 Activation of the $G\alpha_{q/11}$ family ($G\alpha_{q,11,14,15}$) by the CaSR in response to increasing concentrations of Ca^{2+}_e. Cells transfected with (A) $G\alpha_q$, (B) $G\alpha_{11}$, and (C) $G\alpha_{14}$ show a significant increase over endogenous activity ($p<0.0001$). No increase was observed for (D) $G\alpha_{15}$. Values are shown as mean±SEM of 3-4 independent transfections. Two-way ANOVA with Sidak's correction for multiple comparisons was performed using GraphPad Prism 8.4.1. ****$p<0.0001$.

7.2.1.2 $G\alpha_{12/13}$ family

In order to assess signalling via $G\alpha_{12}$ and $G\alpha_{13}$, I tested two specific $G\alpha_{12/13}$ effectors: p115 and pdz[6]. The thromboxane A2 receptor isoform α (TPα) was used as a positive control for $G\alpha_{12/13}$ coupling[305]. Treatment of TPα-transfected HEK293 cells with the TPα agonist U46619 resulted in significantly increased p115 responses compared to WT, in cells overexpressing $G\alpha_{12}$ (up to 1.9-fold, $p<0.0001$) and $G\alpha_{13}$ (up to 2.3-fold, $p<0.0001$). Similarly, $G\alpha_{12}$ and $G\alpha_{13}$ mediated pdz activity were significantly increased upon U46619 stimulation (up to 2.5-fold and up to 4.2-fold, respectively, $p<0.0001$) (Figure 7.3).

Moreover, a small increase in baseline activation was observed for both $G\alpha_{12}$ and $G\alpha_{13}$ (up to 1.5-fold and up to 1.4-fold, respectively, $p<0.05$), however this effect is typical for $G\alpha_{12/13}$ overexpression and therefore likely not receptor specific (unpublished data by Prof. Michel Bouvier).

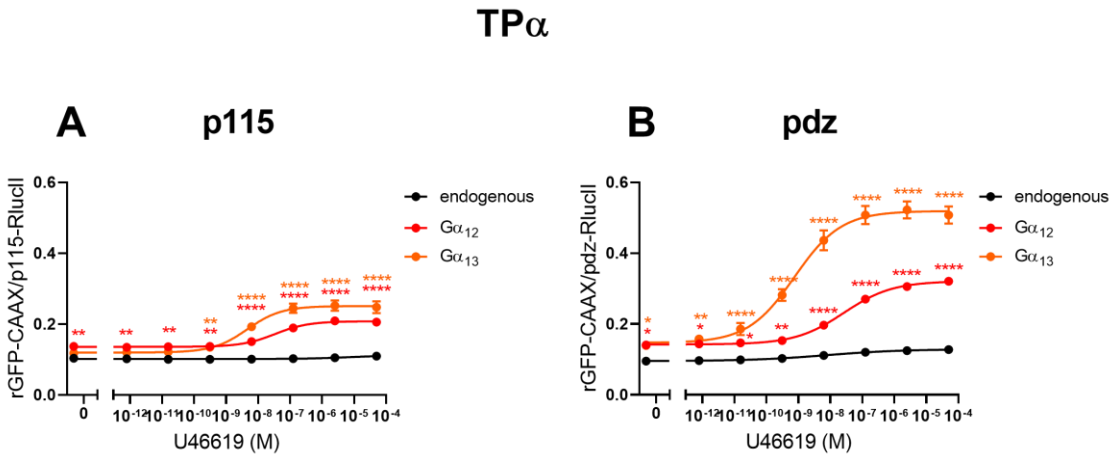


Figure 7.3 U46619-induced mediated activation of (A) p115 and (B) pdz by TPα in cells transfected with control (endogenous), $G\alpha_{12}$ and $G\alpha_{13}$. Values are shown as mean±SEM of 4 independent transfections. Two-way ANOVA with Dunett's correction for multiple comparisons was performed using GraphPad Prism 8.4.1.*p<0.05, **p<0.01, ****p<0.0001.

In contrast, treatment of CaSR-expressing cells with Ca^{2+}_e did not result in significant increases of p115 and/or pdz activity. An increase in baseline activation was observed for both p115 and pdz in cells transfected with $G\alpha_{12}$ (1.3-fold and 1.5-fold, $p<0.0001$) and $G\alpha_{13}$ (1.2-fold and 1.4-fold, $p<0.0001$) (Figure 7.4); however, the effect was similar to what was observed in control experiments with TPα and is therefore likely CaSR-independent.

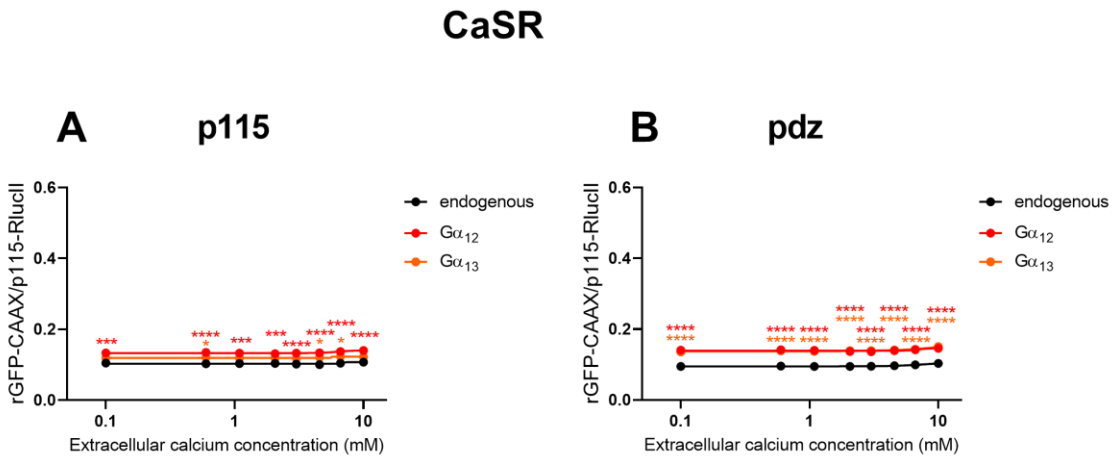


Figure 7.4 CaSR mediated activation of (A) p115 and (B) pdz in response to increasing concentrations of Ca^{2+}_e in cells transfected with control (endogenous), $G\alpha_{12}$ and $G\alpha_{13}$. Values are shown as mean±SEM of 4 independent transfections. Two-way ANOVA with Dunett's correction for multiple comparisons was performed using GraphPad Prism 8.4.1.****p<0.0001.

7.2.1.3 $G\alpha_{i/o}$ family

Activation of pertussis toxin sensitive ($G\alpha_{i1,i2,i3,oA,oB}$) and insensitive ($G\alpha_z$) members of the $G\alpha_{i/o}$ family[306] was measured using rap1gap as an effector[6]. The muscarinic acetylcholine receptor M_2 (M_2R), which is a prototypical $G\alpha_{i/o}$ coupled class A GPCR[304], was used as a positive control (Figure 7.5).

HEK293 cells transfected with M_2R and ebBRET sensors showed significantly increased baseline activity of $G\alpha_{oB}$ (2.3-fold, p<0.0001) (Figure 7.5E) and $G\alpha_z$ (3.7-fold, p<0.0001) (Figure 7.5F), but not $G\alpha_{i1}$, $G\alpha_{i2}$, $G\alpha_{oi3}$, or $G\alpha_{oA}$ (Figure 7.5A-D). Moreover, acetylcholine stimulation led to an increase in signalling via $G\alpha_{i1}$ (up to 1.3-fold, p<0.0001) (Figure 7.5A), $G\alpha_{i2}$ (up to 2.0-fold, p<0.0001) (Figure 7.5B), $G\alpha_{i3}$ (up to 1.2-fold, p<0.001) (Figure 7.5C), $G\alpha_{oA}$ (up to 1.6-fold, p<0.0001) (Figure 7.5D), $G\alpha_{oB}$ (up to 2.9-fold, p<0.0001) (Figure 7.5E), and $G\alpha_z$ (up to 4.0-fold, p<0.0001) (Figure 7.5F).

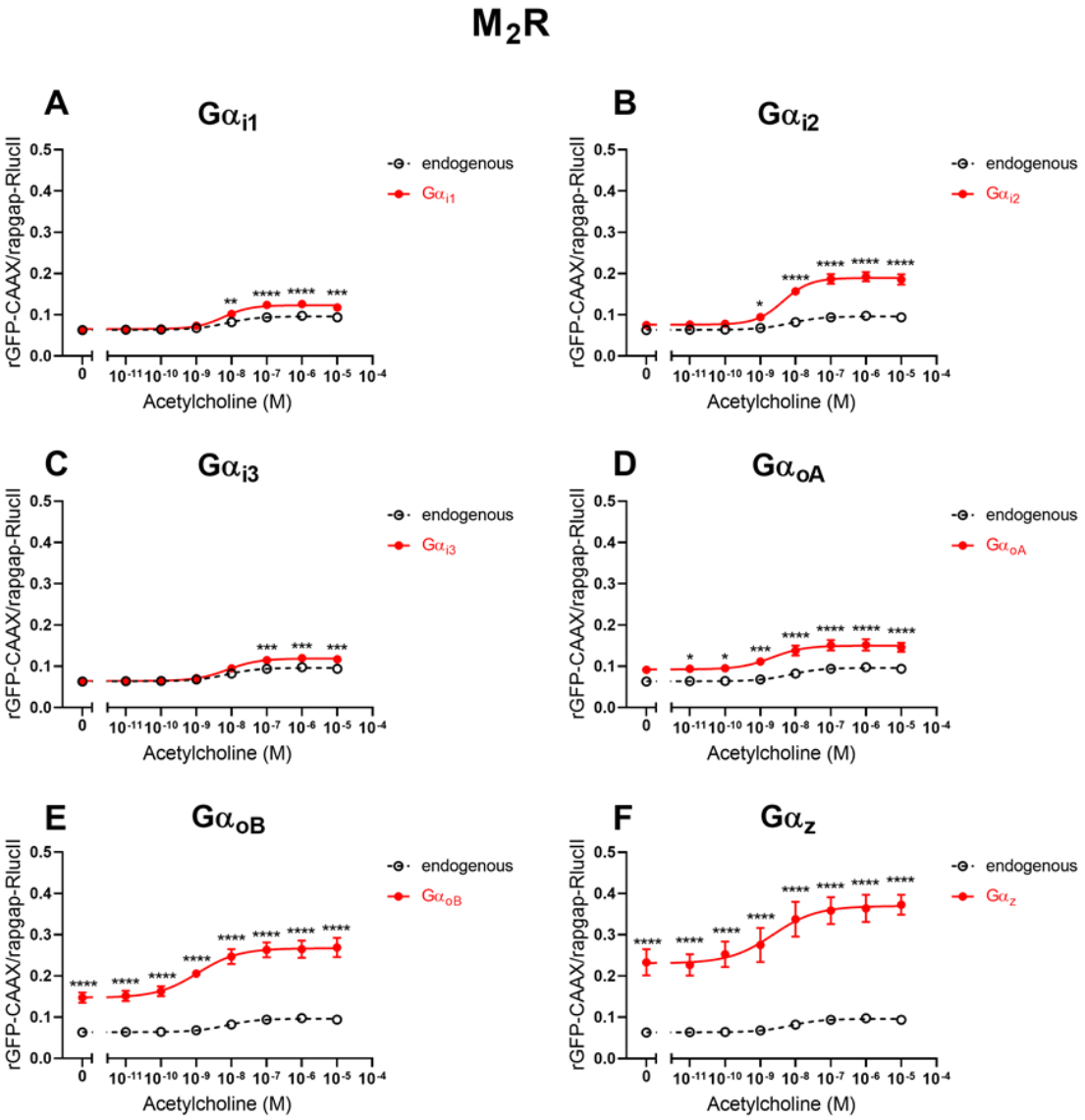


Figure 7.5 Acetylcholine-induced activation of the $G\alpha_{i/o}$ family ($G\alpha_{i1,i2,i3,oA,oB,z}$) by the Muscarinic acetylcholine receptor M_2. Values are shown as mean±SEM of 3-4 independent transfections. Two-way ANOVA with Sidak's correction for multiple comparisons was performed using GraphPad Prism 8.4.1. *p<0.05, **p<0.01, ***p<0.001, ****p<0.0001.

For the CaSR an increase in baseline response was observed for cells transfected with $G\alpha_z$ (3.3-fold, p<0.0001) (Figure 7.6F). Upon Ca^{2+}_e stimulation, a significant increase over endogenous activity was observed for $G\alpha_{i2}$ (up to 1.7-fold, p<0.0001) (Figure 7.6B), $G\alpha_{i3}$ (up to 1.3-fold, p<0.0001) (Figure 7.6C), $G\alpha_{oA}$ (up to 1.4-fold, p<0.0001) (Figure

7.6D), $G\alpha_{oB}$ (up to 2.2-fold, p<0.0001) (Figure 7.6E), and $G\alpha_{z}$ (up to 2.5-fold, p<0.0001) (Figure 7.6F). In contrast, no significant Ca^{2+}_{e} activation of $G\alpha_{i1}$ was observed (Figure 7.6A).

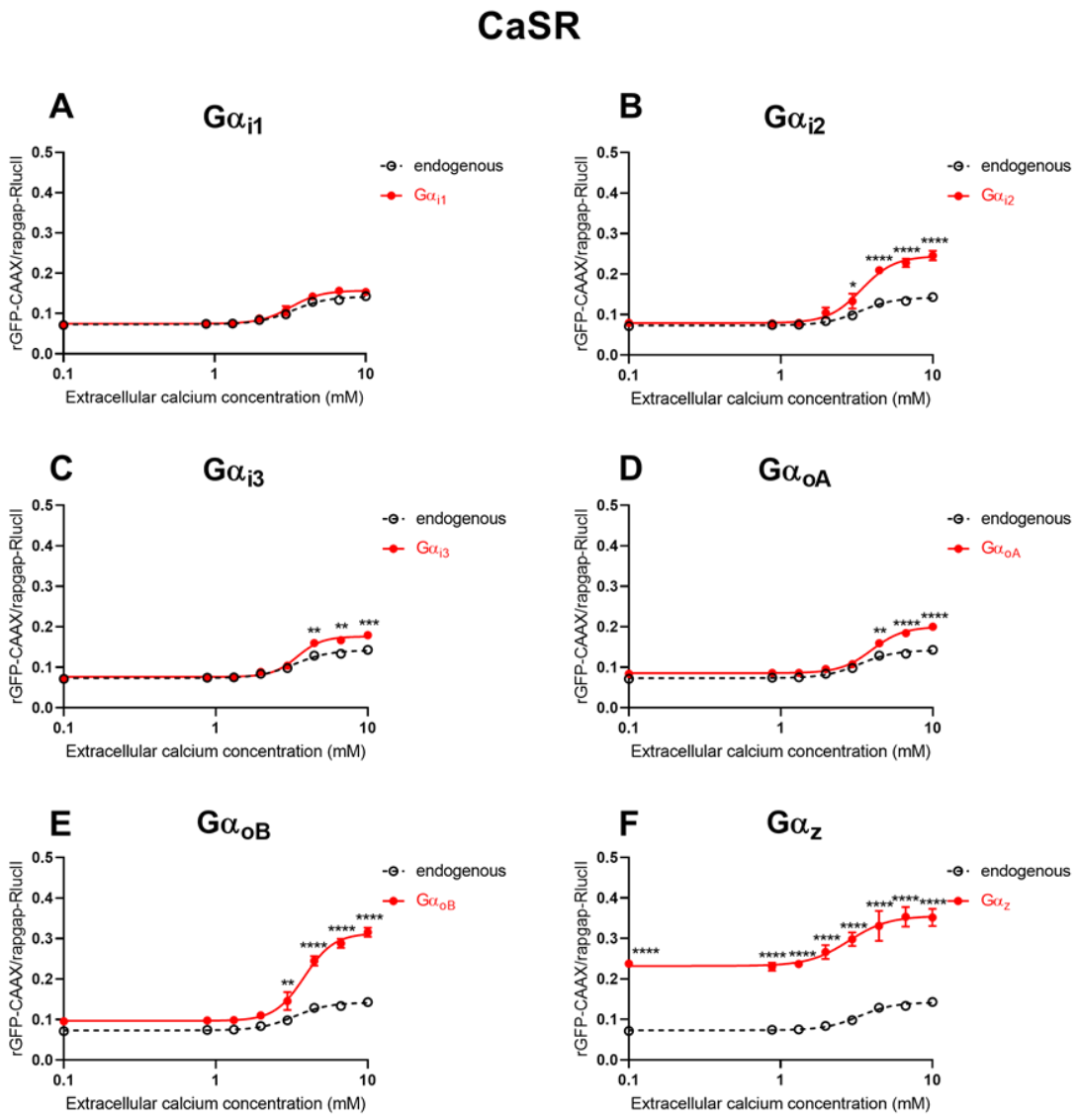


Figure 7.6 CaSR mediated activation of the $G\alpha_{i/o}$ family ($G\alpha_{i1,i2,i3,oA,oB,z}$). Values are shown as mean±SEM of 4-5 independent transfections. Two-way ANOVA with Sidak's correction for multiple comparisons was performed using GraphPad Prism 8.4.1. **p<0.01, ****p<0.0001.

7.2.1.4 Beta arrestins

Agonist-occupied GPCRs recruit ß-arrestins, which mediate receptor desensitisation and endocytosis, and can also participate in signal transduction[6,62,63]. I measured CaSR interaction with ß-arrestin 1 and 2 by comparing HEK293 cells stably expressing the CaSR with parental cells which do not express the CaSR, in the presence and absence of increasing concentrations of Ca^{2+}_e. As a positive control for ß-arrestin recruitment, the ß2 adrenergic receptor (B2AR) was used[163,165]. B2AR was shown to recruit ß-arrestin 1 constitutively (1.1-fold, p<0.0001) (Figure 7.7A), and to recruit both ß-arrestin 1 and ß-arrestin 2 in response to stimulation with isoproterenol (up to 1.3-fold and up to 1.9-fold, respectively, p<0.0001) (Figure 7.7A-B).

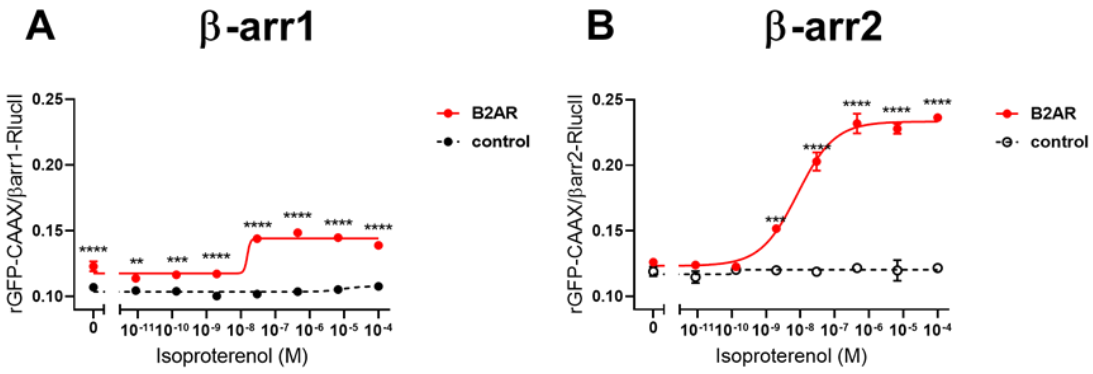


Figure 7.7 Isoproterenol mediated recruitment of (A) ß-arrestin 1 and (B) ß-arrestin 2 in cells transfected with B2AR (black line) or control (red line). B2AR recruits ß-arrestin 1 constitutively, and recruits both ß-arrestin 1 and 2 in response to stimulation with isoproterenol. Values are shown as mean±SEM of 2 independent transfections. Two-way ANOVA with Sidak's correction for multiple comparisons was performed using GraphPad Prism 8.4.1. **p<0.01, ***p<0.001, ****p<0.0001.

Investigation of ß-arrestin recruitment by the CaSR revealed that both ß-arrestin 1 and ß-arrestin 2 are recruited constitutively (1.4-fold and 1.4-fold, respectively, p<0.05)

(Figure 7.8A-B). Moreover, ß-arrestin 1, but not ß-arrestin 2, recruitment could be further stimulated by increasing concentrations of Ca^{2+}_e (up to 1.5-fold increase compared to control, $p<0.001$) (Figure 7.8A).

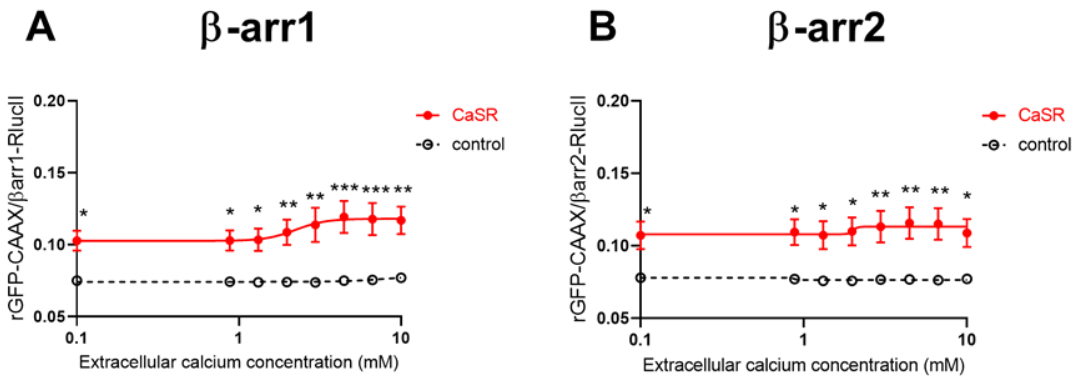


Figure 7.8 Ca^{2+}_e mediated recruitment of (A) ß-arrestin 1 and (B) ß-arrestin 2 in cells stably expressing the CaSR (black line) or parental cells (red line). Values are shown as mean±SEM of 4 independent transfections. Both ß-arrestin 1 and 2 are recruited constitutively and increasing concentrations of Ca^{2+}_e further stimulate ß-arrestin 1 recruitment. Two-way ANOVA with Sidak's correction for multiple comparisons was performed using GraphPad Prism 8.4.1. *p<0.01, **p<0.01, ***p<0.001.

7.2.2 Effects of CaSR modulators on functional selectivity

Next, I assessed the effects of established as well as novel allosteric CaSR modulators on functional selectivity of the CaSR. CaSR-expressing cells that were transiently transfected with biosensors were treated with either increasing concentrations of Ca^{2+}_e and vehicle or increasing concentrations of Ca^{2+}_e and allosteric modulator. Compounds that have a similar effect on every pathway (i.e. increase or decrease) are referred to as "balanced" or "unbiased" drugs, whereas compounds that affect different pathways activated by the CaSR differently are referred to as "biased" drugs[77,162].

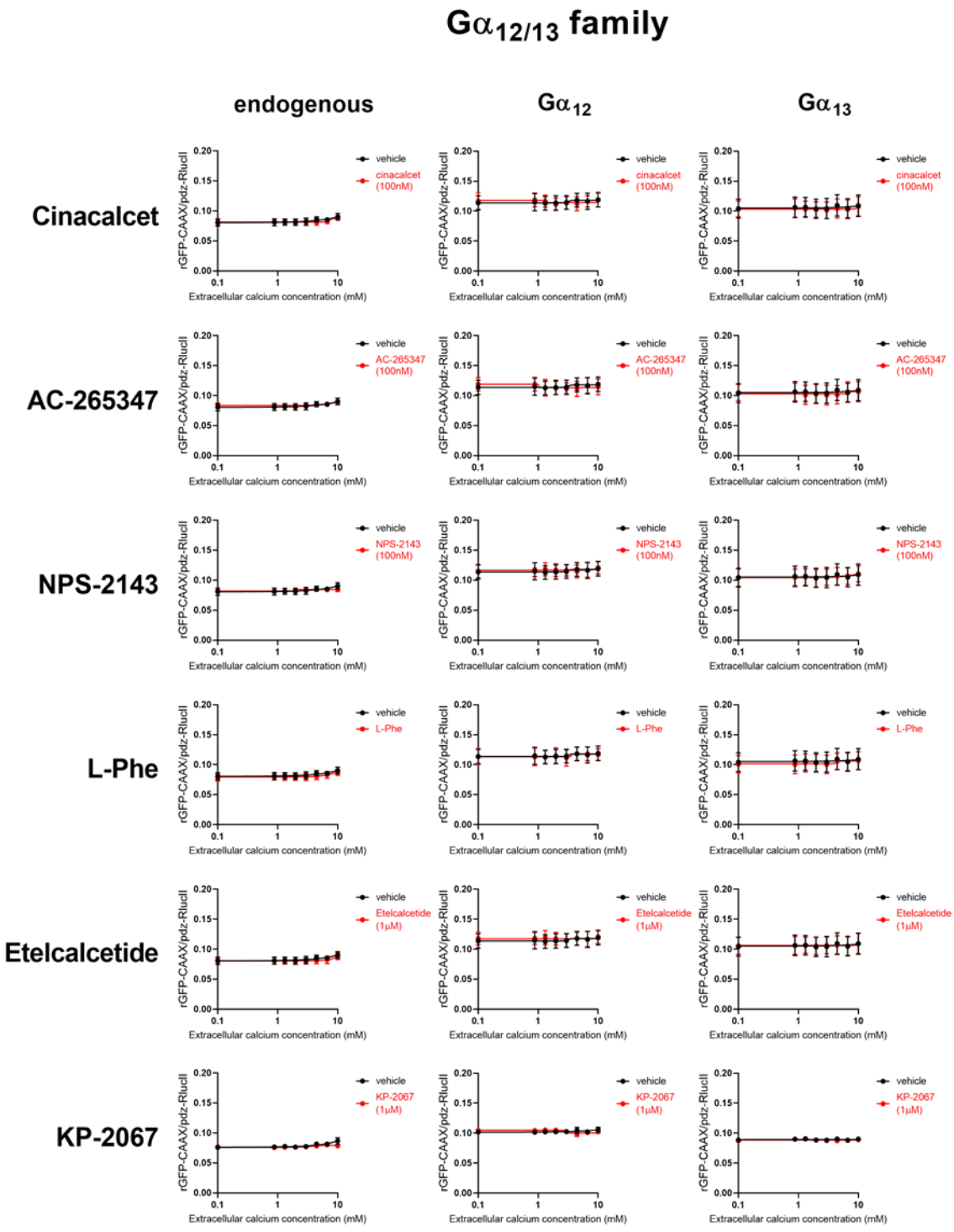


Figure 7.9 CaSR mediated activation of pdz in response to increasing concentrations of Ca^{2+}_e and allosteric modulator or vehicle in cells transfected with control (endogenous), $G\alpha_{12}$ and $G\alpha_{13}$. None of compounds tested altered CaSR signalling by the $G\alpha_{12/13}$ family. Values are shown as mean±SEM of 3 independent transfections.

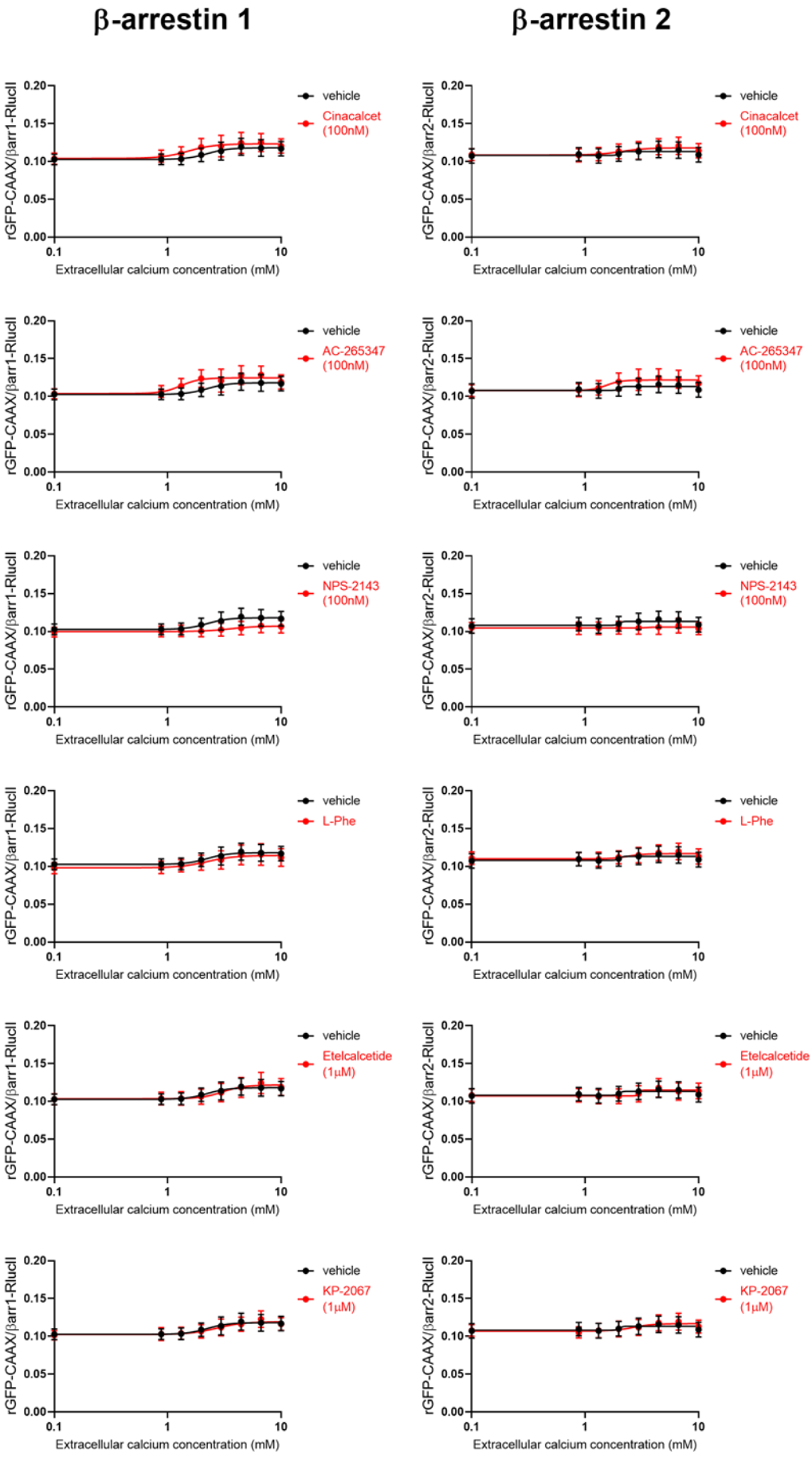

β-arrestin 1
β-arrestin 2
rGFP-CAAX/βarr1-RlucII
rGFP-CAAX/βarr2-RlucII
0.20
0.15
0.10
0.05
0.00
0.1
1
10
Extracellular calcium concentration (mM)
vehicle
Cinacalcet (100nM)
AC-265347 (100nM)
NPS-2143 (100nM)
L-Phe
Etelcalcetide (1μM)
KP-2067 (1μM)

Figure 7.10 CaSR mediated recruitment of ß-arrestin 1 and 2 to the plasma membrane in response to increasing concentrations of Ca^{2+}_e and allosteric modulator or vehicle. No change was found in CaSR signalling by ß-arrestin 1 or 2 for any of the compounds. Values are shown as mean±SEM of 4 independent transfections.

The compounds tested were small molecule calcimimetics (Cinacalcet and AC-265347), small molecule calcilytics (NPS-2143), L-amino acids (L-Phe) and peptide calcimimetics (Etelcalcetide, KP-2067)[98]. Of those, cinacalcet and Etelcalcetide are currently used in the clinic to treat secondary hyperparathyroidism[82,98]. This analysis revealed that none of the compounds tested altered CaSR signalling by the $G\alpha_{12/13}$ family (Figure 7.9) or ß-arrestin 1 and 2 recruitment (Figure 7.10). This was expected for $G\alpha_{12/13}$ due to the lack of CaSR coupling to $G\alpha_{12/13}$ observed in section 7.2.1. However, the CaSR does recruit ß-arrestins, indicating that the compounds could be biased. In contrast, significant effects on the $G\alpha_{q/11}$ and $G\alpha_{i/o}$ families were observed, which are detailed in the following sections.

7.2.2.1 Small molecule calcimimetics

7.2.2.1.1 Cinacalcet

Treatment with 100nM cinacalcet did not significantly alter baseline signalling of the $G\alpha_{q/11}$ family. A significant increase in Ca^{2+}_e mediated signalling was observed for endogenously expressed $G\alpha_{q/11}$ (up to 1.3-fold, $p<0.05$) (Figure 7.11A), $G\alpha_q$ (up to 1.8-fold, $p<0.0001$) (Figure 7.11B), $G\alpha_{11}$ (up to 1.7-fold, $p<0.0001$) (Figure 7.11C) and $G\alpha_{14}$ (up to 1.6-fold, $p<0.0001$) (Figure 7.11D). In cells transfected with $G\alpha_{15}$, activity was increased to an equivalent amount of the endogenous response (1.2-fold, $p<0.05$) (Figure 7.11E). This indicates that cinacalcet stimulates $G\alpha_q$, $G\alpha_{11}$, and $G\alpha_{14}$ but not $G\alpha_{15}$.

Similarly, 100nM cinacalcet did not affect baseline signalling of the $G\alpha_{i/o}$ family, but significantly increased activation of endogenous $G\alpha_{i/o}$ (up to 1.8-fold, $p<0.0001$) (Figure

7.12A), $G\alpha_{i1}$ (up to 2.1-fold, p<0.0001) (Figure 7.12B), $G\alpha_{i2}$ (up to 2.9-fold, p<0.0001) (Figure 7.12C), $G\alpha_{i3}$ (up to 2.3-fold, p<0.0001) (Figure 7.12D), $G\alpha_{oA}$ (up to 2.1-fold, p<0.0001) (Figure 7.12E), $G\alpha_{oB}$ (up to 3.1-fold, p<0.0001) (Figure 7.12F) and $G\alpha_{z}$ (up to 1.6-fold, p<0.01) (Figure 7.12G). This indicates that cinacalcet stimulates CaSR mediated activation of all 6 members of the $G\alpha_{i/o}$ family that were studied.

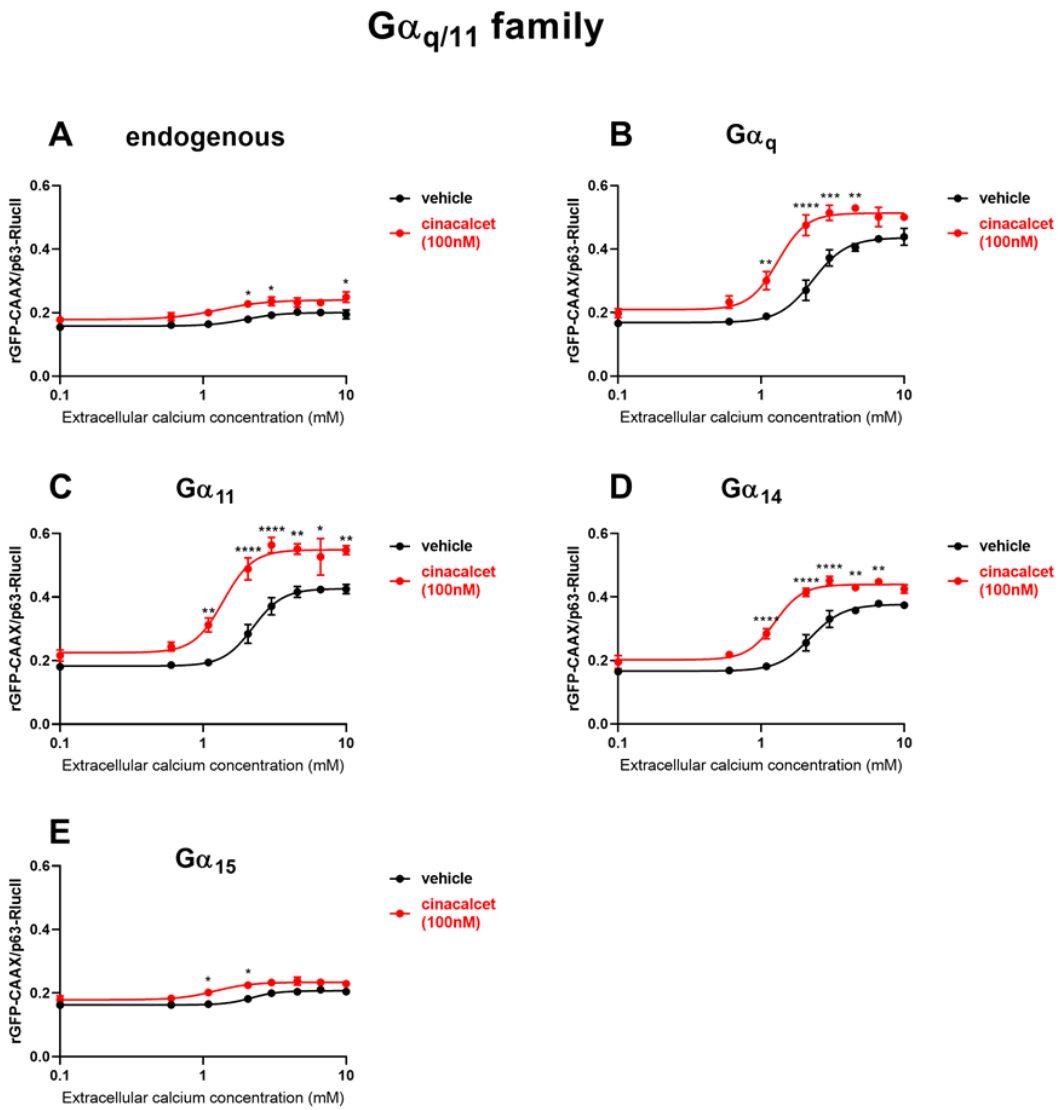


Figure 7.11 Activation of the $G\alpha_{q/11}$ family ($G\alpha_{q,11,14,15}$) by the CaSR in response to Ca^{2+}_{e} in cells treated with vehicle (black line) or 100nM cinacalcet (red line). Values are shown as mean±SEM of 3-4 independent transfections. Two-way ANOVA with Sidak's correction was performed using GraphPad Prism 8.4.1.*p<0.05, **p<0.01, ***p<0.001, ****p<0.0001.

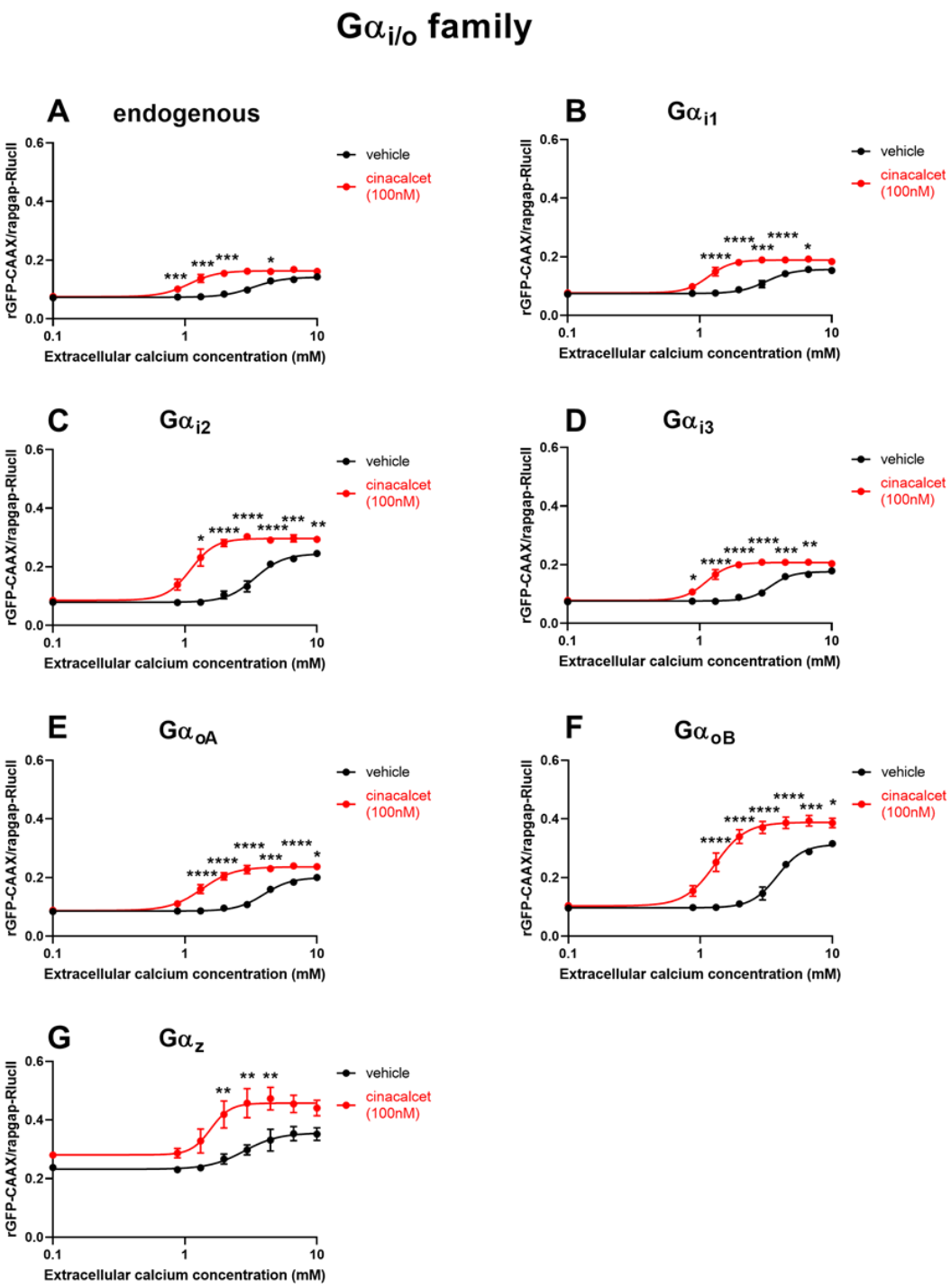


Figure 7.12 Activation of the $G\alpha_{i/o}$ family ($G\alpha_{i1,i2,i3,oA,oB,z}$) by the CaSR in response to increasing concentrations of Ca^{2+}_e in cells treated with vehicle (black line) or 100nM cinacalcet (red line). Values are shown as mean±SEM of 4-5 independent transfections. Two-way ANOVA with Sidak's correction for multiple comparisons was performed using GraphPad Prism 8.4.1.*p<0.05, **p<0.01, ***p<0.001, ****p<0.0001.

7.2.2.1.2 AC-265347

Treatment with 100nM AC-265347 did not have a significant impact on baseline signalling of the $G\alpha_{q/11}$ family. However, compared to vehicle treated cells, a significant increase in Ca^{2+}_e mediated signalling was observed for $G\alpha_q$ (up to 1.8-fold, $p<0.0001$) (Figure 7.13B), $G\alpha_{11}$ (up to 2-fold, $p<0.0001$) (Figure 7.13C) and $G\alpha_{14}$ (up to 1.7-fold, $p<0.0001$) (Figure 7.13D). In cells transfected with $G\alpha_{15}$, activity was increased by 1.2-fold ($p<0.01$) (Figure 7.13E). However, the observed ebBRET response was not significantly higher than for mock transfected cells (endogenous) (Figure 7.13A), thereby indicating that AC-265347 stimulates $G\alpha_q$, $G\alpha_{11}$, and $G\alpha_{14}$ but not $G\alpha_{15}$.

For the $G\alpha_{i/o}$ family, 100nM AC-265347 did not affect baseline signalling, but significantly increased activation of endogenous $G\alpha_{i/o}$ (up to 1.9-fold, $p<0.0001$) (Figure 7.14A), $G\alpha_{i1}$ (up to 2.2-fold, $p<0.0001$) (Figure 7.14B), $G\alpha_{i2}$ (up to 3.2-fold, $p<0.0001$) (Figure 7.14C), $G\alpha_{i3}$ (up to 2.5-fold, $p<0.0001$) (Figure 7.14D), $G\alpha_{oA}$ (up to 2.3-fold, $p<0.0001$) (Figure 7.14E), $G\alpha_{oB}$ (up to 3.4-fold, $p<0.0001$) (Figure 7.14F) and $G\alpha_z$ (up to 1.6-fold, $p<0.01$) (Figure 7.14G). This indicates that AC-265347 stimulates CaSR mediated activation of all members of the $G\alpha_{i/o}$ family.

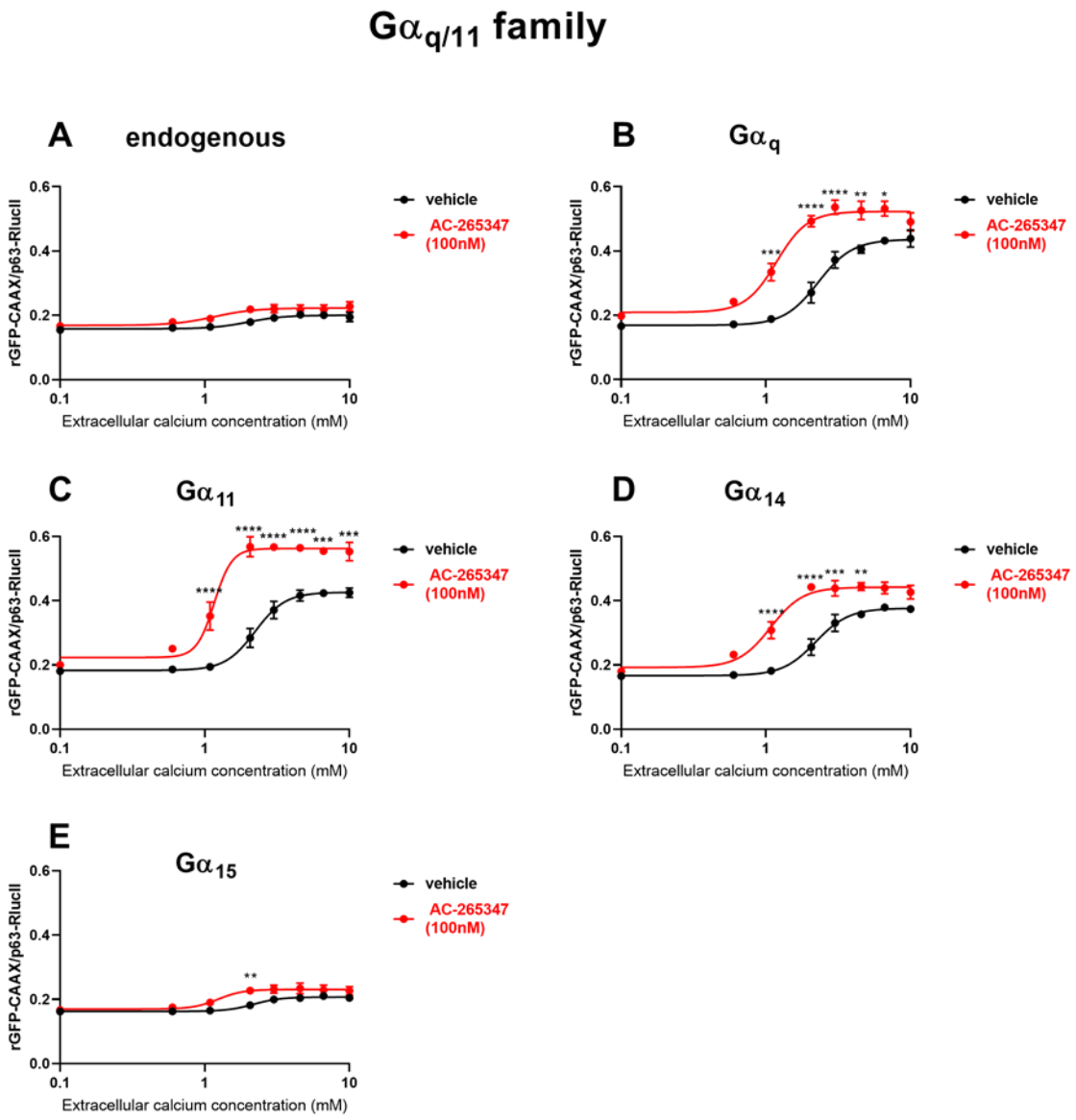


Figure 7.13 Activation of the $G\alpha_{q/11}$ family ($G\alpha_{q,11,14,15}$) by the CaSR in response to increasing concentrations of Ca^{2+}_e in cells treated with vehicle (black line) or 100nM AC-265347 (red line). For $G\alpha_q$, $G\alpha_{11}$, and $G\alpha_{14}$ a significant increase in Ca^{2+}_e mediated signalling was observed. Values are shown as mean±SEM of 3-4 independent transfections. Two-way ANOVA with Sidak's correction for multiple comparisons was performed using GraphPad Prism 8.4.1.*p<0.05, **p<0.01, ***p<0.001, ****p<0.0001.

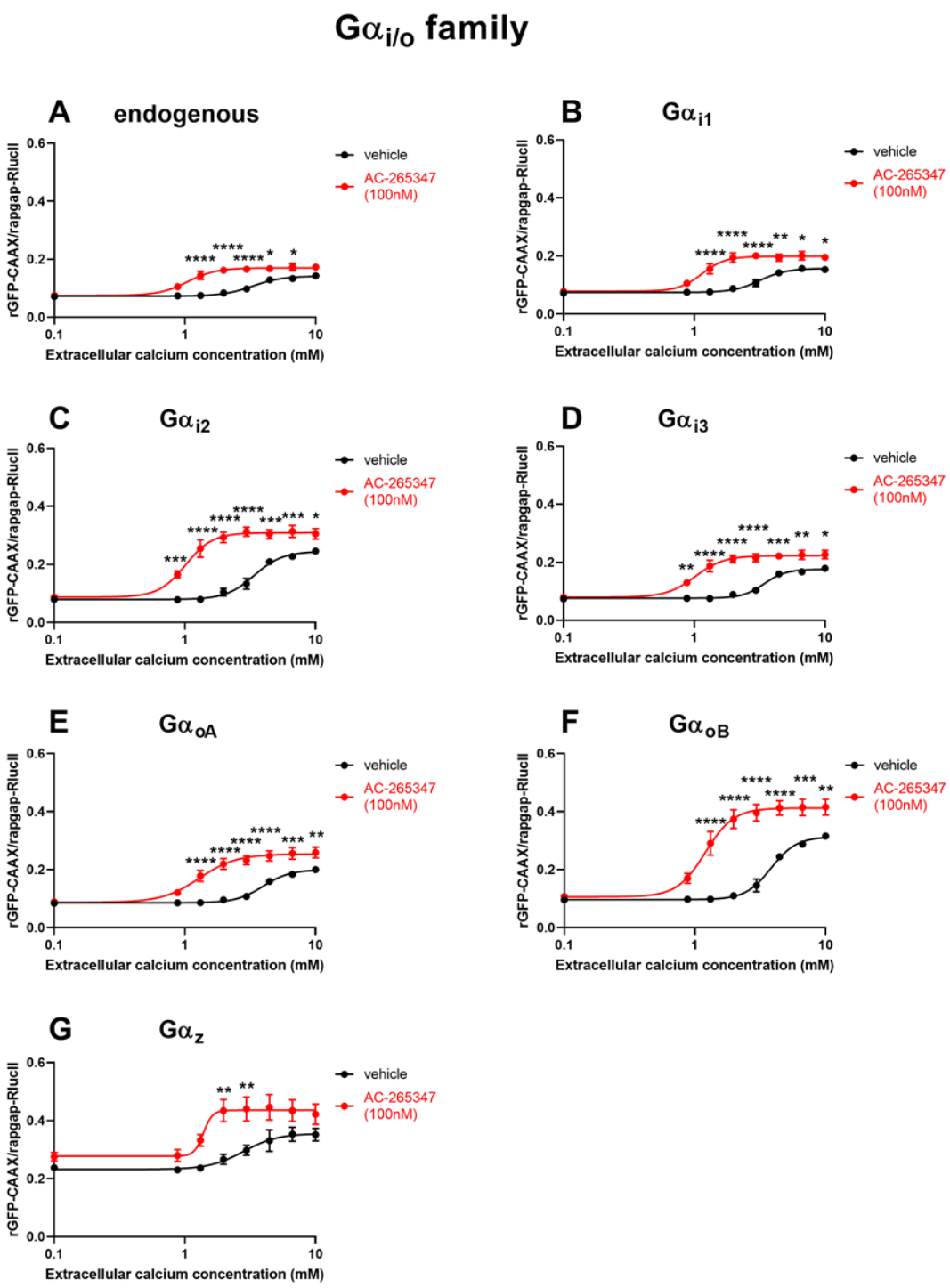


Figure 7.14 Activation of the $G\alpha_{i/o}$ family ($G\alpha_{i1,i2,i3,oA,oB,z}$) by the CaSR in response to increasing concentrations of Ca^{2+}_e in cells treated with vehicle (black line) or 100nM AC-265247 (red line). Values are shown as mean±SEM of 4-5 independent transfections. Two-way ANOVA with Sidak's correction for multiple comparisons was performed using GraphPad Prism 8.4.1.*p<0.05, **p<0.01, ***p<0.001, ****p<0.0001.

7.2.2.2 Aromatic amino acids

Treatment with 10mM L-Phe, reported as a positive allosteric CaSR modulator[98], did not significantly alter baseline or Ca^{2+}_e mediated signalling of endogenous $G\alpha_{q/11}$ (Figure 7.15A), $G\alpha_q$ (Figure 7.15B), $G\alpha_{11}$ (Figure 7.15C), $G\alpha_{14}$ (Figure 7.15D) and $G\alpha_{15}$ (Figure 7.15E), thereby suggesting that L-Phe may increase CaSR signalling via G proteins which are not members of the $G\alpha_{q/11}$ family.

Treatment with 10mM L-Phe did indeed result in significant dose-response activation of $G\alpha_{i2}$ (1.4-fold increase, $p<0.01$) (Figure 7.16C), $G\alpha_{i3}$ (1.4-fold increase, $p<0.01$) (Figure 7.16D), $G\alpha_{oA}$ (1.3-fold increase, $p<0.05$) (Figure 7.16E) and $G\alpha_{oB}$ (1.4-fold increase, $p<0.01$) (Figure 7.16F). In addition, significantly decreased EC_{50} values were observed for endogenous $G\alpha_{i/o}$, $G\alpha_{i1}$, $G\alpha_{i2}$, $G\alpha_{i3}$, $G\alpha_{oA}$, and $G\alpha_{oB}$ (Figure 7.16H). Moreover, 10mM L-Phe did not affect baseline signalling of the $G\alpha_{i/o}$ family. These results indicate that L-Phe is biased towards the $G\alpha_{i/o}$ family.

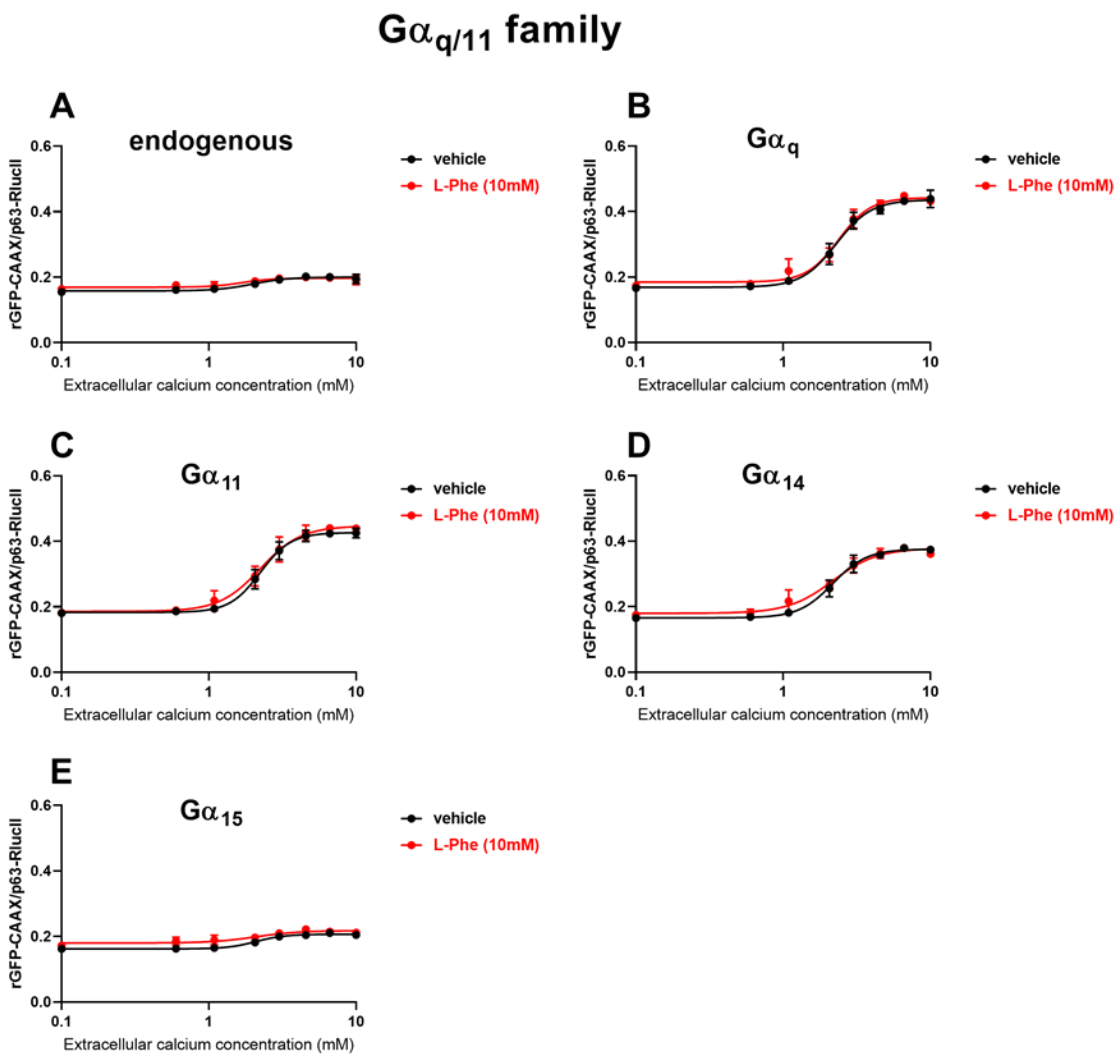


Figure 7.15 Activation of the $G\alpha_{q/11}$ family ($G\alpha_{q,11,14,15}$) by the CaSR in response to increasing concentrations of Ca^{2+}_e in cells treated with vehicle (black line) or 10mM L-Phenylalanine (L-Phe) (red line). L-Phe did not significantly alter baseline or Ca^{2+}_e mediated signalling. Values are shown as mean±SEM of 3-4 independent transfections.

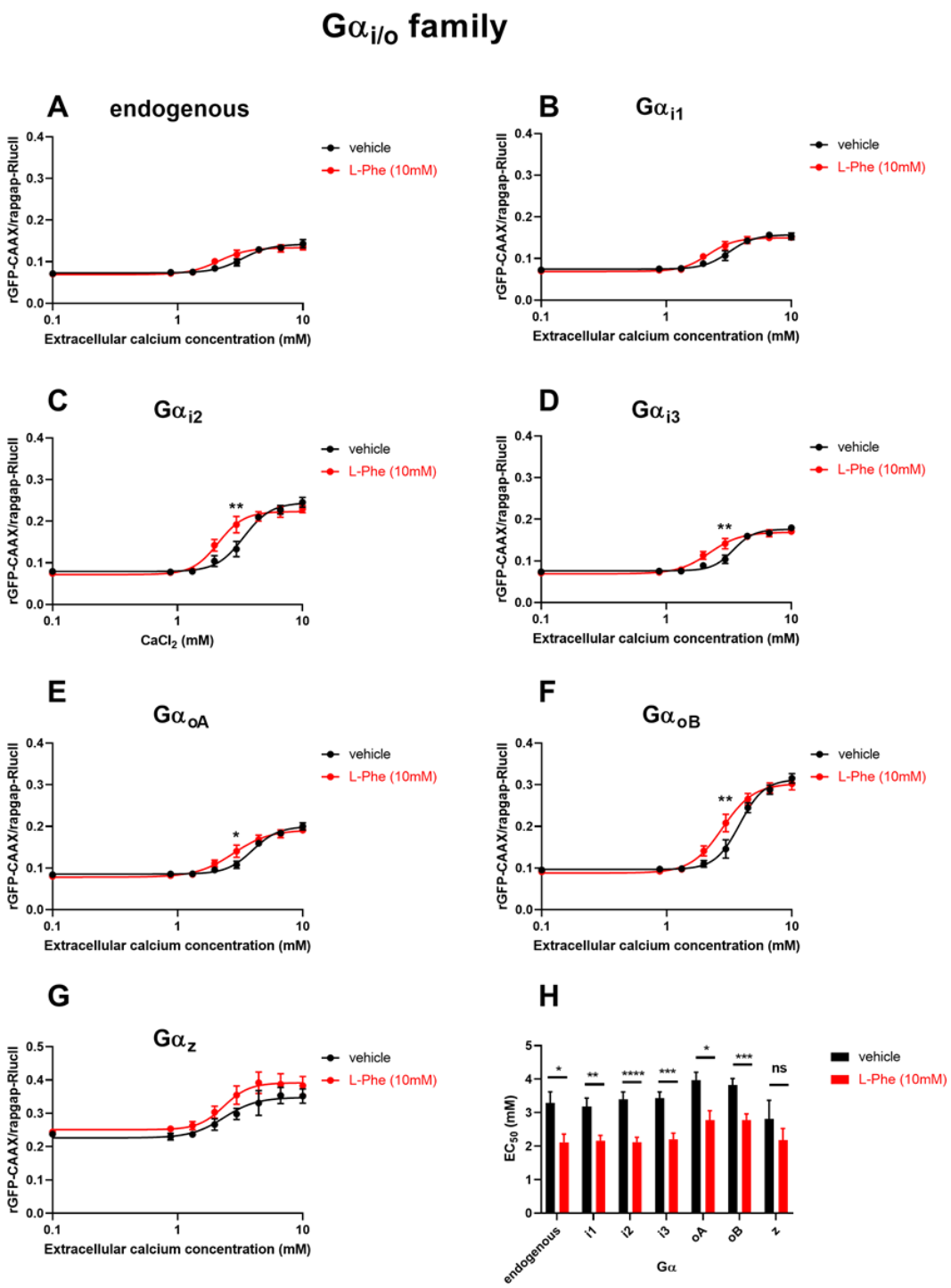


Figure 7.16 Activation of the $G\alpha_{i/o}$ family ($G\alpha_{i1,i2,i3,oA,oB,z}$) by the CaSR in response to increasing concentrations of Ca^{2+}_e in cells treated with vehicle (black line) or 10mM L-Phenylalanine (L-Phe) (red line). Panel H shows EC50 values. Data are shown as mean±SEM of 4-5 independent transfections. Two-way ANOVA with Sidak's correction for multiple comparisons was performed using GraphPad Prism 8.4.1. *p<0.05, **p<0.01.

7.2.2.3 Peptide calcimimetics

7.2.2.3.1 Etelcalcetide

Etelcalcetide has been reported to be a positive allosteric modulator of the CaSR[174], however treatment with 1µM Etelcalcetide did not significantly alter baseline or Ca^{2+}_e mediated signalling of endogenous $G\alpha_{q/11}$ (Figure 7.17A), $G\alpha_q$ (Figure 7.17B), $G\alpha_{11}$ (Figure 7.17C), $G\alpha_{14}$ (Figure 7.17D) and $G\alpha_{15}$ (Figure 7.17E), suggesting that Etelcalcetide may increase CaSR signalling via G proteins which are not members of the $G\alpha_{q/11}$ family.

In contrast, treatment with 1µM Etelcalcetide resulted in significant activation of endogenous $G\alpha_{i/o}$ (up to 1.3-fold increase, $p<0.05$) (Figure 7.18A), $G\alpha_{i1}$ (up to 1.4-fold increase, $p<0.01$) (Figure 7.18B), $G\alpha_{i2}$ (up to 1.8-fold increase, $p<0.0001$) (Figure 7.18C), $G\alpha_{i3}$ (up to 1.6-fold increase, $p<0.0001$) (Figure 7.18D), $G\alpha_{oA}$ (up to 1.5-fold increase, $p<0.01$) (Figure 7.18E) and $G\alpha_{oB}$ (up to 1.7-fold increase, $p<0.01$) (Figure 7.18F). However, no significant difference was observed for $G\alpha_z$ (Figure 7.18G) and baseline activity. These results indicate that Etelcalcetide is biased towards the $G\alpha_{i/o}$ family.

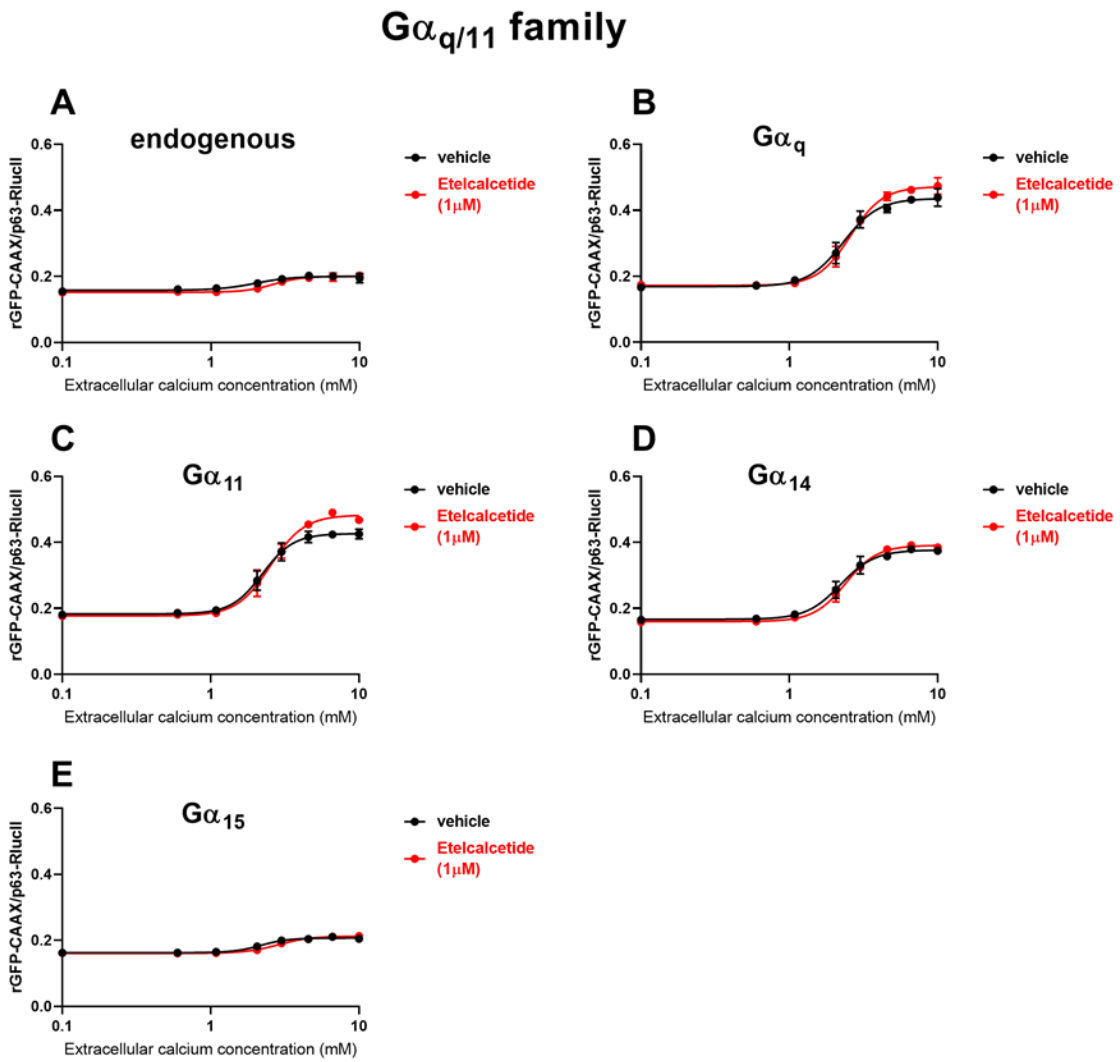


Figure 7.17 Activation of the $G\alpha_{q/11}$ family ($G\alpha_{q,11,14,15}$) by the CaSR in response to increasing concentrations of Ca^{2+}_e in cells treated with vehicle (black line) or 1μM Etelcalcetide (red line). Values are shown as mean±SEM of 3-4 independent transfections.

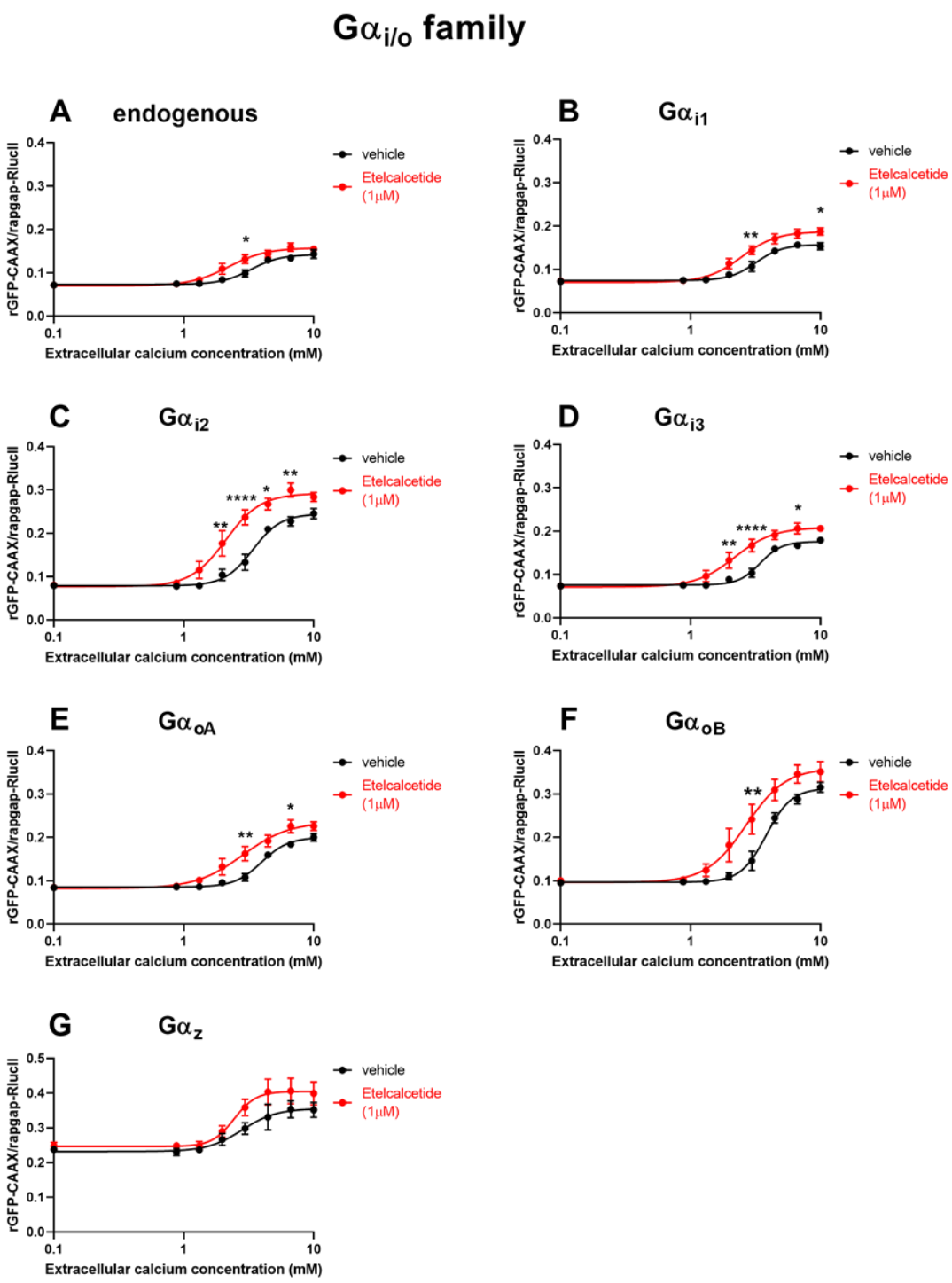


Figure 7.18 Activation of the $G\alpha_{i/o}$ family ($G\alpha_{i1,i2,i3,oA,oB,z}$) by the CaSR in response to increasing concentrations of Ca^{2+}_e in cells treated with vehicle (black line) or 1μM Etelcalcetide (red line). Values are shown as mean±SEM of 4-5 independent transfections. Two-way ANOVA with Sidak's correction for multiple comparisons was performed using GraphPad Prism 8.4.1.*p<0.05, **p<0.01, ****p<0.0001.

7.2.2.3.2KP-2067

KP-2067 is structurally similar to Etelcalcetide and has been reported as a positive allosteric CaSR modulator[174]; however, treatment with 1µM KP-2067 did not significantly alter baseline or Ca^{2+}_e mediated signalling of endogenous $G\alpha_{q/11}$ (Figure 7.19A), $G\alpha_q$ (Figure 7.19B), $G\alpha_{11}$ (Figure 7.19C), $G\alpha_{14}$ (Figure 7.19D) and $G\alpha_{15}$ (Figure 7.19E).

In contrast, treatment with 10mM 1µM KP-2067 resulted in significant activation of endogenous $G\alpha_{i/o}$ (up to 1.3-fold increase, $p<0.05$) (Figure 7.20A), $G\alpha_{i1}$ (up to 1.3-fold increase, $p<0.05$) (Figure 7.20B), $G\alpha_{i2}$ (up to 1.6-fold increase, $p<0.0001$) (Figure 7.20C), $G\alpha_{i3}$ (up to 1.5-fold increase, $p<0.0001$) (Figure 7.20D), $G\alpha_{oA}$ (up to 1.4-fold increase, $p<0.01$) (Figure 7.20E) and $G\alpha_{oB}$ (up to 1.5-fold increase, $p<0.01$) (Figure 7.20F). No significant difference was observed for $G\alpha_z$ (Figure 7.20G) and baseline activity. These results indicate that KP-2067, like Etelcalcetide, is biased towards the $G\alpha_{i/o}$ family.

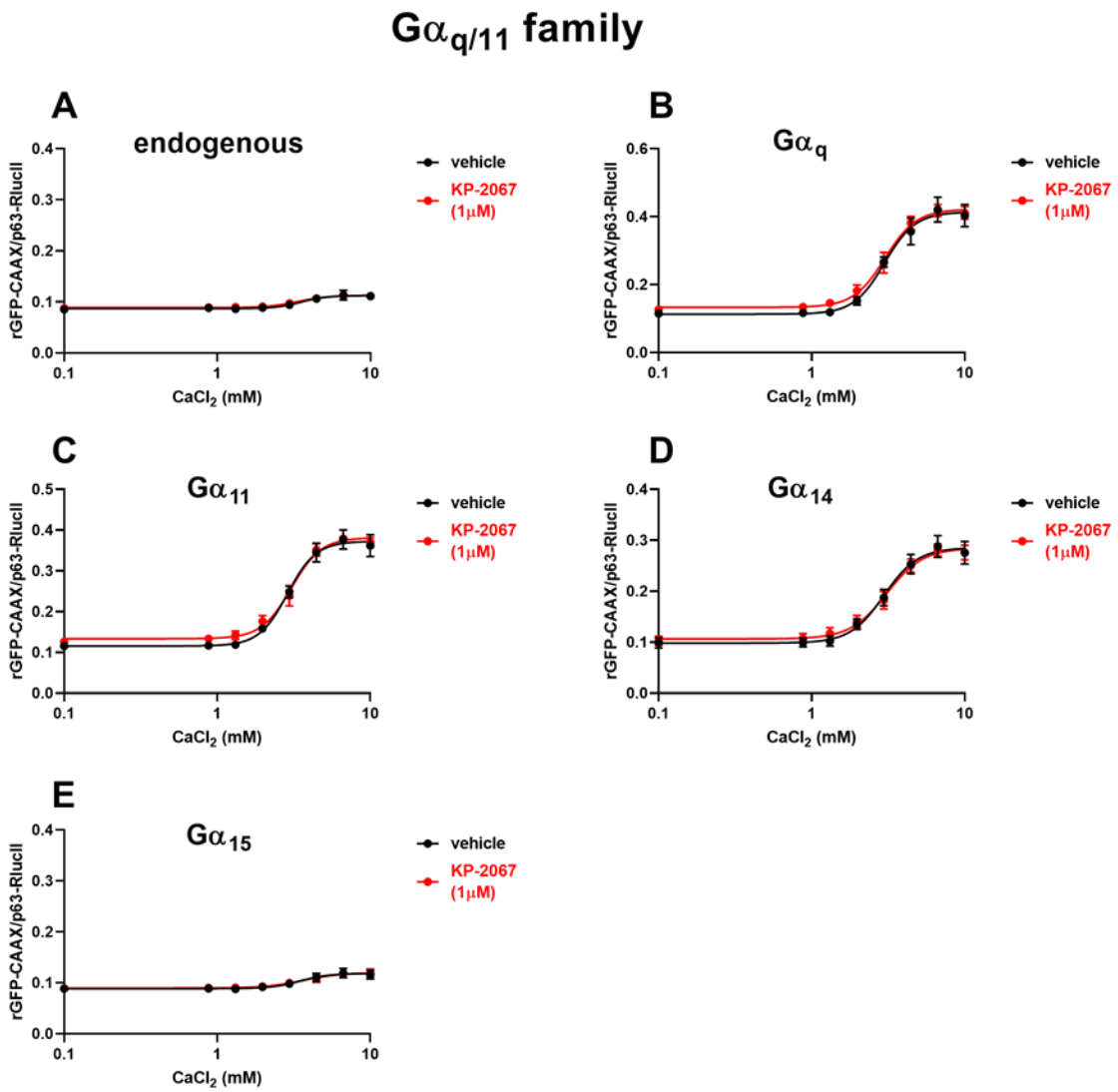


Figure 7.19 Activation of the $G\alpha_{q/11}$ family ($G\alpha_{q,11,14,15}$) by the CaSR in response to increasing concentrations of Ca^{2+}_e in cells treated with vehicle (black line) or 1μM KP-2067 (red line). Values are shown as mean±SEM of 4 independent transfections.

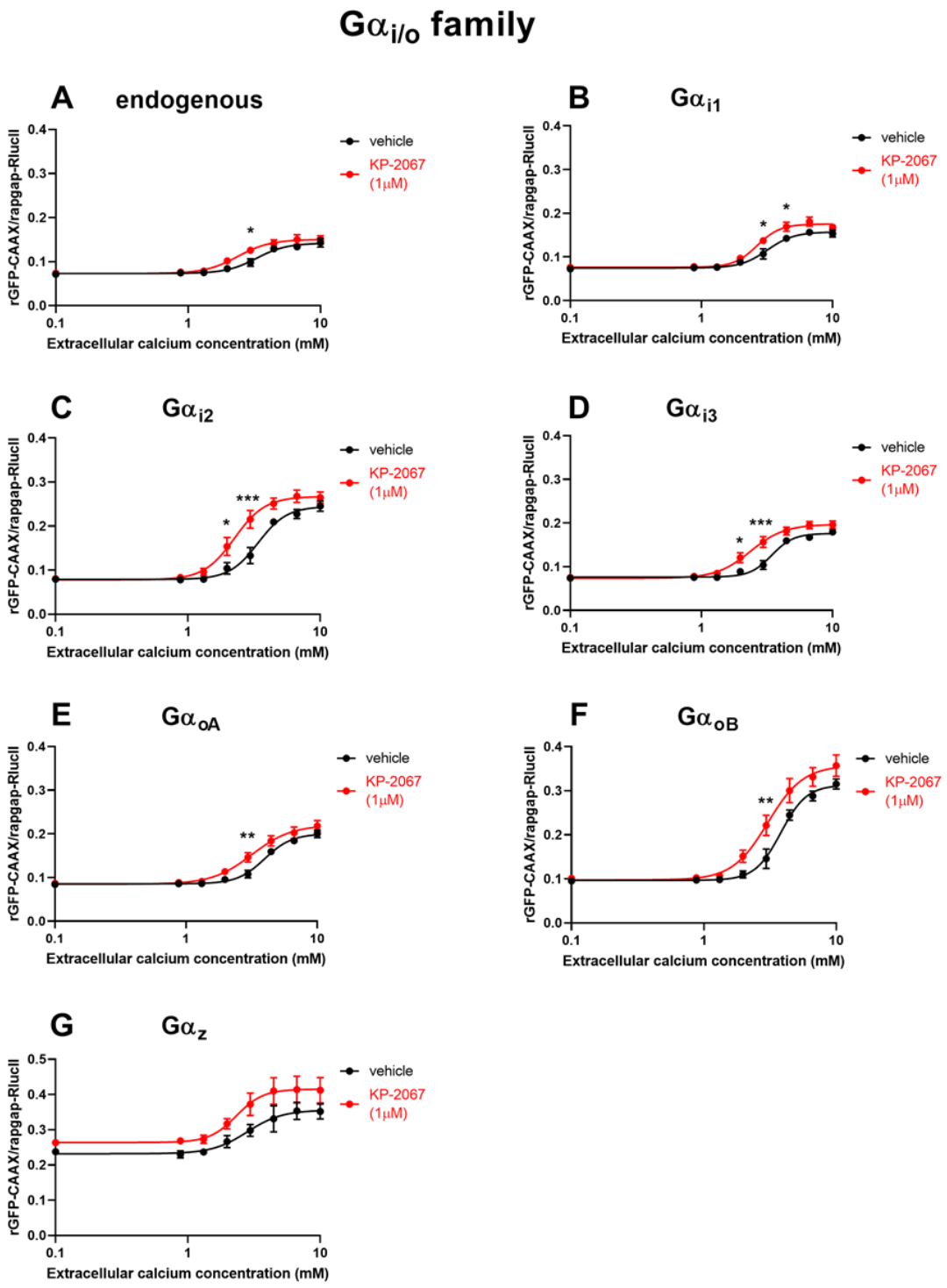


Figure 7.20 Activation of the $G\alpha_{i/o}$ family ($G\alpha_{i1,i2,i3,oA,oB,z}$) by the CaSR in response to increasing concentrations of Ca^{2+}_e in cells treated with vehicle (black line) or 1μM KP-2067 (red line). Values are shown as mean±SEM of 4-5 independent transfections. Two-way ANOVA with Sidak's correction for multiple comparisons was performed using GraphPad Prism 8.4.1.*p<0.05, **p<0.01, ***p<0.001.

7.2.2.4 Small molecule calcilytics

Treatment with 100nM NPS-2143 did not significantly alter baseline signalling of the $G\alpha_{q/11}$ family. However, a significant decrease in Ca^{2+}_e mediated signalling was observed for $G\alpha_q$ (up to 1.7-fold decrease, $p<0.0001$) (Figure 7.21B), $G\alpha_{11}$ (up to 1.7-fold decrease, $p<0.0001$) (Figure 7.21C) and $G\alpha_{14}$ (up to 1.6-fold decrease, $p<0.0001$) (Figure 7.21D). In contrast, no significant difference was observed for endogenously expressed $G\alpha_{q/11}$ (Figure 7.21A) and $G\alpha_{15}$ (Figure 7.21E).

Moreover, 100nM NPS-2143 did not affect baseline signalling of the $G\alpha_{i/o}$ family, but significantly decreased activation of $G\alpha_{oA}$ (1.2-fold reduction, $p<0.01$) (Figure 7.22E) and $G\alpha_{oB}$ (1.3-fold reduction, $p<0.001$) (Figure 7.22F). In contrast, no significant decrease was observed for endogenous $G\alpha_{i/o}$ (Figure 7.22A), $G\alpha_{i1}$ (Figure 7.22B), $G\alpha_{i2}$ (Figure 7.22C), $G\alpha_{i3}$ (Figure 7.22D) and $G\alpha_z$ (Figure 7.22G). This indicates that NPS-2143, out of the $G\alpha_{i/o}$ family, inhibits only the $G\alpha_o$ subunits.

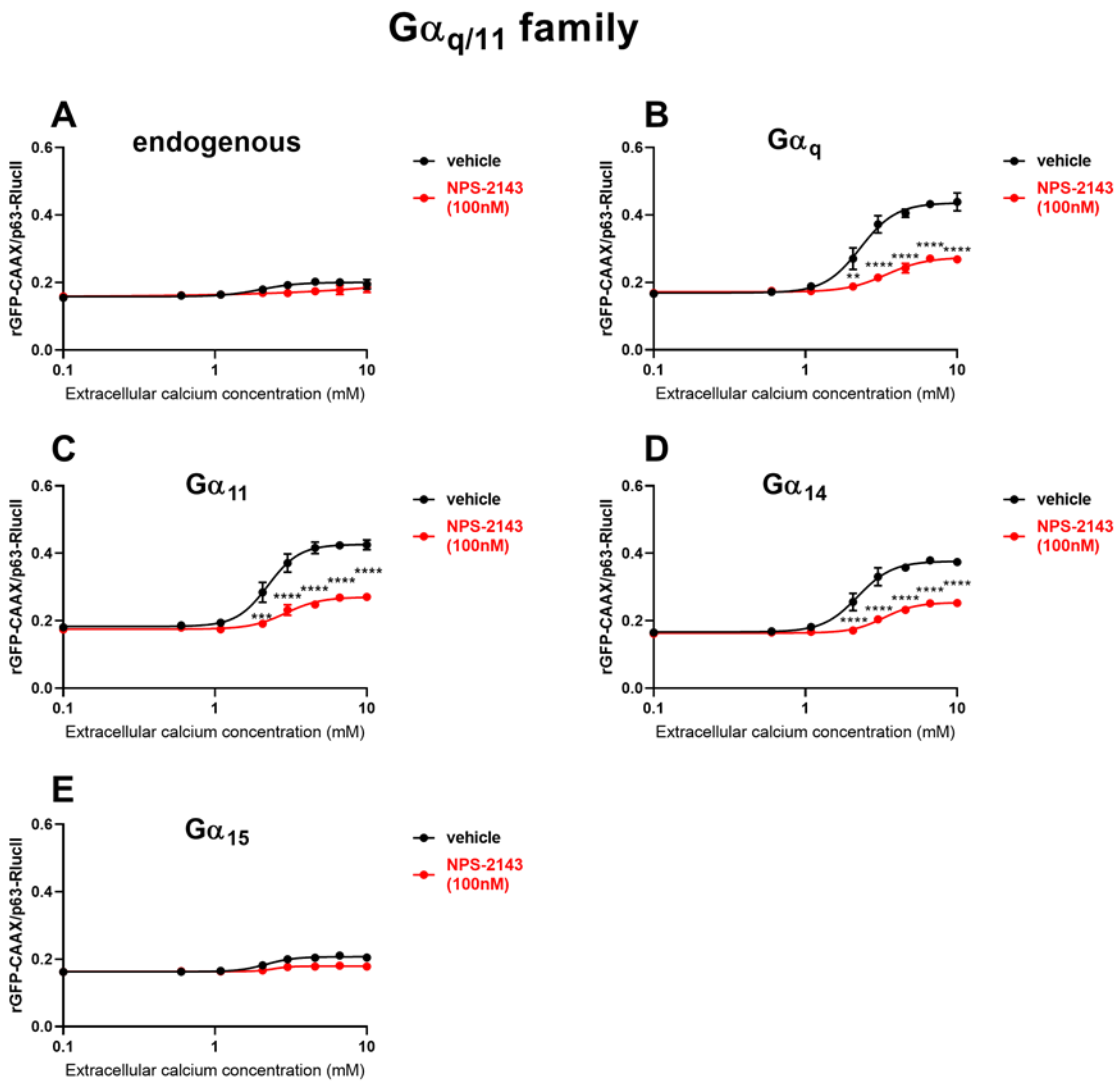


Figure 7.21 Activation of the $G\alpha_{q/11}$ family ($G\alpha_{q,11,14,15}$) by the CaSR in response to increasing concentrations of Ca^{2+}_e in cells treated with vehicle (black line) or 100nM NPS-2143 (red line). Values are shown as mean±SEM of 3-4 independent transfections. Two-way ANOVA with Sidak's correction for multiple comparisons was performed using GraphPad Prism 8.4.1. **p<0.01, ***p<0.001, ****p<0.0001.

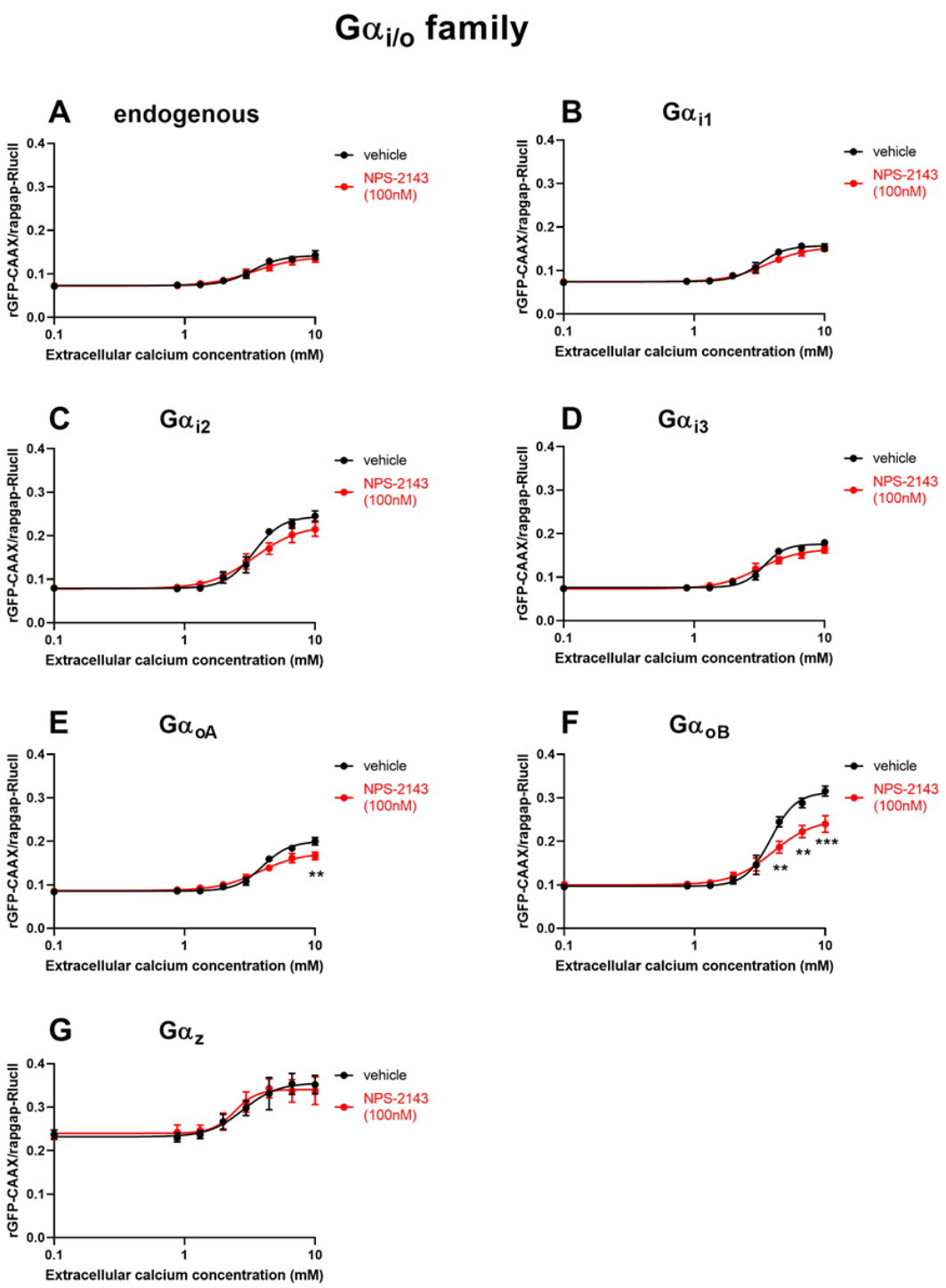


Figure 7.22 Activation of the $G\alpha_{i/o}$ family ($G\alpha_{i1,i2,i3,oA,oB,z}$) by the CaSR in response to increasing concentrations of Ca^{2+}_e in cells treated with vehicle (black line) or 100nM NPS-2143 (red line). Values are shown as mean±SEM of 4-5 independent transfections. Two-way ANOVA with Sidak's correction for multiple comparisons was performed using GraphPad Prism 8.4.1. **p<0.01, ****p<0.0001.

7.2.3 Effects of disease-causing CaSR mutations

Some FHH- and ADH-causing CaSR mutations have been suggested to be biased in downstream signalling assays[261], which may mean they preferentially impair signalling through certain G proteins. The above identified G protein biased allosteric modulators could represent a more targeted therapy for these patients. I therefore investigated whether known disease-causing CaSR mutations are biased.

7.2.3.1 Loss-of-function

Mutation of Arg185 of the CaSR to Gln185 causes FHH1, and results in a loss-of-function of downstream CaSR signalling[261]. Previous studies suggested that this mutation may cause biased signalling[261], and as a first analysis I investigated whether this mutation is biased towards any particular member of the $G\alpha_{q/11}$ family ($G\alpha_{q,11,14,15}$).

P63 ebBRET assays were performed in tetracycline-inducible HEK293-Flp-In-TREX-CaSR-WT and HEK293-Flp-In-TREX-CaSR-Arg185Gln cells (see 3.5.3). The advantage of this system is that any effects that mutants may have on cell growth are limited to the time of induction (in this case 48 hours).

This revealed that Arg185, compared to WT, resulted in significantly impaired signalling via $G\alpha_q$ (up to 2.5-fold reduction, $p<0.0001$) (Figure 7.23B), $G\alpha_{11}$ (up to 2.2-fold reduction, $p<0.0001$) (Figure 7.23C) and $G\alpha_{14}$ (up to 1.9-fold reduction, $p<0.0001$) (Figure 7.23D). An increase in baseline activity was observed for mock transfected cells (endogenous) (up to 1.4-fold reduction, $p<0.0001$) (Figure 7.23A) and $G\alpha_{15}$ (up to 1.3-fold reduction, $p<0.0001$) (Figure 7.23E); however, this was not observed for cells transfected with $G\alpha_q$, $G\alpha_{11}$ and $G\alpha_{14}$.

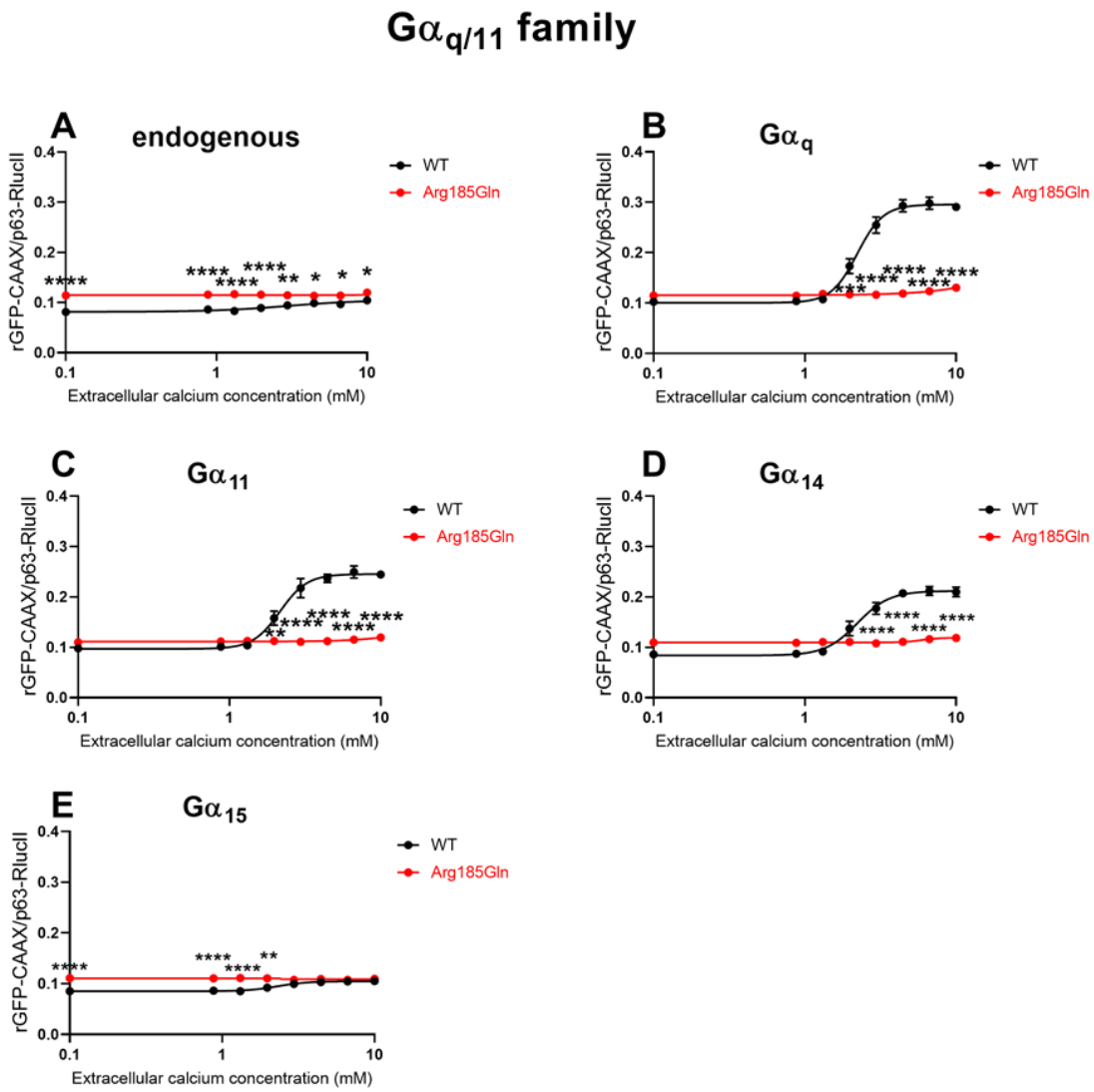


Figure 7.23 Activation of the $G\alpha_{q/11}$ family ($G\alpha_{q,11,14,15}$) by WT (black line) or Arg185Gln mutant (red line) CaSR in response to increasing concentrations of Ca^{2+}_e. Values are shown as mean±SEM of 4 independent transfections. Two-way ANOVA with Sidak's correction for multiple comparisons was performed using GraphPad Prism 8.4.1.*p<0.05, **p<0.01, ***p<0.001, ****p<0.0001.

7.2.3.2 Gain-of-function

Mutation of Ser657 of the CaSR to Cys657 causes ADH1, and results in gain-of-function of signalling downstream of the CaSR[307]. I studied the effects of this mutation on p63 recruitment by members of the $G\alpha_{q/11}$ family ($G\alpha_{q,11,14,15}$), using HEK293-Flp-In-TREX-CaSR-WT and HEK293-Flp-In-TREX-CaSR-Ser657Cys cells. This revealed that Cys657 resulted in significantly increased activity, compared to WT, of endogenous $G\alpha_{q/11}$ (up to 1.4-fold, $p<0.0001$) (Figure 7.24A), $G\alpha_q$ (up to 1.5-fold, $p<0.01$) (Figure 7.24B), $G\alpha_{11}$ (up to 1.4-fold, $p<0.001$) (Figure 7.24C), $G\alpha_{14}$ (up to 1.5-fold, $p<0.001$) (Figure 7.24D) and $G\alpha_{15}$ (up to 1.3-fold, $p<0.01$) (Figure 7.24E). In contrast, no significant changes in baseline activity were observed.

Taken together, these data indicate that the FHH1-causing Arg185Gln mutation causes loss-of-function of all $G\alpha_{q/11}$ family members that are activated by WT CaSR; and similarly, the ADH1-causing Ser657Cys mutation causes gain-of-function of all $G\alpha_{q/11}$ family members that are activated by WT CaSR.

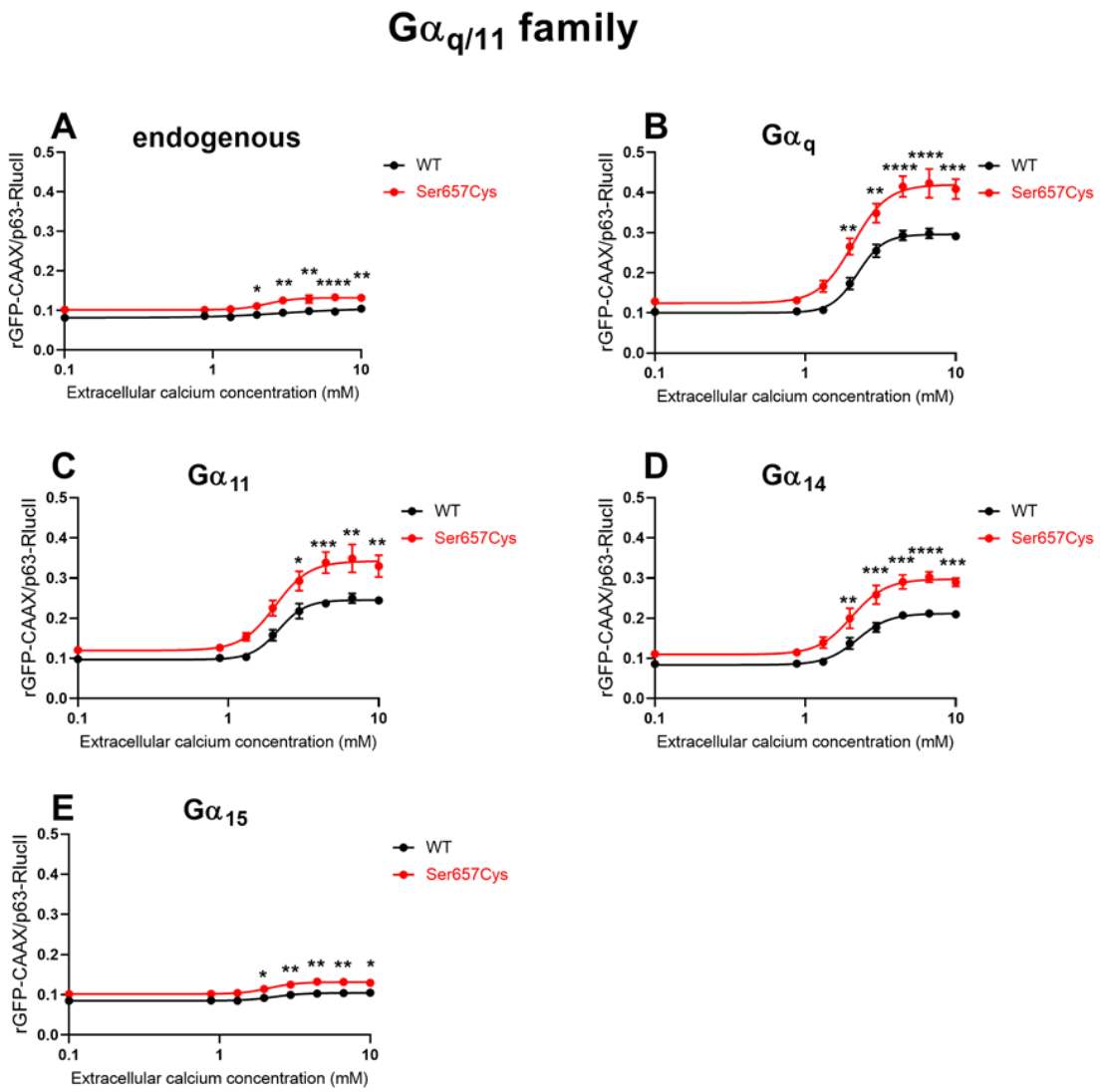


Figure 7.24 Activation of the $G\alpha_{q/11}$ family ($G\alpha_{q,11,14,15}$) by WT (black line) or Ser657Cys mutant (red line) CaSR in response to increasing concentrations of Ca^{2+}_e. Significantly increased activity was observed in all $G\alpha_{q/11}$ family members. Values are shown as mean±SEM of 4 independent transfections. Two-way ANOVA with Sidak's correction for multiple comparisons was performed using GraphPad Prism 8.4.1.*p<0.05, **p<0.01, ***p<0.001, ****p<0.0001.

7.3 Discussion

In this chapter I established ebBRET assays[162,166] as a tool to study CaSR functional selectivity and biased signalling in living cells. The system, which I validated using

prototypical class A receptors, allowed assessment of CaSR activation of 12 G proteins and 2 ß-arrestins. Using these techniques, I was able to show that some allosteric modulators of the CaSR are biased towards particular G proteins, whereas others have a similar effect on every G protein activated by the CaSR. Notably, all effects studied in this chapter are related to the main endogenous ligand Ca^{2+}_e. The CaSR has also been reported to be stimulated by other cations (see Table 1.3) which may have different signalling profiles.

7.3.1 CaSR functional selectivity

CaSR stimulation by increasing concentrations of Ca^{2+}_e has been shown to activate downstream signalling pathways of the $G\alpha_{q/11}$, $G\alpha_{i/o}$ and potentially $G\alpha_{12/13}$ families[77]. Moreover, involvement of ß-arrestins has been suggested for plasma membrane ruffling and Erk1/2 activation. I used ebBRET assays to study upstream G protein activation and ß-arrestin recruitment, and to investigate intra-family and inter-family cell signalling diversity.

I confirmed CaSR signalling by $G\alpha_q$ and $G\alpha_{11}$, which is well established[94], using p63 ebBRET assays[162]. Moreover, I showed that the CaSR is also a potent activator of $G\alpha_{14}$. In contrast, it had no effect on $G\alpha_{15}$. This is remarkable because $G\alpha_{15}$ is a promiscuous G protein which indiscriminately interacts with a wide variety of GPCRs, including many receptors that do not activate other members of the $G\alpha_{q/11}$ family[26]. $G\alpha_{14}$ is the least studied member of the $G\alpha_{q/11}$ family, and its expression is limited to pancreatic islets, taste tissue, spleen, lung, kidney, testis, and hematopoietic cells[25]. Studies in $G\alpha_{11}$ mutant mice (see chapter 5) indicate that in the pancreatic islets and the kidneys G proteins other than $G\alpha_{11}$ may be important for CaSR function, suggesting a potential role for $G\alpha_{14}$. Moreover, in contrast to the M_3R, CaSR did not show any constitutive p63 activation, indicating ligand stimulation is required for CaSR coupling to the $G\alpha_{q/11}$

family.

Investigation of the $G\alpha_{i/o}$ family revealed that the CaSR stimulates $G\alpha_{i2}$, $G\alpha_{i3}$, $G\alpha_{oA}$, $G\alpha_{oB}$ and $G\alpha_z$ (but not $G\alpha_{i1}$) in response to increasing concentrations of Ca^{2+}_e. Moreover, constitutive activation of $G\alpha_z$ was observed in cells transfected with CaSR and $G\alpha_z$. However, a similar baseline activation was also observed in cells expressing the M_2R and $G\alpha_z$. $G\alpha_z$ is a promiscuous G protein[308], and therefore the observed increase in baseline activity may not be mediated by the CaSR.

Previous studies in HEK293-CaSR cells have observed Ca^{2+}_e induced decreases in cAMP, thereby suggesting the activation of $G\alpha_i$[309]. Moreover, Erk1/2 activation in bovine parathyroid cells was reduced after PTX treatment, indicating that the response is likely mediated by $G\alpha_{i/o}$[310]; however, it may also be mediated by Gβγ due to the inhibitory effects of PTX on signalling events activated by Gβγ[6]. My overexpression studies of $G\alpha_{i/o}$ subunits indicate a direct involvement of $G\alpha_{i/o}$. Interestingly, a study using PTX-insensitive $G\alpha_{i1}$, $G\alpha_{i2}$, and $G\alpha_{i3}$ mutants indicated that $G\alpha_{i2}$ is the $G\alpha_{i/o}$ subtype responsible for CaSR mediated Erk1/2 activation[167]. This is in agreement with my results which show $G\alpha_{i2}$ to be the most potent $G\alpha_i$ subunit (up to 2.0-fold increase compared to endogenous). However, $G\alpha_{oB}$, which was not tested in the previous study, showed a similar activation by the CaSR (up to 2.2-fold). $G\alpha_o$ is predominantly expressed in the CNS, suggesting CaSR function in these tissues may be mediated by $G\alpha_o$. Moreover, and in contrast with the previous study, I also observed a small CaSR mediated activation of $G\alpha_{i3}$, suggesting ebBRET assays may potentially be more sensitive than other assays.

To investigate CaSR signalling by $G\alpha_{12}$ and $G\alpha_{13}$ I tested two different effectors of the $G\alpha_{12/13}$ family, p115 and pdz[6]. For both effectors, U46619 treatment of cells transfected with TPα, which was used as a positive control, resulted in a significant dose-dependent

increase in ebBRET activity. In contrast, no Ca^{2+}_e mediated increase was observed in CaSR expressing cells, indicating CaSR does not activate $G\alpha_{12}$ and/or $G\alpha_{13}$.

CaSR activation leads to membrane ruffling and Rho recruitment, which are downstream effectors traditionally linked to $G\alpha_{12/13}$. It has therefore been suggested that the CaSR can couple to $G\alpha_{12/13}$[94]. However, more recent studies have also linked these readouts to activation of the $G\alpha_{q/11}$ family[77,311]. In my studies I found that CaSR stimulation by Ca^{2+}_e led to activation of $G\alpha_{q/11}$ but not $G\alpha_{12/13}$, suggesting that Rho activation by the CaSR is likely mediated by members of the $G\alpha_{q/11}$ family. This is in contrast to a study in Madin-Darby canine kidney cells stably overexpressing CaSR which suggested that Ca^{2+}_e mediated activation of phospholipase D was mediated by $G\alpha_{12/13}$[311].

CaSR-induced membrane ruffling has also been linked to ß-arrestin signalling[312]. I measured Ca^{2+}_e mediated recruitment of ß-arrestin 1 and ß-arrestin 2 to the plasma membrane. This revealed that CaSR expressing cells have higher constitutive levels of ß-arrestin 1 and 2 recruitment compared to parental cells. Treatment with Ca^{2+}_e resulted in a further increase of ß-arrestin 1 recruitment. The observed preference for ß-arrestin 1 is remarkable because class A receptors (such as B2AR which was used as a positive control) preferentially recruit ß-arrestin 2, and class B receptors similarly recruit both ß-arrestin 1 and 2[165]. However, my results agree with previous studies which found that CaSR-induced plasma membrane ruffling was predominantly mediated by ß-arrestin 1[312]. In contrast, both ß-arrestins 1 and 2 were found to be involved in CaSR-mediated Erk1/2 activation[159,262], suggesting ß-arrestin 2 mediated downstream signalling may be independent of plasma membrane recruitment.

In summary, out of the 12 G proteins and 2 ß-arrestins tested, the CaSR was able to engage with 8 and 2, respectively, which were: $G\alpha_q$, $G\alpha_{11}$, $G\alpha_{14}$, $G\alpha_{i2}$, $G\alpha_{i3}$, $G\alpha_{oA}$, $G\alpha_{oB}$,

$G\alpha_z$ and ß-arrestin 1 and 2. However, it is unclear which effectors mediate physiological functions of the CaSR. Although both the $G\alpha_{q/11}$ and $G\alpha_{i/o}$ families have been shown to be critical mediators of CaSR function in the parathyroids[93,94], many of the molecular mechanisms (including the contribution of G protein subunits) governing intrinsic PTH secretion and synthesis are not fully understood[77,83] (see 1.3.1). Moreover, CaSR-mediated stimulation of insulin secretion was only partially blocked by PLC inhibitors (see 1.5.2), suggesting $G\alpha_{q/11}$ in combination with other effectors may mediate non-calcitropic effects of the CaSR[150].

7.3.2 Ligand biased signalling

Several CaSR allosteric molecules have been described, which range from naturally occurring amino acids to clinically used drugs[98]. I tested the effects of 6 CaSR allosteric modulators (the amino acid L-Phe; the small calcimimetic molecules Cinacalcet and AC-265347; the small calcilytic molecule NPS-2143; and the calcimimetic peptides Etelcalcetide and KP-2067) on each of the pathways activated by the orthosteric ligand Ca^{2+}_e. I also tested them on pathways that were not activated by Ca^{2+}_e, such as $G\alpha_{12,13}$. The latter is particularly relevant for positive allosteric modulators (calcimimetics), which may cause a receptor to engage effectors which are not stimulated in a physiological setting.

In order to facilitate comparison of modulator effects across the 14 different pathways, I generated radar plots which show the baseline-corrected area under the curve of Ca^{2+}_e induced responses in the presence of allosteric modulators or vehicle (Figure 7.25). This shows that none of the compounds significantly altered $G\alpha_{12}$ and $G\alpha_{13}$ activity, which was not surprising because the previous results (section 7.2.1) indicated that these G proteins are not engaged by the CaSR.

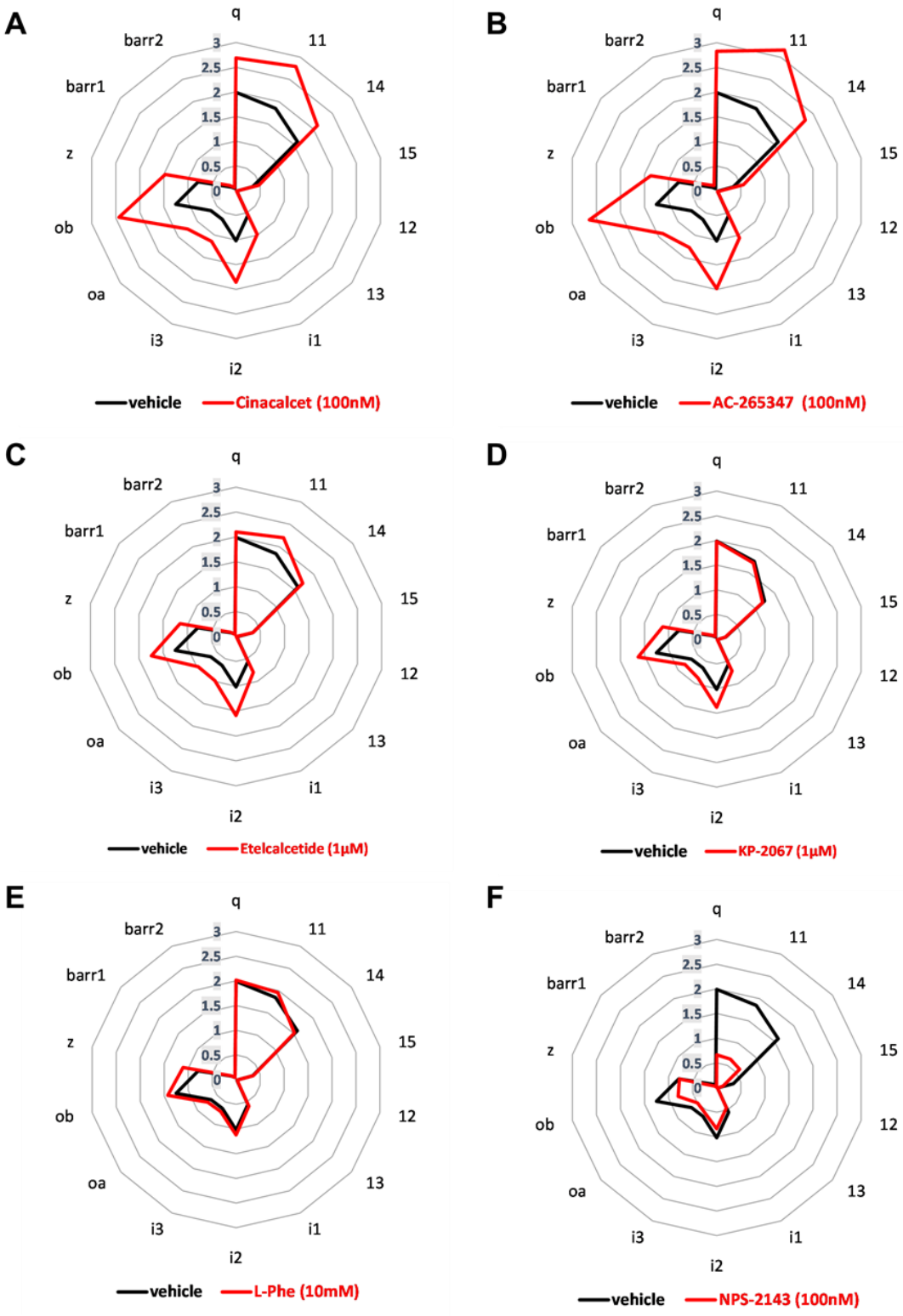


Figure 7.25 Radar plots of baseline-corrected area under the curve of Ca^{2+}_e induced activation of $G\alpha_q$, $G\alpha_{11}$, $G\alpha_{14}$, $G\alpha_{15}$, $G\alpha_{12}$, $G\alpha_{13}$, $G\alpha_{i1}$, $G\alpha_{i2}$, $G\alpha_{i3}$, $G\alpha_{oA}$, $G\alpha_{oB}$, $G\alpha_z$ and ß-arrestin 1/2 in cells treated with vehicle (black line) or CaSR allosteric modulators (red line) (A) cinacalcet (B) AC-265347 (C) Etelcalcetide (D) KP-2067 (E) L-Phe and (F) NPS-2143.

However, significant effects were also not observed for ß-arrestin 1 and 2 recruitment. Interestingly, a recent study that investigated CaSR internalisation using TR-FRET reported reduced CaSR internalisation in cells treated with NPS-2143, however this was not dependent on ß-arrestin 1 or 2[313].

All 6 modulators tested by ebBRET affected CaSR-mediated signalling via the $G\alpha_{q/11}$ and/or $G\alpha_{i/o}$ families. Assessment of these pathways demonstrated that CaSR modulators have the potential to elicit G protein biased signalling towards both families.

The small molecule calcimimetics cinacalcet (Figure 7.25A) and AC-265347 (Figure 7.25B) acted as balanced modulators, i.e. they significantly increased activity of every member of the $G\alpha_{q/11}$ and $G\alpha_{i/o}$ families that was stimulated by Ca^{2+}_e. Notably, cinacalcet is an effective treatment for secondary hyperparathyroidism, however, its clinical use is limited by on-target side effects[98]. This may be due to its stimulation of a wide range of G proteins. A better understanding of the underlying biology of CaSR signalling through multiple G proteins may facilitate the development of biased cinacalcet analogues that stimulate only a small subset of G proteins. These could provide the same clinical benefits as cinacalcet with fewer side effects, analogously to the G protein biased opioids that are currently in clinical development[197,200].

Interestingly, the peptide calcimimetics Etelcalcetide (Figure 7.25C) and KP-2067 (Figure 7.25D), and the L-amino acid L-Phe did not affect CaSR signalling by the $G\alpha_{q/11}$ family but caused significant activation of the $G\alpha_{i/o}$ family (Figure 7.16H). Notably, L-Phe has been reported to improve glucose tolerance via CaSR activation[314], suggesting that the $G\alpha_{i/o}$ family may be important for CaSR mediated effects on glucose homeostasis.

The peptide calcimimetic Etelcalcetide has recently been approved for the treatment of secondary hyperparathyroidism[98]. However, little is known about its effects on CaSR

signalling[98]. Previous studies have revealed a discrepancy between *in vitro* and *in vivo* actions of Etelcalcetide: in IP_1 signalling assays, an EC_{50} of 25μM was found; however, in *in vivo* studies with dogs the maximum plasma concentration of Etelcalcetide was around 300ng/ml, which is equivalent to 286nM, and this caused a profound decrease in plasma calcium[173,174].

This may be explained by the results generated in this chapter. IP_1 signalling is a downstream readout of the $G\alpha_{q/11}$ family, and treatment with 1μM Etelcalcetide/KP-2067 had no effect on the $G\alpha_{q/11}$ family but caused significant activation of all $G\alpha_{i/o}$ family members apart from $G\alpha_z$. This suggests that activation of the $G\alpha_{i/o}$ family by the CaSR is sufficient to induce changes in plasma calcium.

Remarkably, out of the tested modulators, the $G\alpha_{i/o}$ biased compounds were aromatic amino acids and peptides, suggesting that a common structural mechanism of $G\alpha_{i/o}$ biased CaSR modulators may exist. This is supported by the observation that Etelcalcetide has a different binding site than small molecule PAMs: it binds to the ECD of the CaSR rather than the TMD[5,40] (for a detailed description see 1.6.3.2). My study, which shows that Etelcalcetide is biased towards $G\alpha_{i/o}$, elucidates the functional effects of this different binding site and indicates that allosteric effects in the ECD can direct CaSR-G protein coupling.

In contrast, the calcilytic NPS-2143 is $G\alpha_{q/11}$ biased, i.e. it is a potent inhibitor of CaSR mediated signalling via $G\alpha_{q/11}$ but has little effect on $G\alpha_{i/o}$ signalling (Figure 7.25F). Notably, NPS-2143 was assessed as a potential novel treatment for osteoporosis in clinical trials, but these were stopped due to lack of efficacy[98]. This suggests that inhibition of the $G\alpha_{i/o}$ pathway may potentially be important for CaSR effects in bone.

7.3.3 Effects of disease-causing CaSR mutations

Finally, the FHH-causing mutation Arg185Gln[261] and the ADH-causing mutation Ser657Cys[307] altered calcium-mediated CaSR signalling via $G\alpha_q$, $G\alpha_{11}$, and $G\alpha_{14}$ and had no effect on $G\alpha_{15}$, thereby demonstrating that ebBRET assays are a suitable system to study the effects of CaSR mutations on activation of individual G protein subunits. The particular loss- and gain-of function mutants assessed in this chapter showed the same functional selectivity for the $G\alpha_{q/11}$ family as WT CaSR, i.e. they stimulated the same G proteins, albeit at a different magnitude of response. However, other disease-causing mutations may cause a signalling bias even within the $G\alpha_{q/11}$ family. The next step will be to investigate whether these mutations also disrupt signalling by the $G\alpha_{i/o}$ family, and ß-arrestin recruitment. If both biased and unbiased mutations are identified, this would highlight which regions of the receptor are particularly important for CaSR-coupling to particular G proteins, and the patient phenotypes could elucidate which effectors are mediating physiological functions of the CaSR.

In conclusion, this chapter has demonstrated the benefits of ebBRET assays to study a range of CaSR signalling pathways. Moreover, I have identified both $G\alpha_{q/11}$ and $G\alpha_{i/o}$ biased as well as balanced allosteric CaSR modulators. Going forward it will be important to link distinct cellular pathways to particular physiological effects, which will pave the way for the design of biased CaSR ligands with fewer side effects than unbiased ones.

8 CONCLUSION

The aims of my thesis were to: identify and characterise rare *GNA11* variants; investigate glucose metabolism in Dsk7 mice; study functional differences between $G\alpha_{11}$ and $G\alpha_q$; and to elucidate CaSR functional selectivity using BRET biosensors.

My analysis of *GNA11* variants in large exome datasets revealed novel *GNA11* variants that disrupt CaSR signalling in *vitro* and are associated with hypercalcaemia in patients. It highlights that rare variants found in commonly used online databases can represent pathogenic mutations. Some of the identified variants also disrupted signalling by prototypical class A GPCRs and promoted biased and promiscuous signalling. They are therefore likely to have non-calcitropic effects; however, the physiological significance remains to be elucidated.

I investigated one such potential non-calcitropic phenotype by studying the effects of a $G\alpha_{11}$ gain-of-function mutation (Ile62Val) in mice (Dsk7). This revealed that $G\alpha_{11}$ gain-of-function does not influence glucose homeostasis or pancreatic islet architecture. Thus, the glucose phenotype observed in mice with a gain-of-function CaSR mutation (Nuf) is likely transduced by G proteins other than $G\alpha_{11}$ or is due to G protein independent mechanisms.

The obvious candidate for such a G protein is $G\alpha_q$, which shares 90% of its amino acids with $G\alpha_{11}$, and has previously been considered to have identical function to $G\alpha_{11}$. However, my studies revealed significant differences between the two: at the level of human pathology, G protein activation, effector interaction, and transcription.

To further study the differences in CaSR coupling to different G protein subunits, I assessed CaSR signalling across 12 G proteins and 2 ß-arrestins. This revealed that the CaSR is a promiscuous receptor which activated 8 out of 12 G proteins and 2 out of 2 ß-arrestins. I demonstrated the benefits of ebBRET assays to study a range of CaSR signalling pathways and showed that clinically approved CaSR allosteric modulators

can be both biased (e.g. Etelcalcetide) or balanced (e.g. cinacalcet). Further investigation of the signalling properties could facilitate the design of biased CaSR ligands with fewer side effects.

EbBRET studies also revealed that the endogenous ligand L-Phe stimulates CaSR signalling via $G\alpha_{i/o}$ but not $G\alpha_{q/11}$. This supports the finding that Dsk7 mice ($G\alpha_{11}$ gain-of-function) do not have abnormal glucose homeostasis, as L-Phe has been reported to improve glucose tolerance via CaSR activation in the gut[314]. This suggests that the role of CaSR in glucose metabolism may be predominantly mediated by $G\alpha_{i/o}$.

In summary, my thesis provides insights into $G\alpha_{11}$ structure-function and its role in calcium and glucose homeostasis. It highlights the importance of $G\alpha_{11}$, not only for CaSR signalling, but also for other GPCRs. Moreover, it highlights the importance of other G proteins for CaSR signalling.

9 FUTURE PLANS

Chapter 1 has demonstrated that $G\alpha_{11}$ mutations can disrupt signalling by receptors other than the CaSR *in vitro*. Going forward it will be interesting to identify which receptors have the potential to mediate non-calcitropic effects of $G\alpha_{11}$ *in vivo*.

A good candidate receptor family are the melanocortin (MC) receptors. They have previously been described to couple predominantly to $G\alpha_s$[315,316], however, a recent study using a direct readout of G protein activation found strong coupling to $G\alpha_{q/11}$[207].

A non-calcitropic effect that is observed in Dsk7 mice ($G\alpha_{11}$ gain-of-function) is dark skin[35,36]. This could be mediated by MC_1R which is a key mediator of pigmentation[280,282,315]. Human MC_1R loss-of-function mutations are associated with red hair, fair skin and increased melanoma risk[280,317]. Conversely, increased MC_1R activity causes dark coat colour in mice[280,281]. This is similar to the phenotypes observed for germline and somatic activating $G\alpha_{q/11}$ mutations (increased pigmentation in mice[36] and uveal melanoma in humans[33], respectively).

Moreover, the Dsk7 mice have reduced body weight (Figure 5.2). Notably, inactivating MC_4R mutations are the most common cause of human monogenic obesity; however, many do not alter canonical $G\alpha_s$ signalling[282,283]. $G\alpha_{q/11}$ activation by MC_4R in hypothalamic neurons is established, and deletion of $G\alpha_{q/11}$ but not $G\alpha_s$ in the paraventricular nucleus of the hypothalamus causes MC_4R-mediated hyperphagic obesity[283].

I propose that $G\alpha_{11}$ plays a role in MC_1R/MC_4R signalling and hypothesise that MCR-mediated activation of $G\alpha_{11}$ may be altered by germline and somatic *GNA11* mutations as well as MC_1R/MC_4R ligands.

To test this, the first aim would be to establish whether MC_1R signals constitutively through $G\alpha_{11}$ using functional assays established in this thesis, including phospho-ERK AlphaScreen (3.8.5)[210], SRE/NFAT-RE luciferase reporter (3.8.1)[211] and ebBRET

(3.8.6)[162]. The contribution of $G\alpha_{11}$ would be determined through comparison with cells lacking endogenous $G\alpha_{q/11}$[209]. Moreover, it would be interesting to assess the effects of MC_1R and MC_4R ligands to activate $G\alpha_{11}$, i.e. assess the effects of endogenous (e.g. α-MSH, ACTH) and synthetic (e.g. afamelanotide, setmelanotide, BMS-470539) ligands[318] on signalling by $G\alpha_s$ versus $G\alpha_{11}$. Subsequently, I would assess the effects of germline loss-of-function $G\alpha_{11}$ mutations on MC_1R/MC_4R signalling, in the presence or absence of ligands, specifically Ile62Val (which causes dark skin in mice) and the mutations that have impaired class A signalling in chapter 4.2.5.1.

My results have highlighted important differences between $G\alpha_q$ and $G\alpha_{11}$. To further elucidate the mechanisms underlying diversity within the $G\alpha_{q/11}$ family, I propose to investigate the differences and similarities between all members of the $G\alpha_{q/11}$ family ($G\alpha_q$, $G\alpha_{11}$, $G\alpha_{14}$ and $G\alpha_{15}$). Assessment of the effects of FHH2- and ADH2- mutations on signalling by $G\alpha_{14}$ and $G\alpha_{15}$ will shed light on the subtype-specific nature of G protein defects involved with calcitropic disorders.

My final results chapter has demonstrated that CaSR allosteric modulators can be either balanced (e.g. cinacalcet, AC-265347), $G\alpha_q$ biased (NPS-2143) or $G\alpha_i$ biased (e.g. Etelcalcetide, KP-2067, L-Phe). However, the physiological significance of these biases remains to be elucidated. I plan to assess the physiological significance of CaSR functional selectivity, in the first instance by comparing the effects of biased and balanced compounds on the secretion of PTH from parathyroids, and insulin and glucagon from pancreatic islets *ex vivo* in isolated mouse tissues. Comparison of potencies of biased versus balanced compounds will reveal which CaSR signalling pathways drive these distinct physiological functions.

I have also validated ebBRET as a tool to investigate the effects of known disease-causing CaSR mutations on $G\alpha_{q/11}$ activation. The next step will be to investigate

whether these mutations also disrupt signalling by other effectors, such as $G\alpha_{i/o}$ and ß-arrestin. I propose to assess reported CaSR mutations that are located in different regions of the CaSR (e.g. ECD, TMD) for their ability to cause biased signalling. If biased mutations are identified, this would highlight which regions of the receptor are particularly important for CaSR-coupling to effectors, and the patient phenotypes could elucidate which effectors are mediating physiological functions of the CaSR.

Finally, ebBRET sensors can not only be used to assess signalling events that occur at the plasma membrane but can also be used to study receptor endocytosis and trafficking[63,164,165]. This is particularly relevant for the CaSR, as it has been shown that *AP2S1* mutations decrease CaSR signalling and cause hypercalcaemia, despite impairing endocytosis meaning that more receptors are present at the membrane. CaSR has been shown to be enriched in lipid rafts and caveolae[319]. Some GPCRs, such as the GLP1 receptor, require $G\alpha_{q/11}$ for signalling and internalisation in caveolae[320]. I propose to use ebBRET sensors directed at lipid rafts (rGFP-CCIL) and endosomes (rGFP-FYVE) to study CaSR signalling (and the effects of CaSR-targeting drugs) in these subcellular compartments[165,166,233]. This will elucidate CaSR signalling at a spatio-temporal level.

In summary, my thesis highlights the complex functions of CaSR and $G\alpha_{11}$, and how they can be biased and affected by different drugs. This opens up many potential avenues to further explore GPCR and G protein signalling.

APPENDIX

A. Tables

Table 9.1 Formalin-fixed, paraffin-embedded Dsk7 4.5µM pancreas slides used for histology.

Sample ID	slide	gender	genotype
25	7	m	wt
25	14	m	wt
25	21	m	wt
25	28	m	wt
26	7	m	wt
26	14	m	wt
26	21	m	wt
26	28	m	wt
37	7	m	wt
37	14	m	wt
37	21	m	wt
37	28	m	wt
38	7	m	wt
38	14	m	wt
38	21	m	wt
38	28	m	wt
33	7	m	hom
33	14	m	hom
33	21	m	hom
33	28	m	hom
34	7	m	hom
34	14	m	hom
34	21	m	hom
34	28	m	hom
49	7	m	hom
49	14	m	hom
49	21	m	hom
49	28	m	hom
50	7	m	hom
50	14	m	hom
50	21	m	hom
50	28	m	hom
29	7	m	het
29	14	m	het
29	21	m	het
29	28	m	het
30	7	m	het
30	14	m	het
30	21	m	het
30	28	m	het
43	7	m	het
43	14	m	het
43	21	m	het

Sample ID	slide	gender	genotype
43	28	m	het
44	7	m	het
44	14	m	het
44	21	m	het
44	28	m	het
27	7	f	wt
27	14	f	wt
27	21	f	wt
27	28	f	wt
28	7	f	wt
28	14	f	wt
28	21	f	wt
28	28	f	wt
40	7	f	wt
40	14	f	wt
40	21	f	wt
40	28	f	wt
41	7	f	wt
41	14	f	wt
41	21	f	wt
41	28	f	wt
35	7	f	hom
35	14	f	hom
35	21	f	hom
35	28	f	hom
36	7	f	hom
36	14	f	hom
36	21	f	hom
36	28	f	hom
51	7	f	hom
51	14	f	hom
51	21	f	hom
51	28	f	hom
52	7	f	hom
52	14	f	hom
52	21	f	hom
52	28	f	hom
31	7	f	het
31	14	f	het
31	21	f	het
31	28	f	het
32	7	f	het
32	14	f	het
32	21	f	het
32	28	f	het
46	7	f	het
46	14	f	het
46	21	f	het
46	28	f	het
47	7	f	het
47	14	f	het

Sample ID	slide	gender	genotype
47	21	f	het
47	28	f	het

Table 9.2 Synonymous *GNA11* variants found in dbSNP (n=170)

Variant ID	Location	Chr: bp	Alleles	AA coord
rs758302558	19:3094657	19:3094657	T/C	2
rs779989113	19:3094660	19:3094660	G/C/T	3
rs779989113	19:3094660	19:3094660	G/C/T	3
rs768494922	19:3094684	19:3094684	G/C	11
rs1416324400	19:3094696	19:3094696	G/C	15
rs776560028	19:3094699	19:3094699	G/A	16
rs748439096	19:3094705	19:3094705	C/T	18
rs375505077	19:3094720	19:3094720	C/T	23
rs1280763414	19:3094736	19:3094736	C/T	29
rs770035605	19:3094744	19:3094744	G/A	31
rs1205089245	19:3094750	19:3094750	G/A	33
rs1212022673	19:3094765	19:3094765	C/G	38
rs1257166339	19:3094768	19:3094768	G/A	39
rs1422256430	19:3094771	19:3094771	C/G/T	40
rs1422256430	19:3094771	19:3094771	C/G/T	40
rs1342252945	19:3094775	19:3094775	C/T	42
rs368438123	19:3094777	19:3094777	G/A	42
rs534950824	19:3094780	19:3094780	G/A	43
rs371875148	19:3094786	19:3094786	C/T	45
rs776843648	19:3110150	19:3110150	C/T	46
rs61731117	19:3110153	19:3110153	G/A	47
rs147570504	19:3110156	19:3110156	C/T	48
rs759067107	19:3110162	19:3110162	C/T	50
rs149108190	19:3110174	19:3110174	G/A/T	54
rs149108190	19:3110174	19:3110174	G/A/T	54
rs777673683	19:3110195	19:3110195	C/T	61
rs1212104789	19:3110198	19:3110198	C/A	62
rs61731116	19:3110201	19:3110201	C/T	63
rs755663461	19:3110204	19:3110204	C/G/T	64
rs755663461	19:3110204	19:3110204	C/G/T	64
rs576887084	19:3110207	19:3110207	C/T	65
rs369699960	19:3110216	19:3110216	G/A	68
rs1257006905	19:3110222	19:3110222	G/A	70
rs947843389	19:3110231	19:3110231	C/T	73
rs762226968	19:3110234	19:3110234	C/T	74
rs1356330122	19:3110243	19:3110243	G/A	77

Variant ID	Location	Chr: bp	Alleles	AA coord
rs770729214	19:3110246	19:3110246	C/T	78
rs145033220	19:3110252	19:3110252	C/T	80
rs1261175462	19:3110255	19:3110255	G/A	81
rs1171579660	19:3110264	19:3110264	C/T	84
rs140204057	19:3110267	19:3110267	C/T	85
rs774842486	19:3110276	19:3110276	G/A	88
rs763900975	19:3110285	19:3110285	C/A	91
rs749256854	19:3110303	19:3110303	C/G	97
rs750706655	19:3110312	19:3110312	C/T	100
rs933889965	19:3110315	19:3110315	C/T	101
rs758603549	19:3110321	19:3110321	C/T	103
rs1363750968	19:3113335	19:3113335	T/C	109
rs767543072	19:3113338	19:3113338	G/A	110
rs752795403	19:3113342	19:3113342	C/T	112
rs1244219907	19:3113356	19:3113356	G/A	116
rs778378225	19:3113359	19:3113359	C/T	117
rs1298068160	19:3113362	19:3113362	G/A	118
rs757500793	19:3113371	19:3113371	G/A	121
rs559730941	19:3113380	19:3113380	C/T	124
rs531521209	19:3113392	19:3113392	C/T	128
rs747614543	19:3113410	19:3113410	C/G	134
rs769744132	19:3113413	19:3113413	G/T	135
rs1376653921	19:3113419	19:3113419	G/A	137
rs762810586	19:3113422	19:3113422	C/T	138
rs770697543	19:3113425	19:3113425	G/A	139
rs376120835	19:3113428	19:3113428	C/A	140
rs1208615736	19:3113437	19:3113437	A/G	143
rs759718861	19:3113443	19:3113443	C/T	145
rs1181395352	19:3113458	19:3113458	G/A	150
rs760781651	19:3113464	19:3113464	G/A/C	152
rs754374982	19:3113467	19:3113467	C/G/T	153
rs754374982	19:3113467	19:3113467	C/G/T	153
rs200449144	19:3113470	19:3113470	C/T	154
rs754616176	19:3113482	19:3113482	G/A	158
rs1469665156	19:3114944	19:3114944	C/T	159
rs771702042	19:3114953	19:3114953	C/T	162
rs141926949	19:3114956	19:3114956	C/T	163
rs756722832	19:3114968	19:3114968	C/T	167
rs1329989088	19:3114989	19:3114989	C/T	174
rs146295413	19:3115001	19:3115001	C/T	178
rs1405333021	19:3115007	19:3115007	G/A	180
rs1387749615	19:3115010	19:3115010	G/T	181
rs758392443	19:3115016	19:3115016	C/T	183
rs571070788	19:3115028	19:3115028	C/T	187
rs369633640	19:3115031	19:3115031	C/A/T	188

Variant ID	Location	Chr: bp	Alleles	AA coord
rs369633640	19:3115031	19:3115031	C/A/T	188
rs201668624	19:3115037	19:3115037	C/A/T	190
rs201668624	19:3115037	19:3115037	C/A/T	190
rs748179180	19:3115040	19:3115040	G/A	191
rs902387291	19:3115049	19:3115049	C/T	194
rs1210308648	19:3115053	19:3115053	C/T	196
rs527451247	19:3115067	19:3115067	C/A	200
rs1352666663	19:3118924	19:3118924	G/A/T	202
rs1352666663	19:3118924	19:3118924	G/A/T	202
rs751616481	19:3118936	19:3118936	G/A/C	206
rs751616481	19:3118936	19:3118936	G/A/C	206
rs376322895	19:3118939	19:3118939	G/A	207
rs1180738052	19:3118942	19:3118942	C/T	208
rs767395295	19:3118946	19:3118946	C/A	210
rs756381542	19:3118951	19:3118951	G/A	211
rs777912441	19:3118955	19:3118955	C/A/T	213
rs749372899	19:3118960	19:3118960	G/A	214
rs757393272	19:3118981	19:3118981	G/A	221
rs754620313	19:3118984	19:3118984	C/T	222
rs746432688	19:3118993	19:3118993	C/T	225
rs371149978	19:3118996	19:3118996	C/A	226
rs199749164	19:3119005	19:3119005	C/G/T	229
rs199749164	19:3119005	19:3119005	C/G/T	229
rs747291840	19:3119008	19:3119008	C/T	230
rs1220448139	19:3119017	19:3119017	C/T	233
rs138168314	19:3119023	19:3119023	C/T	235
rs762692548	19:3119032	19:3119032	C/G	238
rs149637752	19:3119044	19:3119044	G/A	242
rs752549242	19:3119050	19:3119050	C/T	244
rs778362669	19:3119209	19:3119209	C/A	247
rs1314086635	19:3119211	19:3119211	G/A	247
rs1421576921	19:3119217	19:3119217	G/A	249
rs745528917	19:3119220	19:3119220	G/A	250
rs1473783546	19:3119223	19:3119223	C/T	251
rs997103699	19:3119230	19:3119230	C/T	254
rs771537617	19:3119232	19:3119232	G/C/T	254
rs771537617	19:3119232	19:3119232	G/C/T	254
rs4900	19:3119241	19:3119241	C/T	257
rs776428312	19:3119244	19:3119244	C/T	258
rs1181877931	19:3119247	19:3119247	C/T	259
rs1301540859	19:3119253	19:3119253	C/T	261
rs750681091	19:3119274	19:3119274	C/A/T	268
rs750681091	19:3119274	19:3119274	C/A/T	268
rs1176498408	19:3119280	19:3119280	C/T	270
rs751628153	19:3119283	19:3119283	C/T	271

Variant ID	Location	Chr: bp	Alleles	AA coord
rs755573572	19:3119286	19:3119286	C/T	272
rs1259894142	19:3119298	19:3119298	G/A	276
rs375463765	19:3119322	19:3119322	G/A	284
rs118125169	19:3119328	19:3119328	G/C/T	286
rs118125169	19:3119328	19:3119328	G/C/T	286
rs1161554882	19:3119331	19:3119331	C/T	287
rs1042130457	19:3119337	19:3119337	G/A	289
rs1381946289	19:3119340	19:3119340	C/T	290
rs756612392	19:3119346	19:3119346	C/T	292
rs372711795	19:3119349	19:3119349	C/T	293
rs147368872	19:3119355	19:3119355	C/T	295
rs1198876192	19:3120993	19:3120993	C/G	298
rs1461947710	19:3120997	19:3120997	C/A/T	300
rs1393346370	19:3120999	19:3120999	G/A	300
rs539753774	19:3121002	19:3121002	C/T	301
rs145170690	19:3121011	19:3121011	G/A	304
rs750757769	19:3121014	19:3121014	G/A	305
rs752162469	19:3121038	19:3121038	C/T	313
rs755586030	19:3121053	19:3121053	C/A/T	318
rs755586030	19:3121053	19:3121053	C/A/T	318
rs1363672004	19:3121056	19:3121056	C/T	319
rs150929326	19:3121059	19:3121059	C/T	320
rs1416858721	19:3121065	19:3121065	G/A	322
rs778881101	19:3121068	19:3121068	C/T	323
rs772434708	19:3121071	19:3121071	C/T	324
rs780352816	19:3121074	19:3121074	C/T	325
rs747189004	19:3121083	19:3121083	C/T	328
rs375856122	19:3121086	19:3121086	G/A/C	329
rs375856122	19:3121086	19:3121086	G/A/C	329
rs894185941	19:3121095	19:3121095	C/T	332
rs555203104	19:3121101	19:3121101	G/A	334
rs1290800871	19:3121104	19:3121104	G/A	335
rs928679789	19:3121107	19:3121107	C/T	336
rs763245208	19:3121116	19:3121116	C/T	339
rs140749796	19:3121122	19:3121122	C/G/T	341
rs1321424736	19:3121125	19:3121125	G/C/T	342
rs1321424736	19:3121125	19:3121125	G/C/T	342
rs760222003	19:3121128	19:3121128	C/T	343
rs1421887982	19:3121131	19:3121131	G/A	344
rs763698658	19:3121134	19:3121134	G/A	345
rs1384690235	19:3121152	19:3121152	C/T	351
rs1158680732	19:3121164	19:3121164	G/A	355
rs1436819503	19:3121171	19:3121171	C/T	358
rs1451779777	19:3121173	19:3121173	G/T	358

Table 9.3 *GNA11* missense variants in the dbSNP database (n=144)

Variant ID	Chr: bp	Alleles	AA	AA coord
rs1417344175	19:3094656	C/T	T/I	2
rs1387105467	19:3094667	A/C	M/L	6
rs1401199158	19:3094671	T/C	M/T	7
rs141078172	19:3094674	C/T	A/V	8
rs1338184866	19:3094692	A/G	E/G	14
rs1242029660	19:3094709	C/T	R/W	20
rs1479867877	19:3094733	C/A	Q/K	28
rs200234790	19:3094746	A/G	D/G	32
rs773203722	19:3094757	G/A/T	A/T	36
rs773203722	19:3094757	G/A/T	A/S	36
rs1486864119	19:3094761	G/A/T	R/Q	37
rs1486864119	19:3094761	G/A/T	R/L	37
rs1007210976	19:3094784	C/A	L/I	45
rs762714189	19:3110152	C/T	T/M	47
rs377224539	19:3110163	G/A	G/R	51
rs755993488	19:3110179	T/C	I/T	56
rs587777707	19:3110191	G/A/T	R/H	60
rs1477351940	19:3110202	G/A	G/S	64
rs147528229	19:3110205	G/A/T	A/T	65
rs147528229	19:3110205	G/A/T	A/S	65
rs868681560	19:3110209	G/A	G/D	66
rs140301317	19:3110229	C/T	R/C	73
rs769019097	19:3110230	G/A	R/H	73
rs777092144	19:3110232	G/A	G/S	74
rs1391411006	19:3110239	C/T	T/I	76
rs1232791367	19:3110244	C/A	L/I	78
rs777099166	19:3110247	G/A	V/I	79
rs1402723163	19:3110254	A/G	Q/R	81
rs1487847863	19:3110259	A/G	I/V	83
rs74913870	19:3110263	T/C	F/S	84
rs374089777	19:3110268	G/A	A/T	86
rs1475313918	19:3110271	A/G	M/V	87
rs760710011	19:3110277	G/A	A/T	89
rs753693838	19:3110286	C/T	R/W	92
rs941191833	19:3110287	G/A/T	R/Q	92
rs941191833	19:3110287	G/A/T	R/L	92
rs975342398	19:3110292	A/G	M/V	94
rs1297795462	19:3110296	A/G	E/G	95
rs1456020858	19:3110297	G/C	E/D	95
rs1380208656	19:3110298	A/G	T/A	96
rs756991534	19:3110299	C/T	T/M	96
rs1376341794	19:3110305	A/G	K/R	98
rs1306652036	19:3110329	A/G	N/S	106

Variant ID	Chr: bp	Alleles	AA	AA coord
rs1051216341	19:3110332	A/T	K/M	107
rs751665166	19:3113334	A/G	N/S	109
rs759791665	19:3113337	C/T	A/V	110
rs1215008332	19:3113348	C/T	R/W	114
rs541350337	19:3113349	G/A	R/Q	114
rs1451507571	19:3113351	G/C	E/Q	115
rs1197262629	19:3113353	G/C	E/D	115
rs1368778199	19:3113357	G/T	D/Y	117
rs754271296	19:3113360	G/A	V/M	118
rs1308091091	19:3113373	C/T	T/I	122
rs879188402	19:3113376	C/T	T/I	123
rs1170008066	19:3113381	G/A	E/K	125
rs1165709212	19:3113383	G/C	E/D	125
rs746693359	19:3113385	A/G	H/R	126
rs780718032	19:3113393	G/A/C	V/I	129
rs780718032	19:3113393	G/A/C	V/L	129
rs1568282988	19:3113405	A/G	K/E	133
rs371712160	19:3113409	C/A	T/N	134
rs773074121	19:3113417	G/C	E/Q	137
rs1173495934	19:3113424	C/G	P/R	139
rs778757346	19:3113444	G/A	D/N	146
rs767809613	19:3113447	C/T	R/C	147
rs1035292287	19:3113448	G/A	R/H	147
rs1261353288	19:3113450	A/G	R/G	148
rs752848608	19:3113456	G/A	E/K	150
rs760781651	19:3113464	G/A/C	Q/H	152
rs779191241	19:3113471	G/A	D/N	155
rs750766195	19:3113480	A/G	K/E	158
rs775624350	19:3114957	G/A	V/I	164
rs191421665	19:3114975	T/A	L/M	170
rs1391552100	19:3115008	C/T	R/W	181
rs1555702147	19:3115014	C/T	R/C	183
rs1317391449	19:3115038	G/A	E/K	191
rs769982397	19:3115050	G/A	D/N	195
rs768371546	19:3115059	A/C	N/H	198
rs1431166394	19:3115060	A/G	N/S	198
rs766426049	19:3118925	A/T	M/L	203
rs587777022	19:3118950	C/G/T	S/L	211
rs777912441	19:3118955	C/A/T	R/W	213
rs778948783	19:3118985	G/A	V/M	223
rs1309810840	19:3119006	G/A	V/I	230
rs769503200	19:3119009	G/A	A/T	231
rs1568284925	19:3119025	A/G	D/G	236
rs766046727	19:3119036	G/A	V/M	240
rs1291813342	19:3119037	T/C	V/A	240

Variant ID	Chr: bp	Alleles	AA	AA coord
rs1007967128	19:3119042	T/G	S/A	242
rs773976709	19:3119043	C/T	S/L	242
rs1295243293	19:3119045	G/C	D/H	243
rs767308128	19:3119046	A/G	D/G	243
rs1568285021	19:3119206	A/G	N/D	246
rs1208115313	19:3119210	G/A	R/Q	247
rs775040372	19:3119236	C/T	R/W	256
rs529942770	19:3119237	G/A	R/Q	256
rs1297128070	19:3119246	T/C	I/T	259
rs761542744	19:3119248	A/G	T/A	260
rs1449570989	19:3119252	A/G	Y/C	261
rs765454337	19:3119259	G/C	W/C	263
rs144829732	19:3119275	G/A	V/I	269
rs1471377402	19:3119278	A/G	I/V	270
rs1409264282	19:3119308	G/A	E/K	280
rs1161111839	19:3119310	G/C	E/D	280
rs1444263678	19:3119312	A/C	D/A	281
rs1238030187	19:3119323	T/C	Y/H	285
rs1420026055	19:3119345	T/A	F/Y	292
rs745554999	19:3119350	G/A	E/K	294
rs1208131352	19:3119356	G/A	D/N	296
rs1259650887	19:3120992	C/T	P/L	298
rs1439859917	19:3120995	A/C	Q/P	299
rs1461947710	19:3120997	C/A/T	R/W	300
rs919502623	19:3120998	G/A	R/Q	300
rs139538868	19:3121003	G/A	A/T	302
rs762218250	19:3121010	C/A/T	A/E	304
rs762218250	19:3121010	C/A/T	A/V	304
rs1317335037	19:3121015	C/T	R/W	306
rs928378285	19:3121019	A/G	E/G	307
rs759218880	19:3121024	A/G	I/V	309
rs767110044	19:3121028	T/C	L/P	310
rs1489377886	19:3121034	T/C	M/T	312
rs772471502	19:3121039	G/A/T	V/M	314
rs772471502	19:3121039	G/A/T	V/L	314
rs386352309	19:3121042	G/A	D/N	315
rs777133920	19:3121054	G/A	D/N	319
rs753862594	19:3121058	G/A	S/N	320
rs1427351200	19:3121060	G/A	D/N	321
rs201368515	19:3121069	A/G	I/V	324
rs1364056722	19:3121075	T/G	S/A	326
rs1298964952	19:3121085	C/T	T/M	329
rs1201897778	19:3121094	C/G	T/S	332
rs776555145	19:3121096	G/A	D/N	333
rs1323407613	19:3121097	A/G	D/G	333

Variant ID	Chr: bp	Alleles	AA	AA coord
rs770247248	19:3121106	A/G	N/S	336
rs1356009409	19:3121110	C/G	I/M	337
rs773591539	19:3121111	C/T	R/C	338
rs752451221	19:3121126	G/A	A/T	343
rs1424927429	19:3121127	C/T	A/V	343
rs1383785285	19:3121129	G/A	V/M	344
rs753245806	19:3121150	C/G	L/V	351
rs376124717	19:3121154	A/C/G	N/T	352
rs376124717	19:3121154	A/C/G	N/S	352
rs543962567	19:3121159	A/C/G	K/Q	354
rs543962567	19:3121159	A/C/G	K/E	354

Table 9.4 *GNA11* missense variants in gnomAD (n=90)

rsID	Protein Consequence	Transcript Consequence	Allele Count	Allele Frequency
rs1387105467	p.Met6Leu	c.16A>C	1	5.03084E-06
rs377224539	p.Gly51Arg	c.151G>A	1	4.10078E-06
rs1335558363	p.Thr54Met	c.161C>T	1	4.04757E-06
rs755993488	p.Ile56Thr	c.167T>C	1	4.0281E-06
rs587777707	p.Arg60His	c.179G>A	1	4.01648E-06
rs147528229	p.Ala65Thr	c.193G>A	484	0.001720485
rs147528229	p.Ala65Ser	c.193G>T	1	4.0001E-06
rs1163458352	p.Gly66Ser	c.196G>A	2	7.1051E-06
rs140301317	p.Arg73Cys	c.217C>T	4	1.41889E-05
rs769019097	p.Arg73His	c.218G>A	5	1.99512E-05
rs777092144	p.Gly74Ser	c.220G>A	5	1.77275E-05
rs777099166	p.Val79Ile	c.235G>A	3	1.06275E-05
rs1487847863	p.Ile83Val	c.247A>G	1	3.98384E-06
rs374089777	p.Ala86Thr	c.256G>A	2	7.96762E-06
rs1475313918	p.Met87Val	c.259A>G	1	3.98276E-06
rs760710011	p.Ala89Thr	c.265G>A	1	3.98318E-06
rs753693838	p.Arg92Trp	c.274C>T	6	2.39055E-05
rs1380208656	p.Thr96Ala	c.286A>G	1	3.98511E-06
rs756991534	p.Thr96Met	c.287C>T	13	4.60506E-05
rs1376341794	p.Lys98Arg	c.293A>G	4	1.59431E-05
rs1306652036	p.Asn106Ser	c.317A>G	1	3.19061E-05
rs751665166	p.Asn109Ser	c.326A>G	3	1.19674E-05
rs759791665	p.Ala110Val	c.329C>T	1	3.98899E-06
rs1215008332	p.Arg114Trp	c.340C>T	1	3.98781E-06
rs541350337	p.Arg114Gln	c.341G>A	3	1.1964E-05
rs1451507571	p.Glu115Gln	c.343G>C	1	3.9874E-06
rs1197262629	p.Glu115Asp	c.345G>C	1	3.98769E-06
rs754271296	p.Val118Met	c.352G>A	2	7.97575E-06

rsID	Protein Consequence	Transcript Consequence	Allele Count	Allele Frequency
rs1165709212	p.Glu125Asp	c.375G>C	2	7.97614E-06
rs746693359	p.His126Arg	c.377A>G	1	3.98791E-06
rs780718032	p.Val129Ile	c.385G>A	5	1.77279E-05
rs1568282988	p.Lys133Glu	c.397A>G	1	3.99243E-06
rs773074121	p.Glu137Gln	c.409G>C	5	2.00101E-05
rs767809613	p.Arg147Cys	c.439C>T	1	4.03949E-06
rs1035292287	p.Arg147His	c.440G>A	2	8.09199E-06
rs1261353288	p.Arg148Gly	c.442A>G	1	4.04524E-06
rs752848608	p.Glu150Lys	c.448G>A	1	4.06421E-06
rs760781651	p.Gln152His	c.456G>C	2	7.27638E-06
rs779191241	p.Asp155Asn	c.463G>A	1	4.1691E-06
rs750766195	p.Lys158Glu	c.472A>G	1	4.27456E-06
rs775624350	p.Val164Ile	c.490G>A	2	8.04305E-06
rs191421665	p.Leu170Met	c.508T>A	33	0.000117343
rs769982397	p.Asp195Asn	c.583G>A	3	1.06359E-05
rs768371546	p.Asn198His	c.592A>C	1	3.99211E-06
rs1431166394	p.Asn198Ser	c.593A>G	1	3.99412E-06
rs766426049	p.Met203Leu	c.607A>T	2	7.9647E-06
rs587777022	p.Ser211Leu	c.632C>T	1	3.97959E-06
rs777912441	p.Arg213Trp	c.637C>T	1	3.97924E-06
rs778948783	p.Val223Met	c.667G>A	2	7.95608E-06
rs1309810840	p.Val230Ile	c.688G>A	1	3.97795E-06
rs769503200	p.Ala231Thr	c.691G>A	1	3.97795E-06
rs766046727	p.Val240Met	c.718G>A	2	7.95621E-06
rs1007967128	p.Ser242Ala	c.724T>G	1	3.97861E-06
rs773976709	p.Ser242Leu	c.725C>T	1	3.97896E-06
rs767308128	p.Asp243Gly	c.728A>G	3	1.19369E-05
rs775040372	p.Arg256Trp	c.766C>T	3	1.1934E-05
rs529942770	p.Arg256Gln	c.767G>A	4	1.59122E-05
rs1297128070	p.Ile259Thr	c.776T>C	1	3.9775E-06
rs761542744	p.Thr260Ala	c.778A>G	1	3.97757E-06
rs1449570989	p.Tyr261Cys	c.782A>G	2	7.07424E-06
rs765454337	p.Trp263Cys	c.789G>C	1	3.97735E-06
rs144829732	p.Val269Ile	c.805G>A	6	2.38635E-05
rs1471377402	p.Ile270Val	c.808A>G	1	3.18817E-05
rs1444263678	p.Asp281Ala	c.842A>C	1	3.97788E-06
rs1238030187	p.Tyr285His	c.853T>C	1	3.97924E-06
rs1420026055	p.Phe292Tyr	c.875T>A	1	3.98578E-06
rs1439859917	p.Gln299Pro	c.896A>C	1	3.19428E-05
rs1461947710	p.Arg300Trp	c.898C>T	2	7.17118E-06
rs919502623	p.Arg300Gln	c.899G>A	2	8.06491E-06
rs139538868	p.Ala302Thr	c.904G>A	4	1.61011E-05
rs762218250	p.Ala304Val	c.911C>T	2	8.04447E-06
rs762218250	p.Ala304Glu	c.911C>A	1	4.02223E-06

rsID	Protein Consequence	Transcript Consequence	Allele Count	Allele Frequency
rs1317335037	p.Arg306Trp	c.916C>T	1	4.01626E-06
rs759218880	p.Ile309Val	c.925A>G	2	8.00826E-06
rs767110044	p.Leu310Pro	c.929T>C	1	4.00128E-06
rs1489377886	p.Met312Thr	c.935T>C	1	3.99843E-06
rs772471502	p.Val314Met	c.940G>A	1	3.19673E-05
rs777133920	p.Asp319Asn	c.955G>A	1	3.98988E-06
rs753862594	p.Ser320Asn	c.959G>A	2	7.97734E-06
rs201368515	p.Ile324Val	c.970A>G	1	3.98502E-06
rs1364056722	p.Ser326Ala	c.976T>G	2	7.96997E-06
rs1298964952	p.Thr329Met	c.986C>T	1	3.98575E-06
rs776555145	p.Asp333Asn	c.997G>A	3	1.19516E-05
rs1323407613	p.Asp333Gly	c.998A>G	1	3.984E-06
rs770247248	p.Asn336Ser	c.1007A>G	1	3.98391E-06
rs773591539	p.Arg338Cys	c.1012C>T	2	7.97175E-06
rs752451221	p.Ala343Thr	c.1027G>A	1	3.98689E-06
rs1424927429	p.Ala343Val	c.1028C>T	1	3.98788E-06
rs753245806	p.Leu351Val	c.1051C>G	1	3.20451E-05
rs376124717	p.Asn352Ser	c.1055A>G	1	3.9931E-06

BIBLIOGRAPHY

1. Bourne, H.R., Sanders, D.A. & McCormick, F. The GTPase superfamily: a conserved switch for diverse cell functions. *Nature* **348**, 125-132 (1990). https://doi.org/10.1038/348125a0
2. Rosenbaum, D.M., Rasmussen, S.G. & Kobilka, B.K. The structure and function of G-protein-coupled receptors. *Nature* **459**, 356-363 (2009). https://doi.org/10.1038/nature08144
3. Gilman, A.G. G proteins: transducers of receptor-generated signals. *Annu Rev Biochem* **56**, 615-649 (1987). https://doi.org/10.1146/annurev.bi.56.070187.003151
4. Pierce, K.L., Premont, R.T. & Lefkowitz, R.J. Seven-transmembrane receptors. *Nat Rev Mol Cell Biol* **3**, 639-650 (2002). https://doi.org/10.1038/nrm908
5. Oldham, W.M. & Hamm, H.E. Heterotrimeric G protein activation by G-protein-coupled receptors. *Nat Rev Mol Cell Biol* **9**, 60-71 (2008). https://doi.org/10.1038/nrm2299
6. Wettschureck, N. & Offermanns, S. Mammalian G proteins and their cell type specific functions. *Physiol Rev* **85**, 1159-1204 (2005). https://doi.org/10.1152/physrev.00003.2005
7. Reiner, D.J. & Lundquist, E.A. Small GTPases. *WormBook* **2018**, 1-65 (2018). https://doi.org/10.1895/wormbook.1.67.2
8. Cabrera-Vera, T.M., Vanhauwe, J., Thomas, T.O., Medkova, M., Preininger, A., Mazzoni, M.R. & Hamm, H.E. Insights into G protein structure, function, and regulation. *Endocr Rev* **24**, 765-781 (2003). https://doi.org/10.1210/er.2000-0026
9. Syrovatkina, V., Alegre, K.O., Dey, R. & Huang, X.Y. Regulation, Signaling, and Physiological Functions of G-Proteins. *J Mol Biol* **428**, 3850-3868 (2016). https://doi.org/10.1016/j.jmb.2016.08.002
10. Oldham, W.M. & Hamm, H.E. Structural basis of function in heterotrimeric G proteins. *Q Rev Biophys* **39**, 117-166 (2006). https://doi.org/10.1017/S0033583506004306
11. Sun, D., Flock, T., Deupi, X., Maeda, S., Matkovic, M., Mendieta, S., . . . Veprintsev, D.B. Probing Galphai1 protein activation at single-amino acid resolution. *Nat Struct Mol Biol* **22**, 686-694 (2015). https://doi.org/10.1038/nsmb.3070
12. Kristiansen, K. Molecular mechanisms of ligand binding, signaling, and regulation within the superfamily of G-protein-coupled receptors: molecular modeling and mutagenesis approaches to receptor structure and function. *Pharmacol Ther* **103**, 21-80 (2004). https://doi.org/10.1016/j.pharmthera.2004.05.002
13. Taylor, V.G., Bommarito, P.A. & Tesmer, J.J. Structure of the Regulator of G Protein Signaling 8 (RGS8)-Galphaq Complex: MOLECULAR BASIS FOR Galpha SELECTIVITY. *J Biol Chem* **291**, 5138-5145 (2016). https://doi.org/10.1074/jbc.M115.712075
14. Downes, G.B. & Gautam, N. The G protein subunit gene families. *Genomics* **62**, 544-552 (1999). https://doi.org/10.1006/geno.1999.5992
15. Bastepe, M. The GNAS Locus: Quintessential Complex Gene Encoding Gsalpha, XLalphas, and other Imprinted Transcripts. *Curr Genomics* **8**, 398-414 (2007). https://doi.org/10.2174/138920207783406488
16. Murtagh, J.J., Jr., Eddy, R., Shows, T.B., Moss, J. & Vaughan, M. Different forms of Go alpha mRNA arise by alternative splicing of transcripts from a single gene on

human chromosome 16. *Mol Cell Biol* **11**, 1146-1155 (1991). https://doi.org/10.1128/mcb.11.2.1146
17. Sievers, F., Wilm, A., Dineen, D., Gibson, T.J., Karplus, K., Li, W., . . . Higgins, D.G. Fast, scalable generation of high-quality protein multiple sequence alignments using Clustal Omega. *Mol Syst Biol* **7**, 539 (2011). https://doi.org/10.1038/msb.2011.75
18. Flock, T., Hauser, A.S., Lund, N., Gloriam, D.E., Balaji, S. & Babu, M.M. Selectivity determinants of GPCR-G-protein binding. *Nature* **545**, 317-322 (2017). https://doi.org/10.1038/nature22070
19. Blahos, J., 2nd, Mary, S., Perroy, J., de Colle, C., Brabet, I., Bockaert, J. & Pin, J.P. Extreme C terminus of G protein alpha-subunits contains a site that discriminates between Gi-coupled metabotropic glutamate receptors. *J Biol Chem* **273**, 25765-25769 (1998). https://doi.org/10.1074/jbc.273.40.25765
20. Kostenis, E., Gomeza, J., Lerche, C. & Wess, J. Genetic analysis of receptor-Galphaq coupling selectivity. *J Biol Chem* **272**, 23675-23681 (1997). https://doi.org/10.1074/jbc.272.38.23675
21. Conklin, B.R., Herzmark, P., Ishida, S., Voyno-Yasenetskaya, T.A., Sun, Y., Farfel, Z. & Bourne, H.R. Carboxyl-terminal mutations of Gq alpha and Gs alpha that alter the fidelity of receptor activation. *Mol Pharmacol* **50**, 885-890 (1996). https://www.ncbi.nlm.nih.gov/pubmed/8863834
22. Conklin, B.R., Farfel, Z., Lustig, K.D., Julius, D. & Bourne, H.R. Substitution of three amino acids switches receptor specificity of Gq alpha to that of Gi alpha. *Nature* **363**, 274-276 (1993). https://doi.org/10.1038/363274a0
23. Heydorn, A., Ward, R.J., Jorgensen, R., Rosenkilde, M.M., Frimurer, T.M., Milligan, G. & Kostenis, E. Identification of a novel site within G protein alpha subunits important for specificity of receptor-G protein interaction. *Mol Pharmacol* **66**, 250-259 (2004). https://doi.org/10.1124/mol.66.2.250
24. Kostenis, E., Martini, L., Ellis, J., Waldhoer, M., Heydorn, A., Rosenkilde, M.M., . . . Milligan, G. A highly conserved glycine within linker I and the extreme C terminus of G protein alpha subunits interact cooperatively in switching G protein-coupled receptor-to-effector specificity. *J Pharmacol Exp Ther* **313**, 78-87 (2005). https://doi.org/10.1124/jpet.104.080424
25. Ho, M.K., Yung, L.Y., Chan, J.S., Chan, J.H., Wong, C.S. & Wong, Y.H. Galpha(14) links a variety of G(i)- and G(s)-coupled receptors to the stimulation of phospholipase C. *Br J Pharmacol* **132**, 1431-1440 (2001). https://doi.org/10.1038/sj.bjp.0703933
26. Hubbard, K.B. & Hepler, J.R. Cell signalling diversity of the Gqalpha family of heterotrimeric G proteins. *Cell Signal* **18**, 135-150 (2006). https://doi.org/10.1016/j.cellsig.2005.08.004
27. Rhee, S.G. Regulation of phosphoinositide-specific phospholipase C. *Annu Rev Biochem* **70**, 281-312 (2001). https://doi.org/10.1146/annurev.biochem.70.1.281
28. Wootten, D., Christopoulos, A., Marti-Solano, M., Babu, M.M. & Sexton, P.M. Mechanisms of signalling and biased agonism in G protein-coupled receptors. *Nat Rev Mol Cell Biol* **19**, 638-653 (2018). https://doi.org/10.1038/s41580-018-0049-3
29. Momotani, K. & Somlyo, A.V. p63RhoGEF: a new switch for G(q)-mediated activation of smooth muscle. *Trends Cardiovasc Med* **22**, 122-127 (2012). https://doi.org/10.1016/j.tcm.2012.07.007

30. Lutz, S., Shankaranarayanan, A., Coco, C., Ridilla, M., Nance, M.R., Vettel, C., . . . Tesmer, J.J. Structure of Galphaq-p63RhoGEF-RhoA complex reveals a pathway for the activation of RhoA by GPCRs. *Science* **318**, 1923-1927 (2007). https://doi.org/10.1126/science.1147554
31. Lutz, S., Freichel-Blomquist, A., Yang, Y., Rumenapp, U., Jakobs, K.H., Schmidt, M. & Wieland, T. The guanine nucleotide exchange factor p63RhoGEF, a specific link between Gq/11-coupled receptor signaling and RhoA. *J Biol Chem* **280**, 11134-11139 (2005). https://doi.org/10.1074/jbc.M411322200
32. Kostenis, E., Pfeil, E.M. & Annala, S. Heterotrimeric Gq proteins as therapeutic targets? *J Biol Chem* (2020). https://doi.org/10.1074/jbc.REV119.007061
33. Van Raamsdonk, C.D., Griewank, K.G., Crosby, M.B., Garrido, M.C., Vemula, S., Wiesner, T., . . . Bastian, B.C. Mutations in GNA11 in uveal melanoma. *N Engl J Med* **363**, 2191-2199 (2010). https://doi.org/10.1056/NEJMoa1000584
34. Ayturk, U.M., Couto, J.A., Hann, S., Mulliken, J.B., Williams, K.L., Huang, A.Y., . . . Warman, M.L. Somatic Activating Mutations in GNAQ and GNA11 Are Associated with Congenital Hemangioma. *Am J Hum Genet* **98**, 789-795 (2016). https://doi.org/10.1016/j.ajhg.2016.03.009
35. Van Raamsdonk, C.D., Barsh, G.S., Wakamatsu, K. & Ito, S. Independent regulation of hair and skin color by two G protein-coupled pathways. *Pigment Cell Melanoma Res* **22**, 819-826 (2009). https://doi.org/10.1111/j.1755-148X.2009.00609.x
36. Van Raamsdonk, C.D., Fitch, K.R., Fuchs, H., de Angelis, M.H. & Barsh, G.S. Effects of G-protein mutations on skin color. *Nat Genet* **36**, 961-968 (2004). https://doi.org/10.1038/ng1412
37. Schrage, R., Schmitz, A.L., Gaffal, E., Annala, S., Kehraus, S., Wenzel, D., . . . Kostenis, E. The experimental power of FR900359 to study Gq-regulated biological processes. *Nat Commun* **6**, 10156 (2015). https://doi.org/10.1038/ncomms10156
38. Nishimura, A., Kitano, K., Takasaki, J., Taniguchi, M., Mizuno, N., Tago, K., . . . Itoh, H. Structural basis for the specific inhibition of heterotrimeric Gq protein by a small molecule. *Proc Natl Acad Sci U S A* **107**, 13666-13671 (2010). https://doi.org/10.1073/pnas.1003553107
39. Offermanns, S., Heiler, E., Spicher, K. & Schultz, G. Gq and G11 are concurrently activated by bombesin and vasopressin in Swiss 3T3 cells. *FEBS Lett* **349**, 201-204 (1994). https://doi.org/10.1016/0014-5793(94)00667-9
40. Bastepe, M. Relative functions of Galphas and its extra-large variant XLalphas in the endocrine system. *Horm Metab Res* **44**, 732-740 (2012). https://doi.org/10.1055/s-0032-1316331
41. Bastepe, M. GNAS mutations and heterotopic ossification. *Bone* **109**, 80-85 (2018). https://doi.org/10.1016/j.bone.2017.09.002
42. Sunahara, R.K., Dessauer, C.W., Whisnant, R.E., Kleuss, C. & Gilman, A.G. Interaction of Gsalpha with the cytosolic domains of mammalian adenylyl cyclase. *J Biol Chem* **272**, 22265-22271 (1997). https://doi.org/10.1074/jbc.272.35.22265
43. Tesmer, J.J., Sunahara, R.K., Gilman, A.G. & Sprang, S.R. Crystal structure of the catalytic domains of adenylyl cyclase in a complex with Gsalpha.GTPgammaS. *Science* **278**, 1907-1916 (1997). https://doi.org/10.1126/science.278.5345.1907

44. Qi, C., Sorrentino, S., Medalia, O. & Korkhov, V.M. The structure of a membrane adenylyl cyclase bound to an activated stimulatory G protein. *Science* **364**, 389-394 (2019). https://doi.org/10.1126/science.aav0778
45. Sunahara, R.K., Dessauer, C.W. & Gilman, A.G. Complexity and diversity of mammalian adenylyl cyclases. *Annu Rev Pharmacol Toxicol* **36**, 461-480 (1996). https://doi.org/10.1146/annurev.pa.36.040196.002333
46. Tang, W.J. & Gilman, A.G. Adenylyl cyclases. *Cell* **70**, 869-872 (1992). https://doi.org/10.1016/0092-8674(92)90236-6
47. Offermanns, S., Mancino, V., Revel, J.P. & Simon, M.I. Vascular system defects and impaired cell chemokinesis as a result of Galpha13 deficiency. *Science* **275**, 533-536 (1997). https://doi.org/10.1126/science.275.5299.533
48. Shankaranarayanan, A., Boguth, C.A., Lutz, S., Vettel, C., Uhlemann, F., Aittaleb, M., . . . Tesmer, J.J. Galpha q allosterically activates and relieves autoinhibition of p63RhoGEF. *Cell Signal* **22**, 1114-1123 (2010). https://doi.org/10.1016/j.cellsig.2010.03.006
49. Lutz, S., Freichel-Blomquist, A., Rumenapp, U., Schmidt, M., Jakobs, K.H. & Wieland, T. p63RhoGEF and GEFT are Rho-specific guanine nucleotide exchange factors encoded by the same gene. *Naunyn Schmiedebergs Arch Pharmacol* **369**, 540-546 (2004). https://doi.org/10.1007/s00210-004-0926-5
50. Clapham, D.E. & Neer, E.J. G protein beta gamma subunits. *Annu Rev Pharmacol Toxicol* **37**, 167-203 (1997). https://doi.org/10.1146/annurev.pharmtox.37.1.167
51. Khan, S.M., Sleno, R., Gora, S., Zylbergold, P., Laverdure, J.P., Labbe, J.C., . . . Hebert, T.E. The expanding roles of Gbetagamma subunits in G protein-coupled receptor signaling and drug action. *Pharmacol Rev* **65**, 545-577 (2013). https://doi.org/10.1124/pr.111.005603
52. Kim, D., Lewis, D.L., Graziadei, L., Neer, E.J., Bar-Sagi, D. & Clapham, D.E. G-protein beta gamma-subunits activate the cardiac muscarinic K+-channel via phospholipase A2. *Nature* **337**, 557-560 (1989). https://doi.org/10.1038/337557a0
53. Wickman, K.D., Iniguez-Lluhl, J.A., Davenport, P.A., Taussig, R., Krapivinsky, G.B., Linder, M.E., . . . Clapham, D.E. Recombinant G-protein beta gamma-subunits activate the muscarinic-gated atrial potassium channel. *Nature* **368**, 255-257 (1994). https://doi.org/10.1038/368255a0
54. Robishaw, J.D. & Berlot, C.H. Translating G protein subunit diversity into functional specificity. *Curr Opin Cell Biol* **16**, 206-209 (2004). https://doi.org/10.1016/j.ceb.2004.02.007
55. Smrcka, A.V. & Fisher, I. G-protein betagamma subunits as multi-functional scaffolds and transducers in G-protein-coupled receptor signaling. *Cell Mol Life Sci* **76**, 4447-4459 (2019). https://doi.org/10.1007/s00018-019-03275-2
56. Snow, B.E., Krumins, A.M., Brothers, G.M., Lee, S.F., Wall, M.A., Chung, S., . . . Siderovski, D.P. A G protein gamma subunit-like domain shared between RGS11 and other RGS proteins specifies binding to Gbeta5 subunits. *Proc Natl Acad Sci U S A* **95**, 13307-13312 (1998). https://doi.org/10.1073/pnas.95.22.13307
57. Witherow, D.S., Wang, Q., Levay, K., Cabrera, J.L., Chen, J., Willars, G.B. & Slepak, V.Z. Complexes of the G protein subunit gbeta 5 with the regulators of G protein signaling RGS7 and RGS9. Characterization in native tissues and in transfected cells. *J Biol Chem* **275**, 24872-24880 (2000). https://doi.org/10.1074/jbc.M001535200

58. Hauser, A.S., Chavali, S., Masuho, I., Jahn, L.J., Martemyanov, K.A., Gloriam, D.E. & Babu, M.M. Pharmacogenomics of GPCR Drug Targets. *Cell* **172**, 41-54 e19 (2018). https://doi.org/10.1016/j.cell.2017.11.033
59. Hauser, A.S., Attwood, M.M., Rask-Andersen, M., Schioth, H.B. & Gloriam, D.E. Trends in GPCR drug discovery: new agents, targets and indications. *Nat Rev Drug Discov* **16**, 829-842 (2017). https://doi.org/10.1038/nrd.2017.178
60. Smith, J.S., Lefkowitz, R.J. & Rajagopal, S. Biased signalling: from simple switches to allosteric microprocessors. *Nat Rev Drug Discov* **17**, 243-260 (2018). https://doi.org/10.1038/nrd.2017.229
61. Weis, W.I. & Kobilka, B.K. The Molecular Basis of G Protein-Coupled Receptor Activation. *Annu Rev Biochem* **87**, 897-919 (2018). https://doi.org/10.1146/annurev-biochem-060614-033910
62. Pierce, K.L. & Lefkowitz, R.J. Classical and new roles of beta-arrestins in the regulation of G-protein-coupled receptors. *Nat Rev Neurosci* **2**, 727-733 (2001). https://doi.org/10.1038/35094577
63. Shenoy, S.K. & Lefkowitz, R.J. beta-Arrestin-mediated receptor trafficking and signal transduction. *Trends Pharmacol Sci* **32**, 521-533 (2011). https://doi.org/10.1016/j.tips.2011.05.002
64. Congreve, M., de Graaf, C., Swain, N.A. & Tate, C.G. Impact of GPCR Structures on Drug Discovery. *Cell* **181**, 81-91 (2020). https://doi.org/10.1016/j.cell.2020.03.003
65. Fredriksson, R., Lagerstrom, M.C., Lundin, L.G. & Schioth, H.B. The G-protein-coupled receptors in the human genome form five main families. Phylogenetic analysis, paralogon groups, and fingerprints. *Mol Pharmacol* **63**, 1256-1272 (2003). https://doi.org/10.1124/mol.63.6.1256
66. Lu, M. & Wu, B. Structural studies of G protein-coupled receptors. *IUBMB Life* **68**, 894-903 (2016). https://doi.org/10.1002/iub.1578
67. Maeda, S., Qu, Q., Robertson, M.J., Skiniotis, G. & Kobilka, B.K. Structures of the M1 and M2 muscarinic acetylcholine receptor/G-protein complexes. *Science* **364**, 552-557 (2019). https://doi.org/10.1126/science.aaw5188
68. Zhao, L.H., Ma, S., Sutkeviciute, I., Shen, D.D., Zhou, X.E., de Waal, P.W., . . . Zhang, Y. Structure and dynamics of the active human parathyroid hormone receptor-1. *Science* **364**, 148-153 (2019). https://doi.org/10.1126/science.aav7942
69. Langenhan, T., Aust, G. & Hamann, J. Sticky signaling--adhesion class G protein-coupled receptors take the stage. *Sci Signal* **6**, re3 (2013). https://doi.org/10.1126/scisignal.2003825
70. Arac, D., Boucard, A.A., Bolliger, M.F., Nguyen, J., Soltis, S.M., Sudhof, T.C. & Brunger, A.T. A novel evolutionarily conserved domain of cell-adhesion GPCRs mediates autoproteolysis. *EMBO J* **31**, 1364-1378 (2012). https://doi.org/10.1038/emboj.2012.26
71. Pin, J.P., Kniazeff, J., Liu, J., Binet, V., Goudet, C., Rondard, P. & Prezeau, L. Allosteric functioning of dimeric class C G-protein-coupled receptors. *FEBS J* **272**, 2947-2955 (2005). https://doi.org/10.1111/j.1742-4658.2005.04728.x
72. Whorton, M.R., Bokoch, M.P., Rasmussen, S.G., Huang, B., Zare, R.N., Kobilka, B. & Sunahara, R.K. A monomeric G protein-coupled receptor isolated in a high-density lipoprotein particle efficiently activates its G protein. *Proc Natl Acad Sci U S A* **104**, 7682-7687 (2007). https://doi.org/10.1073/pnas.0611448104

73. Koehl, A., Hu, H., Feng, D., Sun, B., Zhang, Y., Robertson, M.J., . . . Kobilka, B.K. Structural insights into the activation of metabotropic glutamate receptors. *Nature* **566**, 79-84 (2019). https://doi.org/10.1038/s41586-019-0881-4
74. Zhang, X., Dong, S. & Xu, F. Structural and Druggability Landscape of Frizzled G Protein-Coupled Receptors. *Trends Biochem Sci* **43**, 1033-1046 (2018). https://doi.org/10.1016/j.tibs.2018.09.002
75. Qi, X., Liu, H., Thompson, B., McDonald, J., Zhang, C. & Li, X. Cryo-EM structure of oxysterol-bound human Smoothened coupled to a heterotrimeric Gi. *Nature* **571**, 279-283 (2019). https://doi.org/10.1038/s41586-019-1286-0
76. Hannan, F.M., Olesen, M.K. & Thakker, R.V. Calcimimetic and calcilytic therapies for inherited disorders of the calcium-sensing receptor signalling pathway. *Br J Pharmacol* **175**, 4083-4094 (2018). https://doi.org/10.1111/bph.14086
77. Chavez-Abiega, S., Mos, I., Centeno, P.P., Elajnaf, T., Schlattl, W., Ward, D.T., . . . Kallay, E. Sensing Extracellular Calcium - An Insight into the Structure and Function of the Calcium-Sensing Receptor (CaSR). *Adv Exp Med Biol* **1131**, 1031-1063 (2020). https://doi.org/10.1007/978-3-030-12457-1_41
78. Herberger, A.L. & Loretz, C.A. Vertebrate extracellular calcium-sensing receptor evolution: selection in relation to life history and habitat. *Comp Biochem Physiol Part D Genomics Proteomics* **8**, 86-94 (2013). https://doi.org/10.1016/j.cbd.2012.12.004
79. Hendy, G.N. & Canaff, L. Calcium-Sensing Receptor Gene: Regulation of Expression. *Front Physiol* **7**, 394 (2016). https://doi.org/10.3389/fphys.2016.00394
80. Thul, P.J., Akesson, L., Wiking, M., Mahdessian, D., Geladaki, A., Ait Blal, H., . . . Lundberg, E. A subcellular map of the human proteome. *Science* **356**(2017). https://doi.org/10.1126/science.aal3321
81. Uhlen, M., Fagerberg, L., Hallstrom, B.M., Lindskog, C., Oksvold, P., Mardinoglu, A., . . . Ponten, F. Proteomics. Tissue-based map of the human proteome. *Science* **347**, 1260419 (2015). https://doi.org/10.1126/science.1260419
82. Hannan, F.M., Kallay, E., Chang, W., Brandi, M.L. & Thakker, R.V. The calcium-sensing receptor in physiology and in calcitropic and noncalcitropic diseases. *Nat Rev Endocrinol* **15**, 33-51 (2018). https://doi.org/10.1038/s41574-018-0115-0
83. Conigrave, A.D. The Calcium-Sensing Receptor and the Parathyroid: Past, Present, Future. *Front Physiol* **7**, 563 (2016). https://doi.org/10.3389/fphys.2016.00563
84. Brown, E.M. Extracellular Ca2+ sensing, regulation of parathyroid cell function, and role of Ca2+ and other ions as extracellular (first) messengers. *Physiol Rev* **71**, 371-411 (1991). https://doi.org/10.1152/physrev.1991.71.2.371
85. Hofer, A.M. & Brown, E.M. Extracellular calcium sensing and signalling. *Nat Rev Mol Cell Biol* **4**, 530-538 (2003). https://doi.org/10.1038/nrm1154
86. Hannan, F.M., Babinsky, V.N. & Thakker, R.V. Disorders of the calcium-sensing receptor and partner proteins: insights into the molecular basis of calcium homeostasis. *J Mol Endocrinol* **57**, R127-142 (2016). https://doi.org/10.1530/JME-16-0124
87. Bai, M., Pearce, S.H., Kifor, O., Trivedi, S., Stauffer, U.G., Thakker, R.V., . . . Steinmann, B. In vivo and in vitro characterization of neonatal hyperparathyroidism resulting from a de novo, heterozygous mutation in the Ca2+-sensing receptor gene: normal maternal calcium homeostasis as a cause of secondary

hyperparathyroidism in familial benign hypocalciuric hypercalcemia. *J Clin Invest* **99**, 88-96 (1997). https://doi.org/10.1172/JCI119137
88. Graca, J.A., Schepelmann, M., Brennan, S.C., Reens, J., Chang, W., Yan, P., . . . Price, S.A. Comparative expression of the extracellular calcium-sensing receptor in the mouse, rat, and human kidney. *Am J Physiol Renal Physiol* **310**, F518-533 (2016). https://doi.org/10.1152/ajprenal.00208.2015
89. Sigl, V., Jones, L.P. & Penninger, J.M. RANKL/RANK: from bone loss to the prevention of breast cancer. *Open Biol* **6**(2016). https://doi.org/10.1098/rsob.160230
90. Ritter, C.S., Haughey, B.H., Miller, B. & Brown, A.J. Differential gene expression by oxyphil and chief cells of human parathyroid glands. *J Clin Endocrinol Metab* **97**, E1499-1505 (2012). https://doi.org/10.1210/jc.2011-3366
91. Regard, J.B., Sato, I.T. & Coughlin, S.R. Anatomical profiling of G protein-coupled receptor expression. *Cell* **135**, 561-571 (2008). https://doi.org/10.1016/j.cell.2008.08.040
92. Brown, E.M. & MacLeod, R.J. Extracellular calcium sensing and extracellular calcium signaling. *Physiol Rev* **81**, 239-297 (2001). https://doi.org/10.1152/physrev.2001.81.1.239
93. Nesbit, M.A., Hannan, F.M., Howles, S.A., Babinsky, V.N., Head, R.A., Cranston, T., . . . Thakker, R.V. Mutations affecting G-protein subunit alpha11 in hypercalcemia and hypocalcemia. *N Engl J Med* **368**, 2476-2486 (2013). https://doi.org/10.1056/NEJMoa1300253
94. Conigrave, A.D. & Ward, D.T. Calcium-sensing receptor (CaSR): pharmacological properties and signaling pathways. *Best Pract Res Clin Endocrinol Metab* **27**, 315-331 (2013). https://doi.org/10.1016/j.beem.2013.05.010
95. Leach, K., Hannan, F.M., Josephs, T.M., Keller, A.N., Moller, T.C., Ward, D.T., . . . Brauner-Osborne, H. International Union of Basic and Clinical Pharmacology. CVIII. Calcium-Sensing Receptor Nomenclature, Pharmacology, and Function. *Pharmacol Rev* **72**, 558-604 (2020). https://doi.org/10.1124/pr.119.018531
96. Chang, W., Tu, C., Chen, T.H., Bikle, D. & Shoback, D. The extracellular calcium-sensing receptor (CaSR) is a critical modulator of skeletal development. *Sci Signal* **1**, ra1 (2008). https://doi.org/10.1126/scisignal.1159945
97. Loupy, A., Ramakrishnan, S.K., Wootla, B., Chambrey, R., de la Faille, R., Bourgeois, S., . . . Houillier, P. PTH-independent regulation of blood calcium concentration by the calcium-sensing receptor. *J Clin Invest* **122**, 3355-3367 (2012). https://doi.org/10.1172/JCI57407
98. Nemeth, E.F., Van Wagenen, B.C. & Balandrin, M.F. Discovery and Development of Calcimimetic and Calcilytic Compounds. *Prog Med Chem* **57**, 1-86 (2018). https://doi.org/10.1016/bs.pmch.2017.12.001
99. Riccardi, D. & Valenti, G. Localization and function of the renal calcium-sensing receptor. *Nat Rev Nephrol* **12**, 414-425 (2016). https://doi.org/10.1038/nrneph.2016.59
100. Pearce, S.H., Wooding, C., Davies, M., Tollefsen, S.E., Whyte, M.P. & Thakker, R.V. Calcium-sensing receptor mutations in familial hypocalciuric hypercalcaemia with recurrent pancreatitis. *Clin Endocrinol (Oxf)* **45**, 675-680 (1996). https://www.ncbi.nlm.nih.gov/pubmed/9039332
101. Pearce, S.H., Bai, M., Quinn, S.J., Kifor, O., Brown, E.M. & Thakker, R.V. Functional characterization of calcium-sensing receptor mutations expressed in human

embryonic kidney cells. *J Clin Invest* **98**, 1860-1866 (1996). https://doi.org/10.1172/JCI118987

102. Pearce, S.H., Williamson, C., Kifor, O., Bai, M., Coulthard, M.G., Davies, M., . . . Thakker, R.V. A familial syndrome of hypocalcemia with hypercalciuria due to mutations in the calcium-sensing receptor. *N Engl J Med* **335**, 1115-1122 (1996). https://doi.org/10.1056/NEJM199610103351505
103. Nesbit, M.A., Hannan, F.M., Howles, S.A., Reed, A.A., Cranston, T., Thakker, C.E., . . . Thakker, R.V. Mutations in AP2S1 cause familial hypocalciuric hypercalcemia type 3. *Nat Genet* **45**, 93-97 (2013). https://doi.org/10.1038/ng.2492
104. Gorvin, C.M. Molecular and clinical insights from studies of calcium-sensing receptor mutations. *J Mol Endocrinol* **63**, R1-R16 (2019). https://doi.org/10.1530/JME-19-0104
105. Festen-Spanjer, B., Haring, C.M., Koster, J.B. & Mudde, A.H. Correction of hypercalcaemia by cinacalcet in familial hypocalciuric hypercalcaemia. *Clin Endocrinol (Oxf)* **68**, 324-325 (2008). https://doi.org/10.1111/j.1365-2265.2007.03027.x
106. Dershem, R., Gorvin, C.M., Metpally, R.P.R., Krishnamurthy, S., Smelser, D.T., Hannan, F.M., . . . Regeneron Genetics, C. Familial Hypocalciuric Hypercalcemia Type 1 and Autosomal-Dominant Hypocalcemia Type 1: Prevalence in a Large Healthcare Population. *Am J Hum Genet* (2020). https://doi.org/10.1016/j.ajhg.2020.04.006
107. Pollak, M.R., Brown, E.M., Chou, Y.H., Hebert, S.C., Marx, S.J., Steinmann, B., . . . Seidman, J.G. Mutations in the human Ca(2+)-sensing receptor gene cause familial hypocalciuric hypercalcemia and neonatal severe hyperparathyroidism. *Cell* **75**, 1297-1303 (1993). https://www.ncbi.nlm.nih.gov/pubmed/7916660
108. Gorvin, C.M., Cranston, T., Hannan, F.M., Rust, N., Qureshi, A., Nesbit, M.A. & Thakker, R.V. A G-protein Subunit-alpha11 Loss-of-Function Mutation, Thr54Met, Causes Familial Hypocalciuric Hypercalcemia Type 2 (FHH2). *J Bone Miner Res* **31**, 1200-1206 (2016). https://doi.org/10.1002/jbmr.2778
109. Gorvin, C.M., Hannan, F.M., Cranston, T., Valta, H., Makitie, O., Schalin-Jantti, C. & Thakker, R.V. Cinacalcet Rectifies Hypercalcemia in a Patient With Familial Hypocalciuric Hypercalcemia Type 2 (FHH2) Caused by a Germline Loss-of-Function Galpha11 Mutation. *J Bone Miner Res* (2017). https://doi.org/10.1002/jbmr.3241
110. Gorvin, C.M., Rogers, A., Hastoy, B., Tarasov, A.I., Frost, M., Sposini, S., . . . Thakker, R.V. AP2sigma Mutations Impair Calcium-Sensing Receptor Trafficking and Signaling, and Show an Endosomal Pathway to Spatially Direct G-Protein Selectivity. *Cell Rep* **22**, 1054-1066 (2018). https://doi.org/10.1016/j.celrep.2017.12.089
111. Hannan, F.M., Howles, S.A., Rogers, A., Cranston, T., Gorvin, C.M., Babinsky, V.N., . . . Thakker, R.V. Adaptor protein-2 sigma subunit mutations causing familial hypocalciuric hypercalcaemia type 3 (FHH3) demonstrate genotype-phenotype correlations, codon bias and dominant-negative effects. *Hum Mol Genet* **24**, 5079-5092 (2015). https://doi.org/10.1093/hmg/ddv226
112. Howles, S.A., Hannan, F.M., Babinsky, V.N., Rogers, A., Gorvin, C.M., Rust, N., . . . Thakker, R.V. Cinacalcet for Symptomatic Hypercalcemia Caused by AP2S1 Mutations. *N Engl J Med* **374**, 1396-1398 (2016). https://doi.org/10.1056/NEJMc1511646

113. Roszko, K.L., Bi, R.D. & Mannstadt, M. Autosomal Dominant Hypocalcemia (Hypoparathyroidism) Types 1 and 2. *Front Physiol* **7**, 458 (2016). https://doi.org/10.3389/fphys.2016.00458
114. Vargas-Poussou, R., Huang, C., Hulin, P., Houillier, P., Jeunemaitre, X., Paillard, M., . . . Antignac, C. Functional characterization of a calcium-sensing receptor mutation in severe autosomal dominant hypocalcemia with a Bartter-like syndrome. *J Am Soc Nephrol* **13**, 2259-2266 (2002). https://doi.org/10.1097/01.asn.0000025781.16723.68
115. Watanabe, S., Fukumoto, S., Chang, H., Takeuchi, Y., Hasegawa, Y., Okazaki, R., . . . Fujita, T. Association between activating mutations of calcium-sensing receptor and Bartter's syndrome. *Lancet* **360**, 692-694 (2002). https://doi.org/10.1016/S0140-6736(02)09842-2
116. Dong, B., Endo, I., Ohnishi, Y., Kondo, T., Hasegawa, T., Amizuka, N., . . . Matsumoto, T. Calcilytic Ameliorates Abnormalities of Mutant Calcium-Sensing Receptor (CaSR) Knock-In Mice Mimicking Autosomal Dominant Hypocalcemia (ADH). *J Bone Miner Res* **30**, 1980-1993 (2015). https://doi.org/10.1002/jbmr.2551
117. Li, D., Opas, E.E., Tuluc, F., Metzger, D.L., Hou, C., Hakonarson, H. & Levine, M.A. Autosomal dominant hypoparathyroidism caused by germline mutation in GNA11: phenotypic and molecular characterization. *J Clin Endocrinol Metab* **99**, E1774-1783 (2014). https://doi.org/10.1210/jc.2014-1029
118. Tenhola, S., Voutilainen, R., Reyes, M., Toiviainen-Salo, S., Juppner, H. & Makitie, O. Impaired growth and intracranial calcifications in autosomal dominant hypocalcemia caused by a GNA11 mutation. *Eur J Endocrinol* **175**, 211-218 (2016). https://doi.org/10.1530/EJE-16-0109
119. Makita, N. & Iiri, T. Biased agonism: a novel paradigm in G protein-coupled receptor signaling observed in acquired hypocalciuric hypercalcemia. *Endocr J* **61**, 303-309 (2014). https://doi.org/10.1507/endocrj.ej13-0453
120. Ho, C., Conner, D.A., Pollak, M.R., Ladd, D.J., Kifor, O., Warren, H.B., . . . Seidman, C.E. A mouse model of human familial hypocalciuric hypercalcemia and neonatal severe hyperparathyroidism. *Nat Genet* **11**, 389-394 (1995). https://doi.org/10.1038/ng1295-389
121. Howles, S.A., Hannan, F.M., Gorvin, C.M., Piret, S.E., Paudyal, A., Stewart, M., . . . Thakker, R.V. Cinacalcet corrects hypercalcemia in mice with an inactivating Gα11 mutation. *JCI Insight* **2**, e96540 (2017).
122. Hannan, F.M., Stokes, V.J., Gorvin, C.M., Hough, T.A., Stewart, M., Wells, S., . . . Thakker, R.V. Mice harboring a germline heterozygous AP2S1 mutation, Arg15Leu, are a model for familial hypocalciuric hypercalcemia type 3 (FHH3). in *ENDO 2019* (New Orleans, USA, 2019).
123. Hough, T.A., Bogani, D., Cheeseman, M.T., Favor, J., Nesbit, M.A., Thakker, R.V. & Lyon, M.F. Activating calcium-sensing receptor mutation in the mouse is associated with cataracts and ectopic calcification. *Proc Natl Acad Sci U S A* **101**, 13566-13571 (2004). https://doi.org/10.1073/pnas.0405516101
124. Roszko, K.L., Bi, R., Gorvin, C.M., Brauner-Osborne, H., Xiong, X.F., Inoue, A., . . . Mannstadt, M. Knockin mouse with mutant Galpha11 mimics human inherited hypocalcemia and is rescued by pharmacologic inhibitors. *JCI Insight* **2**, e91079 (2017). https://doi.org/10.1172/jci.insight.91079
125. Gorvin, C.M., Hannan, F.M., Howles, S.A., Babinsky, V.N., Piret, S.E., Rogers, A., . . . Thakker, R.V. Galpha11 mutation in mice causes hypocalcemia rectifiable by

calcilytic therapy. *JCI Insight* **2**, e91103 (2017). https://doi.org/10.1172/jci.insight.91103
126. Ellinger, I. The Calcium-Sensing Receptor and the Reproductive System. *Front Physiol* **7**, 371 (2016). https://doi.org/10.3389/fphys.2016.00371
127. Kim, W., Takyar, F.M., Swan, K., Jeong, J., VanHouten, J., Sullivan, C., . . . Wysolmerski, J. Calcium-Sensing Receptor Promotes Breast Cancer by Stimulating Intracrine Actions of Parathyroid Hormone-Related Protein. *Cancer Res* **76**, 5348-5360 (2016). https://doi.org/10.1158/0008-5472.CAN-15-2614
128. Mamillapalli, R., VanHouten, J., Zawalich, W. & Wysolmerski, J. Switching of G-protein usage by the calcium-sensing receptor reverses its effect on parathyroid hormone-related protein secretion in normal versus malignant breast cells. *J Biol Chem* **283**, 24435-24447 (2008). https://doi.org/10.1074/jbc.M801738200
129. Mihai, R., Stevens, J., McKinney, C. & Ibrahim, N.B. Expression of the calcium receptor in human breast cancer--a potential new marker predicting the risk of bone metastases. *Eur J Surg Oncol* **32**, 511-515 (2006). https://doi.org/10.1016/j.ejso.2006.02.009
130. Chiarini, A., Armato, U., Liu, D. & Dal Pra, I. Calcium-Sensing Receptor Antagonist NPS 2143 Restores Amyloid Precursor Protein Physiological Non-Amyloidogenic Processing in Abeta-Exposed Adult Human Astrocytes. *Sci Rep* **7**, 1277 (2017). https://doi.org/10.1038/s41598-017-01215-3
131. Chiarini, A., Armato, U., Gardenal, E., Gui, L. & Dal Pra, I. Amyloid beta-Exposed Human Astrocytes Overproduce Phospho-Tau and Overrelease It within Exosomes, Effects Suppressed by Calcilytic NPS 2143-Further Implications for Alzheimer's Therapy. *Front Neurosci* **11**, 217 (2017). https://doi.org/10.3389/fnins.2017.00217
132. Conley, Y.P., Mukherjee, A., Kammerer, C., DeKosky, S.T., Kamboh, M.I., Finegold, D.N. & Ferrell, R.E. Evidence supporting a role for the calcium-sensing receptor in Alzheimer disease. *Am J Med Genet B Neuropsychiatr Genet* **150B**, 703-709 (2009). https://doi.org/10.1002/ajmg.b.30896
133. Ye, C., Ho-Pao, C.L., Kanazirska, M., Quinn, S., Rogers, K., Seidman, C.E., . . . Vassilev, P.M. Amyloid-beta proteins activate Ca(2+)-permeable channels through calcium-sensing receptors. *J Neurosci Res* **47**, 547-554 (1997). https://doi.org/10.1002/(sici)1097-4547(19970301)47:5<547::aid-jnr10>3.0.co;2-v
134. Babinsky, V.N., Hannan, F.M., Ramracheya, R.D., Zhang, Q., Nesbit, M.A., Hugill, A., . . . Thakker, R.V. Mutant Mice With Calcium-Sensing Receptor Activation Have Hyperglycemia That Is Rectified by Calcilytic Therapy. *Endocrinology* **158**, 2486-2502 (2017). https://doi.org/10.1210/en.2017-00111
135. Roder, P.V., Wu, B., Liu, Y. & Han, W. Pancreatic regulation of glucose homeostasis. *Exp Mol Med* **48**, e219 (2016). https://doi.org/10.1038/emm.2016.6
136. Rorsman, P. & Ashcroft, F.M. Pancreatic beta-Cell Electrical Activity and Insulin Secretion: Of Mice and Men. *Physiol Rev* **98**, 117-214 (2018). https://doi.org/10.1152/physrev.00008.2017
137. Brownlee, M. Biochemistry and molecular cell biology of diabetic complications. *Nature* **414**, 813-820 (2001). https://doi.org/10.1038/414813a
138. Rask-Madsen, C. & King, G.L. Vascular complications of diabetes: mechanisms of injury and protective factors. *Cell Metab* **17**, 20-33 (2013). https://doi.org/10.1016/j.cmet.2012.11.012

139. MacDonald, P.E. & Rorsman, P. Oscillations, intercellular coupling, and insulin secretion in pancreatic beta cells. *PLoS Biol* **4**, e49 (2006). https://doi.org/10.1371/journal.pbio.0040049
140. Rorsman, P. & Braun, M. Regulation of insulin secretion in human pancreatic islets. *Annu Rev Physiol* **75**, 155-179 (2013). https://doi.org/10.1146/annurev-physiol-030212-183754
141. Ashcroft, F.M. & Rorsman, P. K(ATP) channels and islet hormone secretion: new insights and controversies. *Nat Rev Endocrinol* **9**, 660-669 (2013). https://doi.org/10.1038/nrendo.2013.166
142. Rorsman, P., Braun, M. & Zhang, Q. Regulation of calcium in pancreatic alpha- and beta-cells in health and disease. *Cell Calcium* **51**, 300-308 (2012). https://doi.org/10.1016/j.ceca.2011.11.006
143. Ashcroft, F. & Rorsman, P. Type 2 diabetes mellitus: not quite exciting enough? *Hum Mol Genet* **13 Spec No 1**, R21-31 (2004). https://doi.org/10.1093/hmg/ddh066
144. Amisten, S., Salehi, A., Rorsman, P., Jones, P.M. & Persaud, S.J. An atlas and functional analysis of G-protein coupled receptors in human islets of Langerhans. *Pharmacol Ther* **139**, 359-391 (2013). https://doi.org/10.1016/j.pharmthera.2013.05.004
145. Ashcroft, F.M. & Rorsman, P. Diabetes mellitus and the beta cell: the last ten years. *Cell* **148**, 1160-1171 (2012). https://doi.org/10.1016/j.cell.2012.02.010
146. Eliasson, L., Abdulkader, F., Braun, M., Galvanovskis, J., Hoppa, M.B. & Rorsman, P. Novel aspects of the molecular mechanisms controlling insulin secretion. *J Physiol* **586**, 3313-3324 (2008). https://doi.org/10.1113/jphysiol.2008.155317
147. Rasschaert, J. & Malaisse, W.J. The G-protein-coupled, extracellular Ca(2+)-sensing receptor: expression in pancreatic islet B-cells and possible role in the regulation of insulin release. *Mol Genet Metab* **68**, 328-331 (1999). https://doi.org/10.1006/mgme.1999.2928
148. Rasschaert, J. & Malaisse, W.J. Expression of the calcium-sensing receptor in pancreatic islet B-cells. *Biochem Biophys Res Commun* **264**, 615-618 (1999). https://doi.org/10.1006/bbrc.1999.1577
149. Malaisse, W.J., Louchami, K., Laghmich, A., Ladriere, L., Morales, M., Villanueva-Penacarrillo, M.L., . . . Rasschaert, J. Possible participation of an islet B-cell calcium-sensing receptor in insulin release. *Endocrine* **11**, 293-300 (1999). https://doi.org/10.1385/ENDO:11:3:293
150. Gray, E., Muller, D., Squires, P.E., Asare-Anane, H., Huang, G.C., Amiel, S., . . . Jones, P.M. Activation of the extracellular calcium-sensing receptor initiates insulin secretion from human islets of Langerhans: involvement of protein kinases. *J Endocrinol* **190**, 703-710 (2006). https://doi.org/10.1677/joe.1.06891
151. Squires, P.E., Harris, T.E., Persaud, S.J., Curtis, S.B., Buchan, A.M. & Jones, P.M. The extracellular calcium-sensing receptor on human beta-cells negatively modulates insulin secretion. *Diabetes* **49**, 409-417 (2000). https://www.ncbi.nlm.nih.gov/pubmed/10868962
152. Squires, P.E., Jones, P.M., Younis, M.Y. & Hills, C.E. The calcium-sensing receptor and beta-cell function. *Vitam Horm* **95**, 249-267 (2014). https://doi.org/10.1016/B978-0-12-800174-5.00010-7
153. Babinsky, V.N., Hannan, F.M., Youhanna, S.C., Marechal, C., Jadoul, M., Devuyst, O. & Thakker, R.V. Association studies of calcium-sensing receptor (CaSR)

polymorphisms with serum concentrations of glucose and phosphate, and vascular calcification in renal transplant recipients. *PLoS One* **10**, e0119459 (2015). https://doi.org/10.1371/journal.pone.0119459
154. Wolf, P., Krssak, M., Winhofer, Y., Anderwald, C.H., Zwettler, E., Just Kukurova, I., . . . Krebs, M. Cardiometabolic phenotyping of patients with familial hypocalcuric hypercalcemia. *J Clin Endocrinol Metab* **99**, E1721-1726 (2014). https://doi.org/10.1210/jc.2014-1541
155. Straub, S.G., Kornreich, B., Oswald, R.E., Nemeth, E.F. & Sharp, G.W. The calcimimetic R-467 potentiates insulin secretion in pancreatic beta cells by activation of a nonspecific cation channel. *J Biol Chem* **275**, 18777-18784 (2000). https://doi.org/10.1074/jbc.M000090200
156. Gerbino, A., Maiellaro, I., Carmone, C., Caroppo, R., Debellis, L., Barile, M., . . . Colella, M. Glucose increases extracellular [Ca2+] in rat insulinoma (INS-1E) pseudoislets as measured with Ca2+-sensitive microelectrodes. *Cell Calcium* **51**, 393-401 (2012). https://doi.org/10.1016/j.ceca.2012.01.002
157. Zhang, C., Zhang, T., Zou, J., Miller, C.L., Gorkhali, R., Yang, J.Y., . . . Yang, J.J. Structural basis for regulation of human calcium-sensing receptor by magnesium ions and an unexpected tryptophan derivative co-agonist. *Sci Adv* **2**, e1600241 (2016). https://doi.org/10.1126/sciadv.1600241
158. Geng, Y., Mosyak, L., Kurinov, I., Zuo, H., Sturchler, E., Cheng, T.C., . . . Fan, Q.R. Structural mechanism of ligand activation in human calcium-sensing receptor. *Elife* **5**(2016). https://doi.org/10.7554/eLife.13662
159. Thomsen, A.R., Hvidtfeldt, M. & Brauner-Osborne, H. Biased agonism of the calcium-sensing receptor. *Cell Calcium* **51**, 107-116 (2012). https://doi.org/10.1016/j.ceca.2011.11.009
160. Padgett, C.L. & Slesinger, P.A. GABAB receptor coupling to G-proteins and ion channels. *Adv Pharmacol* **58**, 123-147 (2010). https://doi.org/10.1016/S1054-3589(10)58006-2
161. De Blasi, A., Conn, P.J., Pin, J. & Nicoletti, F. Molecular determinants of metabotropic glutamate receptor signaling. *Trends Pharmacol Sci* **22**, 114-120 (2001). https://www.ncbi.nlm.nih.gov/pubmed/11239574
162. Namkung, Y., LeGouill, C., Kumar, S., Cao, Y., Teixeira, L.B., Lukasheva, V., . . . Laporte, S.A. Functional selectivity profiling of the angiotensin II type 1 receptor using pathway-wide BRET signaling sensors. *Sci Signal* **11**(2018). https://doi.org/10.1126/scisignal.aat1631
163. Cahill, T.J., 3rd, Thomsen, A.R., Tarrasch, J.T., Plouffe, B., Nguyen, A.H., Yang, F., . . . Lefkowitz, R.J. Distinct conformations of GPCR-beta-arrestin complexes mediate desensitization, signaling, and endocytosis. *Proc Natl Acad Sci U S A* **114**, 2562-2567 (2017). https://doi.org/10.1073/pnas.1701529114
164. Drake, M.T., Shenoy, S.K. & Lefkowitz, R.J. Trafficking of G protein-coupled receptors. *Circ Res* **99**, 570-582 (2006). https://doi.org/10.1161/01.RES.0000242563.47507.ce
165. Cao, Y., Namkung, Y. & Laporte, S.A. Methods to Monitor the Trafficking of beta-Arrestin/G Protein-Coupled Receptor Complexes Using Enhanced Bystander BRET. *Methods Mol Biol* **1957**, 59-68 (2019). https://doi.org/10.1007/978-1-4939-9158-7_3
166. Namkung, Y., Le Gouill, C., Lukashova, V., Kobayashi, H., Hogue, M., Khoury, E., . . . Laporte, S.A. Monitoring G protein-coupled receptor and beta-arrestin

trafficking in live cells using enhanced bystander BRET. *Nat Commun* **7**, 12178 (2016). https://doi.org/10.1038/ncomms12178
167. Holstein, D.M., Berg, K.A., Leeb-Lundberg, L.M., Olson, M.S. & Saunders, C. Calcium-sensing receptor-mediated ERK1/2 activation requires Galphai2 coupling and dynamin-independent receptor internalization. *J Biol Chem* **279**, 10060-10069 (2004). https://doi.org/10.1074/jbc.M312039200
168. Reyes-Ibarra, A.P., Garcia-Regalado, A., Ramirez-Rangel, I., Esparza-Silva, A.L., Valadez-Sanchez, M., Vazquez-Prado, J. & Reyes-Cruz, G. Calcium-sensing receptor endocytosis links extracellular calcium signaling to parathyroid hormone-related peptide secretion via a Rab11a-dependent and AMSH-sensitive mechanism. *Mol Endocrinol* **21**, 1394-1407 (2007). https://doi.org/10.1210/me.2006-0523
169. Brown, E.M., Fuleihan, G.e.-H., Chen, C.J. & Kifor, O. A comparison of the effects of divalent and trivalent cations on parathyroid hormone release, 3',5'-cyclic-adenosine monophosphate accumulation, and the levels of inositol phosphates in bovine parathyroid cells. *Endocrinology* **127**, 1064-1071 (1990). https://doi.org/10.1210/endo-127-3-1064
170. Miyazaki, H., Ikeda, Y., Sakurai, O., Miyake, T., Tsubota, R., Okabe, J., . . . Moritani, Y. Discovery of evocalcet, a next-generation calcium-sensing receptor agonist for the treatment of hyperparathyroidism. *Bioorg Med Chem Lett* **28**, 2055-2060 (2018). https://doi.org/10.1016/j.bmcl.2018.04.055
171. Padhi, D. & Harris, R. Clinical pharmacokinetic and pharmacodynamic profile of cinacalcet hydrochloride. *Clin Pharmacokinet* **48**, 303-311 (2009). https://doi.org/10.2165/00003088-200948050-00002
172. Nemeth, E.F. & Goodman, W.G. Calcimimetic and Calcilytic Drugs: Feats, Flops, and Futures. *Calcif Tissue Int* **98**, 341-358 (2016). https://doi.org/10.1007/s00223-015-0052-z
173. Alexander, S.T., Hunter, T., Walter, S., Dong, J., Maclean, D., Baruch, A., . . . Tomlinson, J.E. Critical Cysteine Residues in Both the Calcium-Sensing Receptor and the Allosteric Activator AMG 416 Underlie the Mechanism of Action. *Mol Pharmacol* **88**, 853-865 (2015). https://doi.org/10.1124/mol.115.098392
174. Walter, S., Baruch, A., Dong, J., Tomlinson, J.E., Alexander, S.T., Janes, J., . . . Karim, F. Pharmacology of AMG 416 (Velcalcetide), a novel peptide agonist of the calcium-sensing receptor, for the treatment of secondary hyperparathyroidism in hemodialysis patients. *J Pharmacol Exp Ther* **346**, 229-240 (2013). https://doi.org/10.1124/jpet.113.204834
175. Gustafsson, M., Jensen, J., Bertozzi, S.M., Currier, E.A., Ma, J.N., Burstein, E.S. & Olsson, R. Discovery of a class of calcium sensing receptor positive allosteric modulators; 1-(benzothiazol-2-yl)-1-phenylethanols. *Bioorg Med Chem Lett* **20**, 5918-5921 (2010). https://doi.org/10.1016/j.bmcl.2010.07.077
176. Ma, J.N., Owens, M., Gustafsson, M., Jensen, J., Tabatabaei, A., Schmelzer, K., . . . Burstein, E.S. Characterization of highly efficacious allosteric agonists of the human calcium-sensing receptor. *J Pharmacol Exp Ther* **337**, 275-284 (2011). https://doi.org/10.1124/jpet.110.178194
177. Hamano, N., Komaba, H. & Fukagawa, M. Etelcalcetide for the treatment of secondary hyperparathyroidism. *Expert Opin Pharmacother* **18**, 529-534 (2017). https://doi.org/10.1080/14656566.2017.1303482
178. Cozzolino, M., Galassi, A., Conte, F., Mangano, M., Di Lullo, L. & Bellasi, A. Treatment of secondary hyperparathyroidism: the clinical utility of etelcalcetide.

Ther Clin Risk Manag **13**, 679-689 (2017). https://doi.org/10.2147/TCRM.S108490
179. Conigrave, A.D., Quinn, S.J. & Brown, E.M. L-amino acid sensing by the extracellular Ca2+-sensing receptor. *Proc Natl Acad Sci U S A* **97**, 4814-4819 (2000). https://doi.org/10.1073/pnas.97.9.4814
180. Nemeth, E.F. & Shoback, D. Calcimimetic and calcilytic drugs for treating bone and mineral-related disorders. *Best Pract Res Clin Endocrinol Metab* **27**, 373-384 (2013). https://doi.org/10.1016/j.beem.2013.02.008
181. Silva, B.C. & Bilezikian, J.P. Parathyroid hormone: anabolic and catabolic actions on the skeleton. *Curr Opin Pharmacol* **22**, 41-50 (2015). https://doi.org/10.1016/j.coph.2015.03.005
182. Centeno, P.P., Herberger, A., Mun, H.C., Tu, C., Nemeth, E.F., Chang, W., . . . Ward, D.T. Phosphate acts directly on the calcium-sensing receptor to stimulate parathyroid hormone secretion. *Nat Commun* **10**, 4693 (2019). https://doi.org/10.1038/s41467-019-12399-9
183. Russell, R.G. Pharmacological diversity among drugs that inhibit bone resorption. *Curr Opin Pharmacol* **22**, 115-130 (2015). https://doi.org/10.1016/j.coph.2015.05.005
184. Brown, E.M. Is the calcium receptor a molecular target for the actions of strontium on bone? *Osteoporos Int* **14 Suppl 3**, S25-34 (2003). https://doi.org/10.1007/s00198-002-1343-6
185. Stepan, J.J. Strontium ranelate: in search for the mechanism of action. *J Bone Miner Metab* **31**, 606-612 (2013). https://doi.org/10.1007/s00774-013-0494-1
186. Caudrillier, A., Hurtel-Lemaire, A.S., Wattel, A., Cournarie, F., Godin, C., Petit, L., . . . Brazier, M. Strontium ranelate decreases receptor activator of nuclear factor-KappaB ligand-induced osteoclastic differentiation in vitro: involvement of the calcium-sensing receptor. *Mol Pharmacol* **78**, 569-576 (2010). https://doi.org/10.1124/mol.109.063347
187. Bakker, A.D., Zandieh-Doulabi, B. & Klein-Nulend, J. Strontium ranelate affects signaling from mechanically-stimulated osteocytes towards osteoclasts and osteoblasts. *Bone* **53**, 112-119 (2013). https://doi.org/10.1016/j.bone.2012.11.044
188. Hurtel-Lemaire, A.S., Mentaverri, R., Caudrillier, A., Cournarie, F., Wattel, A., Kamel, S., . . . Brazier, M. The calcium-sensing receptor is involved in strontium ranelate-induced osteoclast apoptosis. New insights into the associated signaling pathways. *J Biol Chem* **284**, 575-584 (2009). https://doi.org/10.1074/jbc.M801668200
189. Furness, S.G.B., Liang, Y.L., Nowell, C.J., Halls, M.L., Wookey, P.J., Dal Maso, E., . . . Sexton, P.M. Ligand-Dependent Modulation of G Protein Conformation Alters Drug Efficacy. *Cell* **167**, 739-749 e711 (2016). https://doi.org/10.1016/j.cell.2016.09.021
190. Wootten, D., Simms, J., Miller, L.J., Christopoulos, A. & Sexton, P.M. Polar transmembrane interactions drive formation of ligand-specific and signal pathway-biased family B G protein-coupled receptor conformations. *Proc Natl Acad Sci U S A* **110**, 5211-5216 (2013). https://doi.org/10.1073/pnas.1221585110

191. Thal, D.M., Glukhova, A., Sexton, P.M. & Christopoulos, A. Structural insights into G-protein-coupled receptor allostery. *Nature* **559**, 45-53 (2018). https://doi.org/10.1038/s41586-018-0259-z
192. Wisler, J.W., Xiao, K., Thomsen, A.R. & Lefkowitz, R.J. Recent developments in biased agonism. *Curr Opin Cell Biol* **27**, 18-24 (2014). https://doi.org/10.1016/j.ceb.2013.10.008
193. Grasberger, H., Van Sande, J., Hag-Dahood Mahameed, A., Tenenbaum-Rakover, Y. & Refetoff, S. A familial thyrotropin (TSH) receptor mutation provides in vivo evidence that the inositol phosphates/Ca2+ cascade mediates TSH action on thyroid hormone synthesis. *J Clin Endocrinol Metab* **92**, 2816-2820 (2007). https://doi.org/10.1210/jc.2007-0366
194. Siuda, E.R., Carr, R., 3rd, Rominger, D.H. & Violin, J.D. Biased mu-opioid receptor ligands: a promising new generation of pain therapeutics. *Curr Opin Pharmacol* **32**, 77-84 (2017). https://doi.org/10.1016/j.coph.2016.11.007
195. Viscusi, E.R., Webster, L., Kuss, M., Daniels, S., Bolognese, J.A., Zuckerman, S., . . . Skobieranda, F. A randomized, phase 2 study investigating TRV130, a biased ligand of the mu-opioid receptor, for the intravenous treatment of acute pain. *Pain* **157**, 264-272 (2016). https://doi.org/10.1097/j.pain.0000000000000363
196. Singla, N., Minkowitz, H.S., Soergel, D.G., Burt, D.A., Subach, R.A., Salamea, M.Y., . . . Skobieranda, F. A randomized, Phase IIb study investigating oliceridine (TRV130), a novel micro-receptor G-protein pathway selective (mu-GPS) modulator, for the management of moderate to severe acute pain following abdominoplasty. *J Pain Res* **10**, 2413-2424 (2017). https://doi.org/10.2147/JPR.S137952
197. Viscusi, E.R., Skobieranda, F., Soergel, D.G., Cook, E., Burt, D.A. & Singla, N. APOLLO-1: a randomized placebo and active-controlled phase III study investigating oliceridine (TRV130), a G protein-biased ligand at the micro-opioid receptor, for management of moderate-to-severe acute pain following bunionectomy. *J Pain Res* **12**, 927-943 (2019). https://doi.org/10.2147/JPR.S171013
198. DeWire, S.M., Yamashita, D.S., Rominger, D.H., Liu, G., Cowan, C.L., Graczyk, T.M., . . . Violin, J.D. A G protein-biased ligand at the mu-opioid receptor is potently analgesic with reduced gastrointestinal and respiratory dysfunction compared with morphine. *J Pharmacol Exp Ther* **344**, 708-717 (2013). https://doi.org/10.1124/jpet.112.201616
199. Koblish, M., Carr, R., 3rd, Siuda, E.R., Rominger, D.H., Gowen-MacDonald, W., Cowan, C.L., . . . Lark, M.W. TRV0109101, a G Protein-Biased Agonist of the micro-Opioid Receptor, Does Not Promote Opioid-Induced Mechanical Allodynia following Chronic Administration. *J Pharmacol Exp Ther* **362**, 254-262 (2017). https://doi.org/10.1124/jpet.117.241117
200. Machelska, H. & Celik, M.O. Advances in Achieving Opioid Analgesia Without Side Effects. *Front Pharmacol* **9**, 1388 (2018). https://doi.org/10.3389/fphar.2018.01388
201. Soergel, D.G., Subach, R.A., Burnham, N., Lark, M.W., James, I.E., Sadler, B.M., . . . Webster, L.R. Biased agonism of the mu-opioid receptor by TRV130 increases analgesia and reduces on-target adverse effects versus morphine: A randomized, double-blind, placebo-controlled, crossover study in healthy volunteers. *Pain* **155**, 1829-1835 (2014). https://doi.org/10.1016/j.pain.2014.06.011

202. Violin, J.D., Crombie, A.L., Soergel, D.G. & Lark, M.W. Biased ligands at G-protein-coupled receptors: promise and progress. *Trends Pharmacol Sci* **35**, 308-316 (2014). https://doi.org/10.1016/j.tips.2014.04.007
203. Cook, A.E., Mistry, S.N., Gregory, K.J., Furness, S.G., Sexton, P.M., Scammells, P.J., . . . Leach, K. Biased allosteric modulation at the CaS receptor engendered by structurally diverse calcimimetics. *Br J Pharmacol* **172**, 185-200 (2015). https://doi.org/10.1111/bph.12937
204. Davey, A.E., Leach, K., Valant, C., Conigrave, A.D., Sexton, P.M. & Christopoulos, A. Positive and negative allosteric modulators promote biased signaling at the calcium-sensing receptor. *Endocrinology* **153**, 1232-1241 (2012). https://doi.org/10.1210/en.2011-1426
205. Leach, K., Conigrave, A.D., Sexton, P.M. & Christopoulos, A. Towards tissue-specific pharmacology: insights from the calcium-sensing receptor as a paradigm for GPCR (patho)physiological bias. *Trends Pharmacol Sci* **36**, 215-225 (2015). https://doi.org/10.1016/j.tips.2015.02.004
206. van Unen, J., Rashidfarrokhi, A., Hoogendoorn, E., Postma, M., Gadella, T.W., Jr. & Goedhart, J. Quantitative Single-Cell Analysis of Signaling Pathways Activated Immediately Downstream of Histamine Receptor Subtypes. *Mol Pharmacol* **90**, 162-176 (2016). https://doi.org/10.1124/mol.116.104505
207. Inoue, A., Raimondi, F., Kadji, F.M.N., Singh, G., Kishi, T., Uwamizu, A., . . . Russell, R.B. Illuminating G-Protein-Coupling Selectivity of GPCRs. *Cell* **177**, 1933-1947 e1925 (2019). https://doi.org/10.1016/j.cell.2019.04.044
208. Wright, S.C., Canizal, M.C.A., Benkel, T., Simon, K., Le Gouill, C., Matricon, P., . . . Hoffmann, C. FZD5 is a Galphaq-coupled receptor that exhibits the functional hallmarks of prototypical GPCRs. *Sci Signal* **11**(2018). https://doi.org/10.1126/scisignal.aar5536
209. Alvarez-Curto, E., Inoue, A., Jenkins, L., Raihan, S.Z., Prihandoko, R., Tobin, A.B. & Milligan, G. Targeted Elimination of G Proteins and Arrestins Defines Their Specific Contributions to Both Intensity and Duration of G Protein-coupled Receptor Signaling. *J Biol Chem* **291**, 27147-27159 (2016). https://doi.org/10.1074/jbc.M116.754887
210. Howles, S.A., Wiberg, A., Goldsworthy, M., Bayliss, A.L., Gluck, A.K., Ng, M., . . . Furniss, D. Genetic variants of calcium and vitamin D metabolism in kidney stone disease. *Nat Commun* **10**, 5175 (2019). https://doi.org/10.1038/s41467-019-13145-x
211. Gorvin, C.M., Stokes, V.J., Boon, H., Cranston, T., Gluck, A.K., Bahl, S., . . . Thakker, R.V. Activating Mutations of the G-protein Subunit alpha 11 Interdomain Interface Cause Autosomal Dominant Hypocalcemia Type 2. *J Clin Endocrinol Metab* **105**(2020). https://doi.org/10.1210/clinem/dgz251
212. AgilentTechnologies. (2015). QuikChange Lightning Site-Directed Mutagenesis Kit. [Instruction Manual] Retrieved from https://www.agilent.com/cs/library/usermanuals/public/210518.pdf
213. AppliedBiosystems. (2009). DNA Sequencing by Capillary Electrophoresis. [Chemistry Guide] Retrieved from https://tools.thermofisher.com/content/sfs/manuals/cms_041003.pdf?icid=lsg_gsd_CP1236_PJT8083_blog_seqitout-howsangerworks
214. Hirano, S. Western blot analysis. *Methods Mol Biol* **926**, 87-97 (2012). https://doi.org/10.1007/978-1-62703-002-1_6

215. ThermoFisherScientific. (2016). Coomassie Plus (Bradford) Assay Kit. [User Guide] Retrieved from https://www.thermofisher.com/document-connect/document-connect.html?url=https%3A%2F%2Fassets.thermofisher.com%2FTFS-Assets%2FLSG%2Fmanuals%2FMAN0011203_CoomassiePlus_Bradford_Asy_UG.pdf&title=VXNlciBHdWlkZTogIENvb21hc3NpZSBQbHVzIChCcmFkZm9yZCkgQXNzYXkgS2l0
216. Hnasko, T.S. & Hnasko, R.M. The Western Blot. *Methods Mol Biol* **1318**, 87-96 (2015). https://doi.org/10.1007/978-1-4939-2742-5_9
217. Kim, B. Western Blot Techniques. *Methods Mol Biol* **1606**, 133-139 (2017). https://doi.org/10.1007/978-1-4939-6990-6_9
218. Kiskova, T., Mytsko, Y., Schepelmann, M., Helmer, H., Fuchs, R., Miedl, H., . . . Ellinger, I. Expression of the neonatal Fc-receptor in placental-fetal endothelium and in cells of the placental immune system. *Placenta* **78**, 36-43 (2019). https://doi.org/10.1016/j.placenta.2019.02.012
219. Babinsky, V.N., Hannan, F.M., Gorvin, C.M., Howles, S.A., Nesbit, M.A., Rust, N., . . . Thakker, R.V. Allosteric Modulation of the Calcium-sensing Receptor Rectifies Signaling Abnormalities Associated with G-protein alpha-11 Mutations Causing Hypercalcemic and Hypocalcemic Disorders. *J Biol Chem* **291**, 10876-10885 (2016). https://doi.org/10.1074/jbc.M115.696401
220. Piret, S.E., Gorvin, C.M., Pagnamenta, A.T., Howles, S.A., Cranston, T., Rust, N., . . . Thakker, R.V. Identification of a G-Protein Subunit-alpha11 Gain-of-Function Mutation, Val340Met, in a Family With Autosomal Dominant Hypocalcemia Type 2 (ADH2). *J Bone Miner Res* **31**, 1207-1214 (2016). https://doi.org/10.1002/jbmr.2797
221. Lines, K.E., Stevenson, M., Filippakopoulos, P., Muller, S., Lockstone, H.E., Wright, B., . . . Thakker, R.V. Epigenetic pathway inhibitors represent potential drugs for treating pancreatic and bronchial neuroendocrine tumors. *Oncogenesis* **6**, e332 (2017). https://doi.org/10.1038/oncsis.2017.30
222. Price, M.A., Hill, C. & Treisman, R. Integration of growth factor signals at the c-fos serum response element. *Philos Trans R Soc Lond B Biol Sci* **351**, 551-559 (1996). https://doi.org/10.1098/rstb.1996.0054
223. Treisman, R. The serum response element. *Trends Biochem Sci* **17**, 423-426 (1992). https://doi.org/10.1016/0968-0004(92)90013-y
224. Dalton, S. & Treisman, R. Characterization of SAP-1, a protein recruited by serum response factor to the c-fos serum response element. *Cell* **68**, 597-612 (1992). https://doi.org/10.1016/0092-8674(92)90194-h
225. Norman, C., Runswick, M., Pollock, R. & Treisman, R. Isolation and properties of cDNA clones encoding SRF, a transcription factor that binds to the c-fos serum response element. *Cell* **55**, 989-1003 (1988). https://doi.org/10.1016/0092-8674(88)90244-9
226. Chen, Y., Xu, Z., Wu, D., Li, J., Song, C., Lu, W. & Huang, J. Luciferase reporter gene assay on human 5-HT receptor: which response element should be chosen? *Sci Rep* **5**, 8060 (2015). https://doi.org/10.1038/srep08060
227. Cheng, Z., Garvin, D., Paguio, A., Stecha, P., Wood, K. & Fan, F. Luciferase Reporter Assay System for Deciphering GPCR Pathways. *Curr Chem Genomics* **4**, 84-91 (2010). https://doi.org/10.2174/1875397301004010084
228. PromegaCorporation. (2015). pGL4 Luciferase Reporter Vectors TM259. [Technical manual] Retrieved from https://www.promega.es/-

/media/files/resources/protocols/technical-manuals/0/pgl4-luciferase-reporter-vectors-protocol.pdf?la=en
229. Mondal, S., Hsiao, K. & Goueli, S.A. A Homogenous Bioluminescent System for Measuring GTPase, GTPase Activating Protein, and Guanine Nucleotide Exchange Factor Activities. *Assay Drug Dev Technol* **13**, 444-455 (2015). https://doi.org/10.1089/adt.2015.643
230. Tocris. (2020). Fluo-4 AM. [Certificate of Analysis] Retrieved from https://resources.rndsystems.com/pdfs/tocris_coa/6255_2_coa.pdf?t=1590725888
231. Gee, K.R., Brown, K.A., Chen, W.N., Bishop-Stewart, J., Gray, D. & Johnson, I. Chemical and physiological characterization of fluo-4 Ca(2+)-indicator dyes. *Cell Calcium* **27**, 97-106 (2000). https://doi.org/10.1054/ceca.1999.0095
232. PerkinElmer. (2002). Principles of AlphaScreen™. [Application Note] Retrieved from https://www.perkinelmer.com/lab-solutions/resources/docs/APP_AlphaScreen_Principles.pdf
233. Kobayashi, H., Picard, L.P., Schonegge, A.M. & Bouvier, M. Bioluminescence resonance energy transfer-based imaging of protein-protein interactions in living cells. *Nat Protoc* **14**, 1084-1107 (2019). https://doi.org/10.1038/s41596-019-0129-7
234. Hamdan, F.F., Percherancier, Y., Breton, B. & Bouvier, M. Monitoring protein-protein interactions in living cells by bioluminescence resonance energy transfer (BRET). *Curr Protoc Neurosci* **Chapter 5**, Unit 5 23 (2006). https://doi.org/10.1002/0471142301.ns0523s34
235. Molinari, P., Casella, I. & Costa, T. Functional complementation of high-efficiency resonance energy transfer: a new tool for the study of protein binding interactions in living cells. *Biochem J* **409**, 251-261 (2008). https://doi.org/10.1042/BJ20070803
236. Degorce, F., Card, A., Soh, S., Trinquet, E., Knapik, G.P. & Xie, B. HTRF: A technology tailored for drug discovery - a review of theoretical aspects and recent applications. *Curr Chem Genomics* **3**, 22-32 (2009). https://doi.org/10.2174/1875397300903010022
237. Cisbio. (2020). IP-One Gq KIT. [Technical Manual] Retrieved from https://uk.cisbio.eu/media/asset/c/i/cisbio_dd_pi_62ipapeb-62ipapec-62ipapej.pdf
238. Adzhubei, I., Jordan, D.M. & Sunyaev, S.R. Predicting functional effect of human missense mutations using PolyPhen-2. *Curr Protoc Hum Genet* **Chapter 7**, Unit7 20 (2013). https://doi.org/10.1002/0471142905.hg0720s76
239. Ng, P.C. & Henikoff, S. SIFT: Predicting amino acid changes that affect protein function. *Nucleic Acids Res* **31**, 3812-3814 (2003). https://doi.org/10.1093/nar/gkg509
240. Kircher, M., Witten, D.M., Jain, P., O'Roak, B.J., Cooper, G.M. & Shendure, J. A general framework for estimating the relative pathogenicity of human genetic variants. *Nat Genet* **46**, 310-315 (2014). https://doi.org/10.1038/ng.2892
241. Ioannidis, N.M., Rothstein, J.H., Pejaver, V., Middha, S., McDonnell, S.K., Baheti, S., . . . Sieh, W. REVEL: An Ensemble Method for Predicting the Pathogenicity of Rare Missense Variants. *Am J Hum Genet* **99**, 877-885 (2016). https://doi.org/10.1016/j.ajhg.2016.08.016
242. Dong, C., Wei, P., Jian, X., Gibbs, R., Boerwinkle, E., Wang, K. & Liu, X. Comparison and integration of deleteriousness prediction methods for nonsynonymous

SNVs in whole exome sequencing studies. *Hum Mol Genet* **24**, 2125-2137 (2015). https://doi.org/10.1093/hmg/ddu733
243. Berman, H.M., Westbrook, J., Feng, Z., Gilliland, G., Bhat, T.N., Weissig, H., . . . Bourne, P.E. The Protein Data Bank. *Nucleic Acids Res* **28**, 235-242 (2000). https://doi.org/10.1093/nar/28.1.235
244. Grosdidier, A., Zoete, V. & Michielin, O. SwissDock, a protein-small molecule docking web service based on EADock DSS. *Nucleic Acids Res* **39**, W270-277 (2011). https://doi.org/10.1093/nar/gkr366
245. Aittaleb, M., Nishimura, A., Linder, M.E. & Tesmer, J.J. Plasma membrane association of p63 Rho guanine nucleotide exchange factor (p63RhoGEF) is mediated by palmitoylation and is required for basal activity in cells. *J Biol Chem* **286**, 34448-34456 (2011). https://doi.org/10.1074/jbc.M111.273342
246. Benkert, P., Biasini, M. & Schwede, T. Toward the estimation of the absolute quality of individual protein structure models. *Bioinformatics* **27**, 343-350 (2011). https://doi.org/10.1093/bioinformatics/btq662
247. Bertoni, M., Kiefer, F., Biasini, M., Bordoli, L. & Schwede, T. Modeling protein quaternary structure of homo- and hetero-oligomers beyond binary interactions by homology. *Sci Rep* **7**, 10480 (2017). https://doi.org/10.1038/s41598-017-09654-8
248. Bienert, S., Waterhouse, A., de Beer, T.A., Tauriello, G., Studer, G., Bordoli, L. & Schwede, T. The SWISS-MODEL Repository-new features and functionality. *Nucleic Acids Res* **45**, D313-D319 (2017). https://doi.org/10.1093/nar/gkw1132
249. Bodmann, E.L., Rinne, A., Brandt, D., Lutz, S., Wieland, T., Grosse, R. & Bunemann, M. Dynamics of Galphaq-protein-p63RhoGEF interaction and its regulation by RGS2. *Biochem J* **458**, 131-140 (2014). https://doi.org/10.1042/BJ20130782
250. Miller, T.J., McCoy, M.J., Lee-Pullen, T.F., Anyaegbu, C.C., Hemmings, C., Bulsara, M.K. & Platell, C.F. The Prognostic and Predictive Value of SOX2(+) Cell Densities in Patients Treated for Colorectal Cancer. *Cancers (Basel)* **12**(2020). https://doi.org/10.3390/cancers12051110
251. Simitsidellis, I., Esnal-Zuffiaure, A., Kelepouri, O., O'Flaherty, E., Gibson, D.A. & Saunders, P.T.K. Selective androgen receptor modulators (SARMs) have specific impacts on the mouse uterus. *J Endocrinol* **242**, 227-239 (2019). https://doi.org/10.1530/JOE-19-0153
252. Southan, C., Sharman, J.L., Benson, H.E., Faccenda, E., Pawson, A.J., Alexander, S.P., . . . Nc, I. The IUPHAR/BPS Guide to PHARMACOLOGY in 2016: towards curated quantitative interactions between 1300 protein targets and 6000 ligands. *Nucleic Acids Res* **44**, D1054-1068 (2016). https://doi.org/10.1093/nar/gkv1037
253. Munk, C., Isberg, V., Mordalski, S., Harpsoe, K., Rataj, K., Hauser, A.S., . . . Gloriam, D.E. GPCRdb: the G protein-coupled receptor database - an introduction. *Br J Pharmacol* **173**, 2195-2207 (2016). https://doi.org/10.1111/bph.13509
254. Dewey, F.E., Murray, M.F., Overton, J.D., Habegger, L., Leader, J.B., Fetterolf, S.N., . . . Carey, D.J. Distribution and clinical impact of functional variants in 50,726 whole-exome sequences from the DiscovEHR study. *Science* **354**(2016). https://doi.org/10.1126/science.aaf6814
255. Sherry, S.T., Ward, M. & Sirotkin, K. dbSNP-database for single nucleotide polymorphisms and other classes of minor genetic variation. *Genome Res* **9**, 677-679 (1999). https://www.ncbi.nlm.nih.gov/pubmed/10447503

256. Sayers, E.W., Barrett, T., Benson, D.A., Bolton, E., Bryant, S.H., Canese, K., . . . Ye, J. Database resources of the National Center for Biotechnology Information. *Nucleic Acids Res* **39**, D38-51 (2011). https://doi.org/10.1093/nar/gkq1172
257. Lek, M., Karczewski, K.J., Minikel, E.V., Samocha, K.E., Banks, E., Fennell, T., . . . Exome Aggregation, C. Analysis of protein-coding genetic variation in 60,706 humans. *Nature* **536**, 285-291 (2016). https://doi.org/10.1038/nature19057
258. Karczewski, K.J., Francioli, L.C., Tiao, G., Cummings, B.B., Alföldi, J., Wang, Q., . . . MacArthur, D.G. The mutational constraint spectrum quantified from variation in 141,456 humans. *bioRxiv*, 531210 (2020). https://doi.org/10.1101/531210
259. Karczewski, K.J., Francioli, L.C., Tiao, G., Cummings, B.B., Alfoldi, J., Wang, Q., . . . MacArthur, D.G. The mutational constraint spectrum quantified from variation in 141,456 humans. *Nature* **581**, 434-443 (2020). https://doi.org/10.1038/s41586-020-2308-7
260. Mannstadt, M., Harris, M., Bravenboer, B., Chitturi, S., Dreijerink, K.M., Lambright, D.G., . . . Juppner, H. Germline mutations affecting Galpha11 in hypoparathyroidism. *N Engl J Med* **368**, 2532-2534 (2013). https://doi.org/10.1056/NEJMc1300278
261. Leach, K., Wen, A., Davey, A.E., Sexton, P.M., Conigrave, A.D. & Christopoulos, A. Identification of molecular phenotypes and biased signaling induced by naturally occurring mutations of the human calcium-sensing receptor. *Endocrinology* **153**, 4304-4316 (2012). https://doi.org/10.1210/en.2012-1449
262. Gorvin, C.M., Babinsky, V.N., Malinauskas, T., Nissen, P.H., Schou, A.J., Hanyaloglu, A.C., . . . Thakker, R.V. A calcium-sensing receptor mutation causing hypocalcemia disrupts a transmembrane salt bridge to activate beta-arrestin-biased signaling. *Sci Signal* **11**(2018). https://doi.org/10.1126/scisignal.aan3714
263. MacArthur, D.G., Manolio, T.A., Dimmock, D.P., Rehm, H.L., Shendure, J., Abecasis, G.R., . . . Gunter, C. Guidelines for investigating causality of sequence variants in human disease. *Nature* **508**, 469-476 (2014). https://doi.org/10.1038/nature13127
264. Richards, S., Aziz, N., Bale, S., Bick, D., Das, S., Gastier-Foster, J., . . . Committee, A.L.Q.A. Standards and guidelines for the interpretation of sequence variants: a joint consensus recommendation of the American College of Medical Genetics and Genomics and the Association for Molecular Pathology. *Genet Med* **17**, 405-424 (2015). https://doi.org/10.1038/gim.2015.30
265. Collins, R.L., Brand, H., Karczewski, K.J., Zhao, X., Alfoldi, J., Francioli, L.C., . . . Talkowski, M.E. A structural variation reference for medical and population genetics. *Nature* **581**, 444-451 (2020). https://doi.org/10.1038/s41586-020-2287-8
266. Rasmussen, S.G., DeVree, B.T., Zou, Y., Kruse, A.C., Chung, K.Y., Kobilka, T.S., . . . Kobilka, B.K. Crystal structure of the beta2 adrenergic receptor-Gs protein complex. *Nature* **477**, 549-555 (2011). https://doi.org/10.1038/nature10361
267. Lyon, A.M., Dutta, S., Boguth, C.A., Skiniotis, G. & Tesmer, J.J. Full-length Galpha(q)-phospholipase C-beta3 structure reveals interfaces of the C-terminal coiled-coil domain. *Nat Struct Mol Biol* **20**, 355-362 (2013). https://doi.org/10.1038/nsmb.2497
268. Wess, J., Eglen, R.M. & Gautam, D. Muscarinic acetylcholine receptors: mutant mice provide new insights for drug development. *Nat Rev Drug Discov* **6**, 721-733 (2007). https://doi.org/10.1038/nrd2379

269. Abrams, P., Andersson, K.E., Buccafusco, J.J., Chapple, C., de Groat, W.C., Fryer, A.D., . . . Wein, A.J. Muscarinic receptors: their distribution and function in body systems, and the implications for treating overactive bladder. *Br J Pharmacol* **148**, 565-578 (2006). https://doi.org/10.1038/sj.bjp.0706780
270. Hovden, S., Rejnmark, L., Ladefoged, S.A. & Nissen, P.H. AP2S1 and GNA11 mutations - not a common cause of familial hypocalciuric hypercalcemia. *Eur J Endocrinol* **176**, 177-185 (2017). https://doi.org/10.1530/EJE-16-0842
271. Szalat, A., Shpitzen, S., Tsur, A., Zalmon Koren, I., Shilo, S., Tripto-Shkolnik, L., . . . Meiner, V. Stepwise CaSR, AP2S1, and GNA11 sequencing in patients with suspected familial hypocalciuric hypercalcemia. *Endocrine* **55**, 741-747 (2017). https://doi.org/10.1007/s12020-017-1241-5
272. Stratta, P., Merlotti, G., Musetti, C., Quaglia, M., Pagani, A., Izzo, C., . . . Guarnieri, V. Calcium-sensing-related gene mutations in hypercalcaemic hypocalciuric patients as differential diagnosis from primary hyperparathyroidism: detection of two novel inactivating mutations in an Italian population. *Nephrol Dial Transplant* **29**, 1902-1909 (2014). https://doi.org/10.1093/ndt/gfu065
273. Rubinfeld, B., Munemitsu, S., Clark, R., Conroy, L., Watt, K., Crosier, W.J., . . . Polakis, P. Molecular cloning of a GTPase activating protein specific for the Krev-1 protein p21rap1. *Cell* **65**, 1033-1042 (1991). https://doi.org/10.1016/0092-8674(91)90555-d
274. Mochizuki, N., Ohba, Y., Kiyokawa, E., Kurata, T., Murakami, T., Ozaki, T., . . . Matsuda, M. Activation of the ERK/MAPK pathway by an isoform of rap1GAP associated with G alpha(i). *Nature* **400**, 891-894 (1999). https://doi.org/10.1038/23738
275. Consortium, F., the, R.P., Clst, Forrest, A.R., Kawaji, H., Rehli, M., . . . Hayashizaki, Y. A promoter-level mammalian expression atlas. *Nature* **507**, 462-470 (2014). https://doi.org/10.1038/nature13182
276. Consortium, G.T. The Genotype-Tissue Expression (GTEx) project. *Nat Genet* **45**, 580-585 (2013). https://doi.org/10.1038/ng.2653
277. Hannan, F.M., Walls, G.V., Babinsky, V.N., Nesbit, M.A., Kallay, E., Hough, T.A., . . . Thakker, R.V. The Calcilytic Agent NPS 2143 Rectifies Hypocalcemia in a Mouse Model With an Activating Calcium-Sensing Receptor (CaSR) Mutation: Relevance to Autosomal Dominant Hypocalcemia Type 1 (ADH1). *Endocrinology* **156**, 3114-3121 (2015). https://doi.org/10.1210/en.2015-1269
278. Elia, M., Crozier, C. & Neale, G. Mineral metabolism during short-term starvation in man. *Clin Chim Acta* **139**, 37-45 (1984). https://doi.org/10.1016/0009-8981(84)90190-6
279. Tyler Miller, R. Control of renal calcium, phosphate, electrolyte, and water excretion by the calcium-sensing receptor. *Best Pract Res Clin Endocrinol Metab* **27**, 345-358 (2013). https://doi.org/10.1016/j.beem.2013.04.009
280. Herraiz, C., Garcia-Borron, J.C., Jimenez-Cervantes, C. & Olivares, C. MC1R signaling. Intracellular partners and pathophysiological implications. *Biochim Biophys Acta Mol Basis Dis* **1863**, 2448-2461 (2017). https://doi.org/10.1016/j.bbadis.2017.02.027
281. Wolf Horrell, E.M., Boulanger, M.C. & D'Orazio, J.A. Melanocortin 1 Receptor: Structure, Function, and Regulation. *Front Genet* **7**, 95 (2016). https://doi.org/10.3389/fgene.2016.00095

282. Novoselova, T.V., Chan, L.F. & Clark, A.J.L. Pathophysiology of melanocortin receptors and their accessory proteins. *Best Pract Res Clin Endocrinol Metab* **32**, 93-106 (2018). https://doi.org/10.1016/j.beem.2018.02.002
283. Li, Y.Q., Shrestha, Y., Pandey, M., Chen, M., Kablan, A., Gavrilova, O., . . . Weinstein, L.S. G(q/11)alpha and G(s)alpha mediate distinct physiological responses to central melanocortins. *J Clin Invest* **126**, 40-49 (2016). https://doi.org/10.1172/JCI76348
284. Rogers, A., Nesbit, M.A., Hannan, F.M., Howles, S.A., Gorvin, C.M., Cranston, T., . . . Thakker, R.V. Mutational analysis of the adaptor protein 2 sigma subunit (AP2S1) gene: search for autosomal dominant hypocalcemia type 3 (ADH3). *J Clin Endocrinol Metab* **99**, E1300-1305 (2014). https://doi.org/10.1210/jc.2013-3909
285. Onopiuk, M., Eby, B., Nesin, V., Ngo, P., Lerner, M., Gorvin, C.M., . . . Lau, K. Control of PTH secretion by the TRPC1 ion channel. *JCI Insight* **5**(2020). https://doi.org/10.1172/jci.insight.132496
286. Wu, D.Q., Lee, C.H., Rhee, S.G. & Simon, M.I. Activation of phospholipase C by the alpha subunits of the Gq and G11 proteins in transfected Cos-7 cells. *J Biol Chem* **267**, 1811-1817 (1992). https://www.ncbi.nlm.nih.gov/pubmed/1309799
287. Shaw, W.M., Yamauchi, H., Mead, J., Gowers, G.F., Bell, D.J., Oling, D., . . . Ellis, T. Engineering a Model Cell for Rational Tuning of GPCR Signaling. *Cell* **177**, 782-796 e727 (2019). https://doi.org/10.1016/j.cell.2019.02.023
288. Offermanns, S., Toombs, C.F., Hu, Y.H. & Simon, M.I. Defective platelet activation in G alpha(q)-deficient mice. *Nature* **389**, 183-186 (1997). https://doi.org/10.1038/38284
289. Johnson, G.J., Leis, L.A. & Dunlop, P.C. Specificity of G alpha q and G alpha 11 gene expression in platelets and erythrocytes. Expressions of cellular differentiation and species differences. *Biochem J* **318 (Pt 3)**, 1023-1031 (1996). https://doi.org/10.1042/bj3181023
290. Wirotanseng, L.N., Kuner, R. & Tappe-Theodor, A. Gq rather than G11 preferentially mediates nociceptor sensitization. *Mol Pain* **9**, 54 (2013). https://doi.org/10.1186/1744-8069-9-54
291. Offermanns, S., Hashimoto, K., Watanabe, M., Sun, W., Kurihara, H., Thompson, R.F., . . . Simon, M.I. Impaired motor coordination and persistent multiple climbing fiber innervation of cerebellar Purkinje cells in mice lacking Galphaq. *Proc Natl Acad Sci U S A* **94**, 14089-14094 (1997). https://doi.org/10.1073/pnas.94.25.14089
292. Hartmann, J., Blum, R., Kovalchuk, Y., Adelsberger, H., Kuner, R., Durand, G.M., . . . Konnerth, A. Distinct roles of Galpha(q) and Galpha11 for Purkinje cell signaling and motor behavior. *J Neurosci* **24**, 5119-5130 (2004). https://doi.org/10.1523/JNEUROSCI.4193-03.2004
293. Riccardi, D., Hall, A.E., Chattopadhyay, N., Xu, J.Z., Brown, E.M. & Hebert, S.C. Localization of the extracellular Ca2+/polyvalent cation-sensing protein in rat kidney. *Am J Physiol* **274**, F611-622 (1998). https://doi.org/10.1152/ajprenal.1998.274.3.F611
294. Riccardi, D. & Brown, E.M. Physiology and pathophysiology of the calcium-sensing receptor in the kidney. *Am J Physiol Renal Physiol* **298**, F485-499 (2010). https://doi.org/10.1152/ajprenal.00608.2009
295. Wettschureck, N., Lee, E., Libutti, S.K., Offermanns, S., Robey, P.G. & Spiegel, A.M. Parathyroid-specific double knockout of Gq and G11 alpha-subunits leads to a

phenotype resembling germline knockout of the extracellular Ca2+ -sensing receptor. *Mol Endocrinol* **21**, 274-280 (2007). https://doi.org/10.1210/me.2006-0110
296. Exton, J.H. Regulation of phosphoinositide phospholipases by hormones, neurotransmitters, and other agonists linked to G proteins. *Annu Rev Pharmacol Toxicol* **36**, 481-509 (1996). https://doi.org/10.1146/annurev.pa.36.040196.002405
297. Kalinec, G., Nazarali, A.J., Hermouet, S., Xu, N. & Gutkind, J.S. Mutated alpha subunit of the Gq protein induces malignant transformation in NIH 3T3 cells. *Mol Cell Biol* **12**, 4687-4693 (1992). https://doi.org/10.1128/mcb.12.10.4687
298. Dhanasekaran, N., Tsim, S.T., Dermott, J.M. & Onesime, D. Regulation of cell proliferation by G proteins. *Oncogene* **17**, 1383-1394 (1998). https://doi.org/10.1038/sj.onc.1202242
299. Okashah, N., Wan, Q., Ghosh, S., Sandhu, M., Inoue, A., Vaidehi, N. & Lambert, N.A. Variable G protein determinants of GPCR coupling selectivity. *Proc Natl Acad Sci U S A* **116**, 12054-12059 (2019). https://doi.org/10.1073/pnas.1905993116
300. Wange, R.L., Smrcka, A.V., Sternweis, P.C. & Exton, J.H. Photoaffinity labeling of two rat liver plasma membrane proteins with [32P]gamma-azidoanilido GTP in response to vasopressin. Immunologic identification as alpha subunits of the Gq class of G proteins. *J Biol Chem* **266**, 11409-11412 (1991). https://www.ncbi.nlm.nih.gov/pubmed/1646803
301. Wu, D., Katz, A., Lee, C.H. & Simon, M.I. Activation of phospholipase C by alpha 1-adrenergic receptors is mediated by the alpha subunits of Gq family. *J Biol Chem* **267**, 25798-25802 (1992). https://www.ncbi.nlm.nih.gov/pubmed/1334487
302. Xu, X., Croy, J.T., Zeng, W., Zhao, L., Davignon, I., Popov, S., . . . Wilkie, T.M. Promiscuous coupling of receptors to Gq class alpha subunits and effector proteins in pancreatic and submandibular gland cells. *J Biol Chem* **273**, 27275-27279 (1998). https://doi.org/10.1074/jbc.273.42.27275
303. Connor, M. & Christie, M.D. Opioid receptor signalling mechanisms. *Clin Exp Pharmacol Physiol* **26**, 493-499 (1999). https://doi.org/10.1046/j.1440-1681.1999.03049.x
304. Kruse, A.C., Hu, J., Pan, A.C., Arlow, D.H., Rosenbaum, D.M., Rosemond, E., . . . Kobilka, B.K. Structure and dynamics of the M3 muscarinic acetylcholine receptor. *Nature* **482**, 552-556 (2012). https://doi.org/10.1038/nature10867
305. Wikstrom, K., Kavanagh, D.J., Reid, H.M. & Kinsella, B.T. Differential regulation of RhoA-mediated signaling by the TPalpha and TPbeta isoforms of the human thromboxane A2 receptor: independent modulation of TPalpha signaling by prostacyclin and nitric oxide. *Cell Signal* **20**, 1497-1512 (2008). https://doi.org/10.1016/j.cellsig.2008.04.006
306. Gagnon, A.W., Manning, D.R., Catani, L., Gewirtz, A., Poncz, M. & Brass, L.F. Identification of Gz alpha as a pertussis toxin-insensitive G protein in human platelets and megakaryocytes. *Blood* **78**, 1247-1253 (1991). https://www.ncbi.nlm.nih.gov/pubmed/1908722
307. Gorvin, C.M., Frost, M., Malinauskas, T., Cranston, T., Boon, H., Siebold, C., . . . Thakker, R.V. Calcium-sensing receptor residues with loss- and gain-of-function mutations are located in regions of conformational change and cause signalling bias. *Hum Mol Genet* **27**, 3720-3733 (2018). https://doi.org/10.1093/hmg/ddy263

308. Liu, A.M., Ho, M.K., Wong, C.S., Chan, J.H., Pau, A.H. & Wong, Y.H. Galpha(16/z) chimeras efficiently link a wide range of G protein-coupled receptors to calcium mobilization. *J Biomol Screen* **8**, 39-49 (2003). https://doi.org/10.1177/1087057102239665
309. Chang, W., Pratt, S., Chen, T.H., Nemeth, E., Huang, Z. & Shoback, D. Coupling of calcium receptors to inositol phosphate and cyclic AMP generation in mammalian cells and Xenopus laevis oocytes and immunodetection of receptor protein by region-specific antipeptide antisera. *J Bone Miner Res* **13**, 570-580 (1998). https://doi.org/10.1359/jbmr.1998.13.4.570
310. Kifor, O., MacLeod, R.J., Diaz, R., Bai, M., Yamaguchi, T., Yao, T., . . . Brown, E.M. Regulation of MAP kinase by calcium-sensing receptor in bovine parathyroid and CaR-transfected HEK293 cells. *Am J Physiol Renal Physiol* **280**, F291-302 (2001). https://doi.org/10.1152/ajprenal.2001.280.2.F291
311. van Unen, J., Reinhard, N.R., Yin, T., Wu, Y.I., Postma, M., Gadella, T.W. & Goedhart, J. Plasma membrane restricted RhoGEF activity is sufficient for RhoA-mediated actin polymerization. *Sci Rep* **5**, 14693 (2015). https://doi.org/10.1038/srep14693
312. Bouschet, T., Martin, S., Kanamarlapudi, V., Mundell, S. & Henley, J.M. The calcium-sensing receptor changes cell shape via a beta-arrestin-1 ARNO ARF6 ELMO protein network. *J Cell Sci* **120**, 2489-2497 (2007). https://doi.org/10.1242/jcs.03469
313. Mos, I., Jacobsen, S.E., Foster, S.R. & Brauner-Osborne, H. Calcium-Sensing Receptor Internalization Is beta-Arrestin-Dependent and Modulated by Allosteric Ligands. *Mol Pharmacol* **96**, 463-474 (2019). https://doi.org/10.1124/mol.119.116772
314. Alamshah, A., Spreckley, E., Norton, M., Kinsey-Jones, J.S., Amin, A., Ramgulam, A., . . . Murphy, K.G. l-phenylalanine modulates gut hormone release and glucose tolerance, and suppresses food intake through the calcium-sensing receptor in rodents. *Int J Obes (Lond)* **41**, 1693-1701 (2017). https://doi.org/10.1038/ijo.2017.164
315. Rodrigues, A.R., Almeida, H. & Gouveia, A.M. Intracellular signaling mechanisms of the melanocortin receptors: current state of the art. *Cell Mol Life Sci* **72**, 1331-1345 (2015). https://doi.org/10.1007/s00018-014-1800-3
316. Herraiz, C., Journe, F., Abdel-Malek, Z., Ghanem, G., Jimenez-Cervantes, C. & Garcia-Borron, J.C. Signaling from the human melanocortin 1 receptor to ERK1 and ERK2 mitogen-activated protein kinases involves transactivation of cKIT. *Mol Endocrinol* **25**, 138-156 (2011). https://doi.org/10.1210/me.2010-0217
317. Valverde, P., Healy, E., Jackson, I., Rees, J.L. & Thody, A.J. Variants of the melanocyte-stimulating hormone receptor gene are associated with red hair and fair skin in humans. *Nat Genet* **11**, 328-330 (1995). https://doi.org/10.1038/ng1195-328
318. Ericson, M.D., Lensing, C.J., Fleming, K.A., Schlasner, K.N., Doering, S.R. & Haskell-Luevano, C. Bench-top to clinical therapies: A review of melanocortin ligands from 1954 to 2016. *Biochim Biophys Acta Mol Basis Dis* **1863**, 2414-2435 (2017). https://doi.org/10.1016/j.bbadis.2017.03.020
319. Chini, B. & Parenti, M. G-protein coupled receptors in lipid rafts and caveolae: how, when and why do they go there? *J Mol Endocrinol* **32**, 325-338 (2004). https://doi.org/10.1677/jme.0.0320325

320. Thompson, A. & Kanamarlapudi, V. Agonist-induced internalisation of the glucagon-like peptide-1 receptor is mediated by the Galphaq pathway. *Biochem Pharmacol* **93**, 72-84 (2015). https://doi.org/10.1016/j.bcp.2014.10.015